Chemical Processing Science of

Ceramic Nanoparticles and Films for Biomedicine and Energy

by

Xiao Di Sun Zhou

A Dissertation Presented in Partial Fulfillment
of the Requirements for the Degree
Doctor of Philosophy

Approved November 2014 by the
Graduate Supervisory Committee:

Sandwip Dey, Chair
Stephen Krause
Vinay Janthakahalli Nagaraj
Robert Marzke

ARIZONA STATE UNIVERSITY

December 2014

ABSTRACT

The central theme of this dissertation is to understand the chemical processing science of advanced ceramic materials for biomedicine, including therapy and imaging. The secondary component focuses on the chemical processing of energy materials.

Recently, layered double hydroxide (LDH) nanoparticles (NPs) with various intercalated compounds (e.g. fluorescent molecules, radio-labeled ATP, vitamins, DNA, and drugs) have exhibited versatility and promise as a combined therapeutic and diagnostic (i.e. theranostic) vector. However, its eventual acceptance in biomedicine will be contingent on understanding the processing science, reproducibly synthesizing monodispersed NPs with controlled mean particle size (MPS), and ascertaining the efficacy of the NPs for drug delivery and imaging. First, statistical design of experiments were used to optimize the wet chemistry synthesis of (Zn, Al)-LDH NPs. A synthesis model, which allows the synthesis of nearly monodispersed NPs with controlled MPS, was developed and experimentally verified. Also, the evolution of the nanostructure was characterized, from coprecipitation to hydrothermal treatment, to identify the formation mechanisms. Next, the biocompatibility, cellular uptake and drug delivery capability of LDH NPs were studied. In an *in vitro* study, using cultured pancreatic adenocarcinoma BXPC3 cells, valproate-intercalated LDH NPs showed an improved efficacy (~50 fold) over the sodium valproate alone. Finally, Gd(DTPA)-intercalated LDH NPs were synthesized and characterized by proton (^{1}H) nuclear magnetic resonance. The longitudinal relaxivity (r_1) of 28.38 s^{-1} mM^{-1}, which is over 6 times higher than the clinically approved contrast agent, Gd(DTPA), demonstrated the potential of this vector for use in magnetic resonance imaging.

Visible light-transparent single metal-semiconductor junction devices, which convert ultraviolet photon energy into high open circuit voltage (V_{oc}>1.5-2 V), are highly desirable for transparent photovoltaics that can potentially power an electrochromic stack for smart windows. A Schottky junction solar cell, comprised of sputtered ZnO/ZnS heterojunction with Cr/Au contacts, was fabricated and a V_{oc} of ~1.35 V was measured. Also, a low-cost route to form ZnO/ZnS heterojunctions by partial sulfurization of solution-grown ZnO thin films (350 nm-5 μm thick; conductivity comparable to phosphorus-doped Si) was demonstrated. A final study was on a cathode material for Li-ion batteries. Phase-pure $LiFePO_4$ powders were synthesized by microwave-assisted sol-gel method and characterized.

To my parents and grandparents for their endless love and unconditional support

ACKNOWLEDGEMENTS

First and foremost, I would like to acknowledge my advisor and committee chair, Prof. Sandwip K. Dey—School for Engineering of Matter, Transport and Energy, Arizona State University—for his guidance and mentorship. I am grateful for his support on both a professional and a personal level over the entire period of my study. His persistent and immense dedication has greatly helped my professional development and positively influenced me towards a successful future.

Next, I would also like to thank Prof. Robert Marzke, Prof. Vinay J. Nagaraj, Prof. Hongbin Yu, Prof. Michael Goryll, Prof. Terry Alford and Prof. Stephen Krause, who have spent a great amount of time and effort on the research, given valuable discussion as well as provided help and support at different stages of my study.

Moreover, I would like to thank my friends – Tingting Gao, Jhih-Hong Peng, Cotton Rearick, Aishwarya Ramanchandran, Ebraheem Ahzar and Xiaofeng Wang for their support. My deepest appreciation goes to my friends and family who have been extremely supportive throughout my academic journey.

Finally, I would like to acknowledge financial assistance from the National Science Foundation and the National Institutes of Health-National Cancer Institute.

TABLE OF CONTENTS

Page

LIST OF TABLES

Table Page

LIST OF FIGURES

Figure Page

Figure Page

Figure Page

Figure Page

Figure Page

Figure Page

Figure Page

Figure Page

CHAPTER

1. INTRODUCTION

In modern society, health and energy are closely linked to standard of living and economy development, and have become the two most interesting and important focuses for research and development. In this present study, the central theme is the development of functional materials with advanced applications for biomedicine and energy through chemical processing.

Nanomedicine exploits the high potential of nanotechnology with a progressive understanding of molecular and cellular biology for medical benefits including therapy and diagnosis. A wide array of organic nanoparticles (NPs) and nanomaterials (e.g., polymeric NPs, liposomes, dendrimers, and protein cage architectures) are being evaluated *in vitro* and *in vivo* for their applications in biomedical research including cancer therapy and molecular imaging. However, inorganics including silica NPs, magnetic NPs, sulfide NPs, nanodiamonds, and carbon nanotubes, and quantum dots (QDs), are also making their mark. To date, some drug-loaded polymeric liposomes have already gained FDA approval, and a number of polymeric, QD, silica NP, and magnetic NP platforms, with combined therapeutic and diagnostic capabilities (i.e., theranostics) are now in various stages of preclinical and clinical development. The noteworthy features of inorganic ceramics in nanomedicine are high natural abundance, low cost, and ease of synthesis of nanoparticles with engineerable properties. Within the past one and a half decades, a number of ceramic (e.g., SiO_2, Fe_3O_4, γ-Fe_2O_3, $MnFe_2O_4$, graphitic carbon, carbon nanotubes, nanodiamond, Gd_2O_3, Na_2HPO_4-Na_2SiO_3, and Bi_2S_3)

nanoparticles, in various forms, have undergone successful *in vivo* validation as targeted theranostics.

It is clear that a multifunctional nanotech platform, whether it is in the form of NPs or nanoshells, conjugated with targeting ligands, integrated with imaging agents, or in combinations thereof, the ceramic component mainly serves one specific purpose; SiO_2 the carrier, Bi_2S_3 the X-ray CT contrast agent, or super paramagnetic NP the imaging agent; note, the latter can also have an additional purpose in magnetic targeting. However, another ceramic system, based on the layered double hydroxide (LDH) structure, is unique in the sense that built-in multifunctionality is achievable within a single phase system even prior to conjugating, incorporating, or increasing structural complexity with other phases. The prototypic LDH structure is the natural mineral, Hydrotalcite ($Mg_6Al_2(OH)_{16}CO_3{\cdot}4H_2O$), with positively charged hydroxide layers of octahedral cations (i.e., Mg^{2+}, Al^{3+}) rendered electrically neutral by electrostatically-bound anions (i.e., carbonate). The anions are intercalated within the interlayer space, with water held in place via hydrogen bonding to the hydroxyls. To date, various divalent (e.g., Mg^{2+}, $^{57}Co^{2+}$, Zn^{2+}) and trivalent (e.g., Al^{3+}, $^{67}Ga^{3+}$, Fe^{3+}, Mn^{3+}, Gd^{3+}) cations, as well as anions (e.g., nucleotides, fluorescent molecules, radio-labeled ATP, vitamins, DNA, siRNA, and drugs) have been used to synthesize phase pure and bio-hybridized LDH NPs.

However, to date, the only system that has been extensively studied in crystalline NP and mono-distributed form has been (Mg, Al)-LDH,(Costantino et al. 1998, Ogawa and Kaiho 2002, Xu et al. 2006, Zhao et al. 2002) whereas studies on other biocompatible systems with physiological relevance,(Dey and Sistiabudi 2007) e.g., (Zn, Al)-LDH are

rare despite the fact that Zn-based LDH compositions exhibit higher stability than Mg-based ones.(Boclair and Braterman 1999) Only one study, using a vortex reactor under steady-state conditions and without post-hydrothermal treatment (HT),(Chang et al. 2005) demonstrated the synthesis of $Zn_2Al(OH)_6(CO_3)_{0.5}\cdot 2H_2O$ NPs of relatively low crystallinity. Note, the synthesis window, agglomeration tendency, and stability for each system is different.(Matijevic 1994) For example, conditions that form stable NP suspensions of (Mg, Al)-LDH can cause severe aggregation of (Zn, Al)-LDH NPs.(Bellezza et al. 2009)

Moreover, the lack of understanding of the formation pathways makes the controlled synthesis almost impossible and severely hinders the potential applications of other biocompatible LDH systems in biomedicine. The formation mechanisms of LDH NPs coupled with strong experimental evidence are yet to be revealed.

From LDH NPs for drug delivery application point of view, numerous studies have focused on using (Mg, Al)-based LDH NPs for gene and drug delivery. The main drawback stems from its initial burst. Several studies have studied the drug release profile and showed that a strong initial burst often takes place and make them not ideal for being the core materials of a nanovector. Khan et. al showed that at pH 7, almost 100% gembibrozil was released from gembibrozil-intercalated $[LiAl_2(OH)_6]$ LDH within 10 mins,(Khan and O'Hare 2002) and for the (Mg, Al)-based LDH, even at pH =8, 80% of Ibuprofen was released from (Mg, Al)-Abuprofen LDH after 10 mins.(Li et al. Inorganic layered double hydroxides as a drug delivery system - intercalation and in vitro release of fenbufen 2004) Strategy such as enteric-coating showed effective remediation to the problem,(Li et al. Enteric-coated layered double hydroxides as a controlled release drug

delivery system 2004) however the positively charged surface was being altered and agglomeration took place. The exploration of other biocompatible composition is rare.

Imaging contrast is another critical area that can provide significant benefits to early cancer detection. Following the discovery of the considerable increase in proton relaxation times (both T_1 and T_2) for malignant tumor tissues compared to normal tissues in 1971,(Damadian 1971) magnetic resonance imaging (MRI) –a noninvasive diagnostic technique– has been developed and clinically used to provide the superb spatial resolution and the excellent capacity of distinguishing soft tissues. However, there is often only a very small variation in relaxation times between healthy and early staged pathological regions. The use of clinically approved contrast agents, such as Magnevist® $[Gd(DTPA)(H_2O)]^{2-}$ and Dotarem® $[Gd(DOTA)(H_2O)]^{-}$, etc.,(Caravan et al. 1999) is highly beneficial for increasing the sensitivity of technique.(Aime, Botta, and Terreno 2005) With the advent of nanotechnology to biomedicine, nanovector-based contrast agents have attracted enormous research efforts. By endowing the core nanomaterials with multifunctionalities, i.e., therapeutic drug/imaging agent carrying, selective (multi)targeting, and biological surface modifying capabilities, they are considered a highly potential answer for the early detection of precancerous and neoplastic lesions.(Ferrari 2005) Both the morphology and the composition of the core nanomaterials are decisive for the relaxation times (both T_1 and T_2) of the resultant nanoparticle (NP)-based contrast agents. The exploration of LDH NP-based MRI contrast agent is of interest.

The studies in the first part of this dissertation aim to answer all those unresolved questions and explore the potential application of LDH NP-based for drug delivery and imaging contrast agents. The specific objectives are to:

(i) Develop a wet-chemistry "bottom-up" synthesis method for controlled syntheses of single crystalline biocompatible Cl^- intercalated (Zn, Al)-LDH NPs (between ~200-500 nm and with narrow size distribution) through a systematic optimization approach using statistic design of experiments.

(ii) Understand the underlying individual formation steps behind both the coprecipitation and the HT stages, and unearth the critical factors for obtaining LDH NPs of monodispersed particle size distribution.

(iii) Evaluate the stability of the LDH NPs of other biocompatible compositions, such as (Zn, Al)-based LDH NPs, in physiological-like condition for the development of the nanovectors, study its cell uptaking mechanisms, and prove the efficacy of this drug delivery platform by cell viability studies, i.e., treating the pancreatic cancer cell (BXPC3) with valproate (VP^-)-intercalated (Zn, Al)-LDH NPs, compared to using VP^- alone.

(iv) Develop the LDH NP-based contrast agent by the intercalation of $Gd(DTPA)^{2-}$, and evaluate the longitudinal relaxivity. By using this system as a successful model of NP-based contrast agent, discussions of the driving force for the relaxivity increase and critical factors are exposed with strong experimental support.

Along with biomedicine, research on materials for energy applications has also been extremely important. In modern societies, rapid economic development and

improvements in standard of living are constantly requiring increasing energy consumption. Excessive reliance on fossil fuels is causing serious atmospheric imbalances. Global warming, toxic gas emissions from fossil fuel combustion, diminishing finite resources, and pollution-related health issues are pushing for at least partial replacement of carbon-based fuels by renewable, sustainable, and environment-friendly energy sources. The second part of this dissertation focuses on the development of semiconductor materials for solar-cell applications, and Li-intercalatable electrode material for Li-ion battery applications.

Photovoltaics are a promising way of converting between photonic and electrical energy. As a more cost-effective alternative synthesis method to the vacuum technique for the fabrication of semiconductor materials, solution synthesis has been used to synthesize ZnO (intrinsic n-type semiconductor with 3.37 eV direct band gap) nanorods and thin-films. In order to feature the electrochromic window self-powering capability, visible-light transparent solar cells using large band-gap materials, such as ZnO, ZnS, and large open circuit voltages (V_{oc}), i.e., >1.5 V, are highly desirable. It has been reported that the Schottky barrier height of ZnO-Pt is 0.75 V, however, ZnS (sphalerite)-Au and ZnS (sphalerite)-Cu contacts are reported to have as high as 2.00 V and 1.75 V, respectively. The much higher barrier heights ZnS-based Schottky diodes can translate into a higher V_{oc}. The central theme of this study is to demonstrate the proof-of-concept that a high open circuit voltage of a Schottky diode solar cell formed by ZnO/ZnS thin film with Au or Cu can be obtained.

The intermittent nature of renewable energy sources is generating a pressing need for electrical energy storage systems to balance supply with demand. Rechargeable

batteries provide a very promising way of converting between chemical and electrical energy. Since the commercialization of Li-ion batteries by Sony in the early 90s, they have outmatched other rechargeable battery chemistry, such as lead acid, nickel-cadmium and nickel metal hydride systems. The high cell voltages (≈ 4 V) guarantee both higher volumetric and gravimetric energy densities, as shown in Figure 1.1.

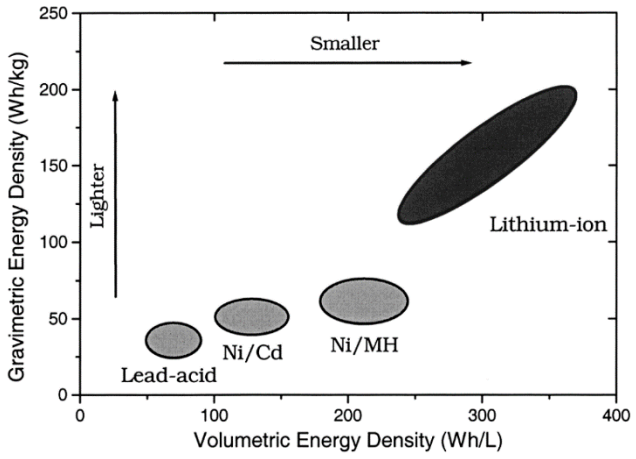

Figure 1.1. Comparison of the gravimetric and volumetric energy densities of various rechargeable battery systems(Nazri and Pistola 2009)

Although the current Li-ion technologies have dominated the market of low to moderate power portable electronic devices, they fall short of meeting the need of high power applications such as stationary renewable energy storages and transportation (like electric vehicles). To date (Dec, 2012), electric cars, such as the Nissan Leaf and Peugeot Ion, tend to cost more than £30,000, mainly due to battery cost. However, the electrified travel ranges are only around 80 miles. Furthermore, it takes about 13 hours to fully charge an empty battery and the estimated battery life is 5-10 years under ideal conditions. From a technological point of view, the key challenges in future Li-ion battery research would be exploration of new Li-ion battery chemistry, improvement of charge/discharge rates, gravimetric and volumetric energy densities, cyclability and

safety. In addition, electrodes need to be made of sustainable and environment-friendly elements. From an economic point of view, the main challenge of Li-ion battery concentrates on the cost-effectiveness, where both material and manufacturing costs become decisive. Cost-effectiveness is critical to large form batteries (one to hundreds of kWh) for electric or hybrid vehicles. Almost all the manufacturers have chosen the Li-ion battery chemistry based on carbon (C) anode and $LiCoO_2$ cathode. However, expensive Co becomes cost-prohibitive for large form batteries. At this moment, the less expensive alternative chemistry, C-based anode and $LiMnO_2$-based cathode, is chosen for electric vehicles. The up-to-date cost is about $600/kWh. According to Ford Motor Company, in order to make the use of Li-ion batteries in transportation economically viable, it is vital to cut down the battery cost to < $100/kWh.

Among many cathode materials for Li/Li-ion batteries, the olivine $LiFePO_4$, a serious competitor of $LiMnO_2$ cathode for the electric vehicle application, is attracting much attention. Currently, it is being commercially used for industrial products by Black and Decker's DeWalt brand, Fisker Karma, Cessna and BAE Systems. The inexpensive and sustainable Fe-based composition allows it to be less toxic than Co, Ni and Mn-based systems. In addition, from safety, cyclability and shelf life points of view, a cathode with a relatively lower voltage (3 to 4 V) is desirable, and $LiFePO_4$ has a flat discharge voltage of 3.3 V vs. Li^+/Li. Among several necessities of this system for improvement, there is a need for a low cost and time-saving manufacturing process.

Microwave dielectric heating is considered energy-efficient, and has been applied to the synthesis of $LiFePO_4$. Several works have reported obtaining $LiFePO_4$ by microwave heating for very short periods of time (several minutes).(Beninati, Damen,

and Mastragostino 2008, Gallis and Landry 2001, Guo, Zhan, and Zhou 2009, Higuchi et al. 2003, Park et al. 2003, Song et al. 2007, Song et al. 2008, Uematsu et al. 2007, Wang et al. Nano-$LiFePO_4$/MWCNT cathode materials prepared by room-temperature solid-state reaction and microwave heating 2007, Preparation and characterization of nano-sized $LiFePO_4$ by low heating solid-state coordination method and microwave heating 2007, Zou, Zhang, and Shen 2010) However, the resulting phase purity and electrochemical performance are not ideal. The motivation of the current study is to prove microwave heating efficiency and cut down the thermal budget for the $LiFePO_4$ synthesis by coupling the polymeric $LiFePO_4$ precursor synthesized by modified Pechini's method with the microwave heat treatment of short duration (several minutes) at a relatively low temperature (< 700 °C).

CHAPTER

2. LAYERE DOUBLE HYDROXIDE NANOPARTICLES FOR BIOMEDICINE

2.1 Background

2.1.1 Basic Structure

Layered double hydroxides (LDHs) LDHs were approached from the fields of mineralogy and descriptive inorganic chemistry. Minerals of the hydrotalcite and pyroaurite family had been known since mid-19th century and were described by 1910. In the late 1930s and 1940s, Feitknecht extensively reported the preparation of such materials, but erroneously regarded them as double layer materials where the Mg-rich and Al-rich layers alternated. The structure was not correctly identified until 1967 when it was realized that the layered structure was one containing both kinds of metal ion.

LDHs are well-known as excellent anion hosts, and can be found as natural minerals or readily synthesized in the laboratory. The prototypic LDH structure is the natural mineral, hydrotalcite [$Mg_{0.75}Al_{0.25}(OH)_2(CO_3)_{0.125}{\cdot}0.5H_2O$]. The isomorphous substitution of Mg^{2+} of the brucite layer -$(Mg(OH)_2)_n$- by Al^{3+} endows the hydroxide layer positive charges, and electrical neutrality is rendered by electrostatically-bound anions (i.e. CO_3^{2-}) within the interlayer region, as shown in Figure 2.1.

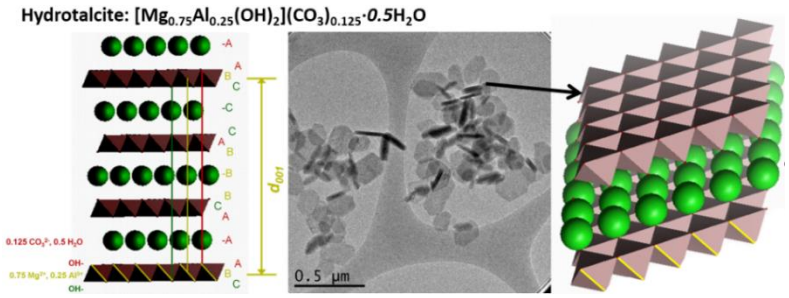

Figure 2.1. Schematic representation of the hydrotalcite nanoparticle: three-dimensional structure and the corresponding bright field TEM micrograph

The general empirical formula of LDH can be denoted as $[M^{II}_{x}M^{III}\ (OH)_{2+2x}]^{+}\ (A^{a-})_{1/a}\cdot mH_2O$ (x = 1-5 typically), where M^{II} and M^{III} are divalent and trivalent cations (e.g., $M^{II} = Mg^{2+}$, Co^{2+}, Zn^{2+}; $M^{III} = Al^{3+}$, Ga^{3+}, Fe^{3+}, Mn^{3+}, Gd^{3+}, etc.), A^{a-} an anion with a negative charges. Here, the M^{II} is octahedrally surrounded by 6 OH^{-}, and the different octahedrons share edges to form an M^{II} hydroxide layer. Isomorphous substitution of the M^{II} by M^{III} furnishes the layer with positive charges, which are then neutralized by the exchangeable anions intercalated between the successive double hydroxide layers, together with water held in the interlayer gallery via hydrogen bonding to the hydroxyls. Note, the charge density is proportional to the molar ratio of M^{III} : (M^{II} + M^{III}) in the hydroxide layer, which can be estimated from the formula $C_d = xe/(a^2 \sin 60°)$, where x is the molar ratio of M^{III} : (M^{II} + M^{III}), a is distance between two nearest OH^{-} ions in the two opposite side layer (refer to the length between OH^{-} of the stack A and C in Figure 2.1).

2.1.2 The Hydroxide Layers

In general, the positively charged hydroxide layer of an LDH material contains the hydroxides of two or more different kinds of metals cations, i.e., cations with oxidation states of 2+ and 3+. A number of combinations of the divalent and trivalent cations can form LDHs with the only requirement that their radii can not to be too different from those of Mg^{2+} and Al^{3+}. Table 2.1 lists the ionic radii of some cations with coordination number of 6 (Braterman, Xu, and Yarberry 2004)

Cations with large radii can be incorporated into the brucite-like layer by combining them with other divalent or trivalent cations with distortion of the close-

stacking configuration, e.g., (Mg, Cd, Al)-LDH and (Mg, Al, La)-LDH. Some tetravalent cations have also replaced part of the trivalent cations in LDH compounds.(Taylor 1984, Velu et al. 1997, Velu et al. 1998, Velu et al. 1999) LDH compounds formed by monovalent cations, Li or $Li_{1-x}Na_x$ along with Al have also been reported.(Serna, Rendon, and Iglesias 1982, Thiel, Chiang, and Poeppelmeier 1993) Moreover, LDH formed by multimetal ions, such as (Cu, Zn, Co, Al, Cr)- and (Cu, Zn, Co, Cr)-LDHs have been reported.(Morpurgo, Lojacono, and Porta 1995, Morpurgo, LoJacono, and Porta 1996, Porta and Morpurgo 1995)

Table 2.1. Ionic radii of some cations with coordination number 6

Cation	**Radius (nm)**	**Cation**	**Radius (nm)**
Li^+	0.076	Fe^{3+}	0.055
Na^+	0.102	Mn^{3+}	0.058
Fe^{2+}	0.061	Ga^{3+}	0.062
Co^{2+}	0.065	Rh^{3+}	0.067
Ni^{2+}	0.069	Ru^{3+}	0.068
Mg^{2+}	0.072	Cr^{3+}	0.069
Cu^{2+}	0.073	V^{3+}	0.074
Zn^{2+}	0.074	In^{3+}	0.080
Mn^{2+}	0.083	Y^{3+}	0.090
Pd^{2+}	0.086	La^{3+}	0.103
Ti^{2+}	0.086	V^{4+}	0.058
Cd^{2+}	0.095	Ti^{4+}	0.061
Ca^{2+}	0.100	Sn^{4+}	0.069
Al^{3+}	0.054	Zr^{4+}	0.072
Co^{3+}	0.055		

2.1.3 Intercalated Anions

A wide variety of anions with different geometry, dimensions, and charges have been intercalated into the LDH compounds. The only requirement is that the anions do not extract the metal ions from the hydroxide layer and have a sufficient negative charge. The intercalated anions are exchangeable, with the increasing stability being:

$NO_3^- < Br^- < Cl^- < F^- < OH^- < MoO_4^{2-} < SO_4^{2-} < CrO_4^{2-} < HAsO_4^{2-} < HPO_4^{2-} < CO_3^{2-}$

The intercalated anions mainly can be classified as:

(i) Inorganic anions: halides, CO_3^{2-}, NO_3^-, OH^-, SO_4^{2-}, $Al(OH)_4^-$ or H_2AlO^-, etc.

(ii) Organic anions: carboxylates, dicarboxylates,glycolate, glycerolate, and organic dyes, etc.

(iii) Poymeric anions: poly(vinylsulonate), poly(acrylate), and polystyrene oligomer, etc.

(iv) Anionic comples: $CoCl_4^{2-}$, $NiCl_4^{2-}$, $IrCl_6^{2-}$, $Fe(CN)_6^{4-}$, $Fe(CN)_6^{3-}$, etc.

(v) Metal complexes with macrocyclic ligands: Cu^{2+}, Co^{2+}, Mn^{3+}, and Zn^{2+} complexes with porphyrin and phthalocyanine derivatives, etc.

(vi) Anionic biomolecules: DNA with 500-1000 base pairs, CMP, AMP, GMP, ATP, ADP, etc.

The interlayer spacing change (contraction or expansion) of the d_{003} due to the intercalation can be clearly reflected in the X-ray diffraction patterns. By assuming the thickness of the brucite-like layer being 0.480 nm, the spacing occupied by the anion (gallery height) and the orientation of the intercalated anion can be inferred.

2.1.4 Water Molecules in LDHs

LDH compounds contain water molecules within the gallery spacing, where they are not occupied by anions. We call those water molecules inherent water molecules. They are held by hydrogen bonds with the hydroxide layer and/or intercalated anions. Moreover, the water content may change with the gallery spacing and whether the LDH is hydrated, i.e., within aqueous solution. Typically, the inherent water can be expelled

from the LDH gallery spacing at T higher than 120 °C while the weakly adsorbed surface water can be removed at 100 °C.

The inelastic neutron scattering investigation by Kagunya et al. shows that the water molecules in the interlayer are not fixed in one position but rotate freely and move about hydroxide oxygen sites within a restricted volume. It is envisaged that rapid formation and breaking of hydrogen bonds take place as the water molecules hop from one hydrogen bonding site to another. (Kagunya, Dutta, and Lei 1997) They also determined by Raman spectroscopy that there are 3 types of structured water: (a) water bonded to the intercalated carbonate (b) water bonded to the hydroxyl surface, and interlamellar water.(Johnson et al. 2002)

2.1.5 Synthesis of LDH Nanoparticles

Almost all the synthesis methods follow the same chemical reactions: base-salt precipitation reaction. However, the exact resulting product, including the phase purity, crystallinity, particle size and morphology, is highly dependent on the synthesis details. The most studied synthesis methods are listed below:

(i) Precipitation in aqueous environment: This method consists of mixing an aqueous solution of salts of two metal cations, in the presence of the desired anion, and a base. When the synthesis is carried out under increasing pH route, i.e., by adding base solution into a salt solution that contains 2 kinds of metal cations and anion, it is proven that the formation of the final LDH phase underwent through $M(OH)_3$, due to the difference of K_{sp} of $M(OH)_3$ and

$M(OH)_2$.(Boclair and Braterman 1999). Although the formation of LDH phase is favored over the individual hydroxides.

(ii) Coprecipitation at constant pH method: In order to minimize the formation of $M(OH)_3$ or to avoid the formation of such intermediate product during the precipitation under increasing pH condition, simultaneous coprecipitation of the salt solution and base solution at constant pH is considered as a more refined method. Typically, the as synthesized materials are quite amorphous; HT and microwave treatments can improve the crystallinity significantly.

(iii) Hydration of metal oxides and hydroxides: This method involves the hydration of metal oxides and/or hydroxides in the presence of anion. The reaction presumably goes through a dissolution/precipitation process.

(iv) Sol-gel method: A solution of metal alkoxides undergoes through hydrolysis, then polymerization process by adding water slowly. The advantages of this method are the good homogeneity, relatively good control of stoichiometry, and high surface and high porosity.

(v) Salt-oxide method: LDH materials have been shown to form by mixing an aqueous metal salt solution with another metal oxide/hydroxide. The proposed chemical reaction is:

$$M^{II}O + xM^{III}X^{m-}_{3/m} + (n+1)H_2O \rightarrow M^{II}_{1-x}M^{III}_{x}(OH)_2X^{m-}_{x/m}\cdot nH_2O + xM^{II}X^{m-}_{2/m}$$

All those synthesis methods are proven to be viable for the synthesis of LDH materials in bulk form. To date, the only system that has been extensively studied in crystalline NP and mono-distributed form has been (Mg, Al)-LDH.(Costantino et al. 1998, Ogawa and Kaiho 2002, Xu et al. 2006, Zhao et al. 2002) The typical synthesis method is by

coprecipitation followed by aging at different T and duration. As Figure 2.2 shows, homogeneous particles with hexagonal or round plate-like NPs were obtained. The resulted NPs are polycrystalline (Mg, Al)-LDH NPs.

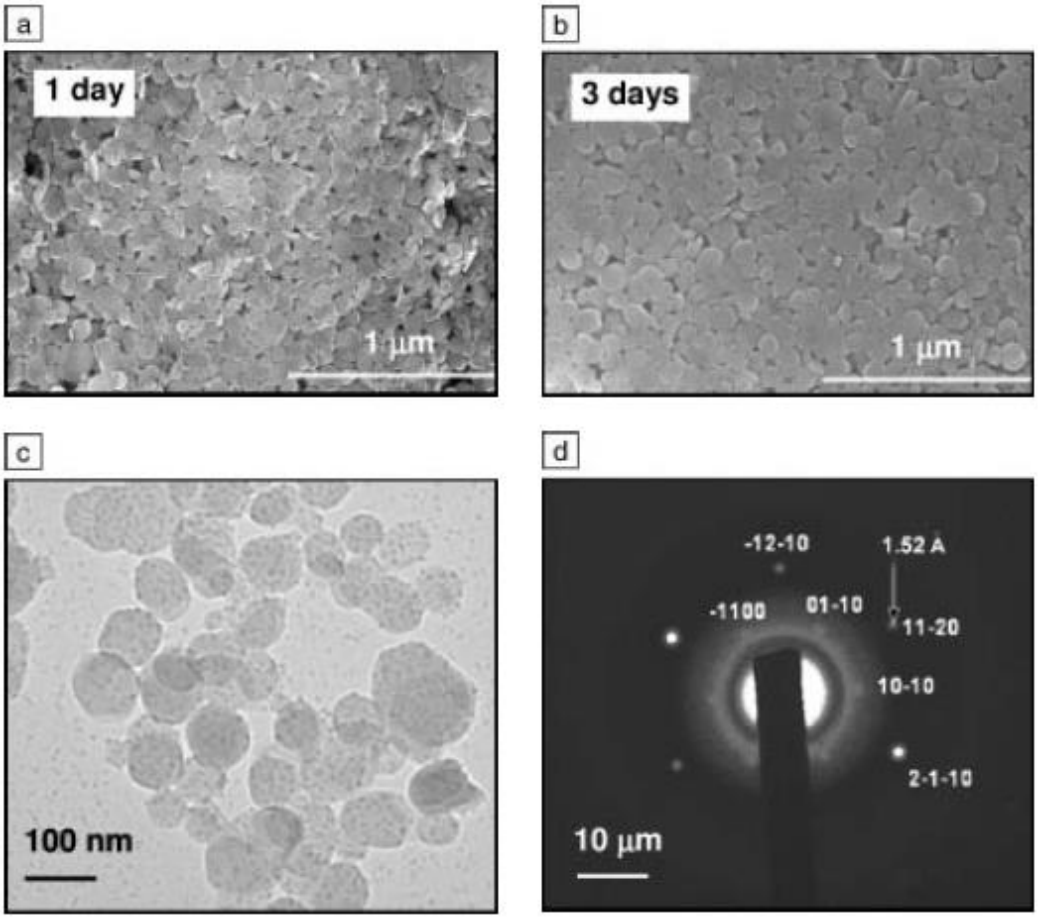

Figure 2.2. SEM micrographs of (Mg, Al)-LDH NPs, synthesized by coprecipitation method followed by aging at room temperature for different duration, are shown in (a) and (b); bright field TEM micrograph in (c) and the corresponding diffraction pattern in (d)

In contrast, studies on other biocompatible systems with physiological relevance,(Dey and Sistiabudi 2007) e.g., (Zn, Al)-LDH, are rare despite the fact that Zn-based LDH compositions exhibit higher stability than Mg-based ones.(Boclair and Braterman 1999)

2.1.6 LDH for Biomedicine Application

Although LDHs are well known for their anion-intercalating capability, the traditional applications in bulk form have been in the areas of catalysis, catalyst support, environmental remediation, and ceramic precursor.(Cantrell et al. 2005, Cavani, Trifiro, and Vaccari 1991, Newman and Jones 1998, Sels et al. 1999, Sels, De Vos, and Jacobs 2001, Vaccari 1999)

Since 2001, LDH particles have been evaluated as a potential vector for drug and non-viral gene delivery. Various kinds of inorganic or organic anions, such as, nucleoside monophosphates, ATP, DNA, fluorescein 5-isothiochyanante, FITC, antisense oligonucleotides, have been intercalated into the structure by ion-exchange method to form bio-LDH nanohybrides. (Choy et al. Inorganic layered double hydroxides as nonviral vectors 2000, Choy et al. 1999, Choy et al. Layered double hydroxide as gene reservoir 2000, Khan et al. 2001) The biomolecules within the LDH material can be released easily if the pH becomes acidic. When the pH is lower than the stable pH value for the LDH material, typically at pH below 4, the release occurs with the disintegration of the LDH material. Another release mechanism could take place if other anions are replacing the biomolecules through ion exchanging.

Choy et al.(Choy et al. Inorganic layered double hydroxides as nonviral vectors 2000) intercalated a variety of biomolecules into (Mg, Al)-LDH and the schematic illustration of the intercalation and expected transfection route is shown in Figure 2.3.

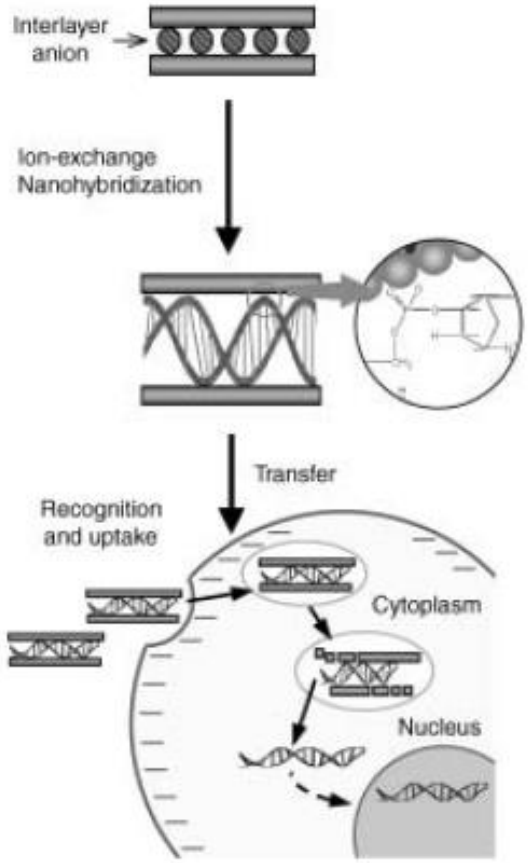

Figure 2.3. Interlayer gallery spacing expansion due to the intercalation of a variety of biomolecules, and the expected transfection route into the cell

Laser confocal fluorescence microcopy and FITC-intercalated (Mg, Al)-LDH NPs were used to investigate the transfection of the LDH into cell.(Choy et al. Inorganic layered double hydroxides as nonviral vectors 2000) As shown in Figure 2.4, the fluorophores were detected in cells within an hour and the intensity increased until 8 hours after the incubation. The fluorophores mainly distributed in the non-nuclear region of the cells. In contrast, cells incubated with 5 mM FTIC only, no fluorophores were observed regardless of the incubation time.

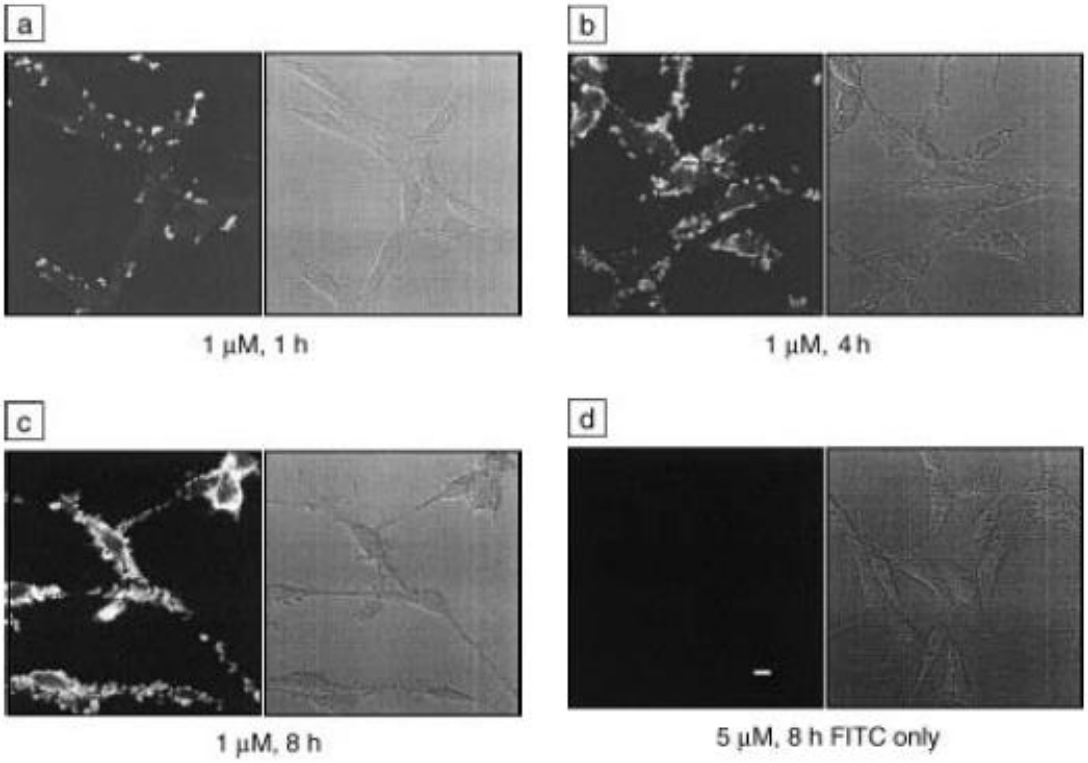

Figure 2.4. Laser confocal fluorescence microscopy images of cellular uptake using FITC-LDH as a probe

The expression experiment of the biomolecule-intercalated (Mg, Al)-LDH in cell was carried out by treating the human promyelocytic leukemia cells with c-myc antisense oligonucleotide-intercalated (Mg, Al)-LDH compared to treatment with As-myc antisense oligonucleotide alone.(Wickstrom et al. 1988) The cell viability was determined by an MTT assay. As shown in Figure 2.5, c-myc antisense oligonucleotide alone showed a very limited inhibition efficacy on the growth of the leukemia cells compared to c-myc antisense oligonucleotide-LDH. It is considered that the LDH materials offer a better protection preventing the c-myc antisense oligonucleotide from being degraded by intracellular nucleases.

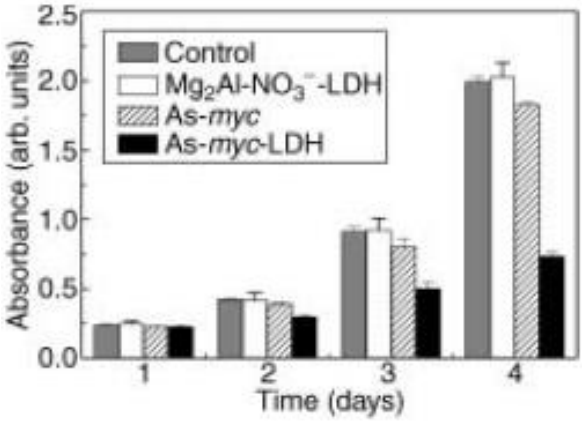

Figure 2.5. Comparison between the effect of c-myc antisense oligonucleotide-LDH and c-myc antisense oligonucleotide alone on the growth of the human promyelocytic leukemia cells.

In summary, (Mg, Al)-LDH nanoparticles (NPs) with different intercalated compounds have exhibited versatility and promise in biomedicine as a theranostic vector, i.e., having therapeutic and imaging attributes.(Choy et al. Inorganic layered double hydroxides as nonviral vectors 2000, Del Hoyo 2007, H. C. Huang et al. 2011, Kriven et al. 2004, Li et al. 2013, Panda and Bahadur 2012, Wang et al. 2013) For example, several *in vivo* multimodal imaging studies(Musumeci et al. 2010, Wei et al. 2012) and a number of *in vivo* studies, using animal models to determine the pharmacokinetics, toxicity, transfection efficiency, and therapeutic efficacy of LDH, have been reported.(Li et al. 2011, Qin et al. 2010, Silion et al. 2010)

2.1.7. Unresolved Issues for LDH to Become a Successful Nanovector

The recent significant progress in fundamental cancer biology has not yielded even remotely comparable clinical benefits. The main responsible problem is the yet unsolved targeted drug/imaging contrast agent delivery. Ideally, the therapeutic drugs or

imaging contrast formulations can reach to the targeted sites accompanied with only marginal or no collateral damages to the healthy tissues.

Nanotechnology is expected to be able to meet these challenges if appropriate NP-based theranostic (i.e. having both therapeutic and diagnostic attributes) agents can be developed and integrated into the current cancer research. In 2005, Mauro Ferrari proposed a model of multifunctional nanoparticles (shown in Figure 2.6).(Ferrari 2005) An ideal nanovector would have at least 3 main constituents: a NP core material, a therapeutic and/or imaging formulation, and biological surface modifiers, which can attain the desired biodistribution and tumor targeting capability.

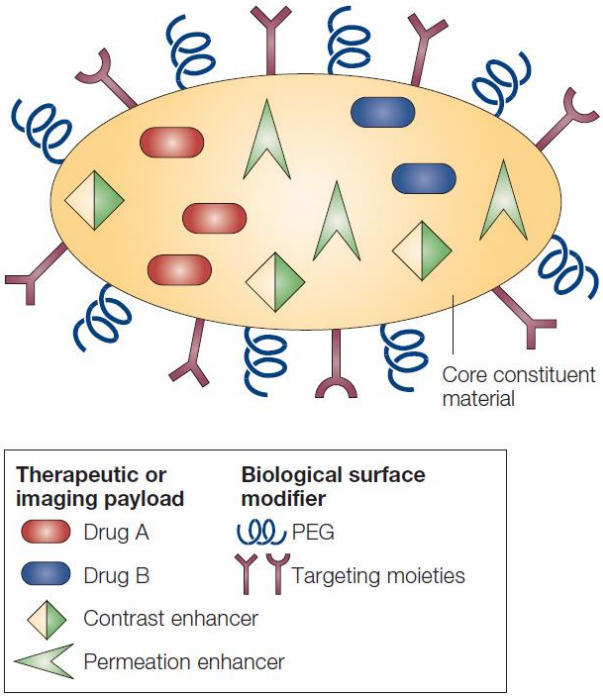

Figure 2.6. Schematic representation of an ideal nanovector

Recently, LDH NPs with different intercalated compounds have exhibited versatility and promise in biomedicine as a theranostic vector. However, to date, only the synthesis of (Mg, Al)-LDH NPs has been extensively studied in order to obtain

crystalline NP and mono-distributed particle size distribution,(Costantino et al. 1998, Ogawa and Kaiho 2002, Xu et al. 2006, Zhao et al. 2002) From LDH NPs for a drug delivery application point of view numerous studies have focused on using (Mg, Al)-based LDH NPs for gene and drug delivery due to the ease of synthesis. The main drawback of (Mg, Al)-LDH system stems from its initial burst. Several studies have studied the drug release profile and showed that a strong initial burst often takes place and makes them not ideal for being the core materials of a nanovector. Khan et. al showed that at pH 7, almost 100% gembibrozil was released from gembibrozil-intercalated $[LiAl_2(OH)_6]$ LDH within 10 mins,(Khan and O'Hare 2002) and for the (Mg, Al)-based LDH, even at pH =8, 80% of Ibuprofen was released from (Mg, Al)-Abuprofen LDH after 10 mins.(Li et al. Inorganic layered double hydroxides as a drug delivery system - intercalation and in vitro release of fenbufen 2004) Strategy such as using enteric-coating showed effective remediation to the problem,(Li et al. Enteric-coated layered double hydroxides as a controlled release drug delivery system 2004) however the positively charged surface was being altered and agglomeration took place.

Whereas studies on other biocompatible systems with physiological relevance,(Dey and Sistiabudi 2007) e.g., (Zn, Al)-LDH, are rare despite the fact that Zn-based LDH compositions exhibit higher stability than Mg-based ones.(Boclair and Braterman 1999) Only one study, using a vortex reactor under steady-state conditions and without post-HT treatment,(Chang et al. 2005) demonstrated the synthesis of $Zn_2Al(OH)_6(CO_3)_{0.5}\cdot 2H_2O$ NPs of relatively low crystallinity. Note, the synthesis window, agglomeration tendency, and stability for each system can be very

different.(Matijevic 1994) For example, conditions that form stable NP suspensions of (Mg, Al)-LDH can cause severe aggregation of (Zn, Al)-LDH NPs.(Bellezza et al. 2009)

Moreover, the lack of understanding the formation pathways makes the controlled synthesis almost impossible and severely hinders the potential applications of other biocompatible LDH systems in biomedicine. The formation mechanisms of LDH NPs coupled with strong experimental evidence are yet to be revealed.

In addition, in order to achieve multifunctionality, a part of its intercalation capability of hosting therapeutic drugs, the surface functionalization is of significant importance for having decisive impact on the pharmacokinetics, biodistributions and the cellular uptake mechanisms. Hence, the stability of the core material under physiological alike environment is critical to avoid partial or complete loss of surface functionalized moieties. The early stage partial dissolution of the (Mg, Al)-based LDH NPs when re-dispersed in deionized water can lead to two main drawbacks that are uncontrolled pre-release of loaded drug before reaching the target sites, and the partial or complete loss of surface targeting moieties, and question this composition as the most ideal LDH core material for nanovector development.

Furthermore, using LDH NPs as imaging contrast agent carrier has not been systematically studied a part of a couple of random reports.(Kim et al. 2008, Xu et al. 2007). Systematic evaluation of using this platform as contrast imaging formulation delivery is of imperative need.

Last but not least, a wide array of organic NPs and nanomaterials (e.g., polymeric NPs, liposomes, dendrimers, and protein cage architectures) are currently being evaluated *in vitro* and *in vivo* for their applications in biomedical research including cancer therapy

and molecular imaging. Inorganics including silica NPs, magnetic NPs, sulfide NPs, nanodiamonds, and carbon nanotubes, and quantum dots (QDs), are also making their mark. To date, some drug-loaded polymeric liposomes have already gained FDA approval, and a number of polymeric, QD, silica NP, and magnetic NP theranostic platforms are now in various stages of preclinical and clinical development. The noteworthy features of inorganic ceramics in nanomedicine are high natural abundance, low cost, and ease of synthesis of nanoparticles with engineerable properties. Within the past one and a half decade, a number of ceramic (e.g., SiO_2, Fe_3O_4, γ-Fe_2O_3, $MnFe_2O_4$, graphitic carbon, carbon nanotubes, nanodiamond, Gd_2O_3, Na_2HPO_4-Na_2SiO_3, and Bi_2S_3) nanoparticles, in various embodiments, have undergone successful *in vivo* validation as targeted theranostics. In order for LDH NP to compete with other platforms and become a successful nanovector, all above described issues need to be assessed and overcome. An ideal multifunctional LDH NP-based core/shell nanovector needs to be developed as proposed in Figure 2.7.

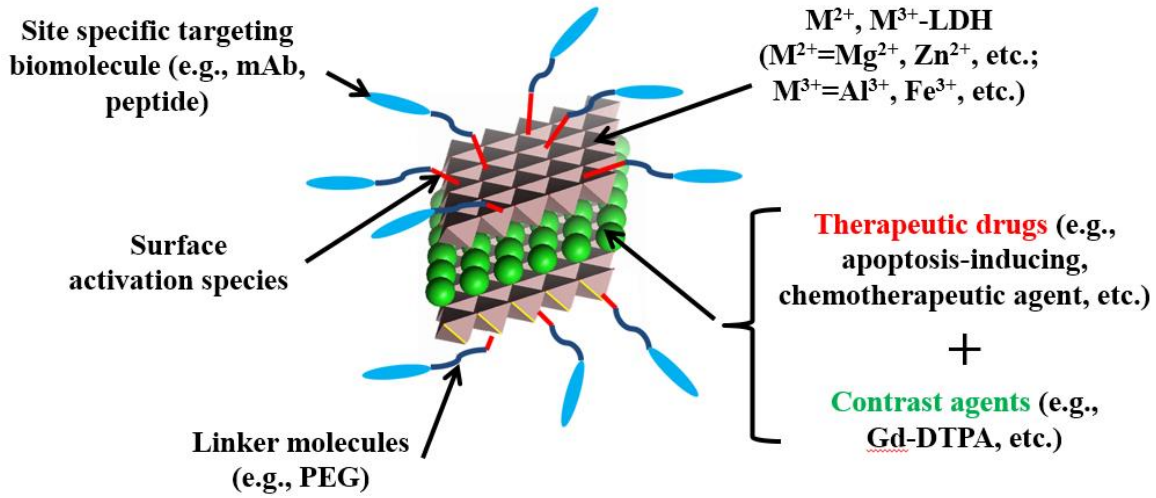

Figure 2.7. Schematic representation of an ideal multifunctional LDH NP-based theranostic nanovector

2.2 Optimization by Statistical Design of Experiments and Controlled Synthesis of Layered Double Hydroxide Nanoparticles

2.2.1 Abstract

Layered double hydroxide (LDH) nanoparticles (NPs) have excellent anion-intercalating property, and their potential as theranostic nanovectors for biomedical applications is high. However, understanding the control of the mean particle size (MPS) and achievement of monodispersed particle size distribution (PSD) remains elusive. Herein, with the aid of statistical design of experiments on a model system of Cl^--intercalated (Zn, Al)-LDH, controlled synthesis of single crystalline NPs by coprecipitation method followed by hydrothermal treatment (HT) was achieved in three steps. First, a 2^{4-1} design enabled the identification of influential parameters for MPS (i.e. salt concentration, molar ratio of carbonate to aluminum, solution addition rate, and interaction between salt concentration and stirring rate) and PSD (i.e. salt concentration and stirring rate), as well as the optimum coprecipitation conditions that achieve a monodispersed PSD (i.e. low salt concentration and high stirring rate). Second, a preliminary explanation of the HT is suggested and the optimum HT conditions for obtaining ideal Gaussian PSD, i.e. chi-squared (χ^2) < 3, were found to be 85 °C for 5 h. Third, using a central composite design, a quantitative MPS model, expressed in terms of the significant factors, was developed and experimentally verified to synthesize nearly monodispersed LDH NPs with MPS ~ 200-500 nm. Additionally, the suitable range of the Zn to Al molar ratio for obtaining stable colloidal suspensions of Cl^--intercalated (Zn, Al)-LDH was determined to be 1-3. Moreover, the optimized synthesis conditions were extended to synthesize NO_3^--intercalated (Mg, Al)-LDH NPs with a monodispersed PSD, but the significant MPS shifts indicated the importance of the type of cations and the polarization of the $M^{II/III}$-OH bonds.

2.2.2 Introduction

Hydrotalcite-like layered double hydroxide (LDH) materials are well-known for their anion-intercalating properties, and the general empirical formula can be denoted as $[M^{II}_{n}M^{III}(OH)_{2+2n}]^{+}(A^{\alpha-})_{1/\alpha}\cdot xH_2O$ (with n = 1 - 5), where M^{II} and M^{III} are divalent and trivalent cations (e.g. $M^{II} = Mg^{2+}$, Co^{2+}, Zn^{2+}; $M^{III} = Al^{3+}$, Ga^{3+}, Fe^{3+}, Mn^{3+}, Gd^{3+}, etc.), and $A^{\alpha-}$ is an anion with a negative charge of α. Here, the M^{II} is octahedrally coordinated by OH^{-}, with the octahedra sharing edges to form the M^{II} hydroxide layer. The isomorphous substitution of M^{II} by M^{III} renders the layer with positive charges, which are then neutralized by exchangeable anions intercalated between the successive double hydroxide layers, together with water held in the interlayer gallery via hydrogen bonding to the hydroxyls.(Allmann 1970) Their applications in bulk form have been in the areas of catalysis, catalyst support, environmental remediation, and ceramic precursor.(Cantrell et al. 2005, Cavani, Trifiro, and Vaccari 1991, Newman and Jones 1998, Sels et al. 1999, Sels, De Vos, and Jacobs 2001, Vaccari 1999) Recently, LDH nanoparticles (NPs) with different intercalated compounds have exhibited versatility and promises in biomedicine as a theranostic vector, i.e. a particulate carrier having therapeutic and imaging attributes.(Choy et al. Inorganic layered double hydroxides as nonviral vectors 2000, Del Hoyo 2007, H. C. Huang et al. 2011, Kriven et al. 2004, Li et al. 2013, Panda and Bahadur 2012, Wang et al. 2013) For example, several *in vivo* multimodal imaging studies(Musumeci et al. 2010, Wei et al. 2012) and a number of *in vivo* studies, using animal models to determine the pharmacokinetics, toxicity, transfection efficiency, and therapeutic efficacy of LDH, have been reported.(Li et al. 2011, Qin et al. 2010, Silion et al. 2010)

Among many synthesis methods for LDH, the most versatile is the coprecipitation method.(Braterman, Xu, and Yarberry 2004) Typically, it consists of precipitating two suitable

metal cations in the presence of the intercalating anions and a base. According to the pH variation curve during the coprecipitation process, a couple of useful routes include coprecipitation at varying pH(Boclair and Braterman 1999, Boclair et al. 1999, Dey and Sistiabudi 2007) and at constant pH. The latter is the most widely used method for LDH preparation due to its main advantage of the minimal formation of undesired metal hydroxides.(Braterman, Xu, and Yarberry 2004) The coprecipitation is comprised of three steps, (i) mixing of the cations with the base, (ii) homogeneous nucleation due to supersaturation, (iii) seed-assisted growth of LDH on the nucleus.(Porter and Easterling 1996) However, from macroscopic point of view, it is impossible to distinguish these individual steps due to significant overlap, especially under supersaturation condition with convection. As a consequence, LDH particles of very different particle sizes and size distributions result. Note also that the synthesis window, agglomeration tendency, and stability for each system is different.(Matijevic 1994) To date, the only system that has been extensively studied in crystalline NP and monodispersed form has been (Mg, Al)-LDH,(Costantino et al. 1998, Ogawa and Kaiho 2002, Xu et al. 2006, Zhao et al. 2002) whereas studies on other biocompatible systems with physiological relevance(Dey and Sistiabudi 2007) (e.g. (Zn, Al)-LDH, (Zn, Fe)-LDH, etc.) are rare despite the fact that Zn-based LDH compositions exhibit higher stability than Mg-based ones.(Boclair and Braterman 1999) Moreover, conditions that form stable (Mg, Al)-LDH colloidal suspensions can cause severe aggregation of (Zn, Al)-LDH NPs.(Bellezza et al. 2009) One study, using a vortex reactor under steady-state conditions and without post-hydrothermal treatment (HT),(Chang et al. 2005) demonstrated the synthesis of semicrystalline $Zn_2Al(OH)_6(CO_3)_{0.5}\cdot 2H_2O$ NPs; however, due to the low crystallinity and the presence of strongly-bound carbonate (CO_3^{2-}), the post-synthesis intercalation of relevant anions was not favored. In general, documented literature does

not reflect systematic studies on the effects of synthesis parameters for LDH NPs. Therefore, from both the colloid science point of view and to address the long-term question of whether crystalline LDH systems will be accepted in biomedicine, initial observations of the effects of synthesis parameters (the central theme of this paper) and understanding of the underlying mechanisms of structure evolution are of primary importance for the reproducible synthesis of biocompatible NPs with controlled mean particle size (MPS) and particle size distribution (PSD).

From the points of view of biocompatibility and anion exchangeability, the authors believe that chloride (Cl^-)-intercalated (Zn, Al)-LDH system is an ideal model system; points in favor of this system are:

(i) Critical parameters for the synthesis of (Zn, Al)-based LDH NP has not been documented.

(ii) To date, most work on the synthesis of (Mg, Al)-LDH NPs have focused on post-synthesis hydrothermal treatment to decrease particle size and achieve crystallinity.(Ogawa and Kaiho 2002, Xu et al. 2006) This approach may not necessarily apply to other systems (e.g. (Zn, Al)-LDH, (Zn, Fe)-LDH, and (Mg, Fe)-LDH) since crystalline perfection can lead to increased size via Ostwald ripening.(Ratke and Voorhees 2002) Also, a relatively high HT temperature (T > 90 °C) can activate condensation reactions of Zn-OH via dehydration to form additional ZnO phase in aqueous media.(Vayssieres 2003) Therefore, control of the coprecipitation conditions is pivotal towards the formation of phase-pure (Zn, Al)-LDH NPs with controlled MPS and PSD.

(iii) Due to the strong interaction between the intercalated CO_3^{2-} and the hydroxide matrix layers, CO_3^{2-} facilitates the formation of crystalline LDH.(Bellezza et al. 2009,

Costantino et al. 1998, Ogawa and Kaiho 2002) However, as a consequence, it is very difficult to replace the CO_3^{2-} with other relevant anions. Thus, the initial synthesis Cl^- intercalated (Zn, Al)-LDH NPs can facilitate the intercalation of biomedically-relevant molecules via ion exchange.

Herein, for the first time using statistical design of experiments, a robust and reproducible coprecipitation process at constant pH followed by HT is reported for the synthesis of stable and crystalline Cl^--intercalated (Zn, Al)-LDH NPs with controlled MPS and narrow PSD. First, the critical synthesis parameters for MPS and PSD and their trends were separately identified using a fractional factorial screening design and ideal coprecipitation conditions were determined, followed by the optimization of the HT conditions. Eventually, using a central composite design, a quantitative MPS model, expressed in terms of the significant factors (salt concentration, molar ratio of carbonate to aluminum, and solution addition rate), was developed and experimentally verified. Another important factor for the synthesis of stable Cl^--intercalated (Zn, Al)-LDH NPs, i.e. the appropriate range of Zn to Al molar ratio, was also studied. Finally, the influence of the divalent/trivalent cation on the resulting particle size was determined through the comparison among (Mg, Al)-LDH, (Zn, Al)-LDH and (Zn, Fe)-LDH systems.

2.2.3 Materials and Methods

2.2.3.1 Materials

Zinc nitrate hexahydrate ($Zn(NO_3)_2 \cdot 6H_2O$), aluminum nitrate nonahydrate ($Al(NO_3)_3 \cdot 9H_2O$), zinc chloride ($ZnCl_2$), aluminum chloride hexahydrate ($AlCl_3 \cdot 6H_2O$), magnesium nitrate hexahydrate ($Mg(NO_3)_2 \cdot 6H_2O$), sodium carbonate (Na_2CO_3) and sodium hydroxide (NaOH) were purchased from Sigma (St. Louis, MO, USA), used as received, and

stored under nitrogen gas (N_2) environment. Deionized nanopure water (Barnstead, 18.2 MΩ·cm), degassed by boiling, was used for the preparation of all solutions.

2.2.3.2 Synthesis and Optimization Methodology

The coprecipitation at constant pH method was chosen for the synthesis of (Zn, Al)-LDH NPs. In order to prevent the contamination of CO_3^{2-}, all chemicals were stored in a N_2 filled glove box (MBraun Labmaster 130); note, the coprecipitations were also carried out at room temperature (RT = 25 °C) within the glove box and the products were withdrawn in sealed hydrothermal bottles. Typically, a 10 ml salt solution of $ZnCl_2$ and $AlCl_3{\cdot}6H_2O$ with a specific molar ratio of Zn to Al of 2:1 and a given total salt concentration, [Zn+Al], and another 10 ml base solution of NaOH containing a specific amount of Na_2CO_3, with the concentration of the NaOH being twice the concentration of [Zn+Al], were simultaneously added into a round-bottom flask (Chemglass 100 ml round bottom flask) using burettes, while stirring at a given speed (Magnetic stirrer: manufactured by Barnant Corp., Barrington, IL, Model 700·0111). The stirring rate was calibrated using a strobe tachometer (Strobette Ameter Model 1000). After completion of the addition of 20 ml precursors, stirring continued for another 3 minutes to ensure thorough mixing. The final pH was ~5.98. The mixture was then transferred into a hydrothermal bottle (PYREX screw cap 100 ml storage bottle), and the HT was carried out at a certain temperature (T), for a given period of time (t). Finally, the colloidal suspension was cooled to RT, and centrifuged (Eppendorf 5810R) to collect the gel-like Cl^--intercalated (Zn, Al)-LDH NPs for physicochemical characterization.

The optimization of the synthesis parameters and control of synthesis were accomplished in three consecutive steps. The objective of the first step was to ascertain the significant factors

that can influence the LDH NPs' MPS and PSD, and to determine the optimum coprecipitation condition for obtaining monodispersed PSD. In an unreplicated resolution IV 2^{4-1} fractional factorial screening design, the [Zn+Al], 2[CO_3^{2-}]/[Al], stirring rate, and addition rate were the screening parameters with MPS and PSD as the responses. To minimize the risk of fitting a model to noise and ensure the reliable effect estimates in an unreplicated design, the distance between the low and high levels of the screening parameters were chosen to be large enough. As listed in Table 2.2, a total of eight runs were generated using JMP Pro. 10.0.0,(Jmp 10 design of experiments guide 2012) and conducted randomly following the synthesis procedure described previously. The T and t of HT for all the screening runs were 70 °C and 7 h, respectively. A relatively low T and short t were chosen to minimize the alternation of MPS and PSD due to coarsening, and to improve the crystallinity. The data analysis was performed with JMP Pro. 10.0.0, and the main effects and interaction effects on the MPS and PSD were identified, separately. The optimum coprecipitation conditions that give monodispersed PSD were then determined.

The second step was the optimization of the HT conditions. For a given sample, six hydrothermal experiments, combining two different T (70 and 85 °C) with three different t (3, 5, and 8 h), were completed to find out the optimum HT conditions that provide monodispersed LDH NPs.

In the third step, the synthesis conditions, i.e. the range for [Zn+Al], 2[CO_3^{2-}]/[Al] ratio, stirring rate, and addition rate, were adjusted and shifted towards the region of interest. A face-centered central composite design with two central points (Table 2.4) was employed to develop a quantitative response surface in which MPS can be controlled through significant factors, i.e. [Zn+Al], 2[CO_3^{2-}]/[Al] ratio, and addition rate. Note, all the experiments were carried out using

the optimum coprecipitation and HT conditions. Once the response surface was generated, the validity of the model was tested experimentally.

Additionally, for the synthesis of stable Cl^--intercalated (Zn, Al)-LDH NPs, the appropriate range of Zn to Al molar ratio was studied; input salt solutions with Zn to Al molar ratios of 1:1, 2:1, 3:1 and 4:1 were used. Finally, the influence of the divalent cation on the resulting particle size was determined through the comparison of (Mg, Al)-LDH and (Zn, Al)-LDH systems, and the influence of the trivalent cation was determined by replacing Al^{3+} with Fe^{3+}.

2.2.3.3 Characterization

The crystalline phase information of LDH NPs was obtained by powder X-ray diffraction (XRD; Rigaku D/Max-IIB instrument with Cu-K_α radiation, λ=0.154059 nm) in 2θ range of 7-35°. The elemental compositions of the LDH NPs were then determined by inductively coupled plasma atomic emission spectroscopy (ICP, iCAP 6300 ICP Spectrometer). Dynamic light scattering (DLS, PSS-NICOMP 380 with zeta potential capability) was used to evaluate the particle size and size distribution. The morphology and particle size of LDH NPs were further examined by bright-field transmission electron microscopy (FEG TEM; Philips CM200 with an electron acceleration voltage of 200 kV) to corroborate the DLS results, and the crystallographic information was obtained by selected area diffraction pattern. To understand the inter-relationship between the surface charges of (Zn, Al)-LDH NPs with different Zn to Al molar ratio and the resulting particle size, Zeta-potential measurements on the LDH NPs were employed.

2.2.4 Results and Discussions

2.2.4.1 Initial Screening of the Critical Synthesis Parameters

Following the coprecipitation and hydrothermal procedures described in the experimental section, Table 2.2 summarizes the coprecipitation conditions of the initial screening experiments along with the results.

Table 2.2. 2^{4-1} design for screening: coprecipitation conditions (with HT at 70 °C for 7 h) and results

Run	Pattern	[Zn+Al] (mM)	Molar ratio $2[CO_3^{2-}]/[Al]$	Stirring rate (rpm)	Addition rate (ml/s)	Mean particle size* (nm)	Major size distribution %	Chi squared χ^2
1	−++−	10	0.3	1300	0.243	241	100	12.48
2	−+−+	10	0.3	1000	0.589	286	93	52.3
3	++++	60	0.3	1300	0.589	562	98	65.7
4	−−++	10	0	1300	0.589	331	100	3.18
5	+−−+	60	0	1000	0.589	620	79	107.71
6	++−−	60	0.3	1000	0.243	572.4	91	207.72
7	+−+−	60	0	1300	0.243	744	69	109.5
8	−−−−	10	0	1000	0.243	494	58	9.89

* Gaussian MPS is used if $\chi^2 \leq 3$; MPS fitted by NICOMP method is used when $\chi^2 > 3$.

Since there is no internal estimate of error (pure error) in an unreplicated design, the sparsity of effects principle is followed assuming that certain higher order interactions are negligible, and their mean squares are combined to estimate the mean square error. To avoid accidental pooling the significant higher order interactions for the estimation of the mean square error, a preliminary assessment of the importance of the effects was first carried out by visually inspecting the normal probability plot (Figure 2.8). The most pronounced significant effect on the influence of MPS is probably [Zn+Al] and $2[CO_3^{2-}]/[Zn+Al]$ with the absence of any significant higher order interactions.

To complement the result, the significance of the estimates of each main and effects and interactions was further judged using a *t* test for the hypothesis that it equals zero. By setting the

significance level at 0.05, the most significant main effects were found to be [Zn+Al], 2[CO_3^{2-}]/[Zn+Al], and addition rate, with an important interaction of [Zn+Al]*stirring rate.

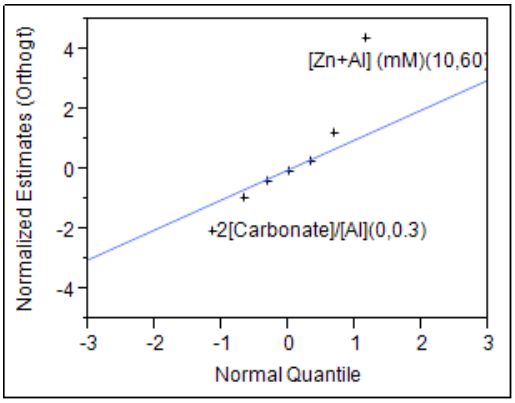

Figure 2.8. Normal probability plot of the effects of the main factors and interactions

In order to retain the hierarchy, a linear regression model of the MPS, with all the significant effects and interaction (i.e. [Zn+Al], 2[CO_3^{2-}]/[Zn+Al], addition rate and [Zn+Al]*stirring rate) along with the stirring rate, was developed by fitting the data using the least square method. The model, with R^2 of 0.997 and R_{adj}^2 of 0.990, is expressed as:

$$MPS=481.3+5.73(C_{salt}-35)-439.67(r_{cs}-0.15)-0.079(R_{sitr}-1150)-182.37(R_{add}-0.416)+0.011(C_{salt}-35)(R_{stir}-1150) \quad (2.1)$$

where *MPS* is the mean particle size in nm, C_{salt} is [Zn+Al] in mM, r_{cs} is the molar ratio of 2[CO_3^{2-}]/[Zn+Al], R_{stir} is the stirring rate in rpm, and R_{add} is the addition rate in ml/s. Note, R^2 reflects the proportion of the variation in MPS that can be attributed to the model parameters rather than to random error, and R^2_{adj} is the adjusted R^2; the closeness of R^2 and R_{adj}^2 and having a magnitude of 1 indicate accuracy.

Figure 2.9 shows the leverage plots of the significant main effects and interaction with their confidence curves (at 5% level) represented in dash lines. Here, the slope represents the degree of influence on the MPS. The exclusion of the horizontal line from the confidence region

for [Zn+Al] and 2[CO_3^{2-}]/[Zn+Al], and close to inclusion of the horizontal line from the confidence region for addition rate and [Zn+Al]*stirring rate, are indicative of significance and borderline significance, respectively. The salt concentration, [Zn+Al], is closely related to the MPS, and as shown in Figure 2.9a, lower [Zn+Al] leads to a smaller MPS. However, as illustrated by Ogawa and Kaiho,(Ogawa and Kaiho 2002) the effect of salt can be completely reversed if overwhelming HT T of 100 °C for 24 h is used; they synthesized micrometer-sized (Mg, Al)-LDH particles which increased in size with decreased salt concentration, perhaps due to severe Ostwald's ripening that masked the results of coprecipitation. The influence of the intercalated anion on the MPS is also considerable (Figure 2.9b), and a stronger interaction between the anions and the double hydroxide layers (as Cl^- is partially substituted by CO_3^{2-}) leads to the diminution of MPS. This result is apparently contrary to the expected as the presence of CO_3^{2-}, exhibiting a strong electrostatic interaction with the hydroxide matrix layers, should have facilitated the rapid growth leading to a larger MPS. Clearly, a more complex growth evolution, than that described by classical nucleation and growth, and which includes intercalating anion (Cl^-+CO_3^{2-})-dependent agglomeration may be in effect. Figure 2.9c and 2.9d shows the inverse and direct relationships (although mild) of addition rate and [Zn+Al]*stirring rate with the MPS, respectively.

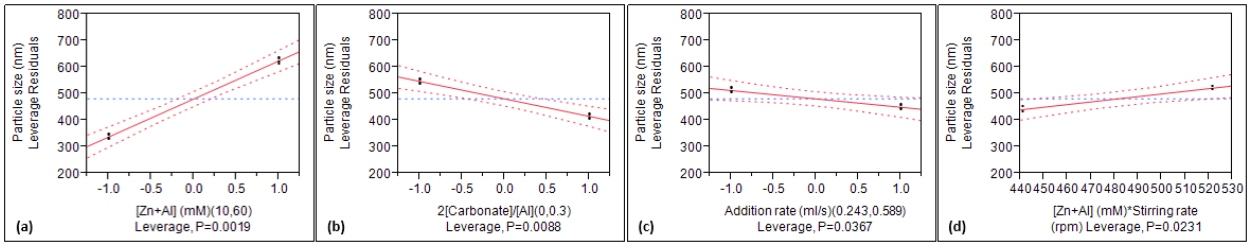

Figure 2.9. Preliminary identification of the critical factors, and their trends and leverages on the mean particle size (MPS)

Figure 2.10 shows the 2^{4-1} design representation and chi-squared (χ^2) plots of PSD as a function of the main effects. Here, χ^2 is used as the key indicator for goodness of fit of PSD to the Gaussian distribution; test of a good fit is a low χ^2 (ideally < 3).(Nicomp 380 DLS user manual 2006) At first glance, the deviation from the ideal Gaussian PSD is distinct with [Zn+Al]. Figure 2.10a and d, for low and high [Zn+Al], clearly shows that a higher stirring rate can lead to PSD with smaller χ^2. Figure 2.10c and f, for low and high [Zn+Al], indicates that PSD of LDH NPs synthesized in the presence of a high level of $2[CO_3^{2-}]/[Zn+Al]$ tend to have larger χ^2 than in the absence of CO_3^{2-}. However, a closer examination reveals that even when the LDH NPs are synthesized under high $2[CO_3^{2-}]/[Zn+Al]$, a higher stirring rate can significantly reduce χ^2 (e.g. Run 1 and Run 3). In contrast, for low and high [Zn+Al], the addition rate does not exhibit obvious trends (figure 2.10b and e). Therefore, among the screening parameters, the main effects that markedly influence PSD are determined to be the [Zn+Al] and stirring rate; note, an optimum coprecipitation conditions to achieve an ideal PSD would be a relatively low [Zn+Al] and more importantly, a high stirring rate.

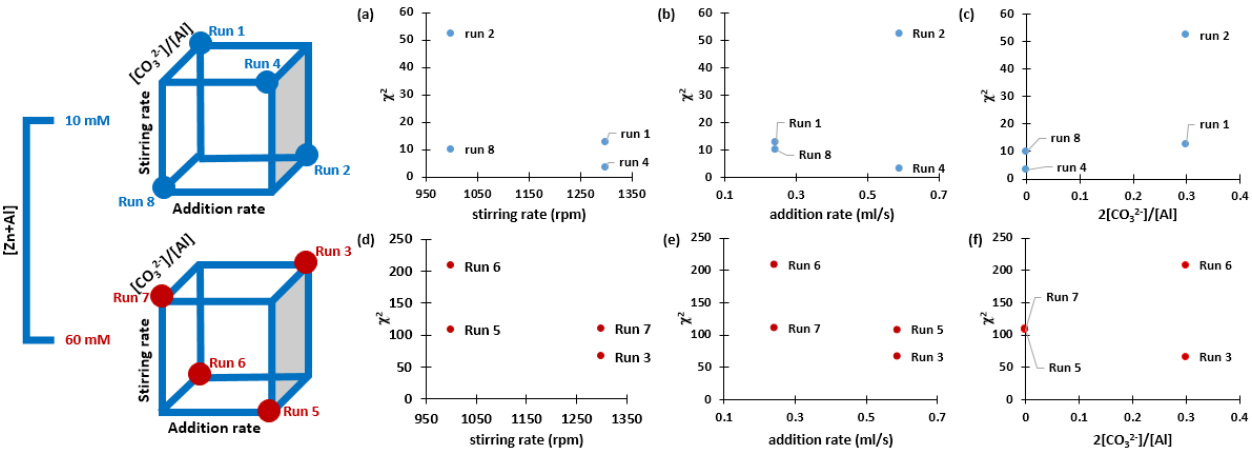

Figure 2.10. Scheme of the 2^{4-1} design with resolution IV, and the graphical representations of χ^2 as functions of [Zn+Al], addition rate, stirring rate, and $2[CO_3^{2-}]/[Zn+Al]$

The Gaussian analysis is limited to describing only simple particle size distributions – symmetric, unimodal populations. A sample with a large value of χ^2 (>3) is indicative of the existence of a more complicated distribution, and NICOMP analysis based on the inversion of the Laplace transform, which may describe up to 4 independent size distributions, was used. Here, the percentage of the scattering intensity of the primary fraction among all is referred to the major size distribution, and is used to an quantitative indicator of the closeness to a unimodal size distribution. Figure 2.11 further illustrates the beneficial effects of high stirring rate on PSD. In runs 4 (i.e. no CO_3^{2-}, high addition rate, and low [Zn+Al]), 1 (i.e. high CO_3^{2-}, low addition rate, and low [Zn+Al]), and 3 (i.e. high CO_3^{2-}, high addition rate, and high [Zn+Al]), a high stirring rate leads to almost monodispersed PSD. The importance of high stirring rates has also been mentioned for the synthesis of various NPs, e.g. $BaTiO_3$(Ould-Ely et al. 2011) and Fe_3O_4.(Karaagac and Kockar 2012, Sun et al. 2007) In essence, a high stirring rate ensures rapid and complete mixing of precursors, reduces the time variation of the homogeneous nucleation and growth events, enables the formation of a single and narrow PSD, and facilitates the formation of phase-pure LDH over individual hydroxides.

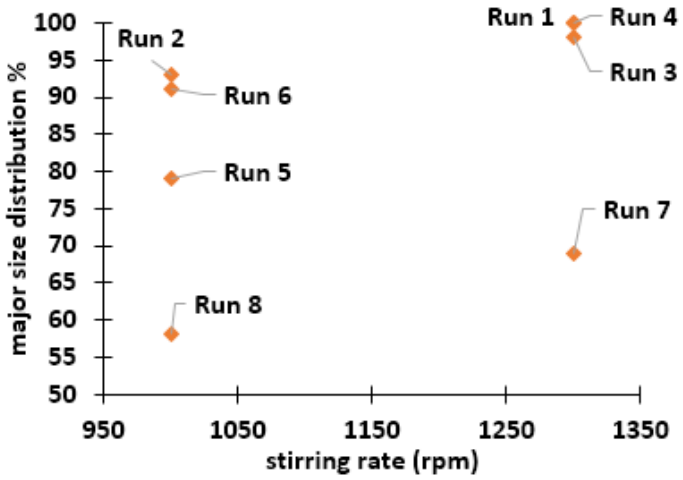

Figure 2.11. Percentage of the main size distribution as a function of the stirring rate

2.2.4.2 Understanding Hydrothermal Treatment and its Optimization

The coprecipitation at RT always led to severe agglomeration of amorphous (Zn, Al)-LDH NPs resulting in a large MPS and non-Gaussian PSD. Hence, as past work have demonstrated, HT in the absence of convection was necessary to form crystalline LDH NP suspensions.

The authors believe that the HT-promoted formation of stable LDH colloidal suspensions can be explained by Ostwald step rule,(Ostwald 1897) the thermodynamics and kinetics of which has been extensively studied.(Navrotsky 2003, 2004, 2011, Navrotsky et al. 2010) The as-coprecipitated metastable amorphous LDH NPs tend to have a lower surface energy, due to a lower number of high-energy sites (i.e. charged sites) per unit surface area, compared to the thermodynamically stable crystalline counterpart. Consequently, hydration on a smaller number of these sites leads to a low hydration enthalpy, which makes agglomeration the principle mechanism for further lowering the energy of the amorphous phase. The t and T-dependent HT can transform the metastable phase to the thermodynamically stable crystalline LDH NPs through atomic rearrangement of the bulk coupled with a surface dissolution-reprecipitation process. The presence of a higher number of charged sites on crystalline NPs leads to repulsion between NPs and increased hydration. Consequently, the high hydration enthalpy lowers the energy of the system to the extent that agglomeration is unnecessary. Moreover, one must be aware that particle coarsening can also occur during HT, perhaps initially via diffusive growth mechanism.(Ratke and Voorhees 2002) As crystalline perfection increases, the energetic costs to incorporate atoms into larger NPs or detach atoms from smaller NPs can lead an interface-driven coarsening mechanism.(Ratke and Voorhees 2002) In essence, suitable HT conditions (i.e. T and t) are critical to improve crystallinity, form stable colloidal suspensions by electrostatic stabilization, and obtain monodispersed PSD.

Since the HT conditions for the screening experiments were not at their optima, the optimization of this step was also essential. Having identified the importance of the stirring rate, the LDH NPs were synthesized under the following conditions: stirring rate of 2250 rpm, [Zn+Al] of 20 mM, 2[CO_3^{2-}]/[Al] of 0.3, and addition rate of 0.416 ml/s. To determine the optimum HT conditions, these samples were treated at 70 and 85 °C for 3, 5 and 8 h. A too high T (> 90 C) can activate condensation reactions of Zn-OH via dehydration to form additional ZnO phase in aqueous media;(Vayssieres 2003) a too low T does not provide enough thermal energy for efficient crystallization (e.g. at 51 °C, it took > 7 h to re-disperse the NPs, data not shown here) Also, according to numerous previous runs, the crystallization at 60-85 °C, the crystallization can complete in 2-6 h, longer duration will emphasize the effect of coarsening process. The results are illustrated in Table 2.3.

Table 2.3. Results of HT for the sample synthesized using the following coprecipitation condition: stirring rate = 2250 rpm, [Zn+Al] = 20 mM, 2[CO_3^{2-}]/[Al] = 0.3 and addition rate = 0.416 ml/s

	3 h	**5 h**	**8 h**
70 °C	χ^2 =35.5 NICOMP: 50 nm (15.6%) 322.5 nm (84.4%)	χ^2 = 2.34 Gaussian: 327.4 nm	χ^2 = 1.68 Gaussian: 309 nm
85 °C	χ^2 =33.31 NICOMP: 114.1 nm (8.06%) 341.6 nm (91.64%)	χ^2 = 0.90 Gaussian: 303.4 nm	χ^2 = 1.32 Gaussian: 323 nm

Clearly, the monodispersed Gaussian distribution with the lowest χ^2 can be achieved by treating the sample at 85 °C for as little as 5 h. Relatively low T (70-85 °C) only allowed a slow

coarsening process (i.e. particle growth), as shown by the comparison between the samples treated at 85 °C for 5 and 8 h. While too low T (< 50 °C) was insufficient to transform the metastable phases to the most thermodynamically stable crystalline phases, too high T (> 90 °C) enhanced Ostwald ripening that led to larger disparities in particle size with time. Additionally, too high T caused compositional change in growing particles, due to the difference in the reprecipitation rates of the divalent and trivalent cations, and agglomeration was observed. Note, although the optimum HT can improve the PSD towards monodispersion, the extent of its efficacy is limited by how ideal the prior coprecipitation conditions are.

2.2.4.3 Quantitative Model Development Using Central Composite Design

Here a more elaborate central composite design with two central points was employed for higher resolution to construct the response surface. The selected main factors with their adjusted ranges for the model were [Zn+Al] (5- 5 mM) and $2[CO_3^{2-}]/[Zn+Al]$ (0-0.3), along with the borderline factor of addition rate (0.243-0.589 ml/s) and included here due to the projection property of the factorial design. Also, based on the results of screening, the highest permissible stirring rate of 3000 rpm of the current stirrer, was chosen for all the runs. The experiments were carried out following the aforementioned procedure, followed by a HT at 85 °C for 5 h. Table 2.4 summarizes the coprecipitation conditions and results for the 16 runs.

Based on the data shown in Table 3, a simple model ($\alpha = 0.05$) that predicts MPS was developed, where no interaction effect was significant, and R^2 and R_{adj}^2 were 0.978 and 0.972, respectively. The model can be expressed as follows:

$$MPS=371.71+4.8(C_{salt}-20)-291.53(r_{cs}-0.15)-93.24(R_{add}-0.416) \quad (2.2)$$

Table 2.4: Face-centered central composite design and results

Run	Pattern	[Zn+Al] (mM)	2[CO_3^{2-}]/[Al] (molar ratio)	Addition rate (ml/s)	Mean particle size* (nm)	Major size distribution %	Chi square χ^2
1	**00a**	25	0.15	0.243	411	85.7	31.93
2	+−−	45	0	0.243	513	100	42.94
3	**000**	25	0.15	0.416	376	100	1.31
4	**0a0**	25	0	0.416	394	88.4	12.51
5	−++	5	0.3	0.589	204	100	1.1
6	+−+	45	0	0.589	502	98	38.12
7	**000**	25	0.15	0.416	360	100	1.6
8	**a00**	5	0.15	0.416	279	100	1.35
9	−+−	5	0.3	0.243	241	100	1.45
10	**00A**	25	0.15	0.589	339	100	0.95
11	**0A0**	25	0.3	0.416	328	92	13.07
12	+++	45	0.3	0.589	427	84.28	20.64
13	++−	45	0.3	0.243	437	96.47	44.09
14	−−+	5	0	0.589	317	100	17.83
15	**A00**	45	0.15	0.416	471	98.42	4.72
16	−−−	5	0	0.243	348.3	100	5.09

* Gaussian MPS is used if $\chi^2 \leq 3$; MPS fitted by NICOMP method is used when $\chi^2 > 3$.

According to the leverage plots shown in Figure 2.12, [Zn+Al] and 2[CO_3^{2-}]/[Al] are significant and the addition rate is at the borderline of significance, consistent with screening results.

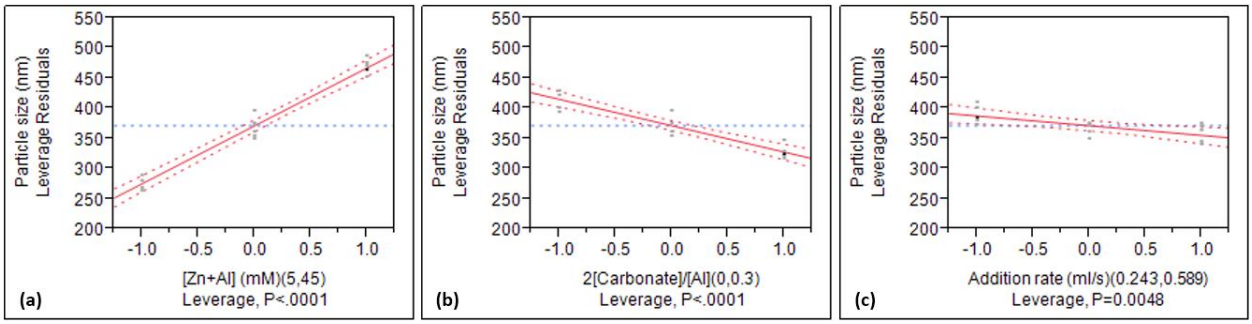

Figure 2.12. Leverage residuals of the significant factors

A two-dimensional response contours of the MPS, for a fixed addition rate (0.589 ml/s), is shown in Figure 2.13. Here the MPS range (~ 200-500 nm) is readily controlled through two easily controllable processing parameters of [Zn+Al] and $2[CO_3^{2-}]/[Al]$.

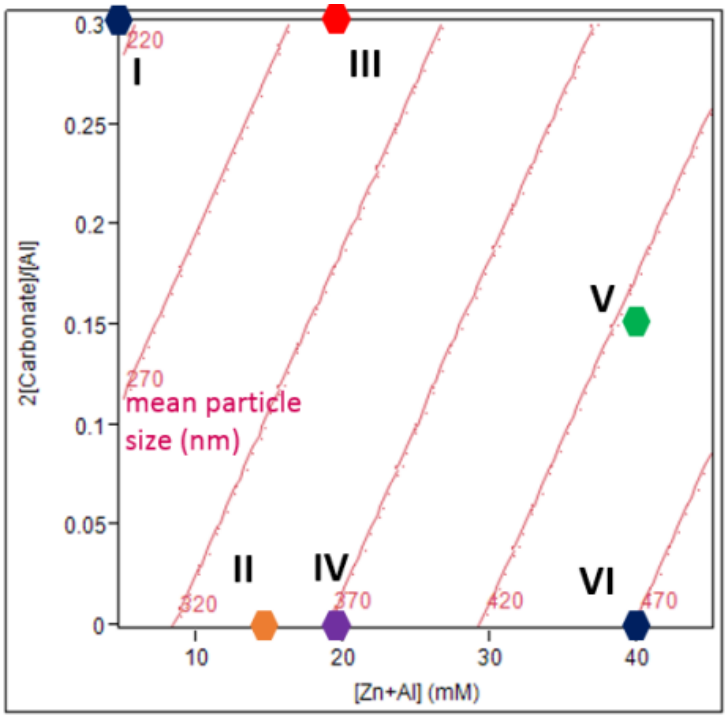

Figure 2.13. Response contours of the MPS as a function of [Zn+Al] (mM) and $2[CO_3^{2-}]/[Al]$, generated at a fixed addition rate of 0.589 ml/s and stirring rate of 3000 rpm

The validity of this model was tested by selecting a few points (I to VI shown as solid circles in Figure 2.13) and carrying out synthesis of Cl^--intercalated (Zn, Al)-LDH NPs under the specified conditions, followed by the comparison of the MPS predicted by the model with the experimental results. After coprecipitation, all samples were hydrothermally treated at 85 °C for 5 h. The bright field TEM images of monodispersed (Zn, Al)-LDH NPs of various particle sizes are displayed in Figure 2.14a.

The NPs were Cl^--intercalated and single crystalline; representative X-ray diffraction pattern and electron diffraction pattern for Sample VI are depicted in Figure 1.14b and c,

respectively. Table 2.5 clearly shows the close correspondence of the MPS predicted by the model with the experimental TEM results.

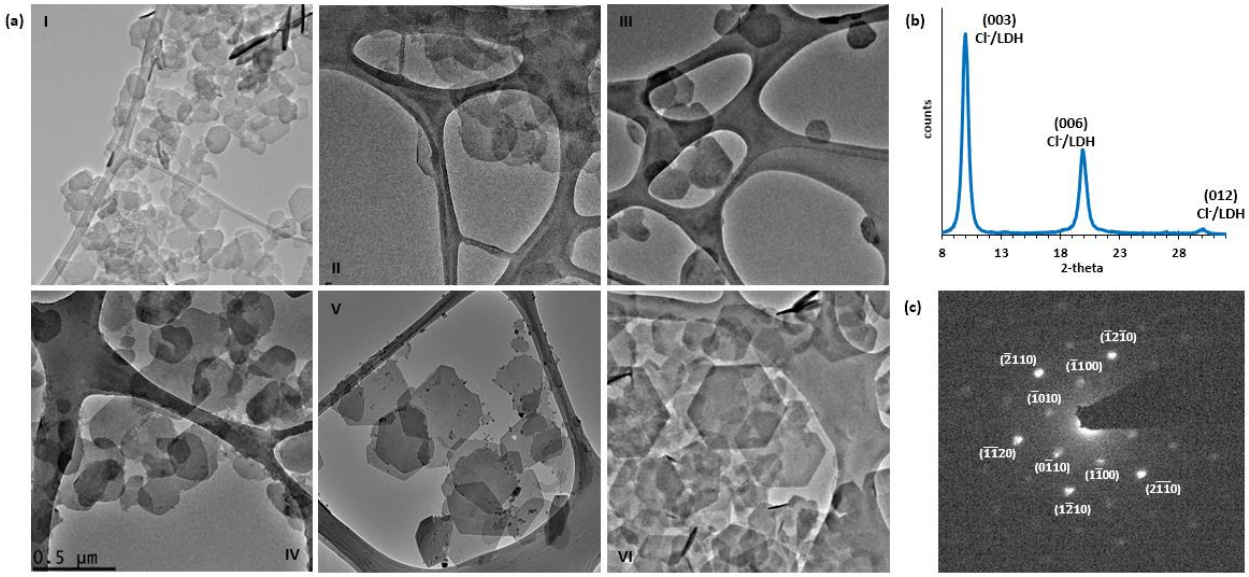

Figure 2.14. TEM micrographs of (Zn, Al)-LDH NPs of Sample I – Sample VI (a), XRD pattern of Sample VI (b) and its corresponding diffraction pattern with [0001] zone axis (c).

The comparisons of sample III with IV and V with VI show that the presence of a small amount of CO_3^{2-} within the gallery spacing stabilizes the LDH NPs under hydrothermal conditions and minimizes the coarsening process. The less stable sample IV and VI were more susceptible to the Ostwald ripening,(Ratke and Voorhees 2002) and as a result, a wider range of particle size was observed.

Table 2.5. Comparison between the predicted MPS and MPS determined by TEM bright field micrograph

Sample	**I**	**II**	**III**	**IV**	**V**	**VI**
Predicted MPS (nm)	216	351	288	375	428	471
TEM MPS (nm)	235	344	305	401	438	512

2.2.4.4 Evaluation of the Effect of [Zn^{2+}]/[Al^{3+}] Molar Ratio on the Resultant Particle Size

The effect of the [Zn]/[Al] ratio on the particle size of Cl^--intercalated (Zn, Al)-LDH NPs were studied by changing the input [Zn]/[Al] molar ratio from 1 to 4. The coprecipitation conditions were as follows: [Zn+Al] of 5 mM, [NaOH]/[Zn+Al] of 2, 2[CO_3^{2-}]/[Al] of 0.3, stirring rate of 3000 rpm, addition rate of 0.589 ml/s and HT conditions of 85 °C for 5 h. The actual composition determined by ICP [Zn]/[Al] for molar ratios of 1 to 4 were $Zn_{0.509}Al_{0.491}(OH)_2(CO_3^{2-})_{0.074}Cl_{0.344}\cdot xH_2O$, $Zn_{0.656}Al_{0.344}(OH)_2(CO_3^{2-})_{0.052}Cl_{0.241}\cdot xH_2O$, $Zn_{0.724}Al_{0.276}(OH)_2(CO_3^{2-})_{0.041}Cl_{0.193}\cdot xH_2O$ and $Zn_{0.781}\ Al_{0.219}\ (OH)_2\ (CO_3^{2-})_{0.033}Cl_{0.153}\cdot xH_2O$, respectively. Figure 2.15 illustrates the effect of [Zn]/[Al] ratio on the zeta-potential and mean hydrodynamic particle size. Except for the $Zn_{0.781}\ Al_{0.219}\ (OH)_2\ (CO_3^{2-})_{0.033}Cl_{0.153}\cdot xH_2O$ sample synthesized with a [Zn]/[Al] ratio of 4, all the samples exhibited a monodispersed size distribution. The large particle size (~1.7 μm in diameter) of the $Zn_{0.781}\ Al_{0.219}\ (OH)_2\ (CO_3^{2-})_{0.033}Cl_{0.153}\cdot xH_2O$ sample can be attributed to severe agglomeration due to the low zeta-potential that results from the low trivalent Al^{3+} content.

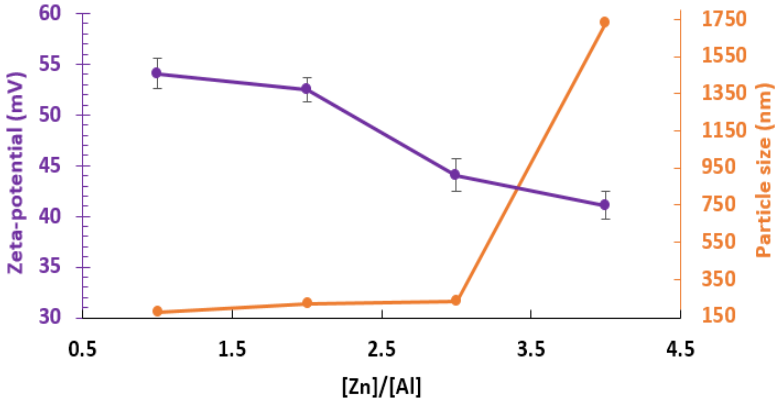

Figure 2.15. Zeta-potential and particle size determined by DLS as a function of [Zn]/[Al] ratio.

Therefore, from the view point of the stabilization by surface charges, the suitable range of the Zn to Al molar ratio should be 1-3. When the divalent to trivalent cation ratio close to 1,

the resulted phased may be disordered.(Cavani, Trifiro, and Vaccari 1991) However, such results especially depend on the synthesis conditions, i.e. starting reactants, pH of reaction and HT treatment conditions. For example, crystalline $[Mg_{0.56}Al_{0.44}(OH)_2]^{0.44}[0.22X^{-}\cdot nH_2O]$, where X^{-} = $½CO_3^{2-}$ or OH^{-}, has been successfully synthesized.(Pausch et al. 1986)

2.2.4.5 Extension of the Optimized Synthesis Conditions to the Synthesis of (Mg, Al)-LDH and NPs

In the previous section it was observed that the [Zn]/[Al] molar ratio influenced the observed particle size via surface charge effects. Therefore, to determine whether the nature of the divalent cation can influence the particle size, NO_3^{-}-intercalated (Mg, Al)-LDH NPs were synthesized simply by replacing Zn with Mg, and using the optimized synthesis parameters as follows: [Mg+Al] of 20 mM, [Mg]/[Al] of 2, [NaOH]/[Mg+Al] of 2, $2[CO_3^{2-}]$/[Al] of 0, stirring rate of 3000 rpm, addition rate of 0.589 ml/s and HT condition of 85 °C for 5 h. As shown by the TEM results of Figure 2.16, the resulting NPs exhibited a monodispersed PSD with a MPS of 70 nm, a significant shift towards a smaller MPS compared to the (Zn, Al)-based LDH NPs.

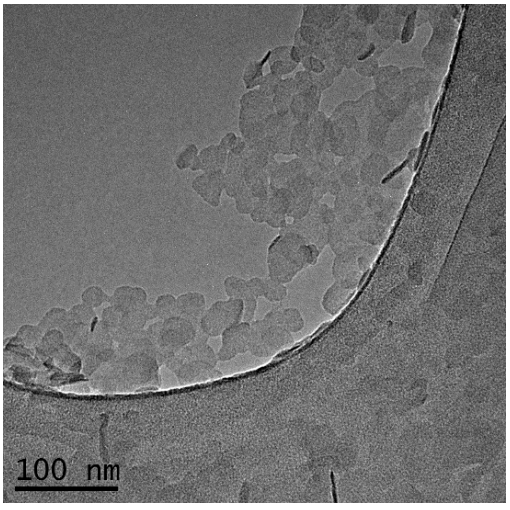

Figure 2.16. TEM micrograph of $Mg_{0.670}Al_{0.330}(OH)_2(NO_3)_{0.33}\cdot xH_2O$ NPs.

Note, such a MPS shift was also observed when the trivalent Al^{3+} was replaced by Fe^{3+} to form (Zn, Fe)-LDH NPs. Apparently, the nature of the divalent and trivalent cations plays an important role in influencing the MPS of LDH NPs, and more polarized $M^{II/III}$-OH bonding tends to provide smaller MPS due to the increased solvation by water molecule and the consequent stabilization by increased hydration enthalpy.

2.2.5 Conclusions

With the aid of statistical design of experiments, the controlled synthesis of single crystalline Cl^--intercalated (Zn, Al)-LDH NPs, using coprecipitation at constant pH followed by HT, was achieved. Among various screening factors, a high stirring rate was identified as the critical parameter to obtain a monodispersed PSD. Here, the highest achievable stirring rate was limited by the current stirrer, and it is envisioned that stirring rates > 3000 rpm could further reduce the width of the PSD, especially for high [Zn+Al]. A quantitative MPS model, expressed in terms of the significant factors, was developed and used to synthesize nearly monodispersed LDH NPs with MPS anywhere in the range of 200-500 nm by controlling the [Zn+Al], 2[CO_3^{2-}]/[Zn+Al], and the addition rate.

Another interesting finding was that a stronger interaction between the intercalated anion and double hydroxide layers, i.e. when Cl^- is partially replaced by CO_3^{2-}, led to a smaller particle size. Such a phenomenon is apparently contradictory to classical nucleation and growth, as a stronger interaction between CO_3^{2-} and double hydroxide layers should have promoted a more rapid growth towards larger particle size. It is believed that agglomeration may play a dominant role, and therefore, the future study will focus on the formation mechanisms of LDH NPs.

Moreover, the ideal range of [Zn]/[Al] molar ratio for obtaining (Zn, Al)-LDH NPs was determined to be between 1 and 3, with ratios approaching 4 led to dramatic increase in particle size. The optimized synthesis conditions were successfully applied to the (Mg, Al)-LDH system to obtain monodispersed (Mg, Al)-LDH NPs. However, the significant MPS shift underscored the importance of the nature of divalent and/or trivalent cation. More polarized M(II)/M(III)-OH bonds increase the solvation and hydration enthalpy, and consequently provide smaller MPS. From a practical point of view, the current methodology can be used to optimize the synthesis parameters of other biocompatible LDH NPs.

2.3 Insights into the Formation Mechanisms of Layered Double Hydroxide Nanoparticles

2.3.1 Abstract

We demonstrate that the formation of crystalline layered double hydroxide nanoparticles proceeded through metastable amorphous primary particles, which were formed during the room temperature coprecipitation and agglomerated at the edges due to the low surface charge density. After the crystallization by the hydrothermal treatment, the agglomerated $Zn_2Al(OH)_6(NO_3)_{0.3}(CO_3)_{0.35}\cdot xH_2O$ primary particles re-dispersed. However, due to the much less stable composition and intrinsically less ordered nanostructure, especially on the edge sites, the agglomeration of $Zn_2Al(OH)_6(NO_3)\cdot xH_2O$ primary particles was irreversible and transformed into secondary particles via aggregational growth. The reversibility of such agglomeration is determined by the crystalline quality and surface charge density, which are strongly influenced by the composition of the intercalated anions. Moreover, the stability studies on $Zn_2Al(OH)_6(NO_3)_y(CO_3)_{0.5(1-y)}\cdot xH_2O$ nanoparticles (y = 0-1) showed that the size difference between the cointercalated anions caused phase separation when $0.9 \geq y \geq 0.6$, leading to the bimodal size distribution. Finally, we proved that the coarsening rate can be controlled through the cointercalated anions. By gradual increasing the ratio of cointercalated NO_3^- to CO_3^{2-}, monodispersed $Zn_2Al(OH)_6(NO_3)_y(CO_3)_{0.5(1-y)}\cdot xH_2O$ ($0.5 \geq y \geq 0$) nanoparticles with gradually increasing particle size of ~200 nm to ~400 nm were obtained after the hydrothermal treatment at 85 °C for 12 h.

2.3.2 Introduction

The emergence of nanoscience and nanotechnology is having a revolutionary impact on almost every realm of society, especially in health care and nanomedicine, and inorganic ceramic nanoplatforms have been and will be the major contributors. Traditionally, due to their inherent biocompatibility and stability in physiological environments, ceramics have been attractive for biological applications.(Hench 1998, Hench and Polak 2002, Hench and Wilson 1993, L. 1973) Recently, a number inorganic nanomaterials including silica, quantum dot, and magnetic nanoparticle (NP)-based vectors or carriers, with combined therapeutic and diagnostic attributes (i.e. theranostics) have been in various stages of preclinical and clinical development.(Farokhzad and Langer 2006) (H.-C. Huang et al. 2011) (Service 2010) Another inorganic ceramic which holds promise in nanomedicine is the layered double hydroxide (LDH), based on the Hydrotalcite ($Mg_6Al_2(OH)_{16}CO_3{\cdot}4H_2O$) structure. The general empirical formula of LDH can be denoted as $[M^{II}_yM^{III}(OH)_{2+2y}]^+(A^{-}_{1/})_{1/}{\cdot}xH_2O$ (typically, y = 1-5), where octahedral M^{II} and M^{III} are divalent (e.g., Mg^{2+}, Co^{2+}, Zn^{2+}) and trivalent (e.g., Al^{3+}, Ga^{3+}, Fe^{3+}, Mn^{3+}, Gd^{3+}) cations, respectively. Here, the positively charged cation hydroxide layers are rendered electrically neutral by intercalation of electrostatically-bound anions ($A^{\alpha-}$, with a negative charge of α) within the interlayer spacing, with water held in place via hydrogen bonding to the hydroxyls.(Dey and Sistiabudi 2007) Moreover, by ion-exchange method, the intercalated anions may be replaced by relevant anions of interest (e.g., nucleotides, fluorescent molecules, radio-labeled ATP, vitamins, DNA, and drugs). Recently, LDH NPs with different intercalated species have shown the versatility and promise in biomedicine as a theranostic vector.(Choy et al. Inorganic layered double

hydroxides as nonviral vectors 2000, Del Hoyo 2007, H. C. Huang et al. 2011, Kriven et al. 2004, Li et al. 2013, Panda and Bahadur 2012, Wang et al. 2013) For example, several *in vivo* multimodal imaging studies(Musumeci et al. 2010, Wei et al. 2012) and a number of *in vivo* studies using animal models to determine the pharmacokinetics, toxicity, transfection efficiency, and therapeutic efficacy of LDH, have been reported.(Li et al. 2011, Qin et al. 2010, Silion et al. 2010) However, despite the synthesis of numerous LDH compositions in the bulk form,(Braterman, Xu, and Yarberry 2004) the only composition that has been extensively studied in NP form is (Mg, Al)-LDH due to the ease of synthesizing crystalline and narrowly-distributed NPs.(Costantino et al. 1998, Ogawa and Kaiho 2002, Xu et al. 2006, Zhao et al. 2002) Studies on other compositions of physiological relevance,(Dey and Sistiabudi 2007) e.g., (Zn, Al)-LDH, (Zn, Fe)-LDH, or (Mg, Fe)-LDH, with increased stabilities(Boclair and Braterman 1999) or potential theranostic attributes are rare.

The success of any theranostic nanoplatforms in biomedicine is highly contingent upon their controlled and reproducible synthesis. In addition to the control of the chemical reactions, the understanding of the formation mechanism, i.e. nanostructure evolution, is critical to the synthesis of NPs with controlled mean particle size and monodispersed particle size distribution (PSD). Often, classical nucleation and growth theory is used to describe the formation of crystalline materials from either solute ions or molecules in solutions, where after the spontaneous formation of nuclei, those nuclei with sizes larger than the critical radius continue to grow by the consumption of solutes followed by coarsening. However, such a model is often too simplistic to adequately describe many nanomaterial systems, especially since the following assumptions may not

be applicable: (1) nucleation is a one-step process in which only one energy barrier exists, (2) the nucleus grows one monomer at a time, (3) the nucleus is spherical and the details of lattice are neglected, and (4) small clusters are considered to have the same properties as their bulk counterparts.(Sear 2012) In "bottom-up" solution synthesis of NPs at relatively low temperatures, non-classical arguments based on the interplay of thermodynamics (especially surface energy) and kinetics are needed to explain the nanostructure evolution. Complex formation mechanisms, such as multiphase transformation described by Ostwald step rule,(Chung et al. 2009, Navrotsky 2003) particle-based aggregational growth,(Banfield et al. 2000, Navrotsky 2004) and oriented attachment growth with or without surfactants(Zhang, Liu, and Yu 2009) have been suggested. Due to the lack of understanding of the formation mechanisms of LDH NPs, the controlled syntheses of many biocompatible compositions to maximize their potential in biomedicine have been severely hindered. Therefore, the only systematic studies for understanding the formation mechanism and controlled synthesis of well-defined LDH NPs of practical relevance -- the central theme of this paper -- will eventually trigger the transformative success of this class of vectors.

Two model systems, $Zn_2Al(OH)_6(NO_3)_{0.3}(CO_3)_{0.35}{\cdot}xH_2O$ and $Zn_2Al(OH)_6(NO_3)_{0.5}{\cdot}xH_2O$ LDH NPs, which exemplify the very stable and the least stable LDH compositions, respectively, were selected for this study. All the NP samples were synthesized by coprecipitation followed by hydrothermal treatment (HT). Note, such a synthesis approach is considered the most refined aqueous solution synthesis method for LDH materials of numerous compositions. The synthesis parameters used in this study were optimized by design of experiments and the detailed procedure was

reported previously. To monitor the nanostructure evolution from the initial coprecipitation at room temperature (RT) to the HT-assisted formation of crystalline LDH NPs, and to identify the formation mechanisms in the presence of anions with contrasting nature, a number of advanced characterization techniques including transmission electron microscopy (TEM), X-ray diffraction (XRD), dynamic light scattering (DLS), and zeta-potential (ζ) techniques were used.

2.3.3 Experimental Section

2.3.3.1 Materials

Zinc nitrate hexahydrate ($Zn(NO_3)_2 \cdot 6H_2O$), aluminum nitrate nonahydrate ($Al(NO_3)_3 \cdot 9H_2O$), zinc chloride ($ZnCl_2$), aluminum chloride hexahydrate ($AlCl_3 \cdot 6H_2O$), sodium carbonate (Na_2CO_3), and sodium hydroxide (NaOH) were purchased from Sigma (St. Louis, MO, USA), used as received, and stored under nitrogen gas (N_2) environment. Deionized nanopure water (Barnstead, 18.2 MΩ cm), used for the synthesis, was degassed by boiling in advance.

2.3.3.2 Synthesis Method

All the syntheses of (Zn, Al)-LDH NPs were carried out using the coprecipitation at constant pH method followed by HT, the details of which are reported in a previously. To control the content of CO_3^{2-} within (Zn, Al)-LDH NPs as accurately as possible, all chemicals were stored in a N_2 filled glove box (MBraun Labmaster 130). Also, all coprecipitations were carried out within the glove box and the products were withdrawn in sealed hydrothermal bottles. Typically, a 10 ml of mixed nitrate salt solution

containing 20 mM of total salt concentration ([Zn+Al]), with a specific Zn to Al molar ratio of 2:1, and another 10 ml NaOH solution containing a designed amount of Na_2CO_3, with the concentration of NaOH being twice that of [Zn+Al], were simultaneously added into a round bottom flask (Chemglass 100 ml round bottom flask) using burettes, while stirring at 3000 rpm (Magnetic stirrer: manufactured by Barnant Corp., Barrington, IL, Model 700·0111). After completion of the addition of 20 ml precursors at an addition rate of 0.589 ml/s, stirring was continued for another 3 minutes to ensure thorough mixing. The mixture was then transferred into the hydrothermal bottle (PYREX screw cap 100 ml storage bottle), and the HT was carried out at a designed temperature (T_{HT}) for a specific period of time. Finally, the colloidal suspension was cooled to RT, and centrifuged (Eppendorf 5810R) to collect the gel-like (Zn, Al)-LDH NPs for physicochemical characterization.

2.3.3.3 Materials Characterization Techniques

The crystalline phase was determined by powder X-ray diffraction (XRD; Rigaku D/Max-IIB instrument with Cu-K_α radiation, λ=0.154059 nm) in the 2θ range of 7.5-70°. Inductively coupled plasma atomic emission spectroscopy (ICP, iCAP 6300 ICP Spectrometer) was used to confirm the elemental compositions. Dynamic light scattering (DLS, PSS-NICOMP 380 with zeta potential capability) was used to extract the mean hydrodynamic radius (r_H) of the NPs and size distributions. Transmission electron microscopy (FEG TEM; Philips CM200 with an electron acceleration voltage of 200 kV), in bright field imaging mode, was used to follow the evolution of the particle size and

morphology to corroborate with the DLS results, and crystallographic information was obtained by selected area electron diffraction.

2.3.3.4 Structure Evolution and Determination of the Formation Mechanisms of LDH NPs

$Zn_2Al(OH)_6(NO_3)_{0.3}(CO_3)_{0.35}{\cdot}xH_2O$ and $Zn_2Al(OH)_6(NO_3){\cdot}xH_2O$ LDH NPs were synthesized at RT following the procedure described above and used as the model systems to determine the formation mechanisms. For $Zn_2Al(OH)_6(NO_3)_{0.3}(CO_3)_{0.35}{\cdot}xH_2O$ NPs, the HTs were carried out at 85 °C for up to 7 h. The evolution of morphology, crystallinity, NP size, and size distribution were monitored by TEM imaging, electron diffraction and zeta-potential techniques, immediately after the coprecipitation and at different stages of the HT. For $Zn_2Al(OH)_6(NO_3){\cdot}xH_2O$ LDH NPs, the HTs were carried out at three different T_{HT}, i.e. 51, 70 and 85 °C, for up to 15 h. Again, the evolution of morphology, crystallinity, NP size, and size distribution were monitored by TEM, DLS, XRD and zeta-potential techniques immediately after the coprecipitation, and at different stages of the HT.

2.3.3.5 Size Difference between the Cointercalated Anions-Induced Phase Separation

The study of phase separation due to the size difference of the cointercalated anions was carried out by comparing two different systems of varying compositions as follows: $Zn_2Al(OH)_6(NO_3)_y(CO_3)_{0.5(1-y)}{\cdot}xH_2O$ (y= 0-1.0) and $Zn_2Al(OH)_6(Cl)_{0.7}(CO_3)_{0.15}{\cdot}xH_2O$. The resulting particle sizes and size distributions, and crystalline phases were characterized by DLS and XRD, respectively.

2.3.3.6 Cointercalated Anion Composition-Controlled Coarsening

Samples of $Zn_2Al(OH)_6(NO_3)_y(CO_3)_{0.5(1-y)}\cdot xH_2O$ (y = 0.5, 0.4, 0.3, 0.2, 0) were synthesized by coprecipitation at RT, followed by HT at 85 °C for 12 h. The resulting particle sizes were monitored by TEM and DLS techniques.

2.3.4 Results and Discussions

2.3.4.1 Formation Mechanisms of LDH NPs

The electrostatic bond strength between different intercalated anions within the gallery space of LDHs and double hydroxide layers can vary significantly,(Miyata 1983) which in turn can affect the stabilities of LDHs in a significant manner.(Allada et al. 2002, Allada et al. 2005) A thermo-chemical study showed that with the introduction of only 1.47 % of the NO_3^- anion, the ΔH_f^0 (-991.79 $KJmol^{-1}$) for pure CO_3^{2-}-intercalated LDH ($Co_{0.756}Al_{0.244}(OH)_2(CO_3)_{0.122}\cdot 0.805H_2O$) changed to -967.89 $KJmol^{-1}$ for mixed (CO_3^{2-}, NO_3^-)-cointercalated LDH ($Co_{0.756}Al_{0.244}(OH)_2(CO_3)_{0.1202}(NO_3)_{0.0036}\cdot 0.805H_2O$), indicating the higher stability of the former.(Allada et al. 2002) Therefore, it was anticipated that intercalated anion composition could have an influence on the formation mechanisms of LDH NPs. Consequently, $Zn_2Al(OH)_6(NO_3)_{0.3}(CO_3)_{0.35}\cdot xH_2O$ and $Zn_2Al(OH)_6(NO_3)\cdot xH_2O$ NPs were used as nanoparticulate model systems, and representing the cases of the very strong and the weakest electrostatic bond strength, respectively.

2.3.4.1.1 Nanostructure evolution of $Zn_2Al(OH)_6(NO_3)_{0.3}(CO_3)_{0.35}{\cdot}xH_2O$ nanoparticles

Figures 2.17 and 2.18 illustrate the time evolution of the morphology, crystallinity, as well as surface charge determined by bright-field TEM imaging, electron diffraction, and zeta-potential measurements, respectively, for $Zn_2Al(OH)_6(NO_3)_{0.3}(CO_3)_{0.35}{\cdot}xH_2O$ NPs. The composition of the as-precipitated primary NPs, determined by ICP, was $Zn_{1.902}Al(OH)_{5.804}(NO_3)_{0.3}(CO_3)_{0.35}{\cdot}xH_2O$, and the particle sizes (~180 nm) were quite uniform (Figure 2.17a), indicating optimum coprecipitation conditions. As reflected in the diffused rings with weak spots in the diffraction pattern (Figure 1a-DP), the kinetically-preferred primary NPs are amorphous with nanocrystalline domains. Additionally, during growth in an aqueous medium at RT, the high-energy (edge) surfaces grow at a higher rate than the low-energy (0001) basal surface resulting in the overall discoid shape that minimizes the surface energy. Moreover, the ζ, which is the key indicator of stability of NPs, was found to be about +36.5 mV (Figure 2.18; $Zn_{1.902}Al(OH)_{5.804}(NO_3)_{0.3}(CO_3)_{0.35}{\cdot}xH_2O$); the positive value is consistent with the positively charged nature of the LDH is due to isomorphous substitution of the Zn^{2+} by Al^{3+}. Note, a colloidal dispersion with high stability typically exhibits a ζ of ± 40-60 mV and for moderate stability, a value between ±30-40 mV.(Greenwood and Kendall 1999, Hanaor et al. 2012) Despite the expected moderate stability, some agglomeration at the edges of the discoid-shaped NPs was observed in the TEM micrograph (Figure 2.17a). Since the positive surface charge mainly stems from the (0001) basal surface, surface energy is preferentially lowered by hydration, with a high enthalpy of hydration, which results in impeded growth in the [0001] direction and

agglomeration. In contrast, the disordered edges with low charge density reduce the surface energy via the observed agglomeration.

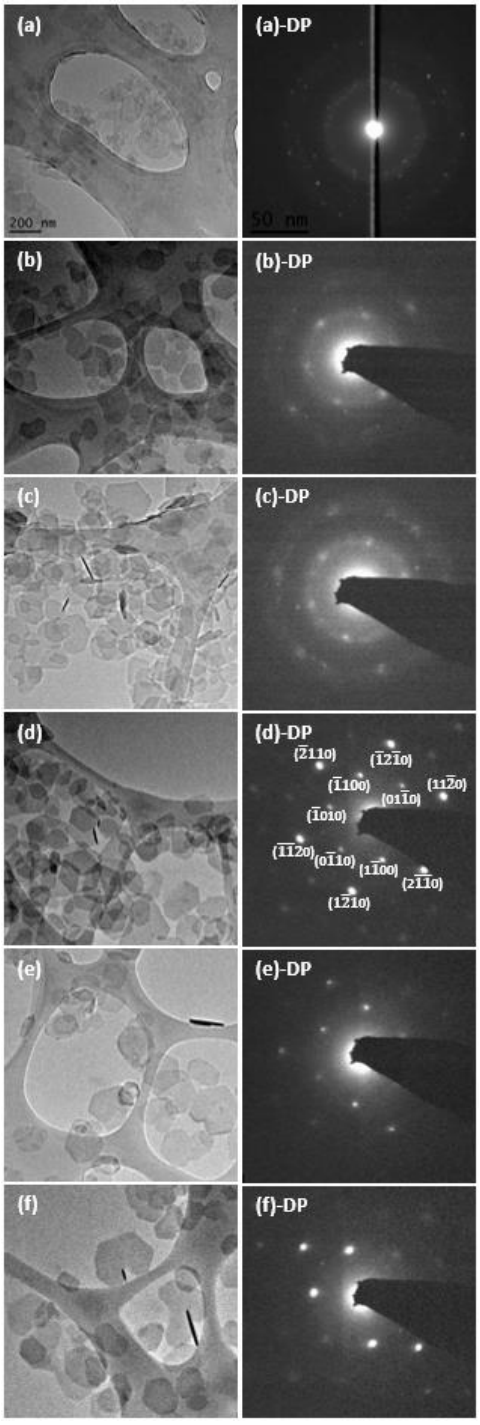

Figure 2.17. TEM study of the morphological and crystallinity evolution of $Zn_2Al(OH)_6(NO_3)_{0.3}(CO_3)_{0.35}\cdot xH_2O$ nanoparticles from the as-precipitated amorphous

nanoparticles at RT until the formation of fully crystalline nanoparticles during the hydrothermal treatment. The bright field TEM micrographs show the morphologies of the as-precipitated nanoparticles and nanoparticles after being hydrothermally treated at 85 °C for 1, 2, 3, 5 and 7 h in (a), (b), (c), (d), (e), and (f), respectively (left column). Their corresponding electron diffraction patterns with [0001] zone axis are shown in (a)-DP, (b)-DP, (c)-DP, (d)-DP, (e)-DP and (f)-DP, respectively (right column).

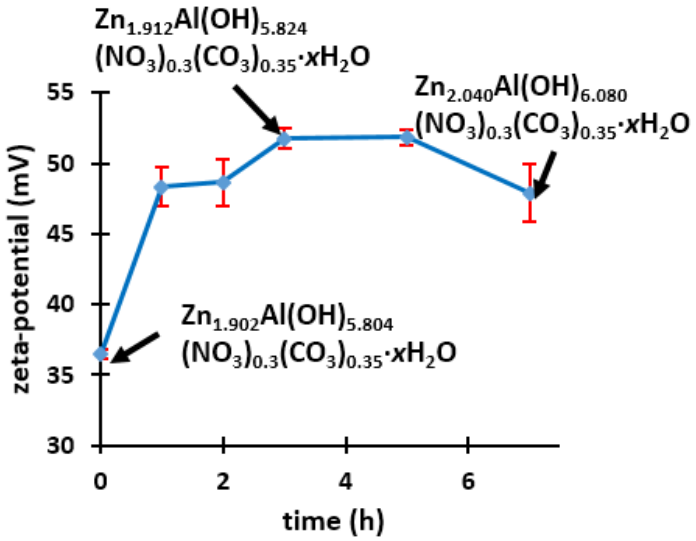

Figure 2.18. The variation of zeta-potential from the as-precipitated state through hydrothermal treatments at 85 °C up to 7 hours

The structure evolution during the HT at 85 °C is shown in Figures 2.17b-d with corresponding diffraction patterns (DPs). The as-precipitated NPs underwent phase transformation to the fully crystalline phase within 3h, the ζ increased to +51.8 mV (Figure 2.18; $Zn_{1.912}Al(OH)_{5.824}(NO_3)_{0.3}(CO_3)_{0.35}\cdot xH_2O$), and absolutely no agglomeration was observed. The latter two can be explained by improved crystallinity, increased charge density on all surfaces and hydration, especially at the ordered edges of hexagonally-shaped NPs.

As the HT progresses, the size of the as-precipitated NPs gradually increased from 180 to 230 nm (Figures 2.17a-f). The ζ also increased but saturated at +51.87 mV in 5 h, after which a diminution was observed; note, at 7 h, the ζ was +47.89 mV (Figure

2.18; $Zn_{2.040}Al(OH)_{6.080}(NO_3)_{0.3}(CO_3)_{0.35}{\cdot}xH_2O$), although the diffraction pattern was invariant in comparison to 5 h HT. Clearly, the composition and size of the LDH NPs, from the as-precipitated state up to the HT, exhibit a change with increasing t_{HT}; Al^{3+}/Zn^{2+} ratio of 0.526 (as-precipitated), 0.523 (3h HT), 0.490 (7h HT). The t and T-dependent HT simultaneously promotes the phase transformation of the metastable phase to the thermodynamically stable crystalline LDH NPs via atomic rearrangement and the coarsening process via a surface dissolution-reprecipitation process. Partial dissolution of NPs with high surface energy followed by re-precipitation of the Zn^{2+} and Al^{3+} species occur during HT. At the early stages of HT, when the NPs are predominantly amorphous with a high surface energy, the high dissolution rate should translate to high supersaturations of Al^{3+} and Zn^{2+}. The reprecipitated Al^{3+}/Zn^{2+} ratio in the LDH can be maintained. However, in the latter stages of HT, once the NPs are completely crystallized, the dissolution rate can decrease significantly due to the much lower solubility of crystalline LDH compared to their amorphous counterparts.(De Yoreo and Vekilov 2003) Under an almost equilibrium condition, the dissolution gives rise to an excess of Zn^{2+} and Al^{3+} with a ratio of 2:1 to the solution. However, since the K_{sp} of $Al(OH)_3$ is of almost 16 orders of magnitude lower than the K_{sp} of $Zn(OH)_2$ (at 25 °C, $K_{sp}(Zn(OH)_2) = 4.1x10^{-17}$ and $K_{sp}(Al(OH)_3) = 1.9x10^{-33}$), the large difference in supersaturation can facilitate the rapid precipitation of Al^{3+} in the form of $Al(OH)_3$; the experimentally-observed whitish solution was indeed indicative of very fine $Al(OH)_3$ NPs. In essence, at the latter stage of HT as the NPs coarsen via the surface dissolution-reprecipitation process, the newly-reprecipitated LDH phase added to the as-precipitated NPs becomes Al^{3+} deficient, and therefore, less positively charged.

2.3.4.1.2 Nanostructure evolution of $Zn_2Al(OH)_6(NO_3)\cdot xH_2O$ nanoparticles

The nanostructure evolution of $Zn_2Al(OH)_6(NO_3)\cdot xH_2O$, which exhibits a much lower stability compared to $Zn_{1.902}Al(OH)_{5.804}(NO_3)_{0.3}(CO_3)_{0.35}\cdot xH_2O$, was also studied to determine significant differences in terms of the morphology of as-precipitated NPs and formation mechanism during HT.

The as-precipitated, primary $Zn_2Al(OH)_6(NO_3)\cdot xH_2O$ NPs (discoid-shaped and ~70 nm) exhibited severe agglomeration at the edges (in Figure 2.19), despite a measured ζ of 43.13 mV. In aqueous medium, these NPs were highly polydispersed and the mean r_H was nearly 7 μm as determined by DLS (Figure 2.20 and inset at time, t = 0 h). The low NP size and high agglomeration tendency in this composition compared to $Zn_2Al(OH)_6(NO_3)_{0.3}(CO_3)_{0.35}\cdot xH_2O$ can be explained as follows. During coprecipitation, both homogeneous nucleation and growth processes compete to reduce the supersaturation (i.e. $\sigma = \ln\frac{Q_{sp}}{K_{sp}}$; where Q_{SP} is the ion product and K_{sp} is the solubility product constant) of the solutes, and consequent NP size is dependent on these rates. If σ is extremely high, the size of the critical nucleus can be smaller than an unit cell dimension, and the induction time (inverse of the nucleation rate) can approach to zero.(De Yoreo and Vekilov 2003) The growth rate is dictated by the difference between the fluxes of ionic species involved in the attachment to and detachment from the growth surface. Under strong convection, the former is high, whereas the latter is solely influenced by the bond strength.(De Yoreo and Vekilov 2003) In the current studies, initial σ and stirring rate in the coprecipitation conditions of the synthesis of both compositions were about the same (97.4 and 3000 rpm, respectively) and rather high.

Therefore, the smaller primary NP size of $Zn_2Al(OH)_6(NO_3)\cdot xH_2O$ (70 nm) compared to $Zn_2Al(OH)_6(NO_3)_{0.3}(CO_3)_{0.35}\cdot xH_2O$ (180 nm) can be attributed to the higher detachment rate stemming from the weaker electrostatic bond strength in the former. Additionally, the severe agglomeration in $Zn_2Al(OH)_6(NO_3)\cdot xH_2O$ composition can be explained by its highly amorphous nature, i.e., decreased charge sites and lowered hydration enthalpy on the disordered edges of the NPs. Therefore, HT was necessary to improve the crystallinity so as to form stable colloidal suspensions via electrostatic stabilization.

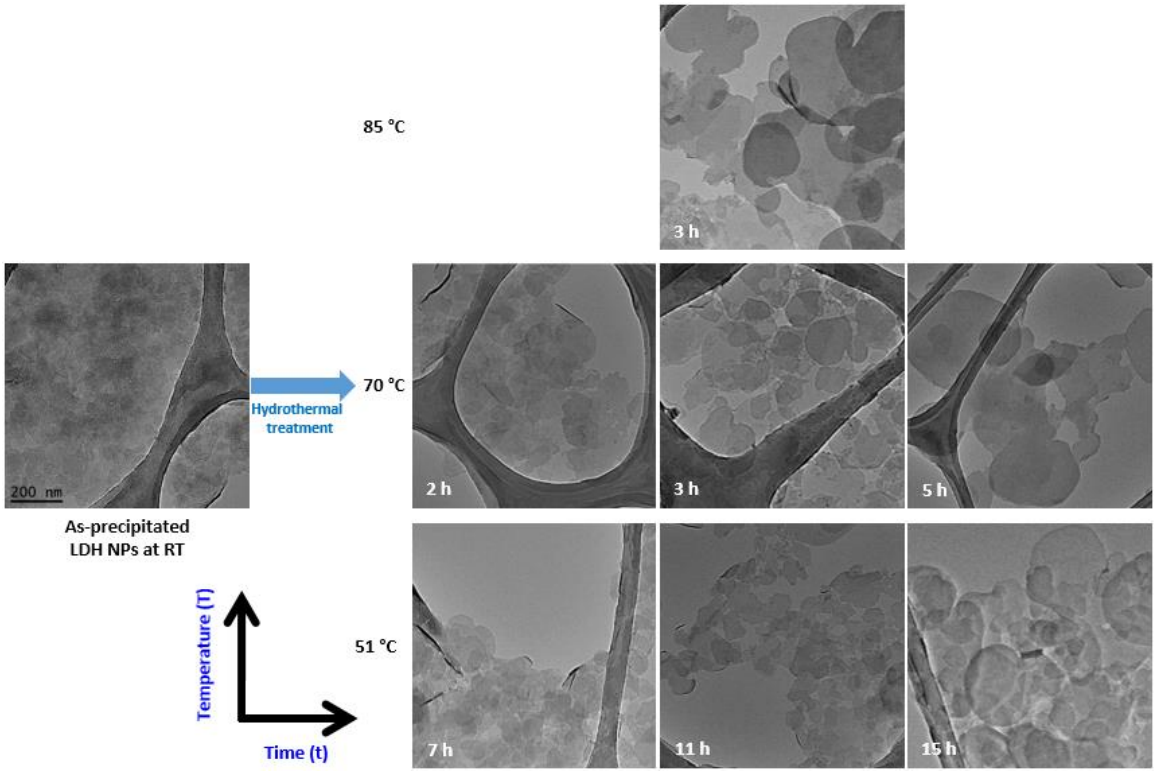

Figure 2.19. Effect of the T_{HT} and t of the hydrothermal treatment on the resulting morphological evolution from the as-precipitated amorphous materials towards the formation of crystalline $Zn_2Al(OH)_6(NO_3)\cdot xH_2O$ LDH nanoparticles

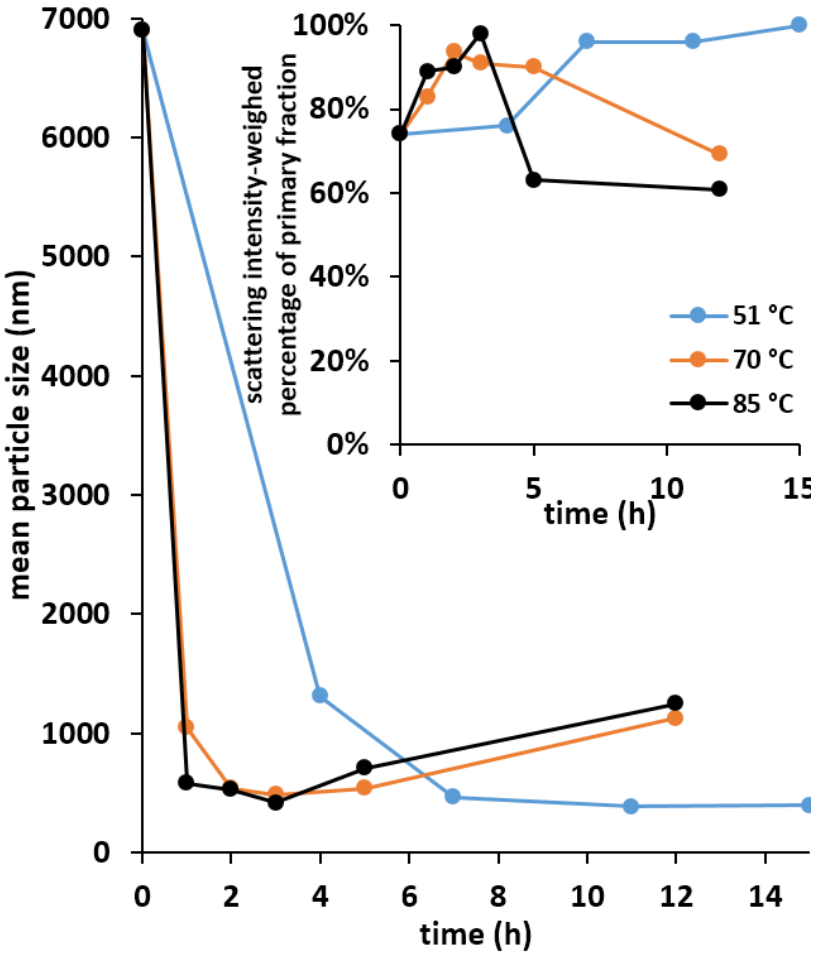

Figure 2.20. Evolution of the particle size and scattering intensity-weighted percentage of the primary fraction, measured by DLS at different T_{HT} for different duration

The HT at 85 °C rapidly dispersed the severely agglomerated, as-precipitated LDH NPs into stable suspensions; at t = 3 h, the mean r_H was about 415 nm and the system exhibited monodispersity (inset of Figure 2.20 at t = 3 h). The corresponding TEM micrograph in Figure 2.19 shows the discoid-shaped NPs with rounded edge. However, longer HT times led to particle coarsening and loss of monodispersity. After 5 h of HT, the mean r_H increased to 700 nm, and the scattering intensity-weighted percentage of the primary fraction decreased to 63% (in inset of Figure 2.20 at t = 5 h) from 98% at t = 3 h. The much higher coarsening rate of these NPs compared to that of

$Zn_2Al(OH)_6(NO_3)_{0.3}(CO_3)_{0.35}{\cdot}xH_2O$ NPs at the same T_{HT} is due to the lower stability and higher dissolution rate.

After HT at 70 °C for 2 h (or 3 h), nearly monodispersed NPs with a mean r_H of ~540 nm (or 484 nm) and a primary fraction percentage of 93.7% (or 91%) were achieved, and TEM micrographs (Figure 2.19) show that these NPs were agglomerated clusters of primary NPs. After 5h of HT, the clusters of primary NPs fully coalesced to form secondary NPs via aggregational growth mechanism, with a mean r_H of ~537 nm and a primary fraction percentage of 90%. Note, longer HT time led to particle coarsening and polydispersity, but less severe compared to that observed at 85 °C.

The HT at 51 °C up to 4 h gradually dispersed the severely agglomerated NPs, and after 7 h (inset of Figure 2.20 at t = 7 h), a nearly monodispersed stable suspension with a mean r_H of 415 nm was measured by DLS. The slow dispersion of as-precipitated NPs observed until 7 h was due to slow kinetics of the crystallization process. Between 7 and 11 h of HT, the individual primary NPs (< 100 nm) were clearly discernible in TEM images (Figure 2.19, 51 °C-7 h and 11 h), but they existed in slightly agglomerated form as secondary NPs in aqueous medium; for example, a mean r_H of ~386 nm with a primary fraction percentage of 96% was measured after 11 h HT. After 15 h HT, the primary NPs coalesced to form monodispersed secondary particles (Figure 2.19, 51 °C-15 h) with a mean r_H of 397 nm. Although the use of low HT temperature (51 °C) minimized the coarsening rate (i.e., invariant r_H of ~386-397 nm and primary fraction percentage of 96-100 % between 7-15 h), longer HTs never stabilized the primary NPs, or prevented the aggregational growth mechanism.

Due to the relatively low crystallinity and stability of NO_3^--intercalated LDH NPs (compared to those of CO_3^{2-}-intercalated ones,(Allada et al. 2006, Allada et al. 2005) after HT, the surface charge density and the hydration enthalpy at edge sites are insufficient to stabilize the individual primary NPs by electrostatic stabilization and hydration. Therefore, crystallized primary NPs further diminish the surface energy by agglomeration, although to a much lower extent compared to the as-precipitated NPs. In this study, the ideal HT window for achieving monodispersed $Zn_2Al(OH)_6(NO_3)\cdot xH_2O$ NPs were determined to be between 70 and 85 °C for 3-5 h. To date, with respect to size, size distribution, and reasonable HT duration, the best HT condition of 80 °C for 3 h gave rise to NPs with a mean r_H of 436.7 nm NPs and a primary fraction percentage of 98.7 %. Although the NO_3^--intercalated LDH is widely accepted as the most ideal composition due the ease of post-synthesis replacement with an application-specific anion, a narrow HT processing window (as determined here) perhaps is a reason why there are no literature reports on the synthesis of monodispersed NO_3^--intercalated LDH NPs.

2.3.4.2. Size Difference between the Co-Intercalated Anions-Induced Phase Separation

Figure 2.21a shows XRD patterns of the as-precipitated $Zn_2Al(OH)_6(NO_3)_y(CO_3)_{0.5(1-y)}\cdot xH_2O$ NPs (for y = 0.7) and crystalline NPs as they transform to the crystalline phase upon HT (at 70 and 85 °C for 12 h). The initial broad peak centered at 2θ ~11° corresponding to the (003) planes for the as-precipitated NPs gradually separates into two distinct peaks (centered at 2-θ of 10 and 11.6°) upon HT. The distinct latter peaks correspond to the (003) planes of NO_3^--intercalated and CO_3^{2-}-intercalated LDH NPs, respectively, which is indicative of phase separation.

Interestingly, the DLS data in Figure 2.21b for this composition, exhibiting a bimodal distribution with 81.29% of the primary fraction (mean r_H ~777.8 nm) and 18.7% of the secondary fraction (mean r_H ~238.3 nm). Moreover, since the mean particle size is dictated by the composition-dependent formation mechanisms and coarsening rates described earlier, these primary and secondary fractions can be correlated with the NO_3^--rich and CO_3^{2-}-rich LDHs, respectively. Literature data (Table 2.6)(Allada et al. 2002) suggests that mixed (CO_3^{2-}, NO_3^-)-cointercalated (Co, Al)-LDH is less stable than pure CO_3^{2-}-intercalated LDH, and considering the low magnitude of the (configurational) entropy of mixing (1-5 $J \cdot mol^{-1}$), the positive enthalpy of mixing (ΔH_{mix}^0) can drive phase separation in mixed anions-cointercalated LDH compositions provided the kinetic barriers can be overcome. Indeed, Figure 2.21a illustrates the propensity of phase separation in $Zn_2Al(OH)_6(NO_3)_{0.7}(CO_3)_{0.15} \cdot xH_2O$ NPs as the T_{HT} increases.

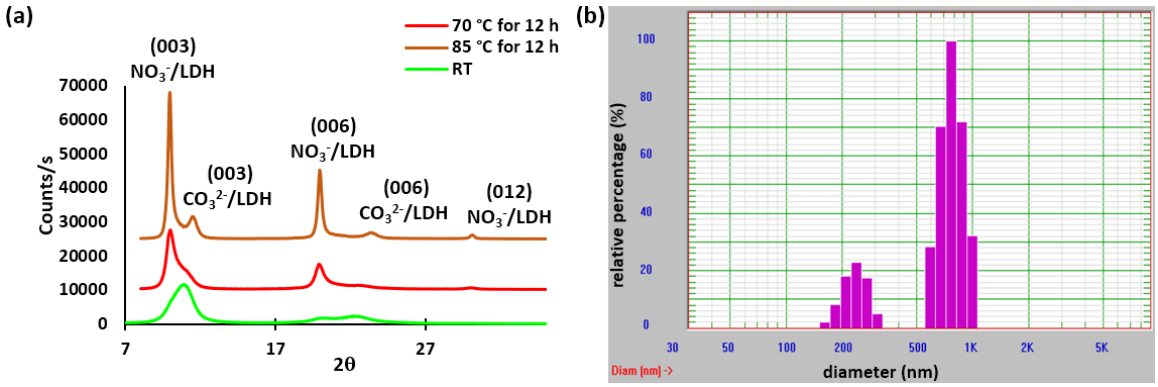

Figure 2.21. Effect of hydrothermal treatments (HT) on the phase stability and scattering intensity-weighted particle size distribution (PSD). (a) Evolution of XRD patterns of $Zn_2Al(OH)_6(NO_3)_{0.7}(CO_3)_{0.15} \cdot xH_2O$ NPs from coprecipitation at room temperature to hydrothermally treated at 70 and 85 °C for 12 h, (b) the bimodal PSD measured by DLS after HT at 85 °C for 12 h.

Table 2.6. Standard enthalpy of formation for pure CO_3^{2-}-intercalated and mixed (CO_3^{2-}, NO_3^-)-cointercalated LDHs

LDH composition	ΔH_f^0 (kJ/mol)
$Co_{0.756}Al_{0.244}(OH)_2(CO_3)_{0.122}\cdot 0.805H_2O$	-1044.17±2.50 (Allada et al. 2002)
$Co_{0.756}Al_{0.244}(OH)_2[(CO_3)_{0.1202}(NO_3)_{0.0036}\cdot 0.810H_2O$	-967.89±3.33 (Allada et al. 2002)

To determine the range of CO_3^{2-} content that may cause phase separation and bimodal PSD in (Zn, Al)-LDH system, cointercalated $Zn_2Al(OH)_6(NO_3)_y(CO_3)_{0.5(1-y)}\cdot xH_2O$ NPs, with y = 0, 0.2, 0.3, 0.4, 0.5, 0.6, 0.7, 0.8, 0.9 and 1.0, were coprecipitated at RT followed by HT at 85 °C for 3 and/or 12 h. The results of DLS are tabulated in Table 2.7. Note, the 3 h HT was used for samples with low stability and having propensity for rapid coarsening, which in turn would cause a bimodal distribution that is unrelated to phase separation. The 12 h HT was used to illustrate the difference in the mean r_H due to the difference in the coarsening rate of phase-separated, NO_3^--rich and CO_3^{2-}-rich fractions.

Table 2.7: Mean r_H and PSD of hydrothermally treated $Zn_2Al(OH)_6(NO_3)_y(CO_3)_{0.5(1-y)}\cdot xH_2O$ NPs

LDH Composition, y	HT: 85 °C for 3 h		HT: 85 °C for 12 h	
	Primary fraction	Secondary fraction	Primary fraction	Secondary fraction
0.0	/		200 (100%)*	
0.2	/		218.4 (100%)*	
0.3	/		231.7 (100%)*	
0.4	/		253.6 (100%)*	
0.5	/		331.3 (100%)*	
0.6	363.5 (75.72%)	153.5 (31.72%)ǂ	512 (80%)	200 (20%)ǂ
0.7	536.3 (65.33%)	196.8 (34.67%)ǂ	777.8 (81.29%)	238.3 (18.70%)ǂ
0.8	/		1009.3 (75.66%)	282.9 (24.34%)ǂ
0.9	645.3 (71.52%)	210.8 (28.48%)ǂ	/	
1.0	416.4 (98.55%)	46.2 (1.45%)ǂ	/	

* Gaussian MPS used if $\chi^2 \leq 3$; ǂ MPS fitted by NICOMP-analyzed MPS used when $\chi^2 > 3$.(Nicomp 380 DLS user manual 2006)

In the composition range, $0.9 \geq y \geq 0.6$, pronounced bimodal PSD due to phase separation were observed after 3 h HT at 85 °C, and the difference between the mean r_H of separated fractions was further enhanced after 12 h of HT. Based on the aforementioned observations and discussions, and trends in available thermodynamic data,(Allada et al. 2002) one may surmise that $Zn_2Al(OH)_6(NO_3)_y(CO_3)_{0.5(1-y)}\cdot xH_2O$ NPs with $0.5 \geq y \geq 0.2$ are probably thermodynamically metastable, and experimental observation of monodispersed PSD is suggestive of kinetic inhibition of phase separation at the relatively low T_{HT} of 85 °C.

Since the application target at hand is nanomedicine, the observed phase separation and consequent bimodal distribution in the NO_3^--rich LDH compositions is detrimental. Therefore, identification of parameters based on existing theories of phase separation and avoidance of phase separation are critical. It is well known that large differences in ionic potential (z/r, where z is the charge and r is the radius) and electrostatic bond strength (z/CN, where CN is the coordination number)(Fevre et al. 2013, West 1989) influence the temperature-dependent miscibility in solid solutions. In LDH systems, the synergistic effects of z, r, and CN of anions in the hydrated gallery influences the d_{003} gallery spacing, and therefore, the magnitude and sign of ΔH_{mix}^0, which in turn dictates the tendency for phase separation in mixed anions-cointercalated systems at a given temperature. To lend credence to this idea, mixed (CO_3^{2-}, Cl^-)-cointercalated (Zn, Al)-LDH NPs were synthesized and tested for phase separation; note, literature data indicate that individual Cl^- and CO_3^{2-}-intercalated LDH have identical d_{003} gallery spacing.(Sato, Wakabayashi, and Shimada 1986) The exact composition tested was $Zn_2Al(OH)_6(Cl)_{0.7}(CO_3)_{0.15}\cdot xH_2O$ so as to compare with the

$Zn_2Al(OH)_6(NO_3)_{0.7}(CO_3)_{0.15}{\cdot}xH_2O$ NP system that had exhibited phase separation and pronounced bimodal PSD. The XRD pattern of $Zn_2Al(OH)_6(Cl)_{0.7}(CO_3)_{0.15}{\cdot}xH_2O$ NPs after HT at 85 °C for 5 h and the corresponding PSD by DLS are shown in Figure 2.22a and b, respectively. Clearly, the mixed (Cl^-, CO_3^{2-})-cointercalated (Zn, Al)-LDH NPs have one d_{003} gallery spacing, but whether phase separation exists cannot be conclusive. However, despite the difference in growth mechanisms and coarsening rates of individual Cl^- and CO_3^{2-}-intercalated LDH, a single Gaussian distribution centered at 303.4 nm was observed clearly indicating that phase separation did not occur. Note, the growth mechanism of Cl^--intercalated (Zn, Al)-LDH NPs was also determined to be aggregational growth as NO^--intercalated LDH NPs due to their similar stability.

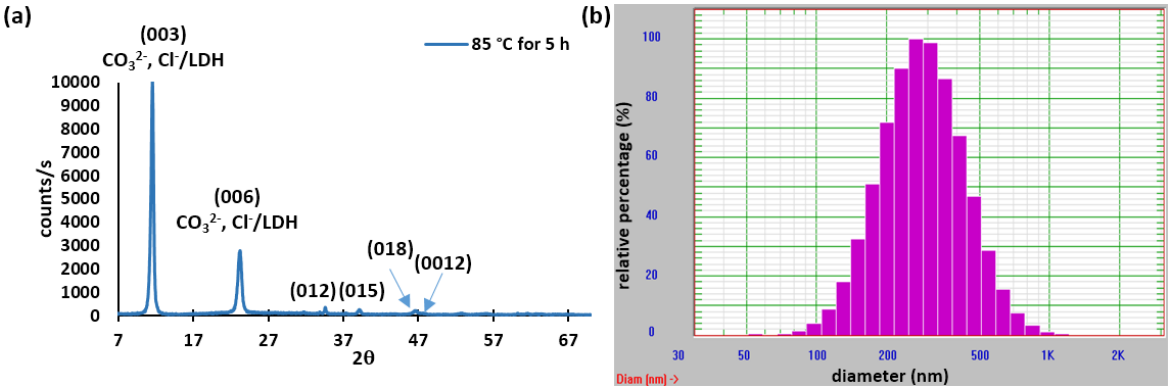

Figure 2.22. XRD pattern of $Zn_2Al(OH)_6(Cl)_{0.7}(CO_3)_{0.15}{\cdot}xH_2O$ NPs, hydrothermally treated at 85 °C for 5 h (a), and the corresponding monodispersed PSD measured by DLS technique (b)

2.3.4.3 Intercalated Anion Composition-Controlled Coarsening

As previously stated, the much higher coarsening rate of NO_3^--intercalated NPs compared to that of $Zn_2Al(OH)_6(NO_3)_{0.3}(CO_3)_{0.35}{\cdot}xH_2O$ NPs at the same T_{HT} is due to the higher dissolution rate. The solubility of the LDH NPs is governed by the cationic composition of the double hydroxide, the intercalated anions, and T.(Allada et al. 2002,

Allada et al. 2006, Allada et al. 2005) Here, we show that LDH NPs with a systematic variation of the particle size can be achieved by controlling the coarsening rate through the intercalated anion composition. HT of $Zn_2Al(OH)_6(NO_3)_y(CO_3)_{0.5(1-y)}{\cdot}xH_2O$ (y = 0.5, 0.4, 0.3, 0.2, 0) at 85 °C for 12 h led to monodispersed LDH NPs with gradual decreased particle sizes, as the CO_3^{2-} content increased (Table 2.7). In Figure 2.23, the TEM bright field micrographs reveal their morphologies, and NPs with higher contents of NO_3^- showed more rounded and thinner morphologies compared to LDH NPs with higher CO_3^{2-} contents. The gradual variation of the cointercalated anion ratios of NO_3^- to CO_3^{2-} allows to gradually vary the stability of the LDH NPs, and in turn their coarsening rates that lead to the gradual size variation (from ~400 nm to ~200 nm in diameter). The fact that $Zn_2Al(OH)_6(NO_3)_y(CO_3)_{0.5(1-y)}{\cdot}xH_2O$ NPs only shows phase separation during the HT when y > 0.5 permits the achievement of monodispersed $Zn_2Al(OH)_6(NO_3)_y(CO_3)_{0.5(1-y)}{\cdot}xH_2O$ NPs (y < 0.5). Moreover, careful choosing the T_{HT} is also critical to the controlled coarsening and achieving monodispersed NPs. In this case, 85 °C was chosen as the T_{HT} because at this T_{HT}, the coarsening rate of CO_3^{2-}-rich LDH NPs is rather slow, while the coarsening rate of NO_3^--intercalated LDH NPs is significantly faster, as previously shown. An adequate T_{HT} can selectively increase the dissolution rate of given sites or NPs, which is critical to achieve self-similarity, i.e. NPs with similar morphology and size. However, if the T_{HT} is very high, too much thermal energy enables a random dissolution, accelerates the coarsening, and therefore polydispersity increases.

In summary, Figure 2.24 schematically represents the results obtained in *Section 2.3.4.1, 2.3.4.2,* and *2.3.4.3* – the effects of the different compositions of the intercalated anions on the formation mechanisms, phase separation, and coarsening rates.

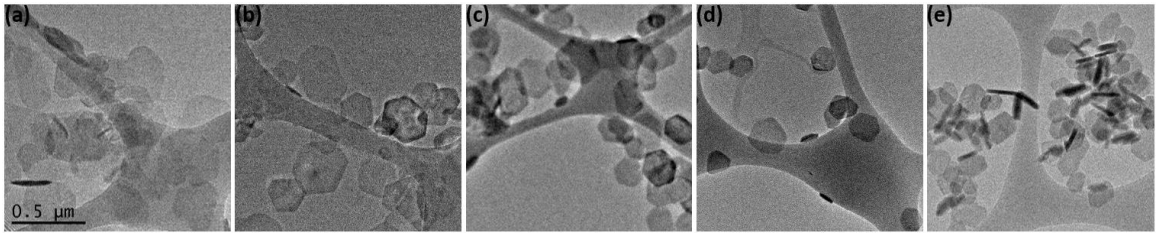

Figure 2.23. Gradual decrease in the particle size of $Zn_2Al(OH)_6(NO_3)_y(CO_3)_{0.5(1-y)}{\cdot}xH_2O$ NPs by controlling the coarsening rate, which is inversely proportional to the stability determined by the intercalated anion composition: (a) y = 0.5, (b) y = 0.4, (c) y = 0.3, (d) y = 0.2, (e) y = 0.

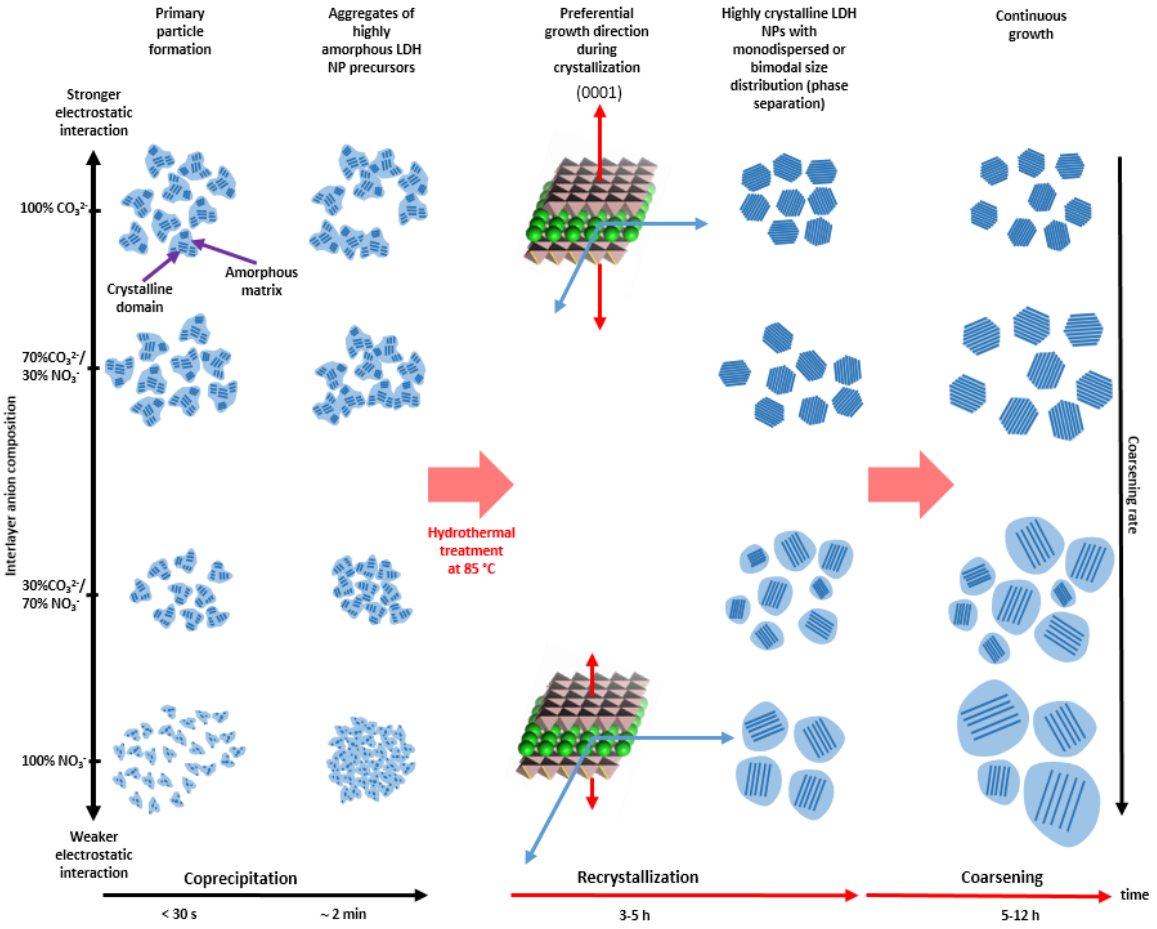

Figure 2.24. Schematic representation of the effect of the (co)intercalated anion composition on the formation mechanisms (nucleation, agglomeration, crystallization, aggregational growth, phase separation, and coarsening) as well as the resulting morphology, MPS and PSD in the processing cycle.

2.3.5 Conclusions

In this study, we have demonstrated by TEM and DLS that the formation of crystalline LDH NPs proceeds through highly amorphous primary particles formed in the initial RT coprecipitation. Such metastable primary particles have a discoidal shape due to the slower growth rate of the (0001) planes, which have the highest surface charge density as well as the hydration enthalpy. Therefore, the agglomeration of the primary particles mainly took place at the edge sites, where the charge density and hydration enthalpy are the lowest. HT can increase the crystallinity of the primary particles, and their surface charge density as well as hydration enthalpy. Whether such agglomeration is reversible or irreversible highly depends on the crystalline quality and surface charge density, which are strongly influenced by the composition of the intercalated anions, especially on the edge sites of the crystalline counterparts. The agglomeration was completely reversible for $Zn_2Al(OH)_6(NO_3)_{0.3}(CO_3)_{0.35}{\cdot}xH_2O$ NPs due to the high CO_3^{2-} content and excellent crystallinity. In contrast, the agglomeration of the $Zn_2Al(OH)_6(NO_3){\cdot}xH_2O$ primary particles was irreversible due to the least stable composition and intrinsically less ordered nanostructure. Even when the crystallization was carried out under conditions that minimize the coarsening process, while individual primary particles were observed using TEM, DLS study showed that in aqueous environment, they existed as nearly monodispersed secondary particles, formed by aggregational growth from the primary particles. Also, we believe the size of the secondary particle, i.e. the extent of irreversible agglomeration, is dictated by the surface energy (including the hydration enthalpy contribution) of the crystalline primary particle.

Moreover, the stability study provided the insight that the size difference between the cointercalated anions can be the responsible driving force for the phase separation and the consequent bimodal size distribution. We also showed that the coarsening rate can be controlled by rationally designing the composition of the cointercalated anions. By gradual increasing the cointercalation ratio of NO_3^- to CO_3^{2-} and staying within the phase separation-free composition range, the increasing coarsening rates led to monodispersed LDH NPs with gradually increasing particle size.

The understanding of the formation mechanisms and the keys for obtaining monodispersed LDH NPs should lead to strategies for controlling the growth direction and/or blocking the aggregational growth of the primary particles, for example by rational use of surfactants. Such knowledge should also guide the synthesis of monodispersed and well-defined LDH NPs of other biocompatible compositions. All above are of high interest to open new pathways for the use of LDH-based nanomaterials in biomedicine.

2.4 *In vitro* Evaluation of the Properties and Drug Delivery Capabilities of (Zn, Al)-Based Layered Double Hydroxide (LDH) Nanoparticles

2.4.1 Abstract

There is a great need for the development of alternative strategies for effective drug delivery to improve the outcome of patients suffering from deadly diseases such as cancer. Nanoparticles, in particular those based on layered double hydroxide (LDH) nanoparticles have great potential as carriers of chemotherapeutic molecules. In the current study we synthesized LDH particles based on zinc and aluminum report its enhanced pH-dependent stability in comparison to the commonly used LDH particles based on magnesium and aluminum. Zn-Al-based LDH nanoparticles were intercalated with valproate or fluorescein isothiocyanate (FITC) to study cellular uptake, drug delivery capabilities and biocompatibility using cultured pancreatic adenocarcinoma BxPC-3 cells. Fluorescence measurements indicated that FITC-intercalated nanoparticles showed a greater degree of active (energy-defendant) uptake rather than passive uptake by BXPC-3 cells, especially at higher nanoparticle concentrations. Cell viability assessment using a tetrazolium-based colorimetric assay indicates that BXPC-3 cells treated with valproate-intercalated LDH nanoparticles showed a significant reduction in cell viability with a 50 fold reduction in the IC_{50} as compared to the drug alone. Exposure to non-drug-intercalated LDH nanoparticles did not affect the viability of cells indicating very low innate cytotoxicity of the (Zn, Al)-LDH nanoparticles. Our research indicates that the superior properties of (Zn, Al)-LDH nanoparticles make them ideal candidates for further development as *in vivo* chemotherapy delivery agents.

2.4.2 Introduction

Conventional chemotherapeutic strategies involve administration of drugs by injections or oral ingestion resulting in a broad distribution of the drug throughout the body. This generally results in only a small fraction of the drug reaching the site of the tumor and impacting the cancerous cells. However, this also exposes non-cancerous cells in the body to the cytotoxicity of the chemotherapeutic agents resulting in off-target effects. Hence, the success of chemotherapy depends on the effective delivery of drugs to the to the tumor cells while minimizing off-target effects. In recent years, nanoparticles (NPs) have shown great potential for the effective delivery of high doses of a number of clinically approved and experimental drugs for cancer therapy (Cukierman and Khan 2010). The incorporation of cancer cell-recognizing moieties on drug-carrying NPs allows the specific targeting of chemotherapeutics to tumor cells, thus reducing damage to healthy tissues and significantly improving patient outcomes. The development of NPs with theranostic capabilities has further expanded the utility of these particles by adding *in vivo* imaging capability that allows diagnosis and/or prognosis (Xie, Lee, and Chen 2010).

An ideal drug delivery NP should be able to encapsulate high doses of the drug; remain stable under physiological conditions; protect the drug from degradation during transport in the body, be specifically and effectively taken up by cancer cells, efficiently release the incorporated drug intracellularily; undergo biodegradation safely and form breakdown products that are biocompatible(Cukierman and Khan 2010). The surface chemistry of the NPs should allow conjugation of biological moieties for targeting tumor cells and in the case of theranostic NPs allow the loading of functional entities for *in vivo*

imaging (Xie, Lee, and Chen 2010). Among many drug delivery platforms, such as liposomes, quantum dot, silica and magnetic NPs, etc., layered double hydroxide (LDH) NPs fulfill many of the requirements of an ideal drug delivery nanoplatform(Xu and Lu 2006).

LDH materials, based on [$Mg_6Al_2(OH)_{16}CO_3{\cdot}4H_2O$] structure, consist of brucite-like positively charged hydroxide layers and interlayer anions which bond to hydroxide layers by electrostatic interaction and maintain the charge neutrality. It is well-known that the interlayer anions are exchangeable, and the intercalation of a variety of biology-relevant species with negative charges, such as nucleotides, fluorescent dye molecules, siRNA, vitamins, acidic drugs, etc., have been demonstrated. The LDH NPs are usually stable in basic condition but can disintegrate at lower pH conditions found in the lysosome to allow the controlled release of the intercalated species inside the cell. (Mg, Al)-based LDH NPs can be easily synthesized in the lab and numerous reports on the synthesis, characterization and drug delivery capabilities of this nanoplatform have been reported. However, several studies related to the drug release profile of (Mg, Al)-LDH NPs have reported a strong initial burst. For example, almost 100% gembibrozil was released from gembibrozil-intercalated [$LiAl_2(OH)_6$] LDH within 10 mins at pH 7 (Khan and O'Hare 2002), while 80% of the intercalated Ibuprofen was released from Ibuprofen-intercalated (Mg, Al)-LDH shortly after 10 mins at pH 8 (Li et al. Inorganic layered double hydroxides as a drug delivery system - intercalation and in vitro release of fenbufen 2004). Stability may be enhanced by enteric-coating of the NP, but this alters the positive charges on the surface and may lead to agglomeration(Li et al. Enteric-coated layered double hydroxides as a controlled release drug delivery system 2004). LDH NPs

with greater stability at physiological pH are advantageous for the efficient drug delivery. Therefore, it is imperative to find alternative biocompatible LDH compositions with improved stability for controlled release of intercalated drugs and surface conjugation with targeting moieties (Xu and Lu 2006).

In this study we report the synthesis of (Zn, Al)-LDH NPs and evaluate their pH-dependent stability in comparison to the most frequently used (Mg, Al)-LDH NPs. Moreover, fluorescein isothiocyanate (FITC)-intercalated (Zn, Al)-LDH NPs were synthesized and used in the cellular uptake study to determine the energetic dependence. Finally, in order to study the drug delivery capabilities, valproate (VP)-intercalated (Zn, Al)-LDH NPs were synthesized and characterized. The form of the intercalated VP inside the LDH NPs was proposed based on the combination of the optimized molecular geometry of VP by density function theory and the calculated interlayer space of the LDH NPs from X-ray diffraction (XRD) pattern. *In vitro* cytotoxicity assessment of VP-intercalated (Zn, Al)-LDH NPs using cultured pancreatic cancer cells (BXPC3) was carried out. In the range of concentrations tested, the biocompatibility of (Zn, Al)-LDH NPs without VP but containing either chloride, nitrate, or carbonate was also assessed.

2.4.3 Materials and Methods

2.4.3.1 Synthesis of (Mg, Al)-LDH NPs, (Zn, Al)-LDH NPs and Their Solubility Studies:

$[Mg_{1.85}Al(OH)_2](NO_3)\cdot xH_2O$ and $[Zn_{2.03}Al(OH)_2](NO_3)\cdot xH_2O$ nanoparticles, denoted as (Mg, Al, NO_3)-LDH, and (Zn, Al, NO_3)-LDH, respectively, were synthesized for the study of the pH-dependent stability using titration method. Detailed synthesis procedures have been described previously. Briefly, a 10 ml metal salt solution that

contains 20 mM of $Zn(NO_3)_2 \cdot 6H_2O$/$Mg(NO_3)_2 \cdot 6H_2O$ and $Al(NO_3)_3 \cdot 9H_2O$ with Zn/Mg to Al molar ratio of 2 and a 10 ml of 40 mM NaOH solution were simultaneously added into a 3-neck flask under a nitrogen atmosphere. Vigorous stirring (3000 rpm) was applied during the coprecipitation process. Following the constant pH synthesis route, the pH was maintained constant during the coprecipitation process and the final pH of the mixture was around 5.98±0.2. After hydrothermally treated at 85 °C for 3h, the mixture was cooled to room temperature. The LDH nanoparticles were then recovered by centrifuge for physicochemical characterization and pH-dependent stability studies.

2.4.3.2 Intercalation of FITC into (Zn, Al)-LDH NPs

Fluorescein isothiocyanate (FITC) was intercalated into (Zn, Al, NO_3)-LDH nanoparticles by ion exchange method(Perioli et al. 2011). First, the pH of a 40 ml solution of 0.833 mM FITC was adjusted to neutral using a 0.25 M NaOH solution, and the pH evolution was continuously monitored using a pH meter. An appropriate amount of (Zn, Al, NO_3)-LDH nanoparticles were then dispersed into a 10 ml FITC solution, the molar ratio of FITC to Al is designed to be around 0.3. The mixture was then aged at 50 °C for a few hours. This specific T was chosen to avoid causing instability to (Zn, Al, NO_3)-LDH nanoparticles and to minimize the coarsening process. After cooling to room temperature, the FITC-intercalated nanoparticles were collected by centrifuge, and used for the investigation of cellular uptaking mechanisms.

2.4.3.3 Intercalation of VP into (Zn, Al)-LDH NPs by Ion Exchange

Sodium valproate salt (VP-Na) was intercalated into (Zn, Al, NO_3)-LDH nanoparticles by ion exchange method(Perioli et al. 2011). The (Zn, Al, NO_3)-LDH nanoparticles were first dispersed in alcohol and recovered by centrifuge. The recovered mixture were then equilibrated with a hydroalcoholic solution containing 1.667 mM VP-Na under a nitrogen atmosphere. The mixture was aged at 50 °C for several hours to facilitate the intercalation reaction. After cooling, the $Zn_{1.91}Al(OH)_6(NO_3, 0.5CO_3)_{0.584}(VP)_{0.416}\cdot xH_2O$ nanoparticles, denoted as (Zn, Al, VP)-LDH, were separated by centrifuge, washed a few times with ethanol, and dried in vacuum at 50 °C.

2.4.3.4 Molecular Geometry Optimization of Valproate by Computational Study

In order to understand in which form VP anions were intercalated within the LDH nanoparticles, the geometry optimization of VP was carried out using density functional theory calculations. Spin-unrestricted B3LYP method combined with 6-31G* basis set, as provided in the Gaussian 03 package, was used. The form of the intercalated VP^- was proposed based on the optimized geometry of VP and the interlayer space calculated from XRD pattern.

2.4.3.5 Physicochemical Characterization of LDH NPs

The morphology and particle size of LDH nanoparticles were examined by bright-field transmission electron microscopy (TEM; Philips CM200 with an electron acceleration voltage of 200 kV). The zeta (ζ)-potential was determined using a zeta potential analyzer (PSS-NICOMP 380 with zeta potential capability). The crystalline

phase information was obtained by powder X-ray diffraction (XRD; Rigaku D/Max-IIB instrument with Cu-K_α radiation, λ=0.154059 nm). The loading capacity of VP in (Zn, Al, VP)-LDH nanoparticles was calculated from the total carbon concentration, determined using a total organic carbon analyzer (Shimadzu TOC-VC/TN). Note, despite the meticulous synthesis conditions, there were some minor CO_3^{2-} contaminants detected in XRD patterns of (Zn, Al, VP)-LDH nanoparticles, and were counted towards the VP loading capacity. The elemental compositions of the LDH nanoparticles were determined by inductively coupled plasma atomic emission spectroscopy (ICP; iCAP 6300 ICP Spectrometer).

2.4.3.6 Studies of pH-Dependent Aqueous stability of (Mg, Al, NO_3)-LDH and (Zn, Al, NO_3)-LDH NPs

Titration experiment was used to study the pH-dependent stability of LDH nanoparticles. First, a given amount of (Mg, Al, NO_3)-LDH and (Zn, Al, NO_3)-LDH nanoparticles were dispersed in deionized water. 0.1 M HNO_3 solution was then added dropwise into the LDH NP suspension at an addition rate of 0.1 ml per every 15 min, while stirring. The changes of pH were monitored using a pH meter (Fisher Scientific™ accumet™ Excel XL60).

2.4.3.7 Cell line and Cell Culture

The human pancreatic adenocarcinoma cell line BxPC3 was obtained from ATCC CRL-1687. Cells were cultured at 37 ^{0}C and 5% CO_2 in RPMI-1640 medium (Thermo scientific, Waltham, MA) supplemented with 10% FBS (Fisherbrand Research Grade

Serum, Thermo scientific) and 0.2% penicillin-streptomycin (Cambrex Bio Science, Walkersville MD). Cells were maintained in T-75 tissue culture flasks and passaged by trypsinization using standard cell culture protocols. All experiments were performed on cells between passage numbers 18 to 29. Cell counts were determined using a Muse Cell Analyzer (EMD Millipore, Billerica, MA)

2.4.3.8 Fluorescence Analysis to Determine Energy-Dependent Cellular Uptake of NPs

BxPC-3 cells were seeded in two 96-well tissue culture plates with 15000 cells per well and incubated for 24 h. Prior to treatment with nanoparticles, one plate was pre-incubated for 30 min at 4^{o}C (to determine passive uptake) while the other plate was maintained at 37^{o}C (to determine active uptake). (Zn, Al)-LDH-nanoparticles intercalated with FITC (fluorescein isothiocyanate, Sigma Aldrich, St. Louis, MO) were also preincubated for 30 min at either 4^{o}C or at 37^{o}C. The cell culture media in the microtiter plate pre-incubated at 4^{o}C was replaced with 200 µl media containing various concentrations of the FITC-containing nanoparticles preincubated at 4^{o}C. Incubation was continued at 4^{o}C for another hour. Similarly the plate maintained at 37^{o}C received FITC-containing nanoparticles preincubated at 37^{o}C and further incubated for another one hour at 37^{o}C. After incubation, the media was removed and the cells were washed with PBS buffer (also preincubated at 4^{o}C or at 37^{o}C). The cells were then lysed by the addition of 100 µl/well of Pierce RIPA Lysis Buffer (Thermo Scientific) and incubation for 10 min at room temperature. Fluorescence from the cell lysates were measured at λ_{Ex}=485 nm and λ_{Em}=520 nm using the BioTek Synergy 2 plate reader.

2.4.3.9 Dose Response of BXPC3 to Valproate-Sodium and Determination of IC_{50}

BxPC-3 cells were seeded in a 96-well tissue culture plate with 6000 cells per well and incubated for 24 h. The cell culture media was replaced with media containing various concentrations of VP-Na. After 72 hours, the viability of cells was assessed using the XTT cell viability assay kit (Gaithersburg, MD) according to the manufacturer's instructions. The cleavage of XTT (a yellow tetrazolium salt) by cells leads to the formation of an orange formazan dye which as quantified by measuring absorbance at 490 nm in a BioTek Synergy 2 plate reader (Biotek, Winooski, VT). All experiments were performed at least three times with quadruple replicates for each treatment. Graph Pad Prism software was used to generate a dose response curve and determine the IC_{50} of VP-Na for BXPC3 cells.

2.4.3.10 Effects of Valproate-Intercalated (Zn, Al)-LDH NPs

BXPC-3 cells were seeded in a 96 well plate with 6000 cells per well starting from a 60-80% confluent flask and incubated for 24 hours. The cell culture media in the microtiter plate was replaced with media containing various concentrations of (Zn, Al)-LDH NPs intercalated with VP. Media containing (Zn, Al)-LDH NPs containing chlorine or nitrate or carbonate ions were used as control to assess the effects of the nanoparticle without drugs intercalated into them. After 72 hours, the viability of cells was assessed using the XTT cell viability assay as described in section 2.4.3.9.

2.4.4 Results and Discussions

2.4.4.1 Aqueous Stability Study of (Mg, Al, NO_3)-LDH and (Zn, Al, NO_3)-LDH NPs

The particle size and surface charge of NPs can strongly influence the pharmacokinetics, biodistributions and cellular uptaking mechanisms(Moghimi, Hunter, and Murray 2001). Moreover, their aqueous solubility usually differs significantly from that of bulk materials due to the change of chemical potential, which is determined by the interfacial tension, the molecular volume and the particle size(Schindle.Pw 1967). To ensure that the $Mg_{1.85}Al(OH)_{5.7}(NO_3)\cdot xH_2O$ ((Mg, Al, NO_3)-LDH) and $Zn_{2.03}Al(OH)_{6.06}(NO_3)\cdot xH_2O$ ((Zn, Al, NO_3)-LDH) NPs used for the aqueous stability study are suitable for theranostic application (i.e. having both therapeutic and diagnostic attributes) as well as their similarity in particle size and shape, TEM was first used to characterize the morphology and particle size; note, the elemental compositions were determined by ICP. As shown in Figure 2.25A and B, the particle sizes of discoidal (Mg, Al, NO_3)-LDH NPs are about 30 - 40 nm in diameter and the sizes of (Zn, Al, NO_3)-LDH NPs, synthesized under the identical conditions, are slightly larger and vary from 200 - 300 nm in diameter; both are within the ideal particle size range for drug delivery applications. Also, the positive ζ-potentials of both types of LDH NPs, i.e., 48.53 mV for (Zn, Al, NO_3)-LDH and 44.82 mV for (Mg, Al, NO_3)-LDH NPs, indicate that their surfaces favor the cellular uptaking.

XRD was used to identify the specie of the intercalated anions. Figure 2.25C shows that the experimentally determined d_{003} spacing of both LDH NPs is 8.8 Å ($2\theta = 10°$). With the published data on the thickness of the Brucite layer of ~4.8 Å, the gallery spacing is found to be ~4 Å, which verifies that NO_3^- was the only intercalated

specie for both LDH NPs. However, the relative intensities of their XRD patterns are indicative that the (Zn, Al, NO_3)-LDH NPs intrinsically tend to have a better crystallinity than (Mg, Al, NO_3)-LDH NPs.

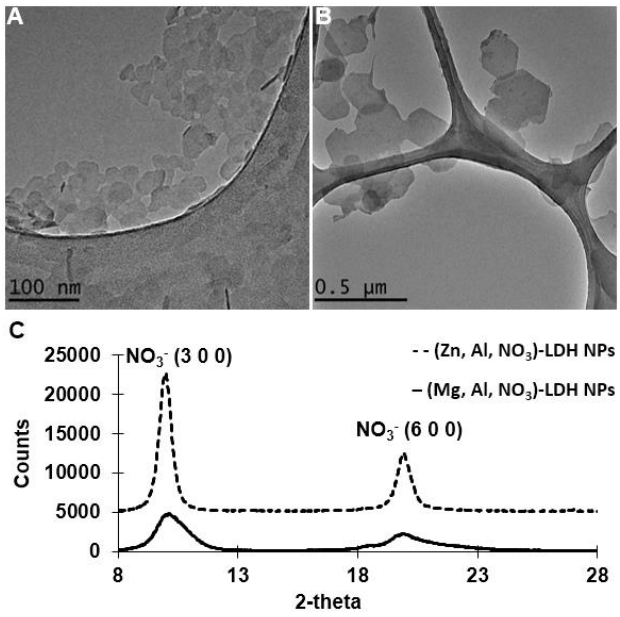

Figure 2.25. TEM bright field images of $Mg_{1.85}Al(OH)_{5.7}(NO_3)\cdot xH_2O$ and $Zn_{2.03}Al(OH)_{6.06}(NO_3)\cdot xH_2O$ NPs are displayed in A and B, respectively, and their XRD patterns are shown in C.

Boclair *et al.* reported that the cationic compositions influence the formation pH of the LDH materials greatly.(Boclair and Braterman 1999, Boclair et al. 1999) Consequently, we also expect them to show a significant effect on the aqueous stability. The aqueous stability studies of (Mg, Al, NO_3^-)-LDH NPs and (Zn, Al, NO_3^-)-LDH NPs at different pH were carried out by titration method. The pH changes were recorded along with the addition of the titrant of HNO_3 (0.1 M) and the results are illustrated in Figure 2.26.

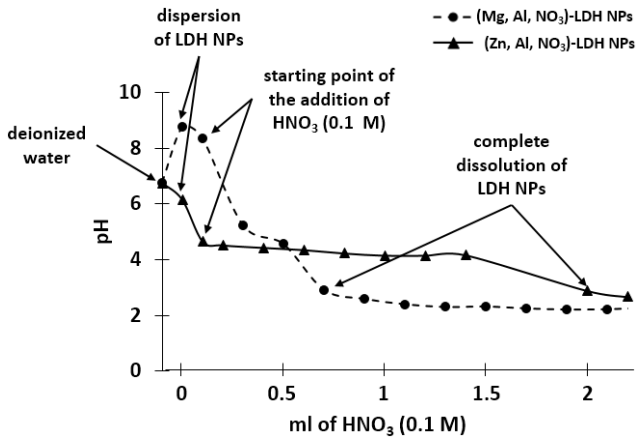

Figure 2.26. Titration curves for aqueous suspensions of (Mg, Al, NO_3)-LDH NPs and (Zn, Al, NO_3)-LDH NPs using HNO_3 (0.1 M) as the titrant

As soon as (Mg, Al, NO_3)-LDH NPs were dispersed into deionized water, the pH raised from 6.76 to 8.91 indicating a rapid and partial dissolution of the NPs, probably $Mg(OH)_2$ was preferentially extracted from the matrix of LDH NPs due to its higher K_{sp} value of 5.61×10^{-12} compared to the K_{sp} value of 3×10^{-34} for $Al(OH)_3$. Along with the addition of HNO_3 solution of 0.1 M, the pH gradually decreased to 4.76 suggesting a further and relatively slow dissolution of the NPs. Then the pH maintained around that value with further addition of the HNO_3 solution. We believe that the crystalline structure became highly unstable and suffered from a very rapid dissolution at this pH. In contrast, after the dispersion of the (Zn, Al, NO_3)-LDH NPs into deionized water, the pH slightly decreased to 6.15. Such minute decrease of the pH reveals its weak acidic nature and implies that the surface of (Zn, Al, NO_3)-LDH is preferentially hydrated by OH^-. The addition of the first 0.1 ml of HNO_3 solution immediately caused the pH to decrease to 4.66 and the pH maintained despite of further addition of HNO_3 solution. The plateau at pH 4.66 indicates that a rapid dissolution of (Zn, Al, NO_3)-LDH NPs was occurring and the dissolution process completed when another sharp pH decrease appeared.

Such aqueous stability results have a profound significance for evaluating the suitability of different cationic compositions for LDH-based theranostic nanovectors. An ideal composition would be sensitive to pH changes, i.e. remaining stable at physiological pH (~7) and releasing drug once having been uptaken into the lysosome of the malignant cells(Oh et al. 2006), where the pH is < 4. In addition, it is highly desirable for LDH NPs to have their surfaces functionalized with appropriate targeting moieties, which show decisive impacts on the pharmacokinetics, biodistributions and the cellular uptake mechanisms. For (Mg, Al)-based LDH NPs, the untimely partial dissolution when dispersed in deionized water can lead to two main drawbacks that question the suitability of this cationic composition. They are the uncontrollable pre-release of loaded drug before reaching the target sites, and the partial or complete loss of surface targeting moieties. In contrast, (Zn, Al)-based LDH NPs have an excellent stability above pH 4.8 to overcome the untimely pre-release and achieve controlled release, e.g. they can dissolve and burst the loaded drug at pH < 4.8 once reaching the lysosomes of the malignant cells. In addition, their stable surfaces can further provide an appropriate stability to covalently bound biological surface modifiers for long-circulation, targetability, etc. Moreover, the better crystallinity compared to (Mg, Al)-based LDH NPs also facilitates the posterior intercalation of negatively charged drugs. Together with all these positive attributes, its outstanding biocompatibility (data shown in section 2.4.4.3) make (Zn, Al)-based LDH NPs ideal as a core material for nanovector development. Therefore, (Zn, Al)-based LDH NPs were used as the model system for incorporating both imaging agent (FITC) and drug (VP) in the current study.

2.4.4.2 Characterization of FITC-Intercalated LDH NPs and Assessment of Energy Dependence on the Cellular Uptake of LDH NPs

The uptake of extracellular material such as NPs may involve multiple mechanisms. Our understanding of the mechanisms involved in the cellular uptake is important since the intracellular fate is usually linked to the entry mechanism. The various molecular pathways for uptake of nanoparticles can be broadly divided into those that require energy (active uptake) or those that do not require energy (passive uptake). In order to determine if the uptake of nanoparticles was an active or passive process, FITC-intecalated LDH NPs were used for the study. $Zn_{2.03}Al(OH)_6(FITC)_xCl_{1-x}{\cdot}yH_2O$ NPs with $x<0.15$ ((Zn, Al, FITC)-LDH) were prepared according to the procedures described in the experimental section. The bright field TEM micrograph is shown in Figure 2.27A. The successful intercalation of $FITC^-$ is validated by XRD pattern shown in Figure 2.27B. The extra bump appearing at 2-theta around 5.18° indicating the expansion of the interlayer gallery spacing from 8.8 Å to 14.7 Å. By subtracting the double hydroxide layer thickness of about 4.8 Å, an interlayer gallery spacing of 10 Å can be obtained, which corresponds to the size of the intercalated FITC. The peaks that appear at 2-theta of 11.47° and 23.4° correspond to the (003) and (006) plans of Cl^--intercalated LDH NPs. During the deprotonation of FITC, a pH electrode filled with saturated KCl solution was used to monitor the pH and the leakage of the Cl^- into the $FITC^-$ solution caused the replacement of NO_3^- by Cl^-.

Cell cultures incubated at either 37°C (normal cell culture temperature) and at 4°C (lower temperature) were treated with (Zn, Al, FITC)-LDH nanoparticles. Since energy dependent pathways tend to be inhibited at lower temperatures and this allowed us to

assess the energy dependence on the cellular uptake of nanoparticles. Relative fluorescence measured from cells (Figures 2.28) shows that the uptake of nanoparticles involves a combination of both active and passive processes. However, at higher concentrations (5mM), there appears to be a greater dependence (50% higher) on energy-mediated pathways for entry of nanoparticles into the cell.

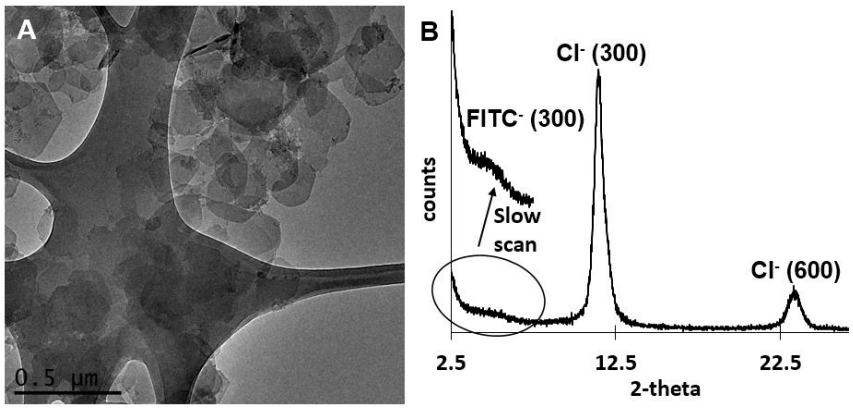

Figure 2.27. TEM bright field micrograph of $Zn_2Al(OH)_6(FITC)_xCl_{1-x}\cdot xH_2O$ NPs, $x<0.15$, is shown in A, the corresponding XRD pattern with a slow scan between 2-θ of 2.5 and 7.5 in B.

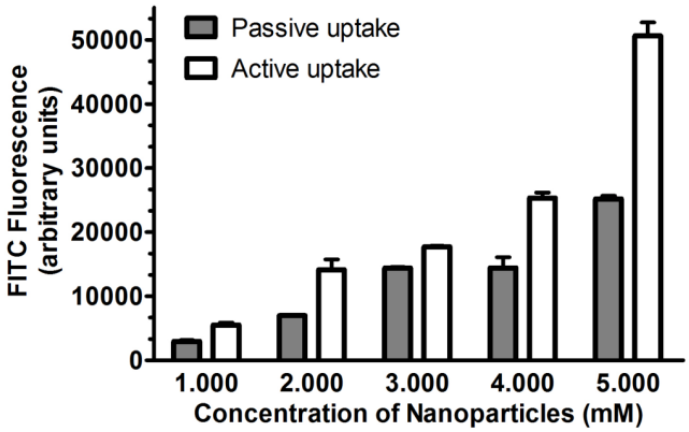

Figure 2.28. Assessment of energy dependence on the uptake of nanoparticles. Fluorescence from BXPC3 cell treated with (Zn, Al, FITC)-LDH nanoparticles at either 37 ^oC (active uptake) or at 4 ^oC (passive uptake). The concentrations of the nanoparticles are expressed in terms of the concentration of aluminum.

Several other studies have utilized endocytosis inhibitors such as genistein, chlorpromazine, nocodazole, etc., to investigate the specific active pathways involved in the cellular uptake of nanoparticles. We were not able to clearly distinguish between the different endocytosis pathways for the uptake of the newly synthesized (Zn, Al)-LDH nanoparticles using these inhibitors (data not shown). Several other reports have indicated ambiguity with their uptake data while using these inhibitors (Khalil et al. 2006)

2.4.4.3 Characterization of Valproate-Intercalated (Zn, Al)-LDH NPs and In vitro Cell Viability Study

Valproic acid (VPA, 2-propylpetanoic acid) is a short chain fatty acid that has been approved by the FDA for the treatment of epilepsia, bipolar disorders and migraine and clinically used for schizophrenia. More recently there has been an interest in VPA as an anti-cancer drug and it is currently being assessed in clinical trials for the treatment of different tumors (Michaelis, Doerr, and Cinatl 2007). While the molecular mechanisms by which VPA can act as anti-cancer drug is not fully understood, its ability to inhibit histone deacetylases as well as activate notch-1 signaling seems to be important (Greenblatt et al. 2007). The ability of VPA to inhibit the proliferation of cultured pancreatic cancer cells is particularly interesting since this is a deadly disease with an extremely high rate of mortality. When we tested the anti-proliferative effects of VPA on cultured human pancreatic adenocarcinoma cell line BXPC3, we found that it is effective at fairly high concentrations (IC50 of 63.21 mM, Figure 2.29). Other studies have shown that this effect is primarily due to the down-regulation of the Alzheimer Amyloid Precursor Protein (Venkataramani et al. 2010). While the high IC50 in vitro on cultured

cells indicates that a very high dose is required in vivo for effective therapy. An efficient drug delivery system should lower the effective dose of VPA and the related side effects.

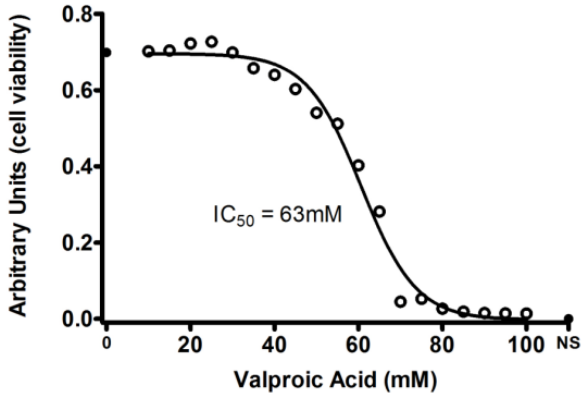

Figure 2.29. Dose response of the viability of BXPC3 cells to various concentrations of valproate sodium to determine the IC_{50} of the drug. Note that (Zn, Al)-LDH nanoparticles were not used in this experiment.

VP-intercalated (Zn, Al)-LDH NPs were synthesized and used for the *in vitro* toxicity study to compare with the efficacy of delivering VP alone to pancreatic cancer cells. The synthesis followed the procedures described in the experimental section. The long hydrophobic tail of VP^- was originally designed in order to balance the partition coefficient, to increase the lipophilicity and the penetration into the cell. However, we found that in aqueous medium, they self-organize to form micelles, which could partially dissolve LDH materials. The use of alcohol-aqueous solution for ion exchange was necessary to provide a better solubility of VP^-, and prevent the formation of micelle and the consequent dissolution of the LDH NPs. After the intercalation of VP^-, the ζ-potential of $Zn_{1.91}Al(OH)_6(NO_3, 0.5CO_3)_{0.584}(VP)_{0.416}{\cdot}xH_2O$ NPs ((Zn, Al, VP)-LDH NPs) slightly decreased to ~ 37 mV from 48.53 mV for (Zn, Al, NO_3)-LDH NPs indicating some surface adsorption of VP^-. The TEM micrograph in Figure 2.30A reveals that the particle

size of (Zn, Al, VP)-LDH NP are ~350-500 nm in diameter and they are formed from the minor agglomeration of primary NPs of ~150 nm, probably due to their relatively low ζ-potentials. The XRD patterns of before and after the intercalation, shown in Figure 2.28B, indicate the successful intercalation of VP^-, although some minor contamination of the intercalated CO_3^{2-} was detected as well. Significant interlayer spacing expansions due to the intercalation of VP^- led to the observation of two peaks at 2θ of 3.74° and 4.72° suggesting the intercalated VP^- could arrange in two different forms.

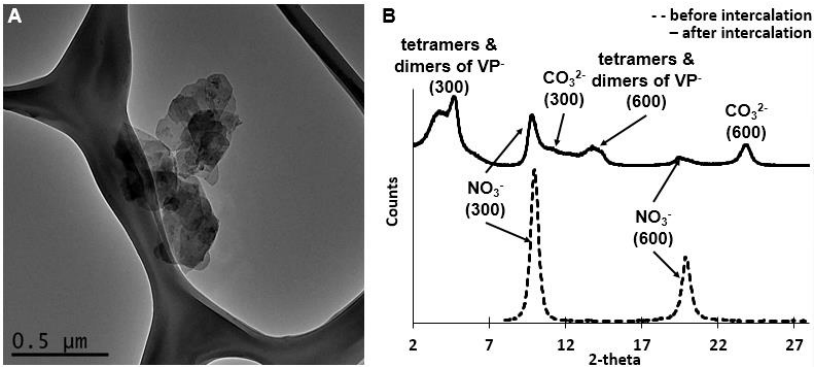

Figure 2.30. TEM bright field micrograph of $Zn_{1.91}Al(OH)_6(NO_3, 0.5CO_3)_{0.584}(VP)_{0.416}{\cdot}xH_2O$ NPs is shown in A, and XRD analysis of before and after intercalation in B shows the partial replacement of the intercalated NO_3^- by VP^- and CO_3^{2-} (as minor contaminants)

To better understand in which form VP exist within the LDH nanoparticles. We optimized the molecular geometry of VP by spin-unrestricted B3YLP method using diffuse function basis set of 6-31G*. The optimized geometry is illustrated in Figure 2.31A. According to the XRD pattern, by assuming the thickness of the double hydroxide layer being ~4.80 Å, the sizes of the interlayer galleries are then 18.8 Å and 13.9 Å, respectively. Such data suggest that VP are intercalated in the dimer form, and the hydration level could vary, as depicted in Figure 2.31B.

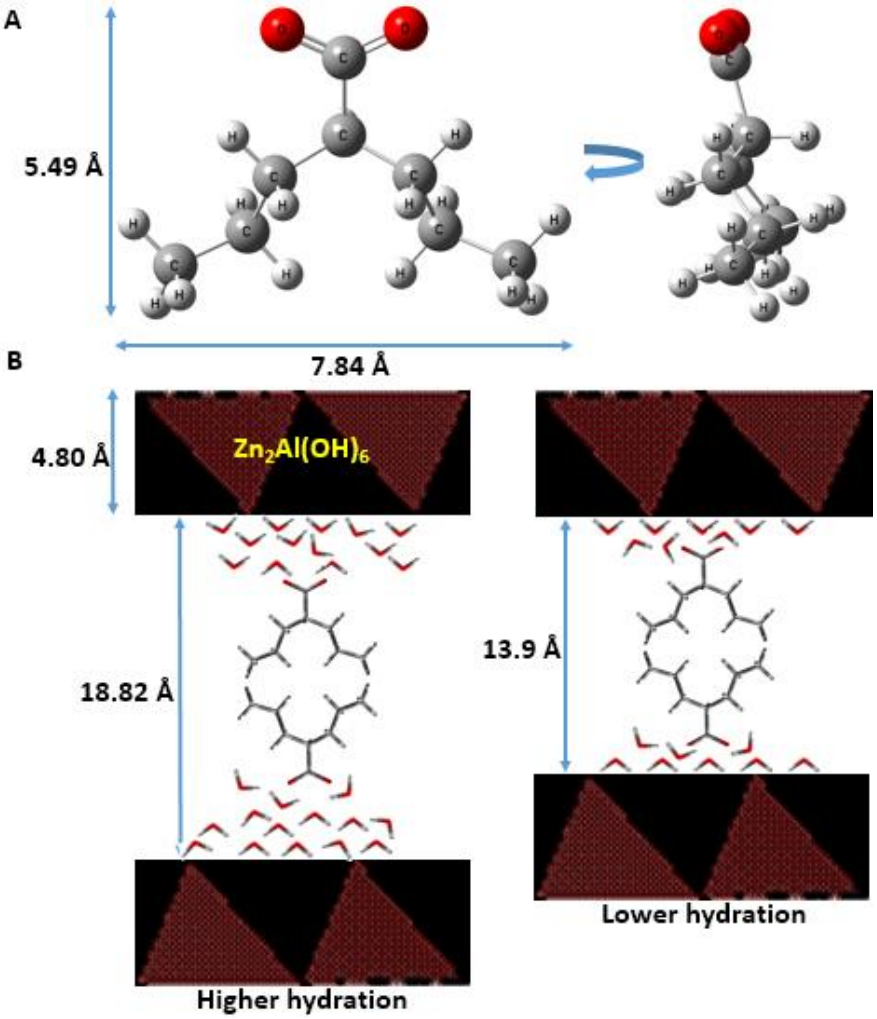

Figure 2.31. A shows the Gaussview 03 generated 3-D representation of the optimized geometry of VP^- by spin unrestricted B3YLP method using 6-31G* basis set; In B, the intercalated VP^- are proposed to be in the dimer form with different hydration levels according to the interlayer spacing calculated from XRD pattern and the optimized geometry of the VP^-.

2.4.4.4 Delivery of Valproate to Pancreatic Cancer BXPC3 Cells using Valproate-Intercalated (Zn, Al)-LDH Nanoparticles

A major challenge with the clinical use of several experimental chemotherapeutics for cancer treatment is a very low bioavailability due to the

physicochemical properties of the drug. A promising strategy to overcome this challenge and improve the therapeutic index of such drugs is the use of LDH nanoparticles for enhanced drug delivery. In this study, we utilized VP for proof-of-concept experiments to demonstrate the utility of the newly synthesized (Zn, Al, VP)-LDH nanoparticles for drug delivery to cultured pancreatic cancer BXPC3 cells. According to our observations, a large dose of VP is required to significantly reduce the viability of BXPC3 cells. This is a cause for concern since the drug has a high risk of side effects due to its psychoactive properties. The use of (Zn, Al, VP)-LDH nanoparticles led to approximately 50 fold reduction in the IC_{50} from 63.21 mM to about 1.25 mM in pancreatic cancer BXPC3 cells. Control nanoparticles (without any VP) containing either chloride, nitrate or carbonate anions did not significantly lower the viability of BXPC3 cells. Figure 2.32 show the effects (Zn, Al, VP)-LDH nanoparticles and control nanoparticles on BXPC3 cells.

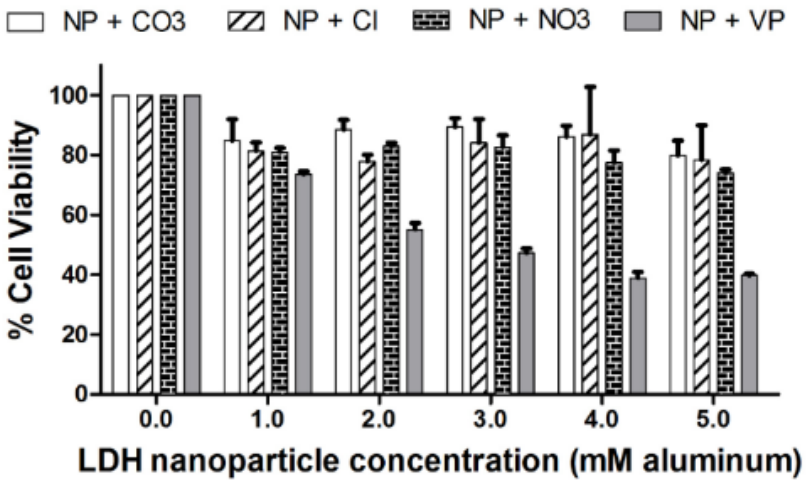

Figure 2.32. The effect of (Zn, Al, VP)-LDH NPs (NP+VP) on the viability of cultured pancreatic cancer BXPC3 cells. The effect of NPs without the drug was assessed by using (Zn, Al)-LDH NPs intercalated with either carbonate ($NP+CO_3$), chlorine (NP+Cl), or nitrate ($NP+NO_3$) ions

The significant reduction in the amount of VP required to lower cell viability can therefore be attributed largely to the ability of (Zn, Al)-LDH nanoparticles to directly deliver larger doses of the drug to the cancer cells. It appears that the (Zn, Al, VP)-LDH nanoparticles are stable in cell culture media, can be efficiently taken by the cells leading to a release of large doses of the drug intracelluarily. The lack of cytotoxicity of the control nanoparticles indicate excellent biocompatibility and that side effects due to the nanoparticle themselves is likely to be minimum when used *in vivo*. While VP was used as proof-of-concept to demonstrate the utility of the newly synthesized (Zn, Al)-LDH nanoparticles for drug delivery, this research can be extended to other drugs to enhance their bioavailability. The high stability, excellent biocompatibility, and superior *in vitro* drug delivery properties of the (Zn, Al)-LDH nanoparticles show promise that these particles may retain their *in vivo* efficacy. However, further modification of these particles to include cancer cell targeting ligands on the surface of the drug-intercalated (Zn, Al)-LDH nanoparticles is likely to enhance drug delivery and minimize off-target effects.

2.4.5 Conclusions

In this study, we showed that (Zn, Al)-based LDH nanoparticles have excellent physicochemical properties as an ideal nanomaterial for pH-sensitive drug delivery. In comparison studies with (Zn, Al)-LDH nanoparticles we found that (Mg, Al)-LDH nanoparticles have poor stability at pH lower than 8.91. This may, in part explain the rapid release of intercalated drugs under physiological conditions (pH ~7.2) from (Mg, Al)-LDH nanoparticles. In contrast, (Zn, Al)-based LDH nanoparticles showed an excellent stability above pH 4.8 which may indicate greater stability under physiological

conditions leading to selective release of the drug upon reaching the lysozomes within cells. Such a greater stability also makes them better candidates for incorporating cell targeting ligands on the surface and targeted delivery of drugs. The use of (Zn, Al, FITC)-LDH nanoparticles revealed that energy dependent cellular uptake mechanisms are more active at higher nanoparticle concentrations. When the ability of (Zn, Al)-LDH nanoparticles to deliver valproate to pancreatic cancer BXPC3 cells was tested, we found a 50 fold reduction in the IC_{50} value of the drug. In addition to the excellent drug delivery capabilities, (Zn, Al)-based LDH nanoparticles were found to be highly biocompatible since control nanoparticles (without drug intercalation) were found to have minimal cytotoxicity. While VP was used as proof-of-concept to demonstrate the utility of the newly synthesized (Zn, Al)-LDH nanoparticles for drug delivery, or goal is to extend this research to other chemotherapeutic drugs currently in use. The biocompatibility and *in vivo* utility of the (Zn, Al)-LDH nanoparticles for drug delivery will have to be tested in animal models to assess its potential for ultimate use in patients.

2.5 Synthesis and Investigation of the Relaxivity Enhancement Mechanisms of Lanthanide Intercalated Layered Double Hydroxide Nanoparticle-Based MRI Contrast Agent

2.5.1 Abstract

Inorganic nanomaterial-based MRI contrast agents have attracted strong research interest because of their intrinsically embodied advantages, such as the restriction of the mobility of paramagnetic complexes and their internal motions, a much longer rotational correlation time and other significant features. We report successful development of $Zn_2Al(OH)_6(Cl, 0.5CO_3)_{1-2x}Gd(DTPA)_x \cdot xH_2O$ nanoparticle (NP)-based T_1 MRI contrast agents, by intercalation of the clinically approved agent $Gd(DTPA)^{2-}$ into the highly hydrophilic layers of the biocompatible $Zn_2Al(OH)_6(NO_3)\cdot xH_2O$ NPs. The highest longitudinal relaxivity (r_1) sample, measured at 15 MHz, RT and pH = 5.8 ± 0.5 was 28.4 s^{-1} mM^{-1}, more than 6 times the r_1 value of solution Gd(DTPA). A principal enhancement mechanism appears to be the slow rotational tumbling correlation time of the water within the layers. Another mechanism may also be rapid relaxation by the second water sphere outside of the intercalated $Gd(DTPA)^{2-}$, formed by the inherent water within the LDH interlayer spacing. r_1 was found to be strongly dependent on the amount of water between neighboring paramagnetic centers, which can be controlled through the $Gd(DTPA)^{2-}$ intercalation percentage. Also, it was shown that the influence on r_1 of particle size is largely slight, although smaller particles tend to provide faster r_1. A temperature-dependent ^{17}O NMR transverse relaxation study showed relatively slow molecular water exchange at room temperature, compared to solution Gd(DTPA). Thus the main proton exchange mechanism may be rapid prototropic exchange, through the hydrogen bonding of the inherent water within the LDH NP. Results obtained from the present study indicate that further increases in r_1 can be

achieved by increasing the second sphere water concentration, via lower percentages of Gd(DTPA) intercalated into the LDH layers. Such challenges can also potentially be met by intercalating Gd(III) chelates with larger ligands into the LDH NPs. The larger interlayer spacing would increase the inherent water content as well, facilitating water accessibility for proton exchange.

2.5.2 Introduction

Since the discovery of the considerable increase in proton relaxation times (both T_1 and T_2) for malignant tumor tissues compared to normal tissues in 1971,(Damadian 1971) magnetic resonance imaging (MRI) –a noninvasive diagnostic technique– has been developed and clinically used to provide the superb spatial resolution and the excellent capacity for distinguishing among soft tissues. However, there is often only a very small variation in relaxation times between healthy and early stage pathological regions. The use of clinically approved contrast agents, such as Magnevist® $[Gd(DTPA)(H_2O)]^{2-}$ and Dotarem® $[Gd(DOTA)(H_2O)]^{-}$, etc.,(Caravan et al. 1999) is thus highly beneficial for increasing the sensitivity of the MRI technique.(Aime, Botta, and Terreno 2005) With the advent of nanotechnology in biomedicine, nanovector-based contrast agents have attracted enormous research efforts. Because of the relative ease of endowing the core nanomaterials with multifunctionalities, i.e., therapeutic drug/imaging agent carrying, selective (multi)targeting, and biological surface modifying capabilities, nanoparticles possess high potential for addressing the problem of early detection of precancerous and neoplastic lesions.(Ferrari 2005)

Both the morphology and composition of the core nanomaterials are decisive for the relaxation times (both T_1 and T_2) of the resultant nanomaterial-based contrast agents.

Superparamagnetic iron oxide (Fe_3O_4) NPs are representative choices for T_2-weighted negative contrast agents, and a variety of particle sizes with or without additional functional groups have been intensively explored.(Barick et al. 2009, Lee et al. 2007, Lee et al. 2006, Lin et al. 2006, Wan et al. 2007, Xu et al. 2008) At 3 tesla magnetic field and room temperature (RT), transverse relaxivity (r_2) values up to 314.6 mM^{-1} s^{-1} hava been reported for Fe_3O_4 monodispersed magnetic nanoparticle (NP) nanoassemblies because of the synergistic interactive magnetism arising from multiple NPs assembled in the whole assembly.(Barick et al. 2009) T_1-weighted imaging contrast agents, which are typically paramagnetic cation (Gd^{3+}, Mn^{3+})-containing NPs, have also been extensively studied. Currently, only molecular contrast agents in solution are being used for clinical MRI, in a typical magnetic field strength of 1.5 tesla (64 MHz proton frequency). At this field the dominant correlation time is almost always the rotational correlation time (τ_R).(Caravan 2006) In contrast, NPs can provide a much longer rotational correlation times and restrain the motional freedom of the Gd-containing complex, both of which tend to contribute towards a larger longitudinal relaxivity (r_1) value. To date the most successful NP-based T_1 contrast agents under research are Au NP functionalized with Gd chelates, and mesoporous silica nanospheres functionalized with Gd-DTTA, which show the RT r_1 values of 60 mM^{-1} s^{-1} at 30 MHz and 28.8 at 127.6 MHz, respectively.(Ahren et al. 2010, Moriggi et al. 2009, Taylor et al. 2008) Other potential systems, such as layered gadolinium hydroxide NPs and $Gd@C_{60}[C(COOH)_2]_{10}$ have showen limited performance as positive contrast agents.(Bolskar et al. 2003, Lee et al. 2009) The longitudinal relaxivity varies extensively depending on the carrier nanomaterials' morphologies and sizes, which are considered as keys to the accessibility of the Gd-based magnetic center by water molecules.(Taylor et al. 2008)

In the present study, we focus on developing layered double hydroxide (LDH) nanoparticle (NP)-based contrast agents by intercalating $Gd(DTPA)^{2-}$ into the interlayer spacing of the LDH NPs. LDH compounds are well-known for their anion-intercalating capability. The hydrotalcite crystalline structure of LDHs was first identified in 1967. The general empirical formula of LDH can be denoted as $[M^{II}_{x}M^{III}(OH)_{2+2x}]^{+}(A^{a-})_{1/a}\cdot mH_2O$ (x = 0.1-0.5 typically), where M^{II} and M^{III} are divalent and trivalent cations (e.g., $M^{II} = Mg^{2+}$, Co^{2+}, Zn^{2+} ; $M^{III} = Al^{3+}$, Ga^{3+}, Fe^{3+}, Mn^{3+}, Gd^{3+}, etc.), and A^{a-} can be a negatively charged specie with *a* negative charges, which is exchangeable. Also, within the interlayers, there are inherent water molecules, which can be exchanged with other polar molecules, such as ethanediol.(Geismar, Lewandowski, and Deboer 1991)

During the course of this work, varied amounts of a clinically approved molecular contrast agent, $Gd(DTPA)^{2-}$, were successfully intercalated into $Zn_2Al(OH)_6(NO_3)\cdot xH_2O$ to form $Zn_2Al(OH)_6(Cl, 0.5CO_3)_{1-2y}Gd(DTPA)_y\cdot xH_2O$ NPs with x = 0.043-0.275. Their longitudinal relaxation rates were measured. By using this system as a successful model of NP-based contrast agent, discussions of the driving force for the relaxivity increase and critical factors can be provided with strong experimental supports. The effects of the loading capacity of Gd(DTPA) and the resultant NP size on the resultant r_1 were evaluated independently. The study of the temperature dependent ^{17}O NMR transverse relaxation rate of the $Zn_2Al(OH)_6(NO_3)_{1-2y}Gd(DTPA)_y\cdot xH_2O$ NPs was carried out to determine the water exchange mechanism.

2.5.3 Experimental Section

2.5.3.1 Materials

Zinc nitrate hexahydrate ($Zn(NO_3)_2 \cdot 6H_2O$), aluminum nitrate nonahydrate ($Al(NO_3)_3 \cdot 9H_2O$), diethylenetriaminepenta-acetic acid gadolinium(III) dihydrogen salt hydrate, Gd(DTPA), (Gd(DTPA) = $C_{14}H_{20}GdN_3O_{10} \cdot xH_2O$), and sodium hydroxide (NaOH) were purchased from Sigma (St. Louis, MO, USA), used as received, and stored under nitrogen gas (N_2) environment. Deionized nanopure water (Barnstead, 18.2 MΩ cm) used for the synthesis was degassed by boiling in advance.

2.5.3.2 Synthesis of $Gd(DTPA)^{2-}$-Intercalated (Zn, Al)-LDH NPs

All the syntheses of NO_3^--intercalated (Zn, Al)-LDH NPs were carried out using the coprecipitation at constant pH method. To avoid the contamination of CO_3^{2-}, all chemicals were stored in a N_2 filled glove box (MBraun Labmaster 130); the coprecipitation was also carried out within the glove box and the products were withdrawn in sealed hydrothermal bottles. The synthesis conditions were previously optimized, as described ealier. The coprecipitation takes place at room temperature (RT = 25 °C). Typically, a 10 ml salt solution of $Zn(NO_3)_2 \cdot 6H_2O$ and $Al(NO_3)_3 \cdot 9H_2O$, containing 20 mM of [Zn+Al] with a specific molar ratio of Zn to Al of 2:1, and another 10 ml base solution with the concentration of the NaOH being twice of the [Zn+Al], were simultaneously added into a round bottom flask (Chemglass) using burettes, while stirring at setting 10 (Magnetic stirrer: manufactured by Barnant Corp., Barrington, IL, Model 700·0111). The addition rate was set to 0.589 ml/s. After completion of the addition of 20 ml precursors, stirring continued for another 3 minutes to ensure thorough mixing. The mixture was then transferred into the hydrothermal bottle (PYREX screw cap 100 ml storage bottle), and the

hydrothermal treatment was carried out at 85 °C for a specified period of time (t). Variation of the particle size can be achieved by varying the hydrothermal treatment duration; longer treatment leads to larger particle size. Afterwards, the colloidal suspension was cooled to RT, and centrifuged (Eppendorf 5810R) to collect the gel-like NO_3^--intercalated (Zn, Al)-LDH NPs for intercalating $Gd(DTPA)^{2-}$.

Appropriate amount of $Gd(DTPA)^{2-}$ was intercalated into NO_3^--intercalated (Zn, Al)-LDH NPs by the ion-exchange method. First, Gd(DTPA) solution was deprotonated with NaOH solution to form $Gd(DTPA)^{2-}$, then the pH meter (accumet excel XL60) was used to monitor the resultant pH and ensure that the final pH of the solution lies between 7.0-8.0. The collected NO_3^--intercalated (Zn, Al)-LDH NPs were re-dispersed into the $Gd(DTPA)^{2-}$ solution with a specific molality of $Gd(DTPA)^{2-}$, calculated according to the desired intercalation percentage. Typically, the concentration of the ion-exchange solution was kept below 1 mM. The intercalation was carried out at 50 °C for 3 hours. Finally, the $Gd(DTPA)^{2-}$-intercalated (Zn, Al)-LDH NPs were cooled to RT and collected by centrifuge for physicochemical characterization.

2.5.3.3 Physicochemical Characterization

The crystalline phase information pertaining to the LDH NPs was obtained by powder X-ray diffraction (XRD; Rigaku D/Max-IIB instrument with Cu-K_α radiation, λ=0.154059 nm) in 2θ range of 1.5-30°. Inductively coupled plasma atomic emission spectroscopy (ICP, iCAP 6300 ICP Spectrometer) was used for determining the elemental compositions of the LDH NPs. Dynamic light scattering (DLS, PSS-NICOMP 380 with zeta potential capability) was used to evaluate the hydrodynamic particle size and zeta-potential values. Transmission electron microscopy (FEG TEM; Philips CM200 with an electron acceleration voltage of 200 kV) bright

field images were used to monitor the morphology and particle size, which corroborated with the DLS results.

2.5.3.4 NMR Measurements

Longitudinal relaxation times, T_1, of water ^1H were measured at RT using a Teachspin (0.362 T, 15.4 MHz) relaxometer. Temperature-dependent transverse relaxation times, T_2, of ^{17}O were measured using Varian CMX300 NMR spectrometer operating at 300MHz frequency for protons. T_1 values were obtained using the inversion recovery method; and Carr-Purcell-Meiboom-Gill spin echo technique was applied to obtain T_2 values.

2.5.4 Results and Discussions

2.5.4.1 Physicochemical Characterization

$Zn_2Al(OH)_6(NO_3)\cdot xH_2O$ NPs of different average particle sizes (~ 300, ~ 400 and ~ 550 nm of diameters) were synthesized by coprecipitation method followed by varying the hydrothermal treatment durations. Different amounts of $Gd(DTPA)^{2-}$ were intercalated into $Zn_2Al(OH)_6(NO_3)\cdot xH_2O$ NPs to obtain Sample A to F, i.e., $Zn_2Al(OH)_6(Cl, 0.5CO_3)_{1-2y}Gd(DTPA)_y\cdot xH_2O$ NPs with y=0.043-0.275. The detailed intercalation condition is described in the experimental section.

Successful intercalation was verified by X-ray diffraction (XRD). A typical XRD pattern evolution of the intercalation process, for example from $Zn_2Al(OH)_6(NO_3)\cdot xH_2O$ NPs to $Zn_2Al(OH)_6(Cl, 0.5CO_3)_{0.652}Gd(DTPA)_{0.174}\cdot xH_2O$ NPs, is shown in Figure 2.33. After the intercalation by the ion exchange method, the d_{003} peak of the NO_3^--intercalated $Zn_2Al(OH)_6(NO_3)\cdot xH_2O$ NPs at 2-θ of 10° shifted to a much lower 2-θ value of 4.60° indicating

the successful intercalation of $Gd(DTPA)^{2-}$. Assuming the thickness of the hydroxide layer to be ~4.8 Å, the interlayer spacing expanded from the original 4.04 Å to 14.39 Å. Also, the appearance of the (003) peak at 2θ of 11.8° indicated the replacement of NO_3^- anion by CO_3^{2-} and/or Cl^- during the intercalation process. The Cl^- was expected to come from the KCl_{sat} filled pH electrode, which was used for controlling the pH during the deprotonation of Gd(DTPA) solution by NaOH; the CO_3^{2-} can be the resultant product of CO_2 in the air and NaOH.

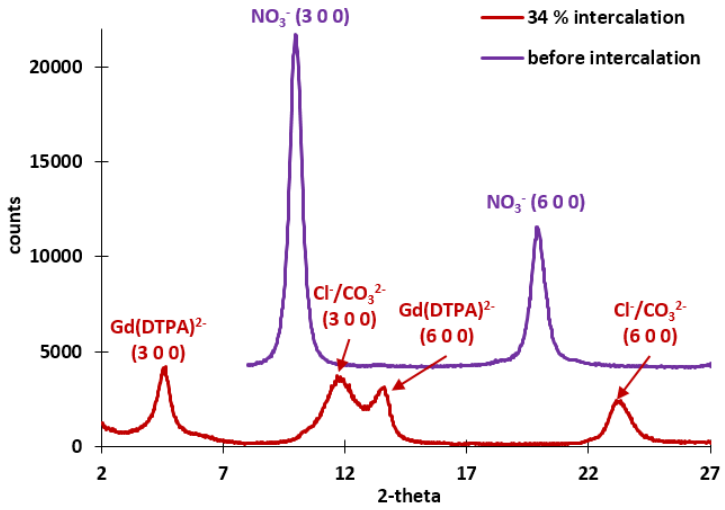

Figure 2.33. XRD pattern evolution from $Zn_2Al(OH)_6(NO_3)\cdot xH2O$ NPs (before intercalation) to $Zn_{2.175}Al(OH)_{6.350}[Gd(DTPA)]_{0.174}(Cl, 0.5\ CO_3)_{0.653}\cdot xH_2O$ NPs (34 % intercalation)

The chemical elemental analysis of Zn, Al and Gd, were carried out using inductively couple plasma spectrometry (ICP) and the corresponding empirical formulas of Sample A to F are listed in Table 1, along with other physicochemical properties. The resulting particle sizes and morphologies were observed by transmission electron microscopy (TEM).

After the dispersion of the samples A-F into deionized water, the pHs of all the samples were 6.8±0.5. The longitudinal relaxation times (T_1) were measured by the inversion recovery method at RT and 0.138 tesla. The calculated r_1 values from the slope of the $1/T_1$ vs [Gd] plot, obtained using four water dilutions, are shown in Table 2.6. Significant longitudinal relaxivity

increases were observed compared to that of the molecular Gd(DTPA). Zeta-potential measurements indicate that LDH NPs' surface became less positive because the adsorption of $Gd(DTPA)^{2-}$ onto the LDH NPs became more significant as the concentration of $Gd(DTPA)^{2-}$ in the intercalation solution increased.

Table 2.8. Physicochemical characterization of Sample A to F

Sample Code	Empirical Formula	$Gd(DTPA)^{2-}$ Intercalation capacity	r_1 (s^{-1} mM^{-1})	Particle size (nm)	ζ-potential (mV)
A	$Zn_{2.162}Al(OH)_{6.324}[Gd(DTPA)]_{0.275}Cl_{0.450}{\cdot}xH_2O$	55.0%	13.74	315±135	32.7
B	$Zn_{2.175}Al(OH)_{6.350}[Gd(DTPA)]_{0.174}Cl_{0.653}{\cdot}xH_2O$	34.8%	12.09	315±135	40.5
C	$Zn_{2.089}Al(OH)_{6.178}[Gd(DTPA)]_{0.060}Cl_{0.880}{\cdot}xH_2O$	12.0%	17.62	315±135	51.6
D	$Zn_{2.218}Al(OH)_{6.436}[Gd(DTPA)]_{0.043}Cl_{0.914}{\cdot}xH_2O$	8.6%	28.38	315±135	51.8
E	$Zn_{2.111}Al(OH)_{6.223}[Gd(DTPA)]_{0.270}Cl_{0.461}{\cdot}xH_2O$	54.0%	12.49	400±90	31.7
F	$Zn_{1.978}Al(OH)_{5.956}[Gd(DTPA)]_{0.258}Cl_{0.484}{\cdot}xH_2O$	51.6%	10.11	540±180	32.5

2.5.4.2 Effect of the Intercalation Percentage on r_1

Sample A, B, C and D were used for the evaluation of the effect of the loading capacity on the r_1. The particle sizes and morphologies were observed by TEM and displayed in Figure 2a. They are of about the same particle size, ~315±135 nm, with different intercalation percentages of $Gd(DTPA)^{2-}$, i.e., 8.6, 12.0, 34.8 and 55 %, respectively. The longitudinal relaxivity is the change in relaxation rate ($1/T_1$) normalized to the concentration of the intercalated $Gd(DTPA)^{2-}$, which is the slope of the $1/T_1$ versus $Gd(DTPA)^{2-}$ concentration plot. As shown in Figure 2.34b, the relaxivity increases as the loading capacity of the $Gd(DTPA)^{2-}$ decreases. Sample A with 8.6 % of $Gd(DTPA)^{2-}$ loading percentage showed an r_1 value of 28.38 s^{-1} mM^{-1} at RT, pH = 6.8, and 0.138 tesla, which is twice as large as that of free Gd^{3+} and more than 6 times higher than the r_1 of the molecular Gd(DTPA) complex. Note: under the same experimental conditions, r_1 values of non-chelated Gd^{3+} in form of $Gd(NO)_3$ and Gd(DTPA) were measured at 14.77 and 4.63 s^{-1} mM^{-1}, respectively.

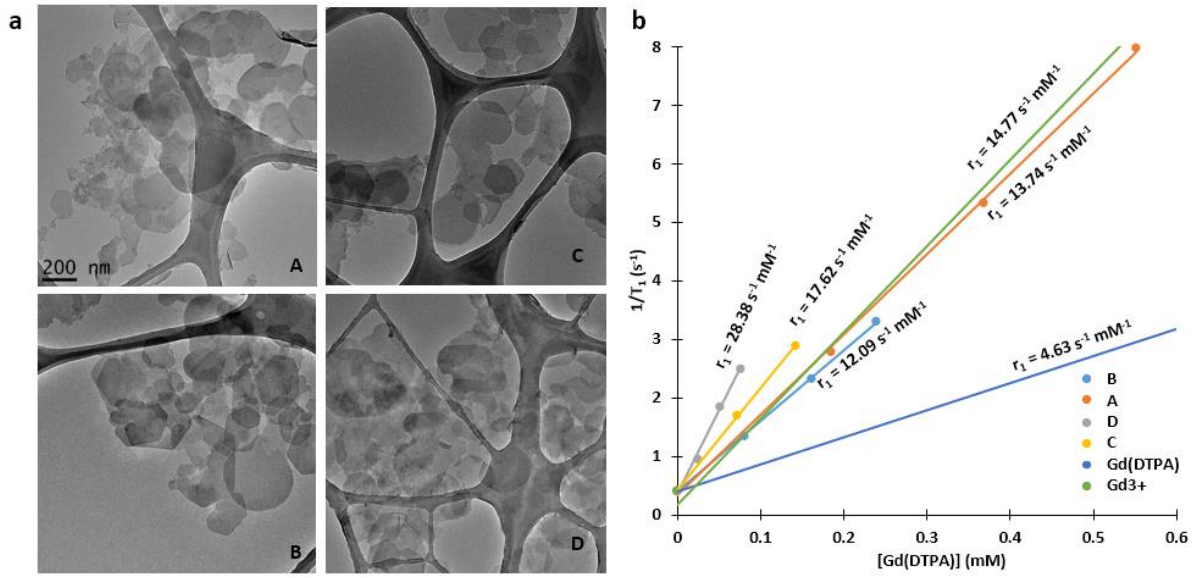

Figure 2.34. The bright field TEM images of Sample A, B, C and D are displayed in (a), and their respective relaxivities are plotted in (b) along with the relaxivities of the non-chelated Gd^{3+} and molecular Gd(DTPA) complex.

Paramagnetic complexes can enhance the relaxivity of water protons by causing time fluctuation of the scalar hyperfine (for ^{17}O) and dipolar coupling between the electron magnetic moment of the metal ion and the nuclear magnetic moment of the proton, in the aqueous solution. Typically, the relaxation through dipolar interaction, as for proton relaxation, can involve three types of water molecules categorized according to their relative position to the paramagnetic center: inner sphere water (water molecules that coordinate directly to the paramagnetic center), outer sphere water (water molecules that are not directly bound to the paramagnetic center but are diffusing next to the complex), and the second sphere water (water molecules that are localized in a well-defined position with respect to metal ion via hydrogen-bonding interactions with polar groups of the ligand.(Aime, Botta, and Terreno 2005) $r_1 = r_{1p}^{IS} + r_{1p}^{OS} + r_{1p}^{SS}$. In general, the extent of the contribution of these three components varies strongly depending on the size of the contrast agent, the motional freedom of the paramagnetic center, the

presence of suitable hydrogen-bond acceptor groups on the surface, the variation in the overall electric charge, and modification of the hydrophilic/hydrophobic domains.

A brief subset of the principal equations of relaxation theory for solution Gd(DTPA) is given here, and the detailed theory can be found in the literature.(Aime, Botta, and Terreno 2005) The expression for the inner sphere longitudinal relaxivity is given by

$$r_{ip}^{IS} = \frac{[CA]q}{55.6}\frac{1}{T_{1M}+\tau_M} \qquad (2.3)$$

where q indicates the number of metal-bound water molecules, τ_M is the mean residence lifetime of water molecule, and T_{1M} is given by Solomon-Bloembergen-Morgan equations and describes the time fluctuation of the water proton-Gd(III) dipolar coupling:

$$\frac{1}{T_{1M}} = \frac{2}{15}\frac{\gamma_H^2 g^2 S(S+1)\beta^2}{r_H^6}\left[\frac{3\tau_{C1}}{1+\omega_H^2\tau_{C1}^2} + \frac{7\tau_{C2}}{1+\omega_S^2\tau_{C2}^2}\right] \qquad (2.4)$$

$$\frac{1}{\tau_{Ci}} = \frac{1}{\tau_R} + \frac{1}{\tau_M} + \frac{1}{\tau_{ie}}, (i = 1, 2) \qquad (2.5)$$

$$\left(\frac{1}{T_{1e}}\right)^{ZFS} = \frac{1}{25}\tau_v^2\{4S(S+1) - 3\}\left(\frac{1}{1+\omega_S^2\tau_v^2} + \frac{4}{1+4\omega_S^2\tau_v^2}\right) \qquad (2.6)$$

$$\left(\frac{1}{T_{2e}}\right)^{ZFS} = \tau_v^2\left(\frac{5.26}{1+0.372\omega_S^2\tau_v^2} + \frac{7.18}{1+1.24\omega_S^2\tau_v^2}\right) \qquad (2.7)$$

S is the electron spin quantum number, γ_H the proton nuclear magnetogyric ratio, g and β the electronic g factor and Bohr magneton, respectively. r_H is the distance between the metal ion and the protons of the coordinated water molecules, ω_H and ω_S ($\omega_S = 658\ \omega_H$) the proton and electron Larmor frequencies, respectively, τ_R is the Gd(DTPA) reorientational correlation time. The longitudinal and transverse electron spin relaxation time T_{1e} and T_{2e} are the electron magnetic field relaxation times, which are dependent on the magnetic field, the electronic zero filed splitting τ_v and the mean-square zero field splitting energy (Δ^2). Note: the relaxivity is field dependent and all the r_1 values in the present study were collected at 15 MHz; our study

represents the very important cases of low magnetic field relaxation, as found at medical clinical MRI frequencies (both 60 MHz and 128 MHz). The investigation of the field-dependence of the r_1 is beyond the objective of this study.

The inner sphere contribution to the longitudinal relaxation can be enhanced through the water exchange rate, the rotational tumbling rate, the number of bonded water molecules to the paramagnetic center, the internal motion freedom of the paramagnetic ion, and the distance between proton of the water molecule and the Gd center.

We exclude the possibility that the enhancement of the relaxivity is brought by the superficial adsorbed $Gd(DTPA)^{2-}$ for several reasons: (1) for Sample D with 8.6 % of Gd loading capacity, the zeta-potential value of 51.8 mV, an almost identical value compared to that of $Zn_2Al(OH)_6(NO_3)\cdot xH_2O$ NPs before intercalation, indicates that the surface adsorption is insignificant. (2) surface adsorption of Gd(DTPA) was achieved by simply dispersing the $Zn_2Al(OH)_6(NO_3)\cdot xH_2O$ NPs into the intercalation solution but without any heat treatment, and the r_1 was determined to be comparable to that of the molecular Gd(DTPA) complex. Hence, it is conclusive that the significant increase in r_1 stems from the intercalated $Gd(DTPA)^{2-}$.

The intercalation of the $Gd(DTPA)^{2-}$ into LDH NPs could offer several advantages for increasing r_1. The relaxivity is strongly dependent on the motion of paramagnetic center. The intercalation of $Gd(DTPA)^{2-}$ into a rigid NP carrier can impose a strong restriction of the mobility freedom of the $Gd(DTPA)^{2-}$ complex and its internal motion. Also, a much longer rotational correlation time can be expected. For the molecular Gd(DTPA) complex, which is proven to be able to accommodate one directly bound water molecule with τ_M estimated to be between 227-263.16 ns, the longitudinal relaxation time of the water molecule in the first coordination sphere is not limited by τ_M, but by T_{1M}, which was estimated to be of the order of

10^{-4}-10^{-6} s.(Micskei et al. 1993) The hydrodynamic rotational motion of a LDH NP can be simplified into two different rotational motions: the rotational motion around the [0001] direction of the LDH NP being the faster one (τ_{R1}) and the rotation around the axis perpendicular to the [0001] direction, the slower one (τ_{R2}), as shown in Figure 2.35. The dominating rotational correlation time would correspond to the fastest one. A rough estimation of τ_{R1} can be estimated from Debye-Stokes equation: $\tau_R = \frac{4\pi r^3 \eta}{3k_B T}$, r is the radius of the NPs, η is the viscosity of the solvent, k_B is the Boltzmann constant, also τ_R is T dependent. The predicted τ_{R1} is of the order of millisecond. A much small value of $1/\tau_r$ compared to $1/\tau_M$ and $1/\tau_{1e}$ makes the latter two terms the dominant factors of τ_{c1} for T_{1M}.

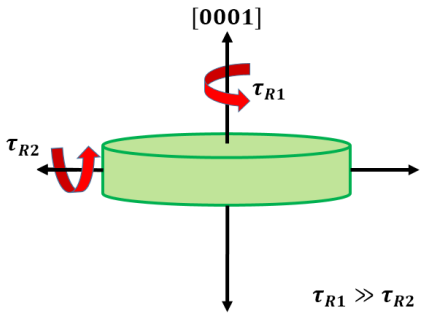

Figure 2.35. Hydrodynamic rotational correlation times of a discoidal LDH nanoparticle

By comparing Sample A, B, C and D of almost the same particle size, one can expect the other physical properties are similar for these samples, such as T_{1e} and τ_M. However, the extent of the relaxivity increase changes almost monotonically as a function of the $Gd(DTPA)^{2-}$ loading capacity, as shown in Figure 2.36. Hence, the variation of the increases in relaxivities cannot be explained only by inner sphere water contribution.

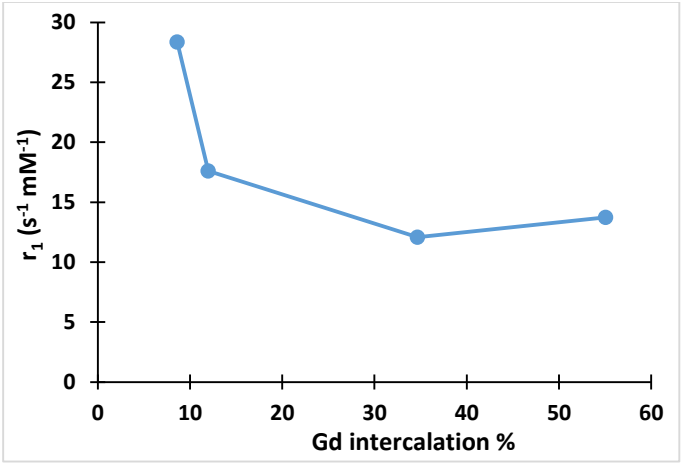

Figure 2.36. Longitudinal relaxivities (measured at 25 °C, 0.138 tesla, pH=5.8±0.5) decrease with increased $Gd(DTPA)^{2-}$ intercalation percentage.

Dried LDH compounds are known to contain water molecules within the gallery spacing, where is not occupied by anions. Here, we call those water molecules as inherent water molecules. An inelastic neutron scattering investigation by Kagunya et al. shows that the inherent water molecules can rotate freely and move about hydroxide oxygen sites within a restricted volume. It is envisaged that rapid formation and breaking of hydrogen bonds take place as the water molecule hop from one hydrogen bonding site to another.(Kagunya, Dutta, and Lei 1997) They also determined by Raman spectroscopy that there are 3 types of inherent water: (a) water bonded to the intercalated carbonate (b) water bonded to the hydroxyl surface, and interlamellar water.(Johnson et al. 2002) A ^1H NMR study showed similar results, namely that the inherent interlayer water possesses rotational freedom around the molecular C_2 axis, which is parallel to the [0001] direction of the LDH. Moreover, the water molecules inside of the LDH materials were proven to be highly ordered, and binding to each other via hydrogen bonding. The experimental data showed that the anisotropy of the chemical shift is about 13 ppm, indicating uniaxial rotation, while the ab initio calculations gave anisotropies in the range of 0.6-1.95 ppm for a freely rotating water molecule. The large discrepancy with the experimental data can be

explained by hydrogen-bonding effects. It was shown by ab initio calculations that the chemical shift anisotropy for the dimer of water is 2.5 ppm and for the pentamer of water 10.5 ppm.(Vanderpol et al. 1994)

When LDH compounds are fully hydrated, the amount of interlayer water can increase significantly, causing noticeable expansion of the interlayer spacing. Such characteristic is unique and essential for the NP-based MRI contrast agents. Hence, a second sphere water formed by the inherent water molecules within the gallery through hydrogen bonding is expected. When the $Gd(DTPA)^{2-}$ loading capacity increases, due to its bulky size, it is expected that the ratio of the inherent water within the interlayer gallery to the amount of $Gd(DTPA)^{2-}$ decreases. Although it is very difficult to estimate the water content when NPs are dispersed in aqueous solution, in a highly hydrated state, the higher concentration of water in the second sphere can contribute to a faster relaxivity. The result of the comparison of r_1 values of Sample A to F indicates that significant increase in r_1 for LDH NPs can only be partly attributed to the increasing τ_R. The ratio of the number of inherent water molecules to the amount of $Gd(DTPA)^{2-}$ is critical, and the contributions of the inherent water molecules within the interlayer gallery spacing as the outer and second sphere water may be needed to explain the very short relaxation times.

2.5.4.3 Effect of the Particle Size on r_1

It is essential for the paramagnetic center to be close/in contact with the proton of water molecules of inner, second and outer sphere, but also, such protons must exchange with other protons in the bulk aqueous solution in order to achieve effective relaxation of the entire population. Note, as expressed in equation (2), the longitudinal nuclear magnetic relaxation time

of the bound water protons is quicker if the proton residence time is long. However, in order to relax the entire population of water protons, it is critical for a bound water proton to exchange with others at a decent rate, as expressed in equation (1). However, once the $Gd(DTPA)^{2-}$ is intercalated into the LDH nanostructure, the proton exchange rate will be unknown.

It is reasonable to assume that (1) the contribution of the second sphere water can be excluded by comparing samples of different average particle sizes with same $Gd(DTPA)^{2-}$ intercalation percentage; (2) τ_{c1} remains the same for all the $Zn_2Al(OH)_6(Cl, 0.5CO_3)_{1-2y}Gd(DTPA)_y{\cdot}xH_2O$ NPs with y=0.043-0.275 provided that the electronic configuration of Gd^{3+} is not altered and the external magnetic field is unchanged; (3) τ_M is NP size-dependent. Samples A, E and F were LDH NPs with about the same $Gd(DTPA)^{2-}$ loading capacity, around 55 % determined by ICP, and increasing particle size from 315 to 550 nm were used for the investigation of the limiting factor of r_{ip}^{IS}, i.e., Whether it is τ_M or T_{1M} is the limiting factor of r_{ip}^{IS} is yet to be revealed.

The bright field TEM images of sample A, E and F are shown in Figure 2.37a, b and c, and their r_1 values determined at RT, 15 MHz are plotted in Figure 2.37d.

Usually, electronic relaxation is field strength dependent and decreases with increasing field strength. At high field (B_0 > 1.5 tesla), electronic relaxation is slow enough not to be considered as the dominant factor for τ_{c1}, and at very low field (B_0 < 0.1 tesla), Relatively $T_{1e} \approx \tau_{c1}$. At 0.36 tesla and with such long rotational correlation time regime, T_{1M} is determined to be limited by T_{1e}.

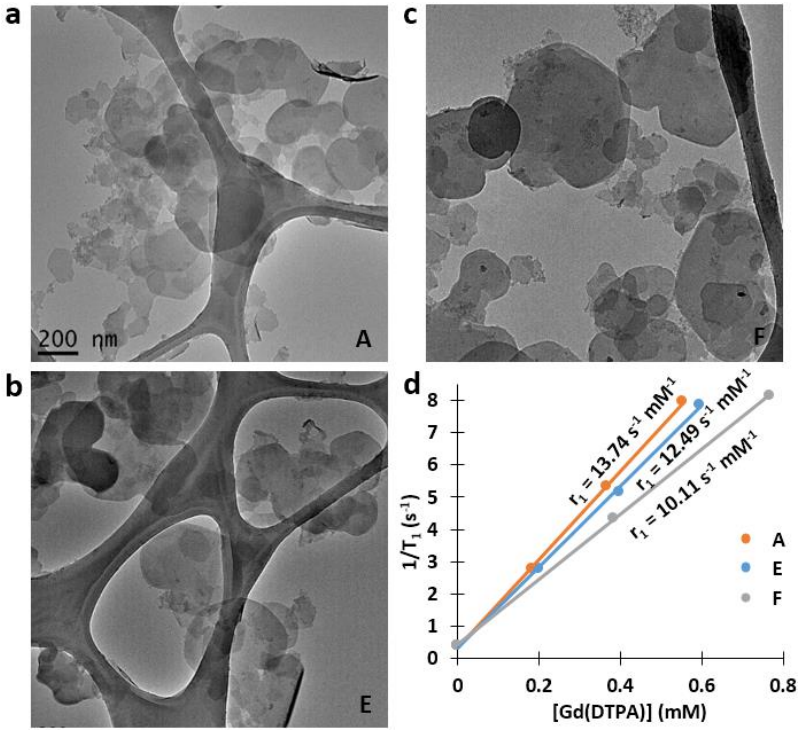

Figure 2.37. Bright field TEM images of sample A, E and F are shown in (a), (b) and (c). Their respective relaxivities are shown in (d)

According to equation (2.3), if T_{1M} is indeed the limiting factor of r_{ip}^{IS}, no difference in r_1 values should be observed. However, as shown in Figure 2.38, small and systematic increases in r_1 values accompanied by decreasing particle sizes were clearly observed. Thus, we conclude that the r_{ip}^{IS} is not limited by T_{1M} alone, and the slight increase in r_1 for smaller particles is probably due to a slightly faster τ_M.

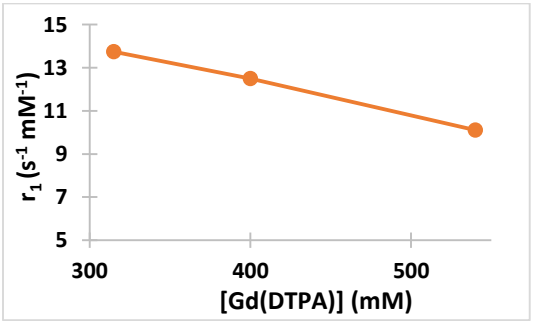

Figure 2.38. Evolution of r_1 as a function of the particle size

2.5.4.4 Relaxivity Mechanism Study-^{17}O T_2 Measurement

The LDH NPs are highly hydrophilic because of its intrinsically positive charged surface. The inherent water also shows the interlayer spacing to be water accessible, which is a key for the development of NS-based contrast agent carriers. However, as previously pointed out, once the $Gd(DTPA)^{2-}$ is intercalated into the LDH nanostructure, the proton exchange rate remains unclear.

An independent study of the exchange rate of water proton with bulk solvent initiated by variable-temperature ^{17}O NMR transverse relaxation measurements at 300 MHz. This complex area is discussed in detail by Mickskei et al.(Micskei et al. 1993) and by Powell et. al.(Powell et al. 1996) Interpretation of the relative transverse relaxation rate ($1/T_2 - 1/T_{2,ref}$) of Gd(DTPA)-intercalated (Zn,Al)-LDH NPs relies on a suspension of $Zn_2Al(OH)_6(NO_3)\cdot xH_2O$ NPs used as the reference, so the result minimizes the effect of oxygen quadrupolar relaxation and other possible mechanisms arising from LDH NPs. The relative relaxation rate is also compared to the relative transverse relaxation rate of the aqueous solution of the same concentration of Gd(DTPA), in which pure water was used as the reference.

As shown in Figure 2.39, first, the transverse relaxation rate ($1/T_2$) of ^{17}O increases with temperature, which means that water is in a slow exchange regime, indicating a longer mean residence time of the inner water relative to the inner water-coordinated intrinsic ^{17}O spin relaxation time T_2. In Moreover, when the Gd(DTPA) concentration was the same for Gd(DTPA)-intercalated NPs suspension and molecular Gd(DTPA) aqueous solution, the absolute value of $1/T_2$ is much lower for the NP suspension. With a very slow water exchange rate, the paramagnetic center induced relaxation of ^{17}O would become small, as with the

suspension of Gd(DTPA)-intercalated LDH NPs, and the relaxation mechanism is still mainly dominated by the huge quadrupolar relaxation of ^{17}O.

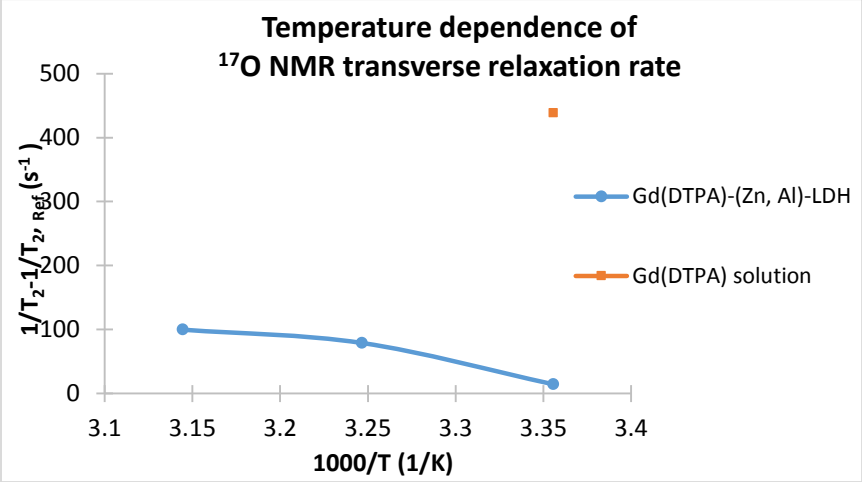

Figure 2.39. Temperature dependence of ^{17}O NMR transverse relaxation rate of Gd(DTPA)-intercalated LDH NPs, and molecular [$Gd(DTPA)^{2-}$] complex

In summary, Gd(DTPA)-intercalated LDH NPs with inherent water molecules and an interlayer spacing of 14.5 Å showed a much slower inner sphere water exchange rate compared to that of molecular Gd(DTPA) solution, and shows that water molecule exchange at RT is almost negligible. However, the very high r_1 per Gd of the Gd(DTPA)-intercalated LDH NPs evidences that proton of the bulk water is still reaching the Gd^{3+} centers, possibly dominated by prototropic exchange mechanism. The exchange lifetime for protons may result from the water molecule exchange ($1/\tau_M^O$) and/or prototropic exchange ($1/\tau_M^H$) and $(\tau_M)^{-1} = (\tau_M^O)^{-1}+(\tau_M^H)^{-1}$.(Aime et al. 1999) This theory may also explain the similar relaxivity increases that have been observed in mesoporous silica NS-based contrast agents, whose pore diameter is about 24 Å.(Taylor et al. 2008)

2.5.5 Conclusions

A highly hydrophilic $Zn_2Al(OH)_6(Cl, 0.5CO_3)_{1-2x}Gd(DTPA)_x \cdot xH_2O$ NPs of different particle size and with x=0.086-0.275 were synthesized. Significant increase in longitudinal relaxivities were obtained with the best sample $Zn_2Al(OH)_6(Cl, 0.5CO_3)_{0.56}Gd(DTPA)_{0.086} \cdot xH_2O$ NPs of highest r_1 value 28.38 s^{-1} mM^{-1}, more than 6 times of increase in r_1 compared to molecular Gd(DTPA).

The most important factors for the relaxivity increase was determined to be the loading capacity, i.e., inherent water molecules to $Gd(DTPA)^{2-}$ paramagnetic center ratio. The contribution of the second sphere water formed by the polymeric nature of the inherent water molecules through hydrogen bonding within the layered structure may need to be taken into account in order to explain the significant increase in r_1. In addition, smaller particle size tends to offer higher relaxivity but only by a little, probably due to a slightly faster water exchange.

As the water exchange rate determined by T-dependent ^{17}O appears low compared to that of the solution Gd(DTPA) complex, we do not consider water molecule exchange as the main proton exchange process. But the prototropic exchange may take place due to the hydrogen bonding formed by the ordered inherent water molecules inside the LDH NPs. In order to increase the water concentration in the second sphere as well the proton exchange rate by both water exchange and prototropic process, we suggest a larger Gd-containing complex to be intercalated into the LDH NPs. As the interlayer gallery spacing can be controlled through the intercalated anion sizes (up to several nm), which can affect the amount of the inherent water molecules as well as facilitate the water accessibility into the inner part of the nanostructure and proton exchange with the bulk water.

CHAPTER

3. ZNO, ZNS-BASED SCHOTTKY JUNCTION PHOTOVOLTAICS

3.1 Backgrounds

3.1.1 The Simple Schottky Model (Electronegativity Approach)

According to the simple Schottky model, the barrier height of a metal-semiconductor interface can be predicted by the difference in the metal work function, ϕ_m, and the electron affinity, χ_s, or the work function, ϕ_s, of the semiconductor.(Milnes and Feucht 1972) The energy diagrams of metal contacts on n-type and p-type semiconductors.(van der Ziel 1968) are shown in Figure 3.1, and Figure 3.2, respectively. Figure 3.1(b) and 1(d) show the rectifying and ohmic behavior of n-type semiconductor-metal junctions with $\phi_m > \phi_s$, and $\phi_m < \phi_s$, respectively. In Figure 3.1(b), while the barrier qV_D for the electron to move from the n-type semiconductors to the metal is $(\phi_m - \phi_s)$, the barrier for the electron to move in the reverse direction from the metal to the n-type semiconductor is $(\phi_m - \chi_s)$.

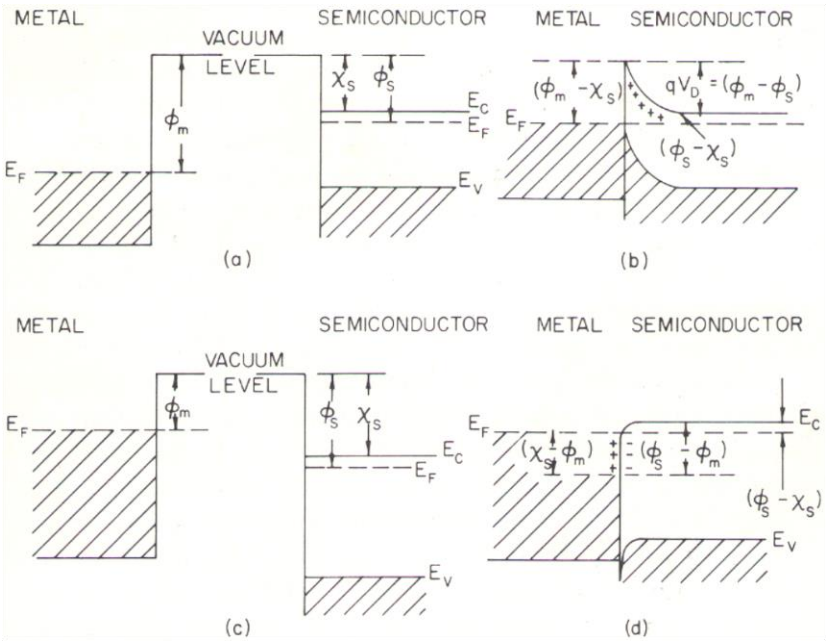

Figure 3.1. Energy diagrams of metal contact on n-type semiconductors

If a forward bias voltage, V_a, is applied on the junction, the forward barrier will become $q(V_D - V_a)$. Note, the semiconductor will be negative with respect to the metal. In contrast, the reverse barrier is relatively unaffected by applied voltage or the doping level of the semiconductor, and used to define the barrier of the metal-semiconductor junction.

Figure 3.2 shows the energy diagrams of metal contacts to p-type semiconductors. The p-type semiconductor-metal junction is hole flow rectifying if $\phi_m < \phi_s$ and ohmic if $\phi_m > \phi_s$.

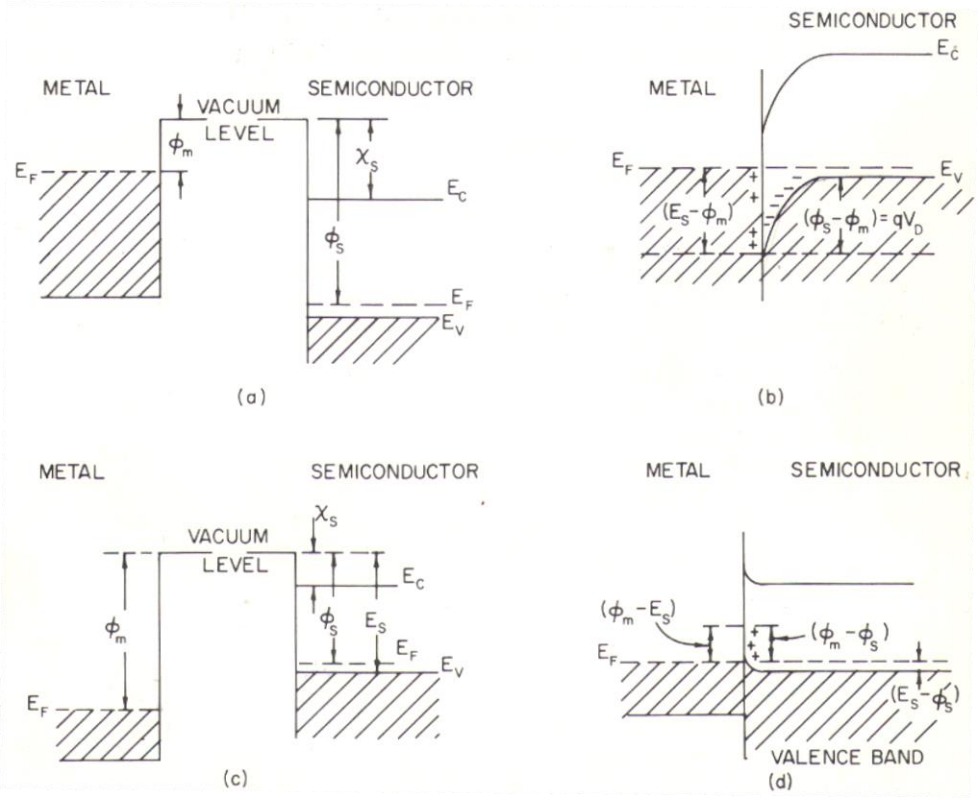

Figure 3.2. Energy diagrams of metal contacts on p-type semiconductors

However, the simple Schottky model neglects the interface states, and does not accurately explain the experimental data for most n-type and p-type semiconductors by using $(\phi_m - \chi_s)$. Moreover, the work functions of metals, determined experimentally, can vary. Table 3.1 lists the work functions of a series of metals.(Milnes and Feucht 1972)

Table 3.1. Work function and electronegativity of metals

Metal	Mean value[a] ϕ_m(eV)	Recent determinations (eV)	Full range (eV)	Electronegativity E_N(eV)
Mg	3.46	—	2.74–3.79	1.2
Al	3.74	4.2	2.98–4.36	1.5
Si	(χ_s = 4.01)	—	—	1.8
Cu	4.47	4.4–4.5	3.85–5.61	1.9
Zn	(3.86)	—	3.08–4.65	1.6
Ge	(χ_s = 4.13)	—	—	1.7
Ni	4.84	4.6–5.1	3.67–5.24	1.8
Ag	4.28	4.2–4.4	3.09–4.81	1.9
Cd	(4.08)	—	3.68–4.49	1.7
Sn	4.11	—	3.12–4.64	1.7
Mo	4.28	—	4.08–4.48	—
Au	4.58	4.7–5.2	4.0–5.2	2.4
W	4.63	—	4.25–5.01	2.3
Pt	5.29	5.48	4.09–6.35	2.2

The effective charger transfer between a metal and a semiconductor at atomic scale can also be understood as the difference of electronegativity values.(Milnes and Feucht 1972) Table 3.2 lists the experimental barrier heights and theoretical values estimated by using the simple Schottky model and the electronegativity approach for contacts of Au and Al on several n-type semiconductors.(Milnes and Feucht 1972) However, due to the negligence of the surface states, both approaches are too simplistic to predict the barrier heights accurately. The effect of the interface states on the band structure was first studied quantitatively by Bardeen (1947).

Table 3.2. Barrier heights estimated by simple Schottky model and electronegativity approach

Semiconductor (n-type)	Metal	Experimental barrier height and/or type of contact (eV)	Theoretical barrier height work function approach $\phi_m - \chi_s$ (eV)	Theoretical barrier electronegativity approach $E_{Nm} - E_{Ns}$ (eV)
Si	Au	0.81	0.57	0.60
	Al	0.70–0.77	– 0.26 ohmic	– 0.30 ohmic
Ge	Au	0.45	0.45	0.70
	Al	0.48	– 0.38 ohmic	– 0.20 ohmic
GaP	Au	1.30	0.55	0.3
	Al	1.05	– 0.29 ohmic	– 0.6 ohmic
GaAs	Au	0.90	0.51	0.4
	Al	0.80	– 0.33 ohmic	– 0.5 ohmic
CdS	Au	0.78	0.08	– 0.1 ohmic
	Al	ohmic	– 0.76 ohmic	– 1.0 ohmic

3.1.2 Experimental Methods for Barrier Heights Determination

The electric current flow at a barrier can be described by the Schottky equation:

$$J = Cexp(-\phi_B/kT)\left[\exp\left(\frac{qV_a}{kT}\right) - 1\right] \qquad (3.1)$$

where C is a constant that depends on the model of carrier flow. Figure 3.3a plots the ln(J) versus the applied voltage, V_a. For a fixed forward bias voltage, V_a, the barrier can be determined from the activation energy plot, as shown in Figure 3.3b.(Milnes and Feucht 1972)

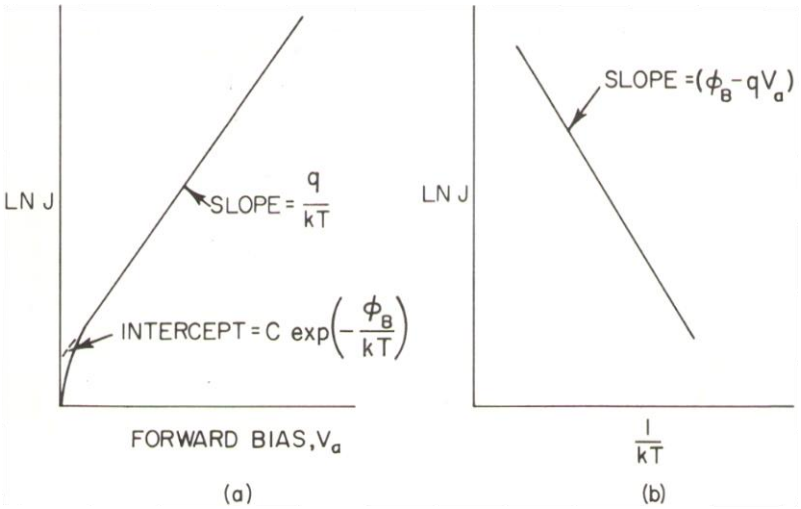

Figure 3.3. I-V plot of a forward biased metal-semiconductor interface (a), activation energy plot (b)

Barrier heights can also be determined by measuring the spectral response of photoexcitation in metal-semiconductor junctions. When light is applied to the photocell, if photon energy exceeds the barrier height but is less than the semiconductor band gap (Figure 3.4a-front wall cell), photoemission of electrons from the metal into the semiconductor (Figure 3.4b-process a) is observed, and the corresponding electric current response can be observed in (Figure 3.4c-photoemission). In case that the photon energy is higher than the band gap of the semiconductor (Figure 3.4a-back wall cell), band-to-band excitation (Figure 3.4b-process b)

takes place, and a sharp increase in photoresponse can be observed (Figure 3.4c-band-to-band).(Milnes and Feucht 1972)

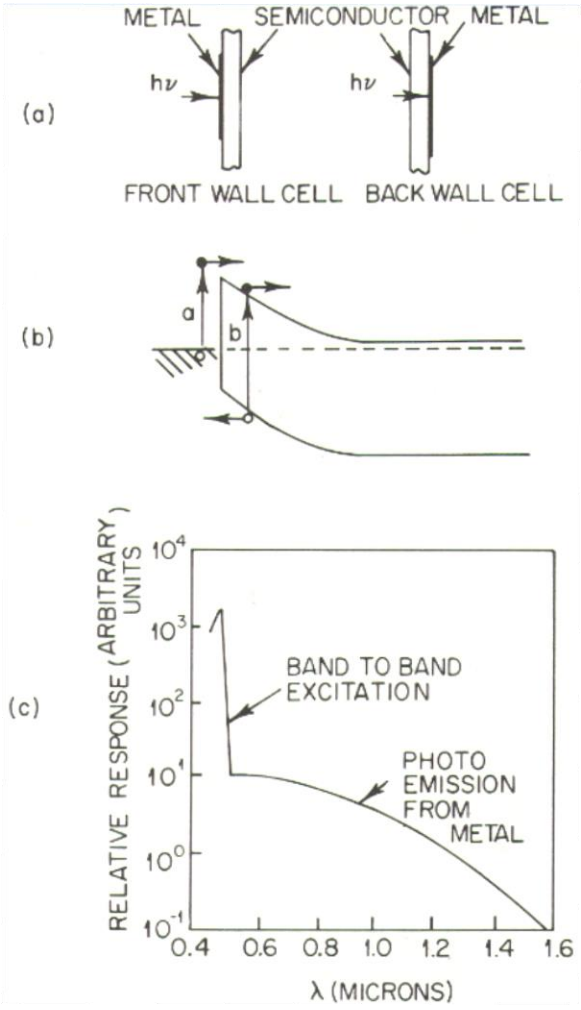

Figure 3.4. Photoresponse of metal-semiconductor junctions

Moreover, the expected short-circuit photocurrent of the photoemission of electrons from the metal into the semiconductor is proportional to $(h\nu - \phi_B)^2$ if $(h\nu - \phi_B)$ is more than a few kT. A straight line should be given by plotting the square root of the photocurrent response, $\sqrt{R}$, against hν, and the extrapolation of this line to intercept the energy axis should give the barrier height ϕ_B. The determination of the barrier heights for Al on n-GaAs and p-GaAs are shown in Figure 3.5a and b, respectively.(Milnes and Feucht 1972)

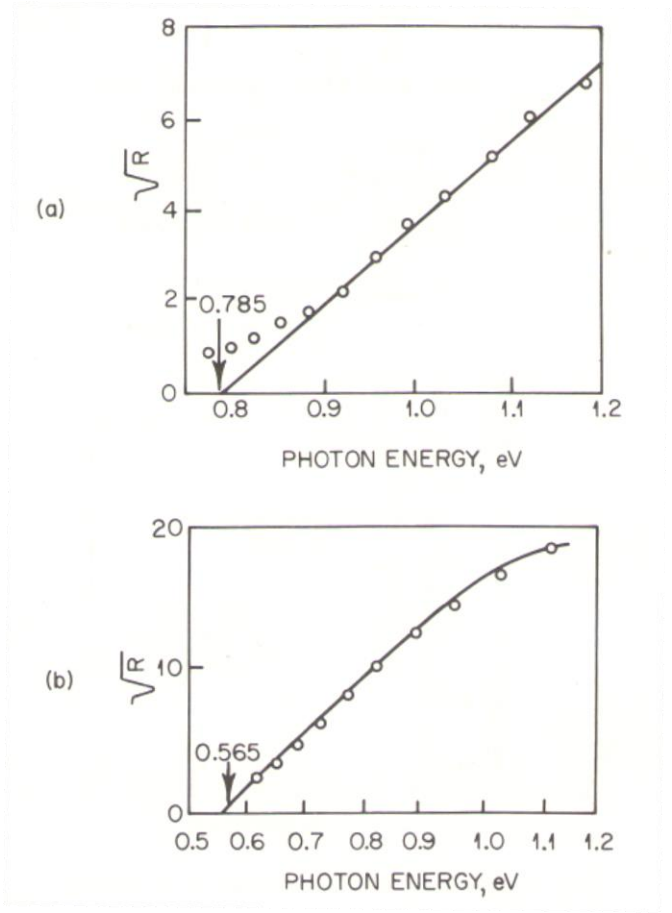

Figure 3.5. Determination of the barrier height of Al/n-GaAs (a) and Al/p-GaAs (b) using photoresponse

Barrier height can also be determined by the measurement of the capacitance versus reverse voltage. For a uniformly doped semiconductor, C^{-2} is linearly proportional to the applied voltage and the voltage intercept is the diffusion barrier height.

The experimentally determined barrier heights of a series of metals/n-type semiconductors are listed in Table 3.3.(Milnes and Feucht 1972)

In order to prepare Schottky junctions with fundamental and reproducible barrier heights, extra precautions need to be taken in the preparation of the semiconductor surface before the evaporation of the metal. The removal of the layers on the surface of the semiconductor by most

chemical preparation methods is actually not complete. Turner and Rhoderick (1968) found substantial differences between cleaved and chemically prepared surfaces in the study of metal/n-type Si Schottky barriers. Their results from C^{-2} plots for various metals on the (111) Si face are shown in Table 3.4.(Milnes and Feucht 1972)

Table 3.3. A summary of the experimentally determined barrier heights for some metals/n-type semiconductors

	Observed barrier heights (eV) 300°K													
Metal	Si	Ge	SiC	GaP	GaAs	GaSb	InP	InAs	InSb	ZnS	ZnSe	CdS	CdSe	CdTe
Al	0.50–0.77	0.48	2.0	1.05	0.80			Ohmic		0.8		Ohmic		0.76
Ag	0.56–0.79			1.20	0.88		0.54	Ohmic	0.18 (77°K)	1.65		0.35–0.56	0.43	0.66
Au	0.81	0.45	1.95	1.30	0.90	0.60	0.49	Ohmic	0.17 (77°K)	2.0	1.36	0.68–0.78	0.49	0.60
Ca	0.40													
Cr	0.57–0.59													
Cu	0.69–0.79	0.48		1.20	0.82					1.75	1.10	0.36–0.50	0.33	
Mg				1.04						0.82	0.70			
Mo	0.56–0.68													
Na	0.43													
Ni	0.67–0.70											0.45		
Pb	0.40–0.79													
Pd	0.71									1.87		0.62		
Pt	0.90			1.45	0.86					1.84	1.40	0.85–1.1	0.37	0.58
PtSi	0.85													
W	0.66	0.48												
WSi_2	0.86													

Table 3.4. The effect of the semiconductor surface preparation on the barrier heights

		Barrier height (eV)		
		Cleaved surfaces		Chemically prepared surfaces after aging
Metal ϕ_m	(eV)	Turner and Rhoderick (1968)	Archer and Atalla (1963)	Turner and Rhoderick (1968)
Pb	4.20	0.79	—	0.41
Al	4.20	0.76	0.77	0.50
Ag	4.31	0.79	0.76	0.56
Cu	4.52	0.79	0.77	0.69
Au	4.70	0.82	0.81	0.81
Ni	4.74	0.70	0.68	0.67

3.1.3 Effect of the Surface States of the Semiconductor on Schottky Barrier Height

Figure 3.6 lists the measured barrier heights of several metals on cleaved n-Si.(Milnes and Feucht 1972) The deviation from the predicted values by using the simple Schottky model is significant.

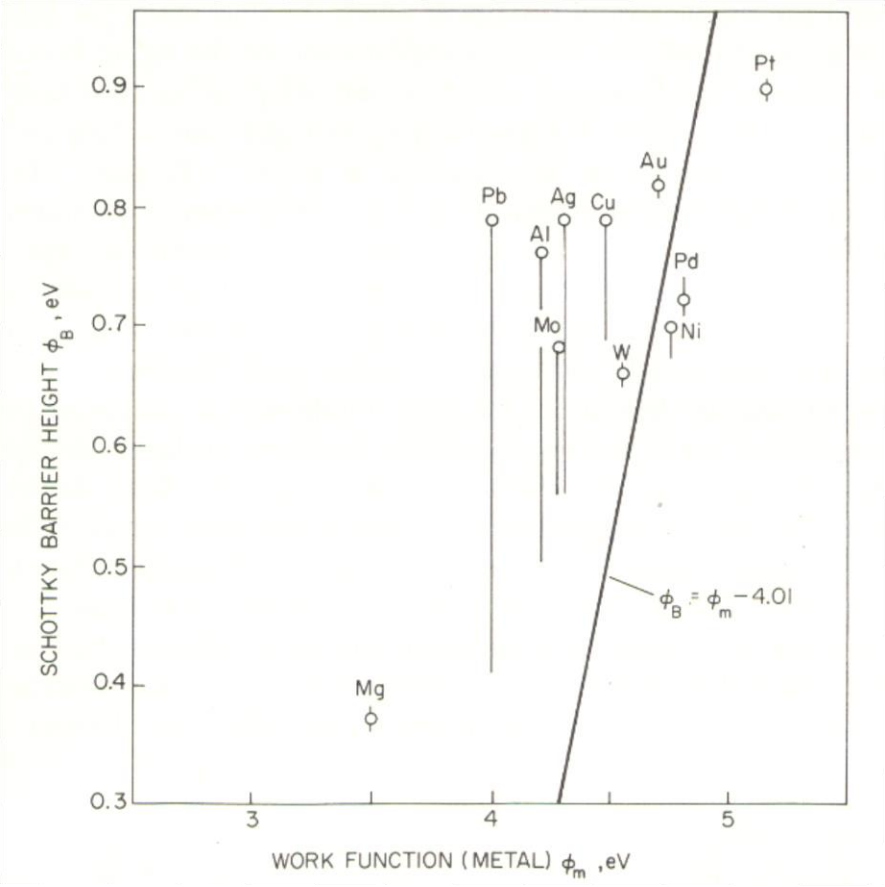

Figure 3.6. Measured barrier heights of various metals on n-Si vs. the simple Schottky model

Figure 3.7 shows that the barrier heights for various metals on GaAs are almost invariant despite the variation of the electronegativity of the metals.(Milnes and Feucht 1972) In contrast, the barrier heights vary systematically following the variation of the electronegativity of the metals. Such results demonstrate that the barrier heights of metal-GaAs junction is surface-state controlled, but ZnS is not and conforms to the simple Schottky model.

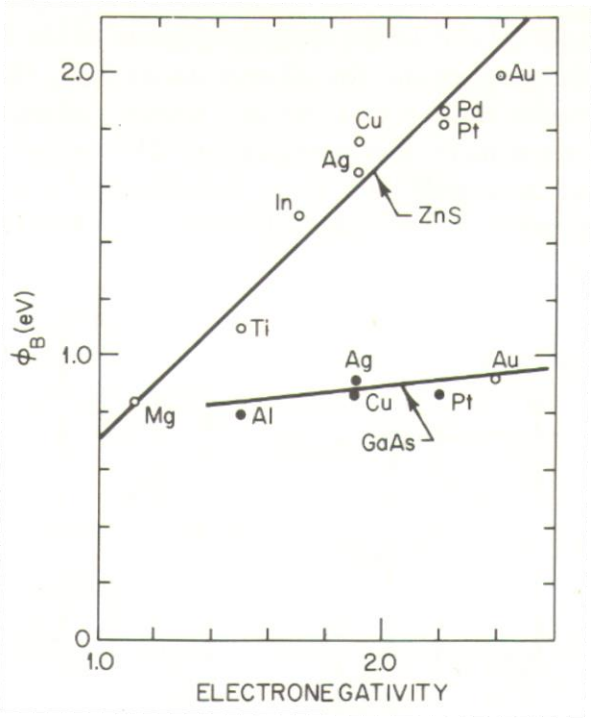

Figure 3.7. Measured barrier heights of various metals with different electronegativities on GaAs and ZnS

In fact, for most semiconductor materials, the barrier heights of their Schottky junctions are completely independent on the work functions or electronegativities of the metal contacts, and follow the pattern represented by Si and GaAs. Mead (1966) reported that many covalently-bonded semiconductors have significant surface states, which can form a narrow band centered within the band gap, and supply or accept charges with relatively little shift of the Fermi level. Because the Fermi level of the metal tends to lock into semiconductor band gap, the barrier ϕ_{Bn} from the metal Fermi level to the conduction band edges of the semiconductor is almost independent of the metal, but proportional to the band gap of the semiconductor. Figure 3.8 reveals that the difference between the Fermi level of the metal and conduction band edge of the semiconductor is proportional to the band gap of the semiconductor for a wide range of surface state-controlled covalent materials.(Milnes and Feucht 1972)

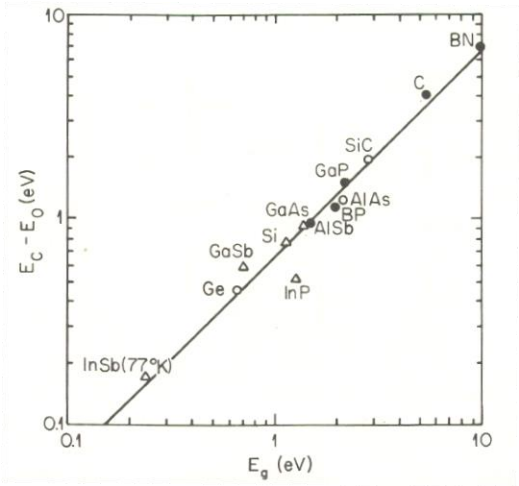

Figure 3.8. Difference between the conduction band edge and the Fermi level (E_c - E_0) for Au contact on various surface state-controlled covalent materials

For more polar covalent materials such as SiO_2 or ZnS the barrier heights are influenced significantly by the electronegativity of the metal contact. The energy diagrams for Al and Au on SiO_2 are shown in Figure 3.9.(Milnes and Feucht 1972)

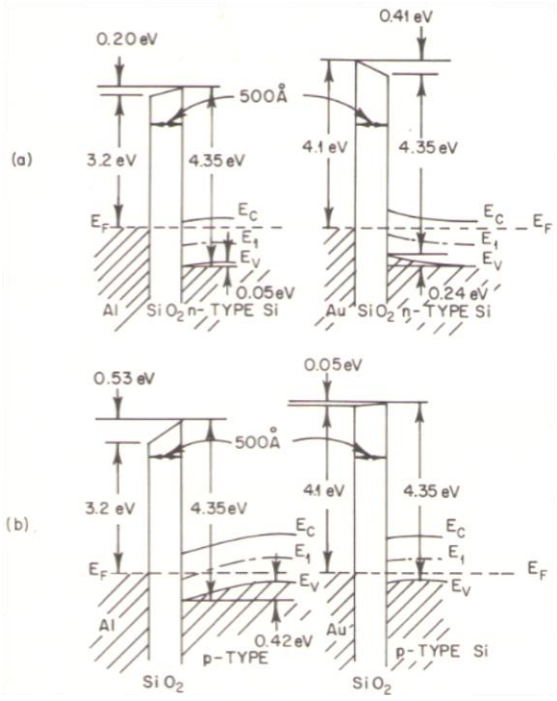

Figure 3.9. Energy band diagrams for Al-SiO_2-Si and Au-SiO_2-Si

Similar experimental results are shown in Figure 3.10,(Milnes and Feucht 1972) for the non-polar covalent GaSe, the variation of ϕ_{Bn} due to electronegativity of the metal is relatively small (with a slope of 0.6). For highly polar covalent SiO_2, the slope is 1. Moreover, for vacuum-cleaved covalent Si, the variation in barrier height due to the variation of metals is negligible (see Table 3.4).

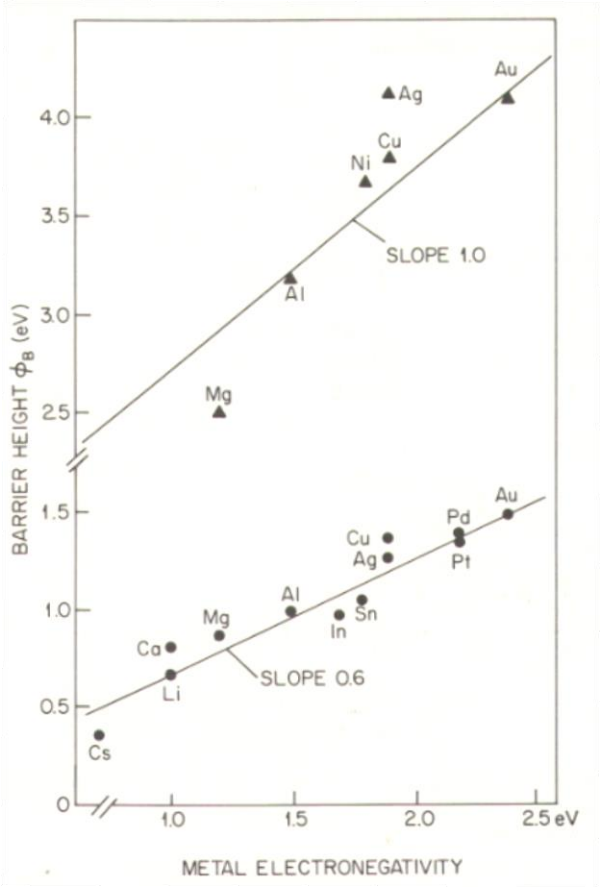

Figure 3.10. Relationship between the metal electronegativity and the observed barrier heights of various metals on highly polar covalent SiO_2 and on non-polar covalent GaSe

The transition of the interfacial property is clearly revealed by plotting the slope factor ($d\phi_B / d\chi_m$) versus electronegativity difference (ΔE_N) of the compound, as shown in Figure 3.11.(Milnes and Feucht 1972) A well-defined transition between the interfacial properties of ionic semiconductors and non-polar covalent ones can be observed.

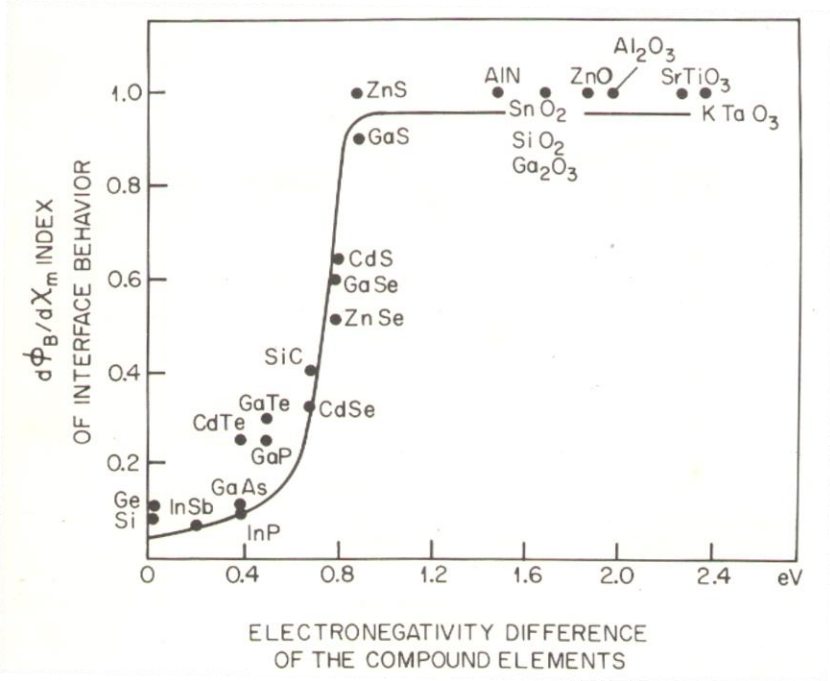

Figure 3.11. Plot of ($d\phi_b$ /$d\chi_m$) versus electronegativity difference of the compound elements

3.2 Cr-Au/ZnS/ZnO Schottky Junction Photovoltaic with High Open Circuit Voltage

3.2.1 Introduction

In order to feature the electrochromic window self-power capability and maintain the architecture of the power supply device simple at the same time, visible-light transparent and ultraviolet-absorbing solar cells based on metal/large band gap semiconductor, such as ZnO and ZnS, with a large open circuit voltage (V_{oc}), i.e. >1.5 V are highly desirable. ZnS is a wide band gap semiconductor material and exists mainly in two different polymorphs: zinc blende (or sphalerite) and wurtzite. Sphalerite with a band gap of ~3.72 eV is the most stable phase at room temperature (T); and wurtzite polymorph with a ~3.77 eV band gap is stable at temperature beyond 1296 K.(Fang et al. 2011) At 300 K, while the highest Schottky barrier height for ZnO is 0.75 V with Pt contact, the barrier heights for Au/ZnS (sphalerite) and Cu/ZnS (sphalerite) junctions are reported to be as high as 2.00 V and 1.75 V, respectively.(Sze 1981) The much higher barrier heights for ZnS-based Schottky diodes can translate into higher V_{oc}. Despite that ZnS-based Schottky junctions can provide high V_{oc}, it is expected that the overall power of the solar cell can be limited by its very low electronic conductivity if ZnS is used as the only photon absorber. The very low cross-film conductance can be mitigated by either doping or reducing the thickness of the film.

Based on the above reasoning, we consider that the use of ZnS/ZnO thin film heterojunction with Au or Cu contact can potentially increase the short circuit current, I_{SC}, and maintain the high V_{OC}. Such an idea is the main driving force behind the current research, and the research activities mainly focus on the following steps:

(i) Vacuum technique-based fabrication and characterization of Au-Cr/ZnS/ZnO Schottky junction photovoltaic

(ii) Solution synthesis of ZnO thin film and the formation of ZnS/ZnO heterojunction

3.2.2 Fabrication of Au-Cr/ZnS/ZnO Schottky Junction Photovoltaic Using Vacuum Techniques and Characterization

3.2.2.1 Experimental

A heavily phosphorous (P)-doped Si wafer was used as the substrate. A Mn-doped ZnO thin film (1 μm) was then sputtered using plasma-assisted sputter deposition technique. The sample was sealed into H_2S atmosphere, and ZnO was partially converted to ZnS at 350 °C for 1 h. The resultant sample was further processed using photolithography to deposit an interdigitated pattern of Cr-Au to form the Schottky contact. The entire procedure can be described in several important steps: hexamethyldisilazane (HMDS) spin coating, photoresist spin coating, photolithography using an interdigital mask, and finishing with Cr-Au metal deposition using thermal evaporation. The electrical and the photovoltaic properties of the resultant Au-Cr/ZnS/ZnO solar cell device was tested by I-V measurements under dark, and UV-illuminated conditions.

3.2.2.2 Results and Discussions

The device configuration is shown in Figure 3.12a: essentially, ZnS/ZnO thin film heterojunction sits on P-doped Si substrate and Au-Cr contact sits on the ZnS surface of the ZnS/ZnO heterojunction. The metal pattern, shown in Figure 3.12(b), was specifically designed

for light to reach the photon-absorbing region, i.e. metal contact and ZnS/ZnO heterojunction. The corresponding energy diagram of the device is illustrated in Figure 3.12(c).

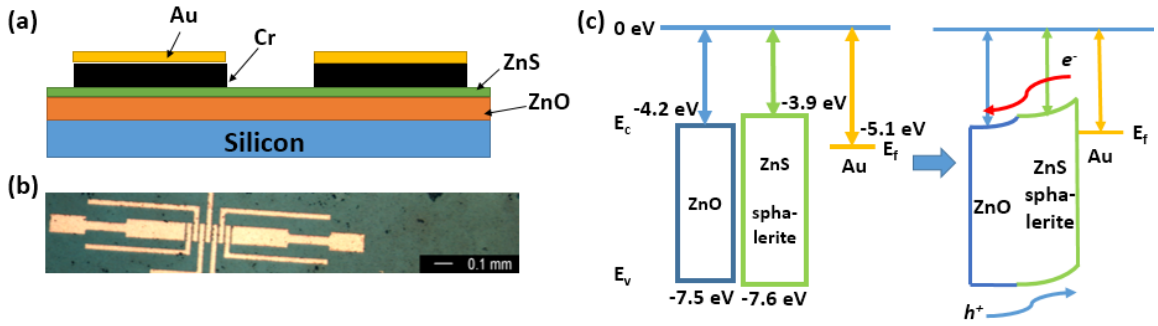

Figure 3.12. (a) Device configuration of Schottky junction photovoltaic: Au-Cr/ZnS/ZnO/n-Si, (b) an interdigital pattern that allows light to reach the photon-absorbing regions, and (c) the relative energy diagram of the device

The I-V measurements demonstrated proof-of-concept of a Schottky heterojunction; the V_{oc} was about 1.35 V. However, as shown in Figure 3.13, the I_{sc} was very low because the sputtering target was Mn-doped ZnO, and rendered the ZnO thin film fairly insulating. The I-V measurement of the 1 μm thick sputtered Mn-doped ZnO thin film are shown in Figure 3.14.

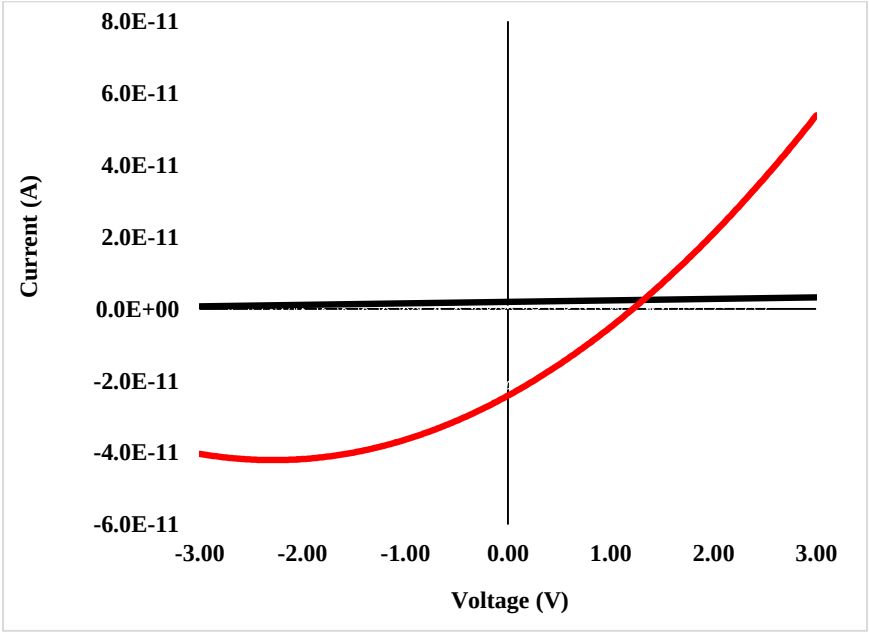

Figure 3.13. I-V measurements of the device under dark (black line) and illuminated with UV light of 302 nm (red line)

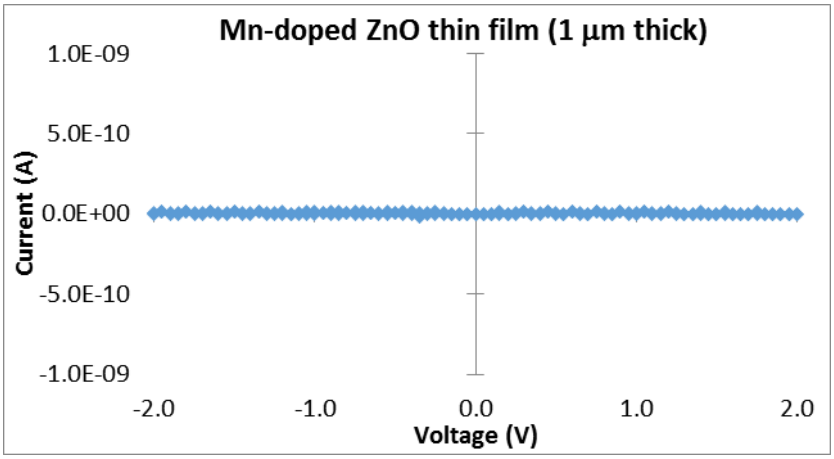

Figure 3.14. I-V measurements of the Mn-doped ZnO thin film (1 µm thick)

3.2.3 Solution Growth of ZnO Thin Film and the Formation of ZnS/ZnO Heterojunction

In order to fabricate cost-effective, visible light-transparent and UV-absorbing solar cells with high V_{OC}, we decided to use solution grown ZnO as the core materials. The advantages of the wet chemical processing over vacuum techniques are the low-cost and the capacity to produce materials of larger scales. However, the challenges are the purity and the crystalline quality of the material, as well as the morphology, which can have decisive impact on device performance. The ZnS/ZnO heterojunction can be obtained by the partial sulfurization of the solution grown ZnO thin film in H_2S atmosphere.

3.2.3.1 Experimental

ZnO seeds were first sputtered onto a heavily P-doped Si substrate using plasma-assisted sputtering technique. The thickness of the ZnO seeding layer was about 10 nm thick. The substrate was then ready for solution growth of ZnO. A typical chemical bath contained a stoichiometric amount of $Zn(NO_3)_2 \cdot 6H_2O$ and hexamethylenetetramine (HMTA); the

concentrations and growth lengths varied as needed. The growth temperature was set to 90 °C. Following the growth, samples were sealed in H_2S atmosphere and heat treated at 350°C to partially convert the top layers of ZnO to ZnS. The electrical property of the resultant ZnS/ZnO heterojunction was characterized by I-V measurements.

3.2.3.2 Results and Discussions

Solution growth of ZnO thin-films is dependent on growth time, temperature, and concentration of the reagents. The ideal growth temperature is 90°C. If the temperature is too low, growth is splotchy or may not occur at all, while if the too high temperature causes too rapid precipitation, and the film becomes uneven. The interrelationship between the effects of the reactant concentration and growth time on the resulting ZnO nanostructure is depicted in Figure 3.15. Longer times resulted in thicker films, and the ideal concentrations of $Zn(NO_3)_2 \cdot 6H_2O$ and HMTA for making the films were found to be about 0.15 M; lower concentrations resulted in nanorods, nanowires, or nanoparticles while higher concentrations released too many precipitates for even growth.

After sputtering the 10 nm thick ZnO seeding layer onto the heavily P-doped Si substrate, the I-V measurements showed that the conductance was almost as good as the n-Si substrate (Figure 3.16) Also, the conductance of the 5 μm-thick solution grown ZnO thin film is much better than that of the 1 μm-thick sputtered Mn-doped ZnO thin film.

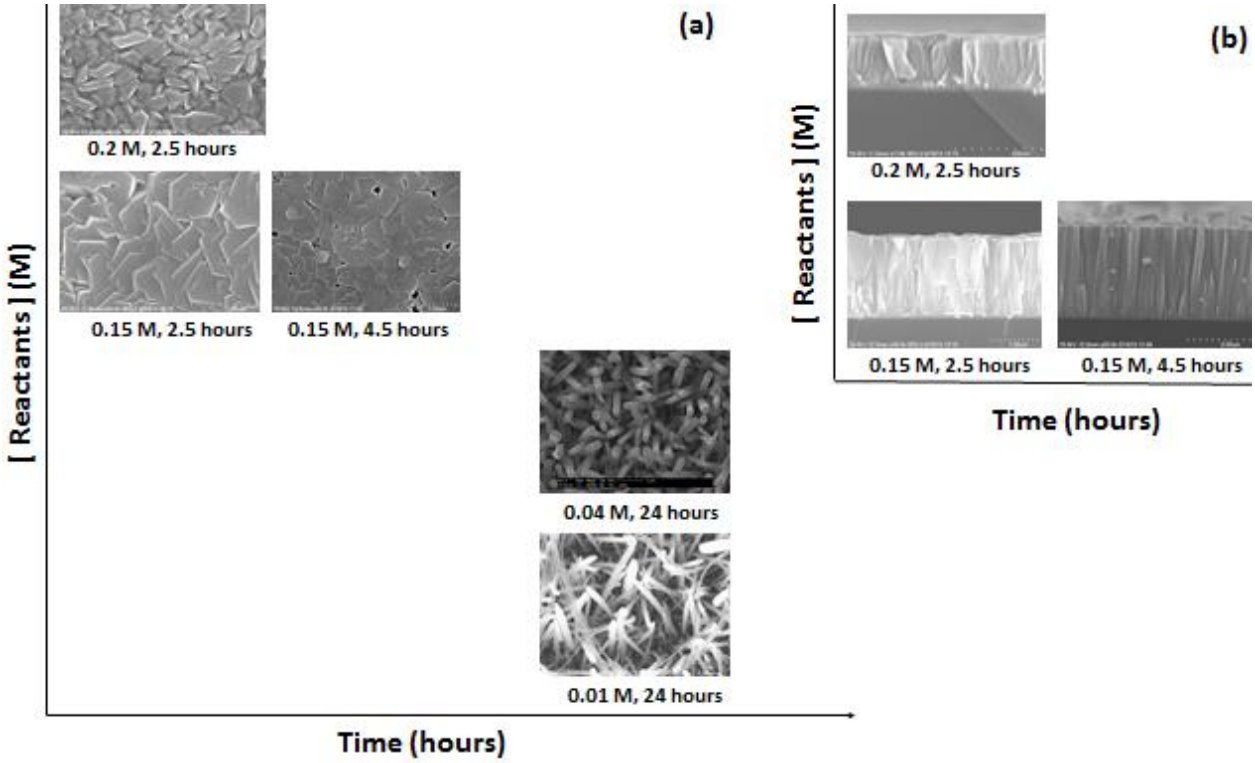

Figure 3.15. (a) SEM top views of solution grown ZnO nanomaterials demonstrating the morphology evolution due to varied concentration and growth time at 90 °C (b) the corresponding SEM cross-sectional views

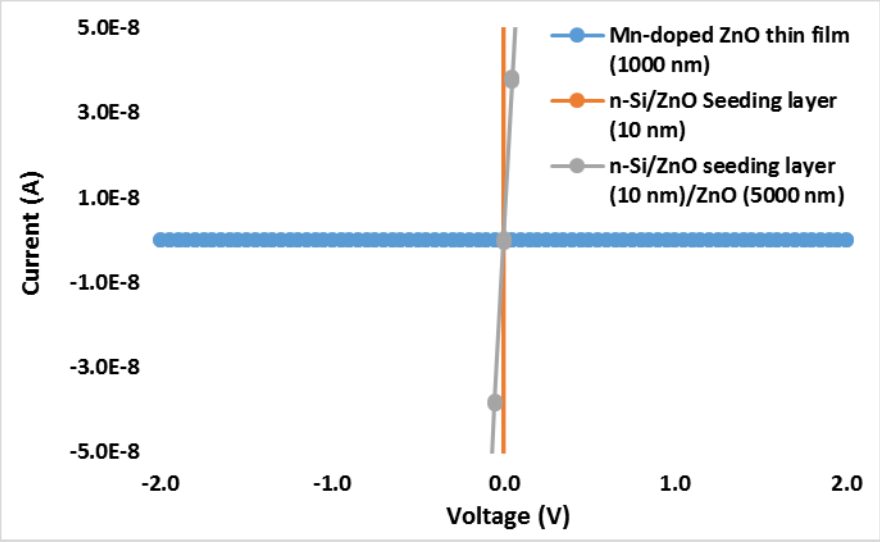

Figure 3.16. I-V measurements of n-Si/Mn-doped ZnO thin film (1000 nm), n-Si/ZnO seeding layer (10 nm) and n-Si/ZnO seeding layer (10 nm)/solution grown ZnO thin film (5000 nm)

The cross-sectional view of a ZnS/ZnO heterojunction formed by partial sulfurization of a solution grown ZnO thin film in H_2S atmosphere is shown in Figure 3.17a. The composition EDX mapping using the Sulfur k-line is shown in Figure 3.17b, and the thickness of the ZnS layer in the heterojunction is about 450 nm. Clearly, the solution grown ZnO thin film route shows high potential for the fabrication of the proposed heterojunction and devices.

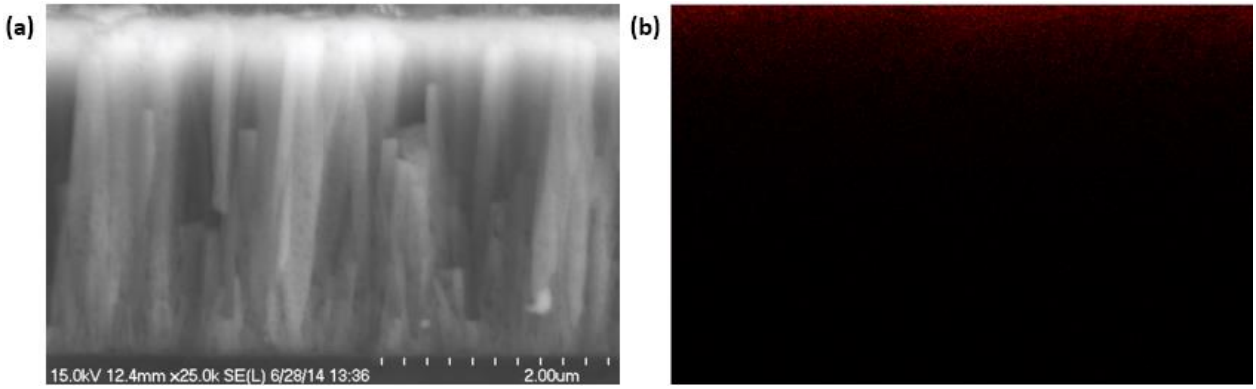

Figure 3.17. SEM cross-sectional view of the n-Si/ZnO/ZnS heterojunction in (a), and its corresponding composition EDX mapping using the Sulfur K-line in (b)

3.2.4 Conclusions and Future Works

The relatively high V_{oc} of the Au-Cr/ZnS/ZnO Schottky junction solar cell was successfully demonstrated. The low I_{SC} of the device was mainly due to the low conductivity of the sputtered Mn-doped ZnO thin film. The partial sulfurization of the ZnO has been demonstrated as a viable route to form ZnS/ZnO heterojunction for eventual fabrication of Schottky junctions. The electrical property of the solution grown ZnO are excellent and solution growth technique is an effective and economic alternative synthesis method to the vacuum deposition techniques. Immediately after the successful solution growth of ZnO thin film and its partial sulfurization, the Au/ZnS/ZnO and Cu/ZnS/ZnO junctions will be fabricated and their photovoltaic performance will be tested.

.

CHAPTER

4. $LiFePO_4$ -- A CATHODE MATERIAL FOR LI/LI-ION BATTERIES

4.1 Background

In modern societies, rapid economy development and living standard improvement are constantly demanding increasing energy consumption. Excessive relying on fossil fuel consumption is causing serious atmospheric imbalances. Global warming, toxic gaseous emissions from combustion of fossil fuel, finite supplies, and pollution-related health issues are pushing the partial replacement of fossil fuels by renewable, sustainable and environment-friendly energy sources, such as solar energy, wind power, hydropower, etc. However, the intermittent nature of renewable energy sources is generating a pressing need for electrical energy storage systems to balance the supply and demand.

Rechargeable batteries provide a very promising way for the conversion between chemical and electrical energies. Since the commercialization of Li-ion batteries by Sony in the early 90s, Li-ion battery has outperformed all other rechargeable battery chemistry, such as lead acid, nickel-cadmium and nickel metal hydride systems; The high cell voltages (~4 V) guarantee both higher volumetric and gravimetric energy densities, as shown in Figure 1.1.

Although the current Li-ion technologies have can meet the need of low to moderate power portable electronic devices, they fall short of meeting the need of high power applications such as stationary renewable energy storages and transportation (or electric vehicles). Up-to-date (Dec, 2012), electric cars, such as Nissan Leaf and Peugeot Ion, tend to cost more than £30,000, mainly because of the battery cost. The estimated battery life is 5-10 years under ideal conditions. Moreover, the electrified travel ranges are only ~80 miles. Furthermore, it takes about 13 hours to fully charge an empty battery.

From technological points of view, the key challenges in future Li-ion battery research would be exploration of new Li-ion battery chemistry, improvement of charge/discharge rates, gravimetric and volumetric energy densities, cyclability and safety. In addition, electrodes need to be made of sustainable and environment-friendly elements. From an economic point of view, the main challenge of Li-ion battery concentrates on the cost-effectiveness, where both material and manufacturing costs become decisive. Cost-effectiveness is critical to large form batteries (one to hundreds of kWh) for electric or hybrid vehicles. Almost all the manufacturers have chosen the Li-ion battery chemistry based on carbon (C) anode and $LiCoO_2$ cathode. However, expensive Co becomes cost-prohibitive for large form batteries. At this moment, the less expensive alternative chemistry, C-based anode and $LiMnO_2$-based cathode, is chosen for electric vehicles. The up-to-date cost is about $600/kWh. According to Ford Motor Company, in order to make the use of Li-ion batteries in transportation economically viable, it is vital to cut down the battery cost to < $100/kWh.

Among many cathode materials for Li/Li-ion batteries, the olivine $LiFePO_4$, a serious competitor of $LiMnO_2$ cathode for the electric vehicle application, is attracting much attention. Currently, it is being commercially used for industrial products by Black and Decker's DeWalt brand, Fisker Karma, Cessna and BAE Systems. The inexpensive and sustainable Fe-based composition allows it to be less toxic than Co, Ni and Mn-based systems. In addition, $LiFePO_4$ has a flat discharge voltage at 3.3 V vs. Li^+/Li, such a relatively lower voltage (3-4 V) of $LiFePO_4$ is desirable from standpoints of safety, cyclability and shelf life. Among several necessities of this system for improvement, there is a need for a cost-effective and time-saving manufacturing process.

Microwave dielectric heating is considered energy-efficient, and has been applied to the synthesis of $LiFePO_4$. Several works have reported obtaining $LiFePO_4$ by microwave heating for very short periods of time—several minutes.(Beninati, Damen, and Mastragostino 2008, Gallis and Landry 2001, Guo, Zhan, and Zhou 2009, Higuchi et al. 2003, Park et al. 2003, Song et al. 2007, Song et al. 2008, Uematsu et al. 2007, Wang et al. Nano-lifepo4/mwcnt cathode materials prepared by room-temperature solid-state reaction and microwave heating 2007, Preparation and characterization of nano-sized lifepo4 by low heating solid-state coordination method and microwave heating 2007, Zou, Zhang, and Shen 2010) However, the resulted phase purity and electrochemical performance are not ideal. The motivation of this study is to prove the microwave heating efficiency and cut down the thermal budget for the $LiFePO_4$ synthesis by coupling the polymeric $LiFePO_4$ precursor synthesized by modified Pechini's method with the microwave heat treatment of short duration (several minutes) at a relatively low temperature (< 700 °C).

In order to help readers to understand the content of this chapter, the essential backgrounds of several topics are furnished in the following sections. The content in section 4.1.1 tries to give a fairly complete but concise revisit to the Li-ion battery chemistry and the essential components of Li-ion batteries. Section 4.1.2 provides a more detailed description of the physicochemical properties of $LiFePO_4$, where the main limitations are discussed as well. A literature review of various synthesis methods of $LiFePO_4$ is given in section 4.1.3, where the resulted compositions, phases, morphologies, electrochemical performances, and different strategies adopted in the syntheses to overcome the drawbacks are discussed. In the last two sections (4.1.4. and 4.1.5.), the background information of sol-gel chemical processing and microwave heating are provided, which is profoundly related to this study.

4.1.1 Fundamental Concepts of Secondary Li-ion Battery

A typical construction of a Li-ion battery essentially includes a cathode and an anode, which are connected by the ion-conducting electrolyte. Both the cathode and the anode are Li^+ insertion compounds. An example is illustrated in Figure 4.1, in which $LiCoO_2$ and Li_xC_6 are used as the cathode and the anode, respectively.

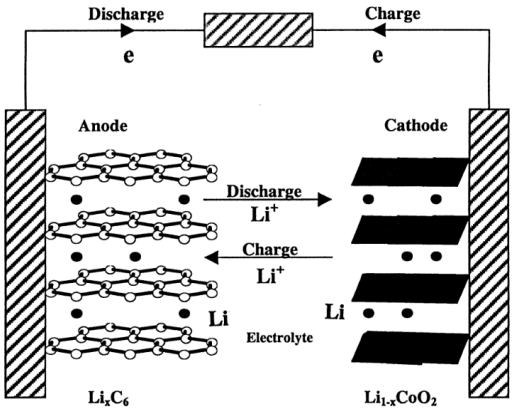

Figure 4.1. Illustration of the charge/discharge process in a typical Li-ion battery

During the discharge process, the reduction reaction takes place at the cathode, accompanied by the insertion of Li^+ into itself; the oxidation occurs at the anode, accompanied by the extraction of Li^+; the electron current is driven by the redox reaction from the anode to the cathode through the external circuit. During the charging process, all the situations are reversed. The reversible redox reactions at the electrodes are:

$$\text{anode: } Li_xC_n \underset{\text{charge}}{\overset{\text{discharge}}{\rightleftharpoons}} xLi^+ + xe^- + C_n$$

$$\text{cathode: } xLi^+ + xe^- + xCoO_2 \underset{\text{charge}}{\overset{\text{discharge}}{\rightleftharpoons}} LiCoO_2$$

Figure 4.2 shows a representative energy diagram of a Li-ion cell. The open circuit voltage (V_{oc}) of the cell is the difference between the chemical potential of lithium of the cathode and that of the anode. The chemical potential of lithium, in turn, is dictated by the redox

transition metal, the crystalline structure of the electrode, and the coordination geometry of the site into/from which Li^+ is being intercalated/deintercalated.

$$V_{oc} = -\frac{\mu_{Li(c)} - \mu_{Li(a)}}{F}$$

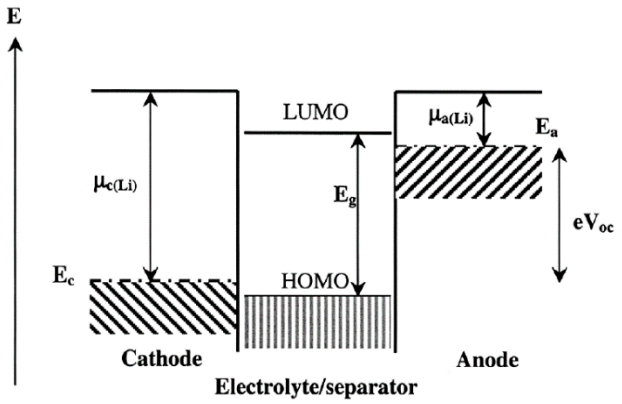

Figure 4.2. Energy diagram of a typical Li-ion cell(Nazri and Pistola 2009)

And in order to avoid any electrolyte-involved side reaction, the band gap (E_g) of the electrolyte should be larger than eV_{oc}.

For a Li^+ insertion compound to be an adequate electrode material for Li-ion batteries, several requirements need to complete:

- A cathode material $Li_xM_yX_z$ (M = transition metal; X = anion) should have a low lithium chemical potential to maximize the V_{oc}; in the delithiated form M_yX_z, M^{n+} should have a high oxidation state that shows a strong tendency of being reduced.
- An anode lithium insertion compound $Li_xM'_yX'_z$ should have a high lithium chemical potential to maximize the V_{oc}; in the delithiated form $M'_yX'_z$, M'^{n+} should have a stable oxidation state, which requires a high voltage for its reduction.
- In order to maximize the energy density, an electrode should be able to reversibly intercalate/de-intercalate a large amount of Li^+. As the energy density is the product of the capacity and the cell voltage.

- To maximize the cyclability of the electrode, the crystalline structure change induced by the Li^+ intercalation and de-intercalation should be small.
- Electrodes should be mixed conductive, i.e., both electronic and ionic conductive, to minimize the polarization losses and ensure a high capacity at a high charge/discharge rate.
- Electrode materials should be chemically inert to electrolytes over the entire range of Li^+ intercalation/de-intercalation.
- The variation in the redox potential of the electrode should be limited over the entire range of Li^+ intercalation/de-intercalation.
- Electrode materials should be inexpensive, sustainable, environmentally friendly, low density, and easy to synthesize.

Several lithium insertion compounds as electrode materials for Li-ion battery are listed in Figure 4.3. Li metal has the largest capacity among all, 3860 mAh/g. However, it reacts with non-aqueous electrolytes and leads to a non-uniform growth during the charging process, which causes dendritic short circuiting and serious local heating. In order to achieve a reasonable cell voltage (> 3 V), the difference in reduction potential between the anode/cathode and Li^+ should be as negative/positive as possible. On one hand, $LiCoO_2$, $LiNiO_2$ and $LiMn_2O_4$ exhibit high electrode potentials around 4 V vs. Li^+/Li, which make them appealing as cathode candidates, but the long-term chemical stability of both the electrolyte and the electrode needs to be evaluated. On the other hand, the low electrode potentials of graphite and coke (< 1 V) make them attractive anodes.

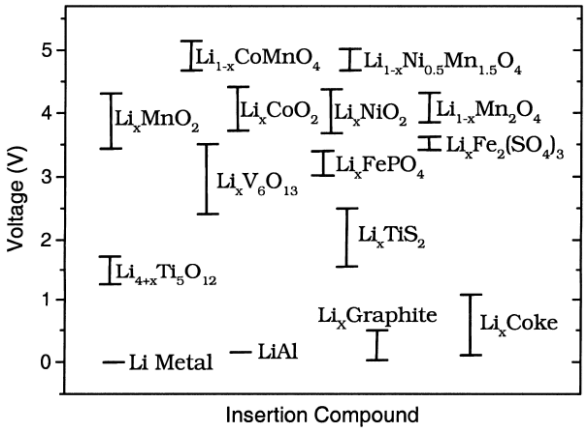

Figure 4.3. Reduction potential respect to Li^+/Li for various lithium insertion compounds(Nazri and Pistola 2009)

4.1.2 Physicochemical Properties of $LiFePO_4$

Padhi *et al.* first discovered the reversible Li^+ intercalation and de-intercalation capability of triphylite ($LiFePO_4$), and 60 % of the theoretical capacity was achieved.(Padhi, Nanjundaswamy, and Goodenough 1997) Since then, it is being considered as a very promising cathode material for Li-ion/Li battery because of its flat discharge plateau at 3.4 V vs. Li^+/Li, high theoretical capacity of 170 mAh/g, low cost, sustainability, and enhanced safety. In addition, it does not suffer from overcharge problem, similar as $LiMn_2O_4$.

As shown in Figure 4.4, $LiFePO_4$ possesses the phospho-olivine structure -- within an oxygen hexagonal packing, Li^+ and Fe^{2+} occupy half of the octahedral sites and P 1/8 of the tetrahedral sites. The lattice constants are: a = 10.33 Å, b = 6.01 Å, c = 4.69 Å and V = 291.2 $Å^3$.

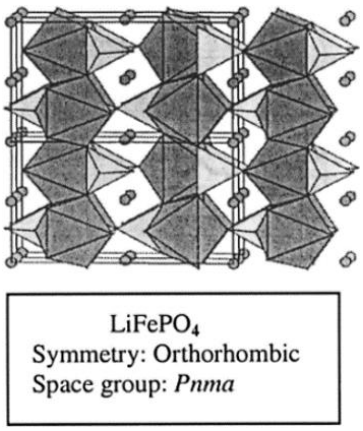

Figure 4.4. Representative crystalline structure of $LiFePO_4$

Li^+ can be extracted from the octahedral sites, and the delithiation process is a kinetically limited phase migration from $LiFePO_4$ to $FePO_4$. Using an optimized $LiFePO_4$/C composite electrode, the complete phase transformation of $LiFePO_4$ into $FePO_4$ was shown by *in situ* X-ray diffraction (Figure 4.5)(Morcrette et al. 2002)

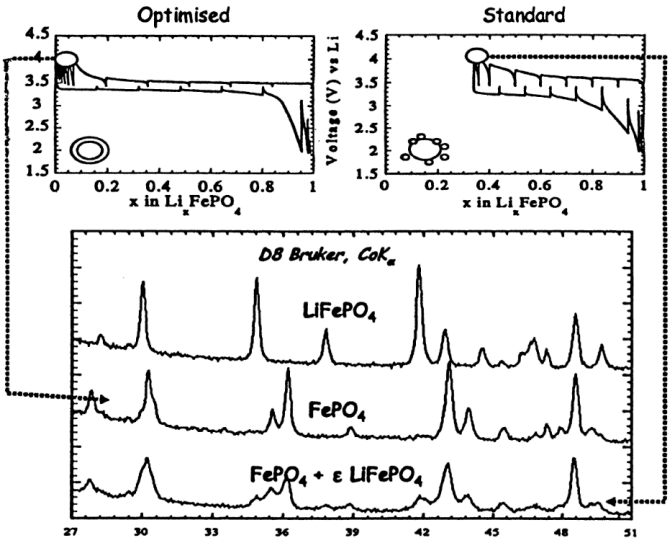

Figure 4.5. In situ phase transformation during Li^+ intercalation/de-intercalation process

The computed lattice constants of $FePO_4$ are: a = 9.81 Å, b = 5.79 Å, c = 4.78 Å and V = 271.5 $Å^3$.(Eventoff, Martin, and Peacor 1972) The lithiation/delithiation process causes a not large volumetric change of 6.8%.

Despite many advantages, the main issues of this system are the capacity loss during cycling, limited rate capability due to low ionic and electronic conductivities compared to the layered and spinel oxide cathodes.

The specific distribution of Li^+ and Fe^{2+} within the octahedral sites within the oxygen hexagonal packing makes FeO_6 octahedral share corners between each other, and impedes the electronic delocalization. The phase-pure $LiFePO_4$ shows an intrinsic electronic conductivity in the order of 10^{-8} S/cm.

By using first-principles methods, Morgan *et al.* found that the Li^+ diffusive motion in $LiFePO_4$ is through 1-D channel (Figure 4.6). Without electrical conductivity limitations, the intrinsic Li^+ diffusivity along [010] is high. This computational prediction was further experimentally confirmed by combining high-T powder neutron diffraction and the maximum entropy method.(Islam et al. 2005, Morgan, Van der Ven, and Ceder 2004, Nishimura et al. 2008, Park et al. 2012)

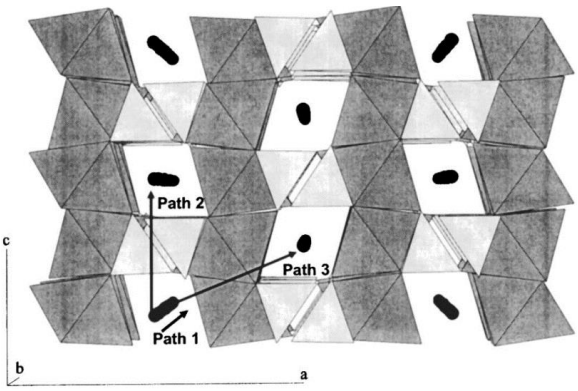

Figure 4.6. The olivine structure: the Fe octahedra are dark gray, the P tetrahedra are light gray, and the Li atoms are black. Black lines show candidate diffusion paths for the Li^+.

A TEM study revealed that the capacity fade from 149 mAh/g to 117 mAh/g after 60 cycles under current density of 30 mA/g at room T are due to the poor electric contact caused by crack formation.(Wang et al. 2005) The formation of cracks should be a result from internal strain at the

sharp interface between two phases $LiFePO_4/FePO_4$ during the lithiation and delithiation process.(Padhi, Nanjundaswamy, and Goodenough 1997)

From synthesis point of view, several strategies have been adopted in order to overcome the rate capability problem and capacity fades during cycling:

- Decreasing the Li^+ diffusion pathway by synthesizing nanoparticles at low T
- Carbon coating to form $LiFePO_4$/C composites
- Doping at Li, Fe, O sites
- Metallic nanoparticle/$LiFePO_4$ composites

4.1.3 A Review of the Synthesis Methods of $LiFePO_4$

Different synthesis methods have been adopted for the $LiFePO_4$ synthesis. The most common methods can be mainly categorized as solid-state sintering, sol-gel method, hydrothermal and solvothermal methods. Other syntheses as emulsion drying, carbothermal reduction, spray pyrolysis, electrospinning and template-assisted methods have also been reported. This section reviews different synthesis methods of $LiFePO_4$ and its related materials as cathodes, the resulted morphologies and their corresponding electrochemical performances.

It was found that the size (and its distribution), morphology and density of the particles play significant roles on the resulted performance. Often, nano-sized particles can provide better cyclability, due to shorter diffusion paths for Li^+, and less stress caused by the volume changes due to higher surface/volume ratio. However, side reactions with electrolytes could often take place. One needs to assess the stability not only at room T, but at high T storage and cycling.

From the point of view of electronic conductivity, the intrinsic $LiFePO_4$ shows an electronic conductivity in the order of 10^{-8} S cm^{-1}. Strategies such as coating particles with

conductive carbons, co-synthesizing the compounds with C, intentional introducing doping elements have been employed to increase the electronic conductivity. Three different doping sites are possible for $LiFePO_4$: Li site, Fe site and PO_4 site. Often, doping at Li site is considered undesirable. It is demonstrated that Mg^{2+} tends to occupy Li^+ site causing diminish in capacity vs. undoped $LiFePO_4$.(Safronov et al. 2012) Very often, doping at Fe^{2+} site could enhance the conductivity, thus the rate capacity of the material. Rarely, the PO_4 site has been reported to be doped by F^-, which also led to a beneficial effect. Detailed examples are enumerated in the following sections.

4.1.3.1 Solid-State Syntheses

Solid sintering often requires high T, long reaction time for the solid state reaction to complete. Regrinding between subsequent firings is also required in order to mix reactants more thoroughly and minimize the secondary phases. Since Padhi *et al.* achieved to reversibly extract 60% of Li^+ from $LiFePO_4$ powders that were synthesized by solid-state sintering at 800 °C,(Padhi, Nanjundaswamy, and Goodenough 1997) Andersson *et al.* studied the structural evolution during the lithium extraction/insertion using X-ray diffraction.(Andersson and Thomas 2001) They pointed out that the first cycle capacity loss can be affected by the following aspects:

(i) The lithium extraction/reinsertion mechanism within a single active $LiFePO_4$ particle

(ii) Electrode morphology, particle size and shape distribution, particle contact, etc.

(iii) The limiting process is a combination of low Li^+ diffusion rate and low electronic conductivity in the $FePO_4$ phase, which prevents the full conversion of $LiFePO_4$ to $FePO_4$, and back again.

Considerable amounts of efforts have focused on optimizing the solid-state reaction parameters, especially the firing T and duration, in order to increase the cathode capacity, enhance the cyclability and improve the electronic/ionic conductivity. A lower firing T tends to give particles with a relatively small size and a rough surface morphology. $LiFePO_4$ prepared at low T of 675 °C showed a higher charge and discharge capacity than prepared at higher T.(Takahashi et al. 2001)

In order to increase the electronic conductivity, extensive efforts have devoted to the synthesis of C/$LiFePO_4$ composites. $LiFePO_4$ was synthesized in the presence of high surface are carbon-black. The full capacity was delivered when discharging the cell at 80 °C and C/10 rate.(Prosini, Zane, and Pasquali 2001) Sugar solution or organic material were also mixed with $LiFePO_4$ powder before firing at 700 °C,(Ravet et al.) and close to theoretical capacity was achieved at high discharge rate. In another study, $LiFePO_4$/C composites were obtained by the pyrolysis of the mixture of agriculture crop and $LiFePO_4$ powder synthesized by solid-state reaction. The pyrolytic carbons treated with poregenic agents gave both high surface area (> 2000 m^2/g) and high porosity.(Jiang 1995) In situ chemical vapor deposition synthesized carbon nanotubes/$LiFePO_4$ was also reported recently.(Sun et al. 2012) The rate capability was shown to be improved by 1.5 and 2.5 times at 1 C and 10 C discharge rates, respectively. Nanosized $LiFePO_4$/C core/shell nanocomposites were synthesized.(Jiang and Jiang 2012) by the formation of polyaniline coated $FePO_4$ followed by the successive calcination of $FePO_4$ in the presence of CH_3COOLi and sucrose. The best sample with 8.6 wt% carbon showed an initial capacity of 160.3 mAh/g at 1 C discharge rate. Even at 10 C rate, the capacity remained 118.3 mAh/g. Solid-state reaction developed graphene-coated $LiFePO_4$ nanoparticles has been reported several time.(Xu et al. 2012) (Y. Wang et al. 2012) The 20 nm nanoparticles were wrapped tightly with a

3D graphene network and gave a 166.6, 90.6 mAh/g at 0.1 C and 10 C, respectively. The capacity decay is < 9 % at 10 C charge/discharge for 300 times. In another very simple process, graphite as carbon source was ball milled with other precursors.(X. L. Yang et al. 2012) After one step heat treatment, graphite and amorphous carbon coated $LiFePO_4$ were obtained. And 98 % of theoretical capacity at 0.2 C and 91.1 mAh/g at 10 C were achieved. Polystyrene nano-sphears were also used as carbon precursors.(S. X. Yu et al. 2012) The resulted composite material showed a 167 and 150 mAh/g at 0.1 and 1 C, respectively.

Additionally, significant amount of works have devoted to increasing the electronic conductivity by doping mechanism. The synthesis of Mn-doped $LiFePO_4$ using solid state reaction was reported.(Yamada and Chung 2001) Various doped LiFePO4/C composites have also been prepared using solid-state synthesis. $LiFe_{1-x}Gd_xPO_4/C$ was reported to reach a discharge capacity of as high as 150.7 mAh/g and 81.3 mAh/g at 0.2 and 10 C, respectively.(Pang et al. 2012)

Another way to enhance the conductivity of $LiFePO_4$ is the preparation of non-stoichiometric material. Ceder *et al.* first reported the ultrafast charging and discharging $LiFe_{0.9}P_{0.95}O_{4-\alpha}$(Kang and Ceder 2009) At 2 C and 20 C discharge rates, a theoretical capacity and 145 mAh/g were achieved; even at 60 C, the capacity was around 100 mAh/g, as shown in Figure 4.7.

The strategy of controlled introduction of impurity has also been adopted to improve the electrochemical performances. When (Fe, P)-deficient in $LiFe_{0.9}P_{0.95}O_{4-\alpha}$, impurities as $Li_4P_2O_7$, Li_3PO_4 take place.(Z. H. Wang et al. 2012) $Li_4P_2O_7$ leads to degradation of cyclability, whereas a small amount of Li_3PO_4 is beneficial for the capacity and rate capability. With the incorporation of Na^+, $Li_4P_2O_7$ phase disappears while Li_3PO_4 content increases. 1% Na-doped $LiFe_{0.9}P_{0.95}O_{4-\alpha}$

exhibits the best electrochemical performance. In another study, a $LiFePO_4/Fe_2P/C$ composite cathode was prepared by solid-state method.(Rahman et al. 2012) The existence of electronically conducting Fe_2P on the surface of $LiFePO_4$ greatly enhances the electrochemical performance, while the carbon containing precursors created a porous structure. The resulting material showed 167 mAh/g at 0.2 C and 131 mAh/g at 10 C rate, with 96% capacity retention after 1000 cycles.

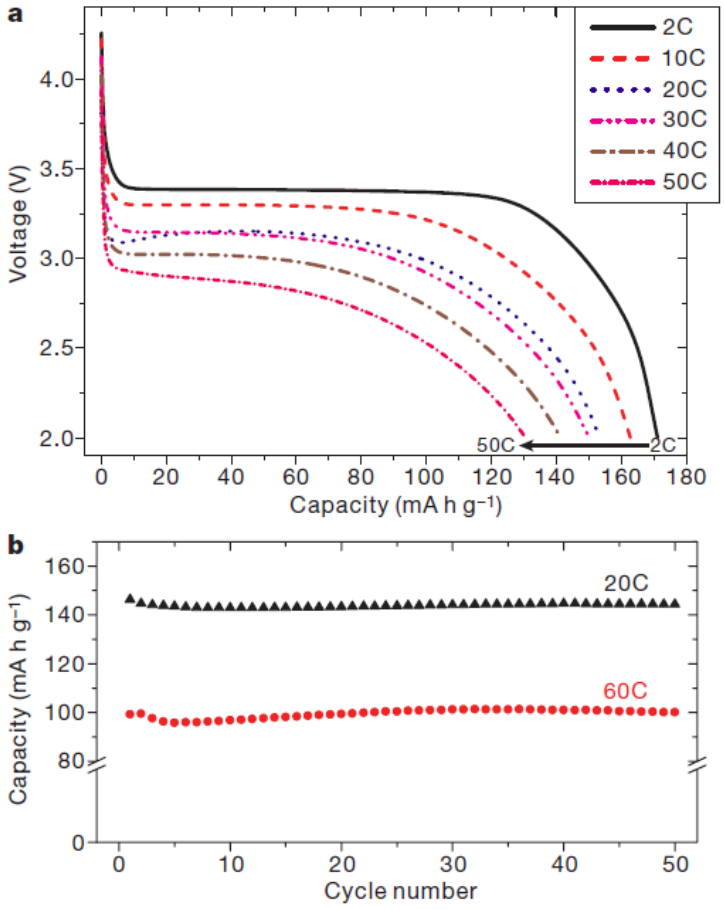

Figure 4.7. Discharge rate capability and capacity retention for $LiFe_{0.9}P_{0.95}O_{4-\alpha}$ synthesized at 600 °C

4.1.3.2 Sol-Gel Syntheses

Sol-gel method stems from the development of an alkoxide precursor that has high solubility in organic solvents and can be easily hydrolyzed by water. The subsequent heat

treatment transforms the hydrolysis product into oxides. Presently, typical sol-gel precursors can be distinguished between polymeric and aqueous precursors.(Ohya 2005) The sol-gel process allows obtaining products with high purity and homogeneity, as the reactants are homogeneously intermixed at molecular level in the precursors. In consequence, the lower firing T and shorter reaction time are needed. Often, products obtained by sol-gel method tend to have smaller particle size, as well.

Polymeric precursor has been extensively used in the syntheses of the $LiFePO_4$/C composites. Sol-gel technique was first implemented to the synthesis of $LiFePO_4$/C composite by Huang *et al.*(Huang, Yin, and Nazar 2001) Stoichiometric amounts of reactants were mixed with a carbon gel formed from the polymerization of resorcinol-formaldehyde. The mixture was treated at 350 °C for 5 h, and then at 700 °C for 10 h under flowing N_2. The resulted cathode material achieves 90 % theoretical capacity at C/2 with very good rate capability and excellent stability. The polymeric $LiFePO_4$ precursor was also prepared by the gelation between ethanol and citric acid, which was also used as carbon precursor.(Ma et al. 2012) After the heat treatment, the resulted $LiFePO_4$/C composite with 4.5 wt % residual carbon presented excellent rate capability and cycling capability.

Aqueous precursor solutions are advantageous because water is inexpensive, nontoxic and less volatile.(Ohya 2005) Especially for applications in an industrial scale, the use of alcohols and other organic solvents in conventional sol-gel method could result in potential danger. A typical aqueous sol-gel synthesis of $LiMn_2O_4$ is shown in Figure 4.8. Often the control of the pH and concentration of the chelating agent are considered of great importance.

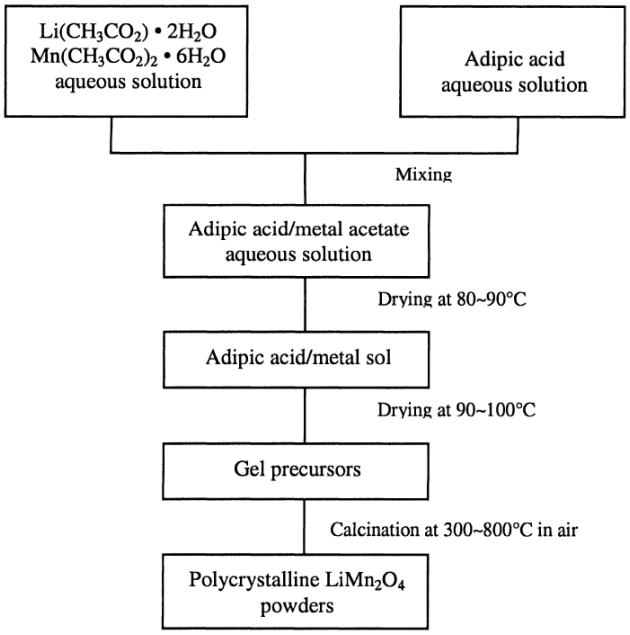

Figure 4.8. A typical aqueous sol-gel synthesis scheme

$LiFePO_4$/C composite material was synthesized, where the citric acid was usually used to chelating metal ions. Appropriate amount of reactants were dissolved in citric acid solution, upon the removal of excess of water, a gel precursor resulted. The calcination of the precursor led to the formation of the phase-pure $LiFePO_4$/C composite. The formation of $LiFePO_4$ formation took place at T as low as 450 °C. However, the sample sintered at 850 °C showed the best electrochemical performance of a 148 mAh/g capacity at 0.025 C discharge rate.(Hsu, Tsay, and Hwang 2004) In another study, porous olivine composites were synthesized in a very similar fashion, except that the organic acid content in the precursor was higher. The resulted porous material had a 140m Ah/g capacity at 0.5 C.(Dominko et al. 2006) A novel 3-D hierarchical $LiFePO_4$/graphene composite cathode with a porous structure can be prepared by heat treat the precursors prepared by the aqueous sol-gel method. The precursor consist in a xerogel of graphene, Li^+, Fe^{3+} and PO_4^{3-}.(J. L. Yang et al. 2012) This composite material gives a capacity of 146 mA/g at 17 mA/g. Cetyltrimethylammonium bromide was also used as a surfactant to

prepare porous $LiFePO_4$/C composite material, which gave a capacity of 152.1 mAh/g at 0.1 C rate.(Liang et al. 2012)

Aqueous sol-gel technique can also be used for preparing doped $LiFePO_4$ cathode materials. Successful preparation of phase-pure $LiM_xFe_{1-x}PO_4$ compounds, M=Mg^{2+}, Ti^{4+}, Zr^{4+} were reported.(Wang et al. 2006) Both polyacrylic acid and citric acid were used as the complexing agents for the formation of the gel. For Ti^{4+} and Zr^{4+} doping, they intended to substitute at Fe^{2+} sites, whereas for Mg^{2+} doping, they intended to substitute at Li^{+} site. Slightly reducing atmosphere was employed during the sintering process. The undoped $LiFePO_4$ and $LiTi_{0.01}Fe_{0.99}PO_4$ had capacities of 160-165 mAh/g at C/8 rate. Other doped compounds tended to have lower capacities.(Safronov et al. 2012) In another study, Mg^{2+} and Co^{2+}-doped $LiFePO_4$ was synthesized using sol-gel method. Mg^{2+} increased the resistivity significantly, while Co^{2+} doping favors the electronic conductivity.

Another unique way to improve the conductivity of $LiFePO_4$ was proven to be the dispersion of metal at a very low concentration, i.e. 1% of Ag or Cu, in $LiFePO_4$ synthesized by sol-gel method.(Croce et al. 2002) The crystallinity structure was not altered, but capacity and cycle life were improved considerably.

4.1.3.3 Solution Precipitation Method

$LiFePO_4$ can also be prepared by a heat treatment of the precursor, which is prepared by aqueous solution precipitation. $FePO_4$ synthesized by coprecipitation method was chemically lithiated to form amorphous $LiFePO_4$. With appropriate post heat treatment, this material could achieve full theoretical capacity when cycled as the C/10 rate.(Prosini et al. 2002)

Using solution precipitation method, $Li_{1-x}K_xPO_4/C$ (x=0-0.07) was synthesized.(Fang et al. 2012) At 0.1 C discharge rate, the capacity is about 153.7 mAh/g due to the replacement of the Li^+ by K^+. However, the slightly enlarged lattice constants of the K-doped material provide an increase of 11 % in the capacity than undoped material at 1 C. It also shows good cycle retention at 11 C discharge rate.

4.1.3.4 Hydrothermal Method

Another interesting method is the hydrothermal synthesis, where the solvent is aqueous solution. The controlling of the pH of the medium, T, reactant concentration, surfactant, and reaction time is critical. Typically, after the formation of the desired $LiFePO_4$ phase at relatively low T, annealing process is followed to improve the crystallinity. Hydrothermal technique was first implemented to the synthesis of $LiFePO_4$ by Yang *et al.* And 80 % of theoretical capacity could be achieved.(Yang, Zavalij, and Whittingham 2001)

Surfactant assisted hydrothermal synthesis could result $LiFePO_4$ of different morphologies. A surfactant, dodecylbenzenesulfonic acid sodium, was proven to have significant impact on the resulted $LiFePO_4$ geometry.(Chen et al. 2012) $LiFePO_4$ with hierarchical spindles nanostructures showed best rate performance and cycle stability than irregular materials. In another study, a simple sodium dodecylbenzenesulfonate mediated hydrothermal method allows the synthesis of $LiFePO_4$ with different morphologies.(Pei et al. 2012) Nanoparticles of 200 nm, nanorods of 90 nm in diameter along the b-axis and 200 nm - 1 μm in length, and nanoplates of 20 nm of thickness along the b-axis and 50 nm in width showed 145.3, 149.0 and 162.9 mAh/g at 0.1 C rate. At 10 C rate, the capacities for these materials were 33.9, 61.3 and 107.9 mAh/g, respectively. Porous platelike $LiFePO_4/C$ composite material was also synthesized using

hydrothermal process, where the carbon precursors were ascorbic acid and glucose or citric acid.(W. Y. Yu et al. 2012) The composite material using glucose shows a slightly better rate capacity of 88 mAh/g at 5 C than using citric acid. At 0.1 C the capacities of both composite materials are about the same, 153 mAh/g.

Controlled doping can also be achieved by hydrothermal method. The synthesis of $LiFe_{1-x}Mn_xPO_4/C$, with x=1/4 to 3/4 by hydrothermal method was reported.(Zhao et al. Hydrothermal synthesis and properties of manganese-doped lifepo4 2012) The $LiFe_{3/4}Mn_{1/4}PO_4$ exhibited the highest capacity, 164 mAh/g at 0.1 C. Although the increasing doping concentration enhanced the electronic conductivity, the capacity resulted lower. $LiFe_{3/4}Co_{1/4}PO_4/C$ synthesized via hydrothermal route produced a capacity of 170 mAh/g at 0.1 C.(Zhao et al. Synthesis and properties of co-doped lifepo4 as cathode material via a hydrothermal route for lithium-ion batteries 2012) In addition, it can achieve a higher discharge plateau (≈ 3.5 V) than does pure $LiFePO_4$ (≈ 3.4 V).

4.1.3.5 Solvothermal Method

Solvothermal method works in a very similar way as the hydrothermal technique, except that the aqueous solvent is replaced by non-aqueous solvent(s).

$LiFePO_4/C$ composite has been prepared using alcohol as the reaction media. Diethylene glycol was used as the solvent, Ketjen Black as the carbon precursor, with other required reactants, the $LiFePO_4/C$ composite material was synthesized at 170 °C.(Lim et al. 2012) The as synthesized nanocomposite material showed a capacity of 160 mAh/g at 0.1 mA/cm^2 when the initial carbon addition was 10 wt%.

By controlling the solvent/s and surfactants, a variety of nanostructures can be achieved. Highly uniform $LiFePO_4$ nanoplates (20 - 30 nm thick, 120 - 160 nm wide and 120 - 250 nm long) with large exposure of (100) face was successfully prepared in a mixture of water and dimethyl sulfoxide.(Ju et al. 2012) Vittal *et al.* synthesized $LiFePO_4$ nanoplates with large exposure of (010) faces using ethylene glycol as solvent.(Saravanan et al. 2010, Saravanan et al. 2009) The 30-40nm thickness favors the short diffusion lengths of Li^+ ions. Kim *et al.* achieved the nanoplates, which grew preferentially along [100] and [010] directions, by low T polyol solvothermal method.(Lim et al. Plate-type lifepo4 nanocrystals by low temperature polyol-assisted solvothermal reaction and its electrochemical properties 2011, Lim et al. One-pot synthesis of multi-morphous lifepo4 nanoparticles in polyol medium 2011) In terms of the electrochemical performance, large exposure of (100) or (010) face are more favorable morphologies. Only very slight advantage was found for nanostructure with large exposure of (010) at discharge rate higher than 5 C. Such result is contradicting with the 1-D Li^+diffusion restriction.

Other interesting morphologies can also be prepared by solvothermal method. Cage-like $LiFePO_4$/C microspheres were prepared at 185 °C using ethylene glycol as the solvent.(Deng et al. Synthesis of cage-like lifepo4/c microspheres for high performance lithium ion batteries 2012) Capacities of 160 mAh/g at 0.1 C over 300 cycles and 120 mAh/g at 10 C can be achieved with this material. Microsized Nest-like $LiFePO_4$/C composite material was synthesized using inexpensive and stable Fe^{3+} as the iron precursor and ethylene glycol as the solvent.(Deng et al. Nest-like lifepo4/c architectures for high performance lithium ion batteries 2012) Followed by heat treatment in Ar/H_2 atmosphere, the capacity can maintain 159 mAh/g at 0.1 C and 120 mAh/g at 10 C.

4.1.3.6 Microwave-Assisted Syntheses

Recently, the microwave-assisted syntheses have been widely reported in the syntheses of $LiFePO_4$ material and related composites. The energy efficient microwave heating has been used for both high T heating (solid-state reactions, calcination of precursors made by sol-gel processing) and low T heat treating (hydrothermal and solvothermal syntheses).

4.1.3.6.1 Microwave-assisted high temperature syntheses

In 2003, the first study of the implementation of microwave in the solid-state synthesis of $LiFePO_4$ was reported by Higuchi *et al.*(Higuchi et al. 2003) The only controllable parameter was the duration of microwave irradiation. The electrochemical performance was not ideal; at room T, the capacity was about 100 mAh/g at 10 mA/g.

In same year (2003), Park *et al.* reported the synthesis of $LiFePO_4$/C by co-precipitation and microwave heating.(Park et al. 2003) After the precursor being synthesized by conventional aqueous co-precipitation method, the carbon black was mixed with the precursor. On one side, the carbon black was used to enhance the electronic conductivity and reduce the particle size. On the other side, carbon black is known to be an extremely good microwave susceptor. It is reported that non-metallic compounds such as Co_2O_3, NiO, and activated carbon can reach T higher than 1000 °C in 1 min.(Gallis and Landry 2001) $LiFePO_4$/C obtained after 4 min-microwave heating showed reasonably good capacities of 151 and 134 mAh/g at C/10 and 1 C, respectively. With the addition of citric acid and multi-walled carbon nanotubes (MWCNT) into the other essential reactants, the 10 min microwave-assisted solid-state reaction led to phase-pure nano-sized $LiFePO_4$/MWCNT with a 145 mAh/g discharge capacity at C/2. Good capacity retention was proven, too.(Wang et al. Nano-lifepo4/mwcnt cathode materials prepared by room-

temperature solid-state reaction and microwave heating 2007, Preparation and characterization of nano-sized lifepo4 by low heating solid-state coordination method and microwave heating 2007) Several other similar works that vary the chemical reactants, additives such as carbon precursors, microwave reactors, and heat treating durations were reported.(Beninati, Damen, and Mastragostino 2008, Guo, Zhan, and Zhou 2009, Uematsu et al. 2007, Zou, Zhang, and Shen 2010) The best results of microwave-assisted solid-state synthesis of $LiFePO_4$/C composite achieved a capacity of 165 mAh/g at C/10, because of the presence of Fe_2P.(Song et al. 2007) Note, the Fe_2P, restrained below a critical concentration, enhances the conductivity. Higher concentration of Fe_2P can block the Li^+ diffusion pathway.(Song et al. 2008)

Mo-doped $LiFePO_4$/graphitic C composite was synthesized via microwave-assisted solid-state reaction.(D. Li et al. 2012) The combined effects of Mo-doping and the 3-D C network dramatically enhanced the electrochemical performance. It delivered a capacity of 162 mAh/g at 0.5 C.

Polyethylene glycol was used as carbon precursor in a microwave-assisted sol-gel synthesis of $LiFePO_4$/C.(Zhang et al. 2009) The best sample of the obtained nanocomposites showed a capacity of 152 mAh/g at 0.2 C.

4.1.3.6.2 Microwave-assisted low temperature syntheses

Microwave is also found to be very useful to fulfill the need of relatively low T heat treatment in solvothermal and hydrothermal syntheses.

Manthiram's group replaced conventional heating in the solvothermal and hydrothermal syntheses of $LiFePO_4$/C composites by microwave irradiation.(Murugan et al. 2009, Murugan, Muraliganth, and Manthiram Comparison of microwave assisted solvothermal and hydrothermal

syntheses of lifepo4/c nanocomposite cathodes for lithium ion batteries 2008) $LiFePO_4$/C nanoparticles resulted from microwave-assisted solvothermal method showed better discharge capacity (162 mAh/g) than materials made by hydrothermal reaction because of smaller particle size. Later this group reported the $LiFePO_4$/MWCNT nanocomposite synthesis, and achieved 161 mAh/g at 0.1 C rate;(Muraliganth, Murugan, and Manthiram 2008) The same group also reported that the $LiFePO_4$ coated with conducting *p*-toluene sulfonic acid (*p*-TSA) doped poly(3,4-ethylenedioxythiophene) (PEDOT) showed a discharge capacity as high as 166 mAh/g at C/15 rate.(Murugan, Muraliganth, and Manthiram Rapid microwave-solvothermal synthesis of phospho-olivine nanorods and their coating with a mixed conducting polymer for lithium ion batteries 2008, 2009)

Niederberger's group has demonstrated that microwave-assisted solvothermal syntheses could be very efficient for the synthesis of inorganic nanoparticles.(Bilecka, Djerdj, and Niederberger 2008, Bilecka, Elser, and Niederberger 2009) They carried out an extensive works related to $LiFePO_4$ syntheses. Phase pure $LiFePO_4$ were synthesized in 2.45 GHz microwave reactor using benzyl alcohol as the solvent at 180 °C for 3 min.(Bilecka et al. 2009) A specific capacity of 150 mAh/g was obtained at 2C. In another study, microwave-assisted solution synthesis produced highly crystalline materials at 180 °C.(Bilecka et al. 2011) With the introduction of the doping elements (Ni, Zn, Al, Mn, Ti) during the synthesis, the initial specific capacity became 168 mAh/g with 97 % capacity retention after 300 cycles. Even at discharge rate of 8C the capacity still remained 152 mAh/g. Recently, $LiFePO_4$ sticks with [001] preferential growth direction were synthesized by microwave-assisted solvothermal method at 195 °C for 30 min.(Carriazo et al. 2012) The resulted materials without carbon coating or further annealing show a capacity of 56% of the theoretical capacity.

Microwave-assisted hydrothermal synthesis of $LiMn_{0.08}Fe_{0.92}PO_4$ was also reported, which was carried out at 180 °C.(Niu, Qi, and Wang 2011) The as-synthesized material was further sintered at 700 °C for 2 h with the addition of glucose. However, the electrochemical performance was not ideal.

4.1.3.7 Other Methods

Other reported synthesis methods for $LiFePO_4$ and the related materials are emulsion drying, and carbothermal reduction, spray pyrolysis, electrospinning and template-assisted methods.

Emulsion drying method was implemented by Lin *et al.* to synthesize the precursor of $LiFePO_4$/C.(Lin and Chen 2012) A water-in-oil type microemulsion was prepared from aqueous solution, cyclohexane, poly(oxyethlene) nonylphenyl ether (NP-x series) or poly(oxyethlene) octyl phenyl ether (OP series) surfactants and n-butanol. The precursor powders were obtained after drying at 180 °C. Heat treatment was followed to yield $LiFePO_4$/C composites. Particles sizes are closely related to the surfactants' hindrance capability. Smaller particle size with larger surface area provides better capacity. The best sample presented a 105 mAh/g capacity at 2C, and 157 mAh/g at 0.1 C.

Carbothermal reduction method was used to synthesize $LiFe_{0.9}Mg_{0.1}PO_4$, the resulted material found to have excellent ionic reversibility and showed a capacity of over 150 mAh/g.(Barker, Saidi, and Swoyer 2003) $LiFePO_4$/C sphere-like nanoparticles with carbon film on the surface was also synthesized by carbothermal reduction, where the iron precursor was $FePO_4$.(Kong et al. 2012) The sphere-like nanoparticles delivered capacities of 161 and 122 mAh/g at 0.2 C and 5 C rates, respectively. F-doped $LiFePO_4$/C composite was synthesized by

carbothermal reduction process, where the F precursor was NH_4F, and starch as the reducing agent.(Pan, Lin, and Zhou 2012) $LiFe(PO_4)_{1-x}F_{3-x}/C$ with x=0.05 gave capacities of 156.1 and 119.1 mAh/g at 0.1 C and 5 C, respectively.

$LiFePO_4/C$ nanoparticles can also be synthesized using a combination of electrospinning and annealing.(M. J. Li et al. 2012) Polyvinylpyrrolidone (PVP) was used as the fiber-forming agent in the electrospinning method. After heat treatment, the resulted nanoparticles coated and connected by interlaced carbons in the size range 50-80 nm showed discharge capacities of 163.5 mAh/g and 110.7 mAh/g at 0.1 C and 10 C, respectively.

A scalable flame spray pyrolysis was implemented to the synthesis of $LiFePO_4/C$ nanoparticle, where amorphous $FePO_4$ was used as precursor, followed by the solid-state reaction with Li_2CO_3 and glucose at 600 °C for 16 h to obtain $LiFePO_4/C$ composite material. The discharge capacity is around 142 mAh/g at 0.05 C.(Hamid et al. 2012) Wang, and *et al.* reported the syntheses of $LiFePO_4$ and $Li_{1-x}Mg_xFePO_4$ by spray pyrolysis followed by high T sintering,(Wang et al. 2004) and a capacity of only 100 mAh/g was achieved.

Several template-assisted syntheses have been reported. Hydrophilic surfactant (Brij 78) modified polystyrene template assisted synthesis of highly ordered $LiFePO_4$ cathode material was reported.(Yim et al. 2012) The final cathode material containing 23-28 wt % showed an initial capacity of 158 mAh/g at high discharge rates (2-5 C). Mesoporous $LiFePO_4$ resembling the structure of Swiss-cheese was prepared using hydrophilic carbon nanoparticles (20 - 30 nm) as the template.(Ren and Bruce 2012) It demonstrated 160 mAh/g and 105 mAh/g discharge capacities, at the rate of C/10 and 5C, respectively.

4.1.4 Pechini's Method

Sol-gel method is an attractive way for synthesis of high phase purity multicomponent ceramics and glasses for several main advantages: relatively low synthesis T, high degree of purity of multicomponent thin film formability, thin films with nanostructural control or mesoporous structures formability. Traditionally, metal alkoxides have been employed in sol-gel process, which readily undergo hydrolysis and condensation to form nanoscale oxide or hydroxide particles.

Metal salts are better alternatives to alkoxides for being inexpensive, easy to handle, and soluble in many kinds of organic solvents in which metal complexes are formed. Note, if metal salts are just dissolved in solvents without being chelated, they recrystallize upon solvent evaporation. Also, it is important to stabilize the metal ions in solutions without coordination by inorganic anions such as Cl^-, NO_3^-.

Pechini's method (PC) is an effective method for preparing metal oxide powders. Polymeric precursors are formed by polymerization of metal citrates with ethylene glycol at low T. This method allows the metal cations to be mixed at a molecular level. Consequently, several advantages are offered: low cost, high phase purity, homogeneous compositions, and relatively low heat-treatment T. A typical example of the synthesis procedure of polymeric precursor by Pechini's method is illustrated in Figure 4.9.(Chai et al. 2002)

Typically, three steps are involved in the formation of the gel precursor:

(i) Metal chelation: suitable metal salts are introduced into the ethylene glycol (EG) containing dissolved citric acid (CA), which is usually in a large excess to form metal citrate.

(ii) Aqueous solvent evaporation (if applicable) and gel formation: the T for the formation of polyester is speed up at 80-120 °C

(iii) Removal of excess of ethylene glycol solvent at higher T

(iv) The obtained relatively hard polymeric precursor should be heat treated at 450-600 °C to oxidize the organic compounds, and form desired ceramic material.

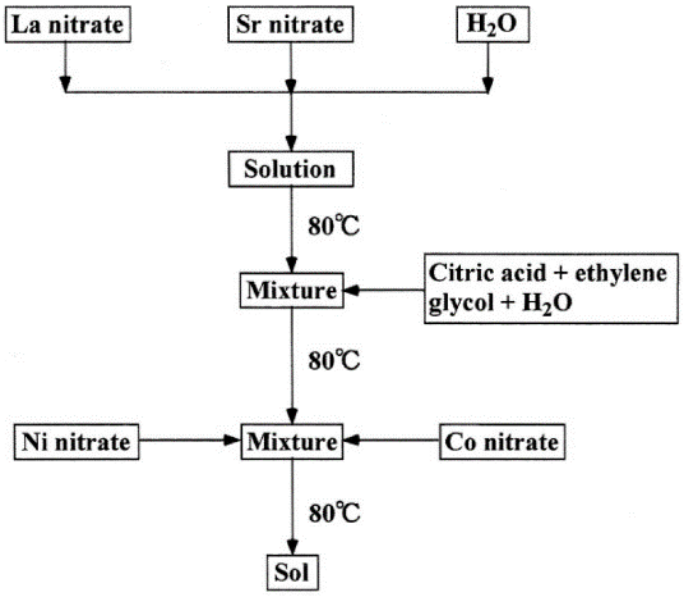

Figure 4.9. Synthesis of the polymeric precursor of $La_{0.8}Sr_{0.2}Co_{0.5}O_{3-x}$ by Pechini's method

The range of CA concentrations in the EG from 50-60 mol% was found to be the most appropriate for the complex oxide powder preparation since it provides the maximum viscosity of the obtained gel, as shown in Figure 4.10. Strong foaming also prevents segregation during thermal decomposition of the polymer.

Often, an excess ratio of CA to metal ions keeps around 3-5. Another major problem is that precipitation could occur during solvent evaporation. In order to avoid this problem, the optimal pH value of the initial solution is critical to the chemical homogeneity. $NH_{3(aq)}$ or

ethylenediamine can be used to adjust the pH to 5.5-7.0 in order to promote the formation of more stable alkaline-earth citrate complex and improves the gel quality.

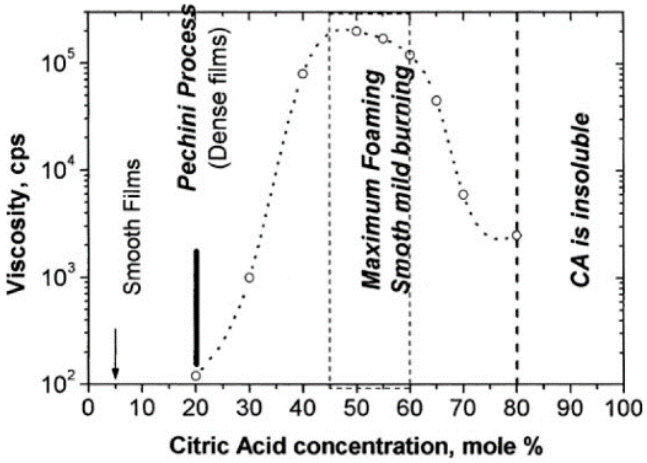

Figure 4.10. Gel viscosity versus citric acid/ethylene glycol ratio

Other chelating agents have also been used in modified Pechini's methods for preparation of metal oxide. Citric acid was replaced by ethylene diamine tetraacetic acid (EDTA), which has a stronger chelating capability to metal ions, and therefore, the uniformity of the metal ions in the solution is improved.

The success of the Pechini method stems from the homogeneity of metal cations in the precursor and low-T pyrolysis due to shorter diffusion paths of the reactants compared to those in a typical solid-state reactions of mixed oxide salts. As a result, phase-pure multi-component oxides can form directly upon pyrolysis of the polymeric precursor, and often at T that are significantly below any liquid phase formation T. Additional attributes of the Pechini method are: (1) one can uniformly distribute small amounts of multivalent dopants into a system; (2) due to the slow grain growth at low processing T, as well as the gas evolution and consequent polymer foaming during pyrolysis, ultrafine powders with high surface areas are achievable. To

date, numerous literature reports on the use of the Pechini method and its modified versions are abundant;(Hiromitsu 2005) some examples are listed below:

(i) Marcilly and co-workers (1970) demonstrated the syntheses of various multi-component oxide materials by a solution method, which uses a hydroxycarboxylic acid such as citric acid to trap or chelate metal ions, to form a glass-like gel upon the evaporation of water.(Marcilly, Courty, and Delmon 1970) This method is known as "aqueous citrate gel" or "amorphous metal complex" method. Upon pyrolysis of the gel, oxides form. Such a method has been used to synthesize lead-free piezoelectrics ($xBaTiO_3 \cdot (1\text{-}x)Bi_{0.5}Na_{0.5}TiO_3$),(Kozuka and MacKenzie 1991, West and Payne 2003) ferrites,(Sileo, Rotelo, and Jacobo 2002) perovskite manganites,(Duprat et al. 1994) and high-T_c superconductors,(Mazaki, Kakihana, and Yasuoka 1991, Sato et al. 2002) and ferromagnetic Ru-Sr-Gd-Ce-Cu-O superconductors.(Petrykin et al. 2002)

(ii) Many studies report the synthesis of multicomponent ceramic oxides by using various chelating agents. In 1996, Mao *et al.* used ethylenendiaminetetracetic acid (EDTA) for the synthesis of superconducting Bi-2223 oxide compound by the polymeric sol-gel technique;(Mao et al. 1996) the EDTA chelator provided better stability of complexes, and allowed the fabrication of tapes with J_c reaching $4.1 \cdot 10^4 A/cm^2$. In 1998, You *et al.* studied the effect of various chelators such as oxalic, succinic, 1,6-adipic, malic, tartaric, and citric acids for the synthesis of superconducting $La_3CaBa_3Cu_7O_y$ powder by the PC route.(You et al. 1998) They found that the influence on standard deviation for cation concentration, residual carbon content, and $1/T_c$ were follows: citric < tartaric < adipic < malic < oxalic = succinic acid. Based on the number of functional groups of the chelators and the resultant polymers, these

results were explainable; acids with two functional groups such as succinic and oxalic acid formed linear polymers and acids with four functional groups such as tartaric and citric acids formed 3D-polymers. The latter efficiently trapped cations, and led to improved homogeneity and superior properties.

(iii) In a number of studies, with EDTA or citric acid-chelated metal ions, the use of hydrogen peroxide or azobisisobutyronitrile along with monomeric acrylamide and acrylic acid was reported to initiate free radical polymerization for the synthesis of $YBa_2Cu_3O_{7-x}$,(Gotor et al. 1993) $YBa_2Cu_3O_7$,(Rao et al. 1995) and Bi(Pb)-Sr-Ca-Cu-O system.(Mani et al. 1992) The advantages of this route over the traditional Pechini method are that the polymerization by free radical is a low-T and irreversible process. Moreover, it uses inexpensive water as the solvent, and since the complex formation and gelation are independent steps, one can control of these steps separately.

(iv) Water-soluble polymers such as polyvinyl alcohol (PVA), polyethyleneimine (PEI), polyethylene glycol (PEG) can also chelate metallic ions to form gels. The concentration at which gelation takes place depends on the nature and the length of the polymer chain. T. Gülgün *et al.* showed that dissolved cations promote gelation through cross-linking of the polymer.(Gulgun, Popoola, and Kriven 1995) To achieve stronger chelation and highly homogeneous gels, Mandal and Ram added sucrose with PVA for the synthesis of PZT nanoparticles. Note, one shortcoming of the usage of water-soluble polymer is that since the –OH groups of the polymer cannot strongly chelate alkaline and alkaline earth cations, they eventually tend to coordinatate with nitrates or acetates during gelation. Additional examples include the synthesis of various aluminates, yttrium-aluminium garnet (YAG), and components of

Portland.(Gulgun, Nguyen, and Kriven 1999, Lee, Benson, and Kriven 1999, Lee and Kriven 1998, Nguyen, Lee, and Kriven 1999)

(v) Several researchers have used the PC method to synthesize electrode materials. In 1999, Ogihara and co-workers prepared $LiMnO_2$ samples via PC method using ethylene glycol and malic acid.(Ogihara, Azuma, and Katayama 1999) In 2002, Guo *et al.* synthesized the $LiMn_{1-x}Cr_xO_2$ compounds with $NaFeO_2$ layer-type crystal structure via the original Pechini method.(Guo et al. 2002) Compared to the solid-state reaction, the compound made by the Pechini method yielded higher specific capacity for both charge and discharge, and the rate capability also improved due to the smaller particle size and better homogeneity. Wu (2007) successfully obtained the orthorhombic $LiMnO_2$ powders using Pechini method.(Wu and Yu 2007) The powders showed promising cycling performance with a maximum discharge capacity of 158 mAh/g, and a capacity loss of 3% between 20^{th} and 80^{th} cycles at 30 °C. Several reports describe the synthesis of $LiFePO_4$ by the existing PC method. In 2004, Hsu et al. synthesized $LiFePO_4$ by the "aqueous citrate gel" method. They demonstrated that at a discharge rate of 1/40 C, the capacity of the best sample, calcined at 850 °C, was 148 mAh/g; but lower than the theoretical capacity of 170 mAh/g.(Hsu, Tsay, and Hwang 2004) In 2010, using ethanol as the solvent and adipic acid as the chelating agent, Lee synthesized $LiFePO_4$. The final product however, obtained at T below 650 °C, had impurities; perhaps $Li_3Fe_2(PO_4)_3$. Overall, for the $LiFePO_4$ case, the inhomogeneous distribution of cations and anions in the polymeric matrix, as well as undesirable precipitates of metal phosphate salts lead to the low capacity and need for high processing T.

In summary, although the PC method and its variations have been extensively used, critical issues that need to address are:

(i) Avert the formation of precipitates in the solution, prior and during gelation.

(ii) Prevent the change of oxidation state of a cation by the redox reaction between the organic chelating compounds and metal ions.

(iii) Avert evaporation or decomposition of one of the reactants of the inorganic compound, as well as the formation of stable and inert compounds prior to the pyrolysis of the polymer precursors.

In the specific case for the synthesis of $LiFePO_4$, maintaining the oxidation state of Fe^{2+} is crucial. Without extra precaution, Fe^{2+} can readily oxidizes to Fe^{3+} in solution even at room T. Additionally, instead of being a simple oxide in which the anion is oxygen, the anion in $LiFePO_4$ is a phosphate (PO_4^{3-}), a.k.a. poly-anion or oxo-anion. Unlike the metal oxide where the oxygen source is from the atmosphere, there is a need for introducing the PO_4^{3-} group as a precursor. Typically, the organic polyacids chelate the cations and homogeneously distributes the cations in the polymeric matrix. However, there are no literature reports of a method for distributing the oxo-anions, e.g. PO_4^{3-} or SO_4^{2-}, homogeneously in the polymer matrix. Indeed, the original patent of the Pechini method[6] clearly states that oxo-anionic compounds such as oxalates, tartartes, sulphates, etc., that form insoluble salts in the presence of alkaline earth cations, are not used in the PC method.

Obviously, the limitation of the Pechini method, in terms of incorporating oxo-anions that readily and selectively form undesirable precipitates with metal ions, is clear. Therefore, it is necessary to make some modification of the Pechini method other than just using an inert gas

atmosphere to control the cation oxidation states. In addition, the prevention of undesired precipitates is crucial in both the polymeric gel formation step and the decomposition step.

4.1.5 Microwave-Assisted Heating

Microwaves are electromagnetic (EM) waves in the frequency band from 300 MHz to 300 GHz, and its industrial use is set aside at frequencies of 915 MHz, 2.45 GHz (most common), 5.8 GHz, and 24.124 GHz. It is a powerful, economical, environmentally friendly, and significantly novel tool to synthesize and process ceramic,(Sutton 1989, Whittaker and Mingos 1995) metallic (Gupta and Leong 2007, Roy et al. 1999, Whittaker and Mingos 1995) and polymeric(Chen, McGrath, and Ward 1989, Lagarkov, Matitson, and Sarychev 1992, Levan and Gourdenne 1987) materials that may not be amenable to conventional means of processing or to vastly improve the performance characteristics of existing materials through nanostructure and nanochemistry control. For example, the application of microwaves to the synthesis of oxide and non-oxide ceramics, and the direct consequence of volumetric and selective heating conditions, has offered unique benefits such as producing nanomaterials with controlled compositions and structures. Additionally, a number of fundamental synthesis reactions and processes,(Bullard and Lynch 1992, Kladnig and Horn 1990, Komarneni et al. 1988, Kozuka and MacKenzie 1991, Larhed, Moberg, and Hallberg 2002, Mingos and Baghurst 1992, Vollath and Sickafus 1993, Willert-Porada et al. 1992) have exhibited increased yields and enhanced kinetics over conventional techniques. These microwave processes have not yet been scaled to production, but numerous advantages have been realized at the laboratory scale. A few reports warrant brief mention elaboration.

Vollath *et al.*(Vollath and Sickafus 1993) decomposed, in microwave-generated plasma, atomized droplets of aqueous solutions containing the nitrates of Zr and Al, yielding spherical and very fine crystalline particles of γ-Al_2O_3 and ZrO_2 (100-500 nm in dia). The simultaneous atomization of nitrate salts of Zr, Al, and Y produced a solid solution of ZrO_2, Al_2O_3, and Y_2O_3; note, a process efficiency to transfer thermal energy to the chemical reactions was 80%. One can avoid the large volume of solvent removal that is typical during solvent decomposition/evaporation process in conventional processing. Willert-Porada *et al.* reported single-phase Al_2O_3 and ZrO_2 powders from Al-triisopropanolate or Zr-tetrapropylate (ZTP), and mixed-oxide powders (e.g., Al_2O_3 + ZrO_2, Al_2O_3 + CuO or $CuAlO_2$, $MgAl_2O_4$) from appropriate precursor mixtures coupled with pyrolysis. They also produced a wide variety of fine ceramic powders by solvent-free microwave pyrolysis of precursors (i.e., alcoholates and acetylacetonates of Al, Zr, Ti, Si, Cu, and Mg) that readily absorb microwaves).(Willert-Porada et al. 1992)

One may control the powder characteristics through chemical modification of reaction mixtures, use of specially designed microwave applicators, and control over certain decomposition profiles. Moreover, composite powders were also prepared by coating inert particles (e.g., Al_2O_3, BN, and SiC) or reactive powders (e.g., carbon) with a thin layer of Zr-tetrapropylate or other precursors to form carbide/oxide composite powders. Interestingly, the enhanced decomposition occurred at lower temperatures compared to conventional thermal processing. Clearly, use of microwave heating of metalorganic precursors, coupled with the use of microwave couplers, gives rise to a wide selection of single or multiple phase powders with high surface areas (10-700 m^2/g).

In addition to microwave-derived powders, the introduction of microwaves in organic synthesis chemistry in 1986 has offered an interesting alternative for providing thermal energy to chemical reactions, as well as many other advantages. Since polar solvents couple readily with microwaves, an efficient in-situ heating of chemical reactants can result compared to conventional heating, where one relies on conduction and convection. Consequently, there is a reduced tendency for seed formation (i.e., the initiation of boiling) and superheating is possible.(Larhed, Moberg, and Hallberg 2002) In addition, since microwaves can interact with a polar transition state, the product formed via a more polar transition state will be favored, and one may alter the regioselectivity of a given compound under a microwave field.(Langa et al. 2000) In comparison with conventional heating, microwaves have also enabled the synthesis of compounds with much better stereo-selectivity control as in the case of an esterification reaction of candida antartica lipase on acrylic resin (novozym). The plausible explanations are efficient removal of low molecular weight alcohols or water, and the entropic effect due to dipolar polarization.(Loupy et al. 1998) Recently, in 2009, Kiss reported a novel synthesis of phosphinates; 1-hydroxy-3-phospholene oxides and phenyl-H-phosphinic were converted to the corresponding phosphinic esters by reaction with a variety of simple alcohols under microwave irradiation. Note, in some cases, esterification did not occur under conventional heating, and in others, were highly incomplete.(Kiss et al. 2009) Overall, the pros of microwave heating over conventional heating during wet chemical synthesis fall under the following categories:

- Acceleration of reaction rate,
- Milder reaction conditions,
- Higher chemical yield,

- Lower energy usage, and
- Regioselective

Based on the preceding analysis, the modification of the PC method coupled with microwave heat treatment at various steps in the synthesis cycle (described below) to synthesize nanomaterials of alkali-based oxide anodes and cathodes, as well as alkali based oxo-anion cathodes is warranted. Although emphasis here is given on electrode materials for batteries, one can readily extend this general approach to synthesize a whole host of single and multi-component oxides for various applications in the electronics, optics, electromechanical, chemical and biochemical sensing, energy, and magnetic sectors.

4.2 Microwave-Assisted Synthesis and Characterization of $LiFePO_4$ as a Cathode Material for Li/Li-ion Batteries

4.2.1 Research Objective

The motivation of the current study is to considerably cut down on the thermal budget and the processing time of the $LiFePO_4$ synthesis, in which high T sintering or heat treatment (≥700 °C) is usually used for a prolonged period of time (8-20 hours). The central theme of this project is to prove the feasibility of obtaining the mesoporous phase-pure $LiFePO_4$ nanostructures using sol-gel method (modified Pechini's method) for the synthesis of the polymeric precursor, followed by microwave heat treatment at a relatively low T for a very short period of time (10-15 min). The resulting $LiFePO_4$ will be compared to the materials synthesized by microwave-assisted solid-state synthesis.

4.2.2 Research Methodology

4.2.2.1 Microwave-Assisted Modified Pechini's Method for the Synthesis of Mesoporous Phase-Pure $LiFePO_4$ and its Characterization

4.2.2.1.1 Synthesis of mesoporous phase-pure $LiFePO_4$

In traditional Pechini's method, only the metal cations need to be stabilized by complexing with the polyester-based matrix for obtaining high quality oxides or carbonates. In the synthesis of $LiFePO_4$, not only the metal cations but also PO_4^{3-} needs to be stabilized.

The modification comparing to the original Pechini's method is the stabilization of the polyanions, e.g., PO_4^{3-} will be incorporated into the ethylene glycol via the formation of the phosphate esters. Li^+ and Fe^{2+} will be stabilized by the excess of citric acid.

Furthermore, aqueous solution is usually used in traditional Pechini's method since metal salts usually have excellent solubility in aqueous solution. Later, the excess of water needs to be removed completely. However, it is hard to remove all the water. Consequently, Fe^{2+} can be oxidized during a rapid heat treatment. To avoid this potential problem, an excess of ethylene glycol or a mixture of ethylene glycol and ethanol are proposed to be used as the solvent. After the complete removal of the solvent, the gelation reaction is planned to be carried out at around 80-150 °C.

The synthesized polymeric precursor is then subject to the microwave heat treatment in an inert or slightly reducing atmosphere to prevent the oxidation of Fe^{2+}. Different heat treatment trials will be carried out under Ar and H_2/N_2 forming gas (5 % and 10 %). The heat treatment T is targeted < 700 °C from both a thermal budget and material phase purity points of view. Note, Fe_2P tends to form at higher T. In addition, according to Ellingham diagram, the formation of CO is favored over CO_2 at high temperatures, and the reducing gas CO could also cause side reactions.

The phase purity of the sintered samples in different atmospheres and at different T will be evaluated. Also, the impact of the solvent used for the polymeric precursor syntheses (organic solvent vs. a mixture of aqueous and organic solvent) on the phase purity of the final products will be evaluated.

4.2.2.1.1 Physicochemical characterization

Phosphate ester characterization. Proton decoupling phosphorus NMR spectroscopy will be used to characterize the chemical shift of the ^{31}P, which could indicate the formation of phosphate ester. Chemical shifts will be referenced to 85 % phosphoric acid. Fourier transform

infrared spectroscopy can also be used to identify the stretching/vibration frequencies of the phosphate ester.

Gel characterization. After the gelation, metal salt precipitation usually can be a problem, as it indicates the presence of the non-chelated free metal ions in the polymer matrix. X-ray diffraction (XRD) is a useful technique to detect the presence of the salt precipitations such as $Li(COOCH_3)$, $Fe(C_2O_4)$ and $Fe(COOCH_3)_2$. Differential thermal analysis-thermogravimetry analysis (DSC-TGA) will be used to understand the decomposition characteristics of the polymeric precursor.

Microwave sintered sample characterization. After the microwave heat treatment, the crystalline phase and the morphology information will be studied using XRD and scanning electron microscopy (SEM), respectively. To study the thin carbon coating on the particle surface, transmission electron microscopy (TEM) will be used. Raman spectroscopy can also be used to determine the hybridization nature of the C contained in the sample, i.e. C sp^2/sp^3 ratio. The potential presence of Fe^{3+}-containing impurity can be detected by X-ray photoelectron spectroscopy (XPS). In order to determine the particle surface area, $N_{2(g)}$ adsorption/desorption isotherm test at 77 K will be conducted. First, samples will be dried for 12 h at 623 K under a pressure of 10^{-3} Torr. Brunauer-Emmett-Teller (BET) surface area can be deduced from the isotherm analysis in the relative pressure (p/p^0) range of 0.04-0.20. The total pore volume (V_p) is calculated from the amount adsorbed at a relative pressure of 0.99. The average pore size and pore size distribution can be calculated according to the N_2 adsorption isotherm result using Barrett-Joyner-Halenda (BJH) method.(Zhang et al. 2010)

4.2.2.2 Electrochemical Performance Characterization

4.2.2.2.1 Study of redox reactions on cathode by cyclic voltammetry

Cyclic voltammetry (CV) will be used to study the electrochemical reactions on the cathode, the stability of the cathode and the peak voltage of reduction and oxidation shifts.(Bard and Faulkner 2001)

1 M $LiPF_6$ in a mixture of propylene carbonate (PC) and dimethyl carbonate (DMC) (PC/DMC = 1:1 wt %) will be used as the electrolyte solution. Li metal will be used as both the anode and the reference electrode. The cathode for CV study will be fabricated in a similar way as indicated in Figure 4.11. The cathode will be made of $LiFePO_4$/C black/polyvinylidene fluoride (PVdF) with a weight ratio 75:15:10 wt %. First, the mixture will be ballmilled in the absence of air, or dispersed in N-methyl-2-pyrrolidone with mortar and mixed using ultrasonification. In another study, it showed that using polyacrylic acid as the binder can improve the cycle performance of $LiFePO_4$ cathode.(Zhang et al. 2012) After 200 cycles, there was almost no capacity fade, while conventional PVdf was used as the binder, the capacity retention is only 86.6%.

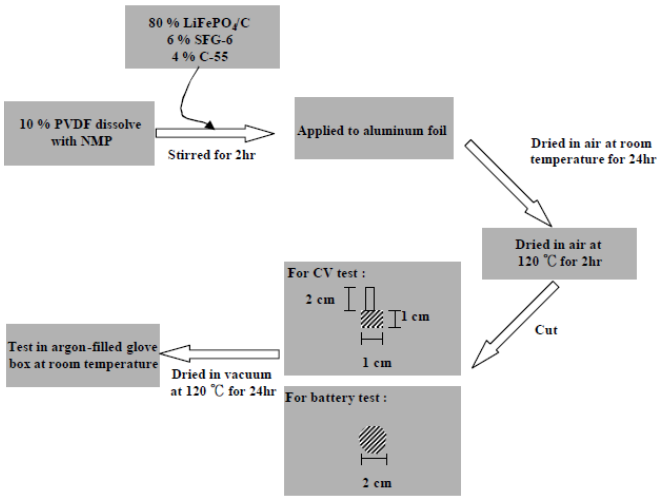

Figure 4.11. Cathode fabrication scheme for CV study(Lin, Wang, and Chen)

Cyclic scans will be carried out in the range of 3 – 4 V, starting at 3 V and using a 0.1 mV/s scan rate.

4.2.2.2.2 Charge/discharge capacity measurement

To obtain the specific discharge/charge capacity of the cathode material, a complete electrochemical cell needs to be assembled. Two different types of cells are usually used for charge/discharge capacity measurements: (1) coin cell of size 2025 and (2) Swagelok-type cell whose structure is shown in Figure 4.12.(Lin, Wang, and Chen)

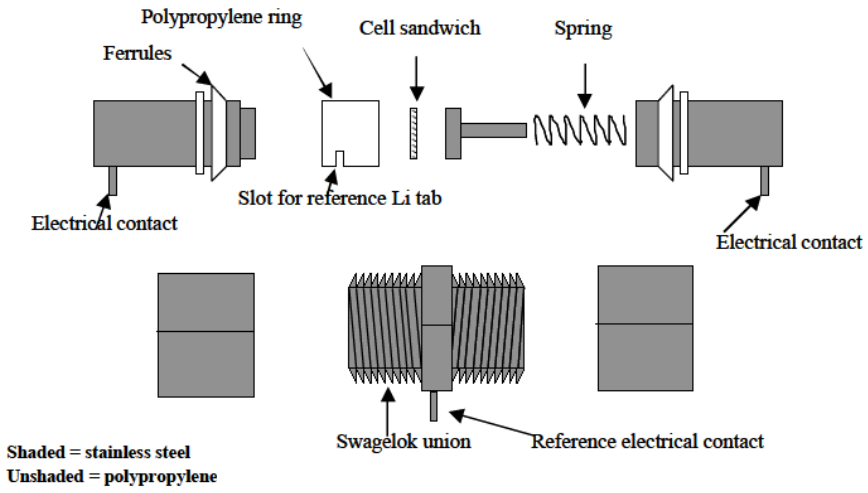

Figure 4.12. Structure of Swagelock-type cell

Li metal will be used as the anode. 1 M $LiPF_6$ in a mixture of PC and DMC with PC/DMC = 1:1 wt % will be used as the electrolyte solution. The cathode can be prepared as previously described.

First, a constant charge/discharge rate will be selected. The cell will be charged until the cell voltage reaches 4.5 V or the current density is <0.012 mA/cm^2. The discharge process will be stopped at cell voltage < 2.0 V.

To study the rate capability, the charge/discharge capacity will be measured at different charge/discharge rates, e.g., C/20 – 5 C. In the cyclability study, the charge/discharge process at a given rate will be repeated as many times as needed.

Three types of useful plots can be generated using the obtained data: (1) charge/discharge capacity vs. cell voltage at a given rate, (2) charge/discharge capacity vs. charge/discharge rate and (3) charge/discharge capacity vs. cycle number at a given rate.

4.2.2.2.3 Resistance study by electrochemical impedance spectroscopy

Important parameters such as electrolyte ions transportation barrier, charge transfer resistance, Li^+ diffusion process from the surface to the interior of the cathode material can be obtained by AC impedance spectroscopy.(Bard and Faulkner 2001, Pan, Lin, and Zhou 2012)

AC Impedance measurements (ac conductivity) are usually carried out over a frequency range of 0.01 to 200 KHz within the T range of 30 to 150 °C.(Anandhakumar, Sundar, and Selladurai 2007) A tiny oscillating voltage is applied to a system in equilibrium. The magnitude of the applied voltage typically varies from 5-10 mV and angular frequency ($\omega=2\pi/f$). As soon as the potential is applied, we will read a current measurement, which depends on the magnitude of the system's resistance to reaction, ohmic resistance, etc. The different processes respond to voltage changes with different response time scale. If the frequency of the oscillation is varied, different processes can be separated, and the relative magnitude of each process reveals.

The applied purely sinusoidal voltage is expressed as $V = E\ \sin(\omega t)$, where ω is the angular frequency. The current and the voltage rotate at the same frequency, but they generally will not be in phase; thus their phasor will be separated by a phase angle, ϕ, $I = I\ \sin(\omega t + \phi)$. With Eulers relationship $\exp(j\varphi) = \cos\varphi + j\sin\varphi$, the potential can be described as $E_t =$

$E_0 e^{j\omega t}$, and the current response as $I_t = I_0 e^{(j\omega t - j\varphi)}$. And the impedance is represented as $Z(\omega) = \frac{E}{I} = Z_0 e^{j\varphi} = Z_0(\cos\varphi + j\sin\varphi)$.

For example, for a circuit that only contains a pure resistor, R, from Ohm's Law, $E = I\,R$, so $I = \frac{E}{R}\sin(\omega t)$.

And for a pure capacitor, $I = C\,\frac{dV}{dt} = C\,\omega\,E\,\cos(\omega t) = C\,\omega\,E\,\sin(\omega t + \frac{\pi}{2})$; $I = \frac{E}{X}\sin\left(\omega t + \frac{\pi}{2}\right)$, where $X = \frac{1}{\omega C}$, the capacitive reactance.

In case that the resistance R and the reactance X are in series, the impedance is Z, and $Z = R + Xi$, i is the imaginary number. The variation of the impedance with frequency is often of interest and can be displayed in different ways. In a Bode plot, $\log|Z|$ and ϕ are both plotted vs. $\log\omega$. An alternative way is Nyquist plot, which displays Z_{Im} vs. Z_{Re} for different values of ω. At high frequencies, the capacitors shorts out the resistor, and at low frequencies the capacitor becomes insulating, which means the diameter of the circle is the resistance of the resistor.

In order to fit the measured impedance data, a real system needs to be simulated as a circuit, in which different electrical elements' impedances are combined. For impedances in series, the overall impedance is the sum of the individual values (expressed as complex vectors). For those in parallel, the inverse of the overall impedance is the sum of the reciprocal of the individual vectors.

4.2.3 Microwave-Assisted Solid-State Synthesis

4.2.3.1 Experimental

The solid-state reaction is chosen to prepare $LiFePO_4$ cathode. Stoichiometric amounts of Li_2CO_3, $FeC_2O_4•2H_2O$, $NH_4H_2PO_4$, and a small amount of L-ascorbic acid (5 % molar ratio to $FeC_2O_4•2H_2O$) were mixed by ballmilling using SiC coated Pb balls for 5 hours in the presence of acetone. A small amount of L-ascorbic acid was added in order to minimize the oxidation of $FeC_2O_4•2H_2O$ during the mixing period. The molar ratio between L-ascorbic acid and $FeC_2O_4•2H_2O$ is 5:100. The resulted mixture was dried in air for 36 hours. 5 g of powders were pressed into one pallet using a pressure of 4 tones. To prevent the formation of Fe^{3+}, and its compounds such as $LiFeP_2O_7$, $Li_3Fe_2(PO_4)_3$ and/or amorphous $Fe(PO_4)$. The pallets were sintered using microwave furnace in inert and reducing atmospheres, i.e., Ar, 5 % forming gas (H_2/N_2), 10% forming gas (H_2/N_2). Note, in order to minimize the variation among precursors, the powders of the same batch were used in all the microwave heat treatment runs.

Crystalline phase information is obtained from XRD spectrum. SEM was used for morphology study, and energy dispersive X-ray spectroscopy (EDX) for impurity detection.

4.2.3.2 Results and Discussions

XRD patterns showed that the heat treatment T and the atmosphere used in microwave heat treating had big impacts on the final products' crystalline phases.

In order to prevent the oxidation of Fe^{2+}, 10% forming gas was first chosen as the heat treatment atmosphere. Samples heat treated in 10 % forming gas showed that the main crystalline phase $LiFePO_4$ is accompanied by metallic Fe phase, whose amount can vary widely with heat treatment T. Figure 4.13 shows that the ratio between $LiFePO_4$ and Fe decreases as

heat treatment T lowers. The side reaction of H_2 + Fe(oxalate)→ Fe + oxalic acid competes with the formation of $LiFePO_4$. At high temperatures, the formation of $LiFePO_4$ favors over the formation of Fe metallic phase. For example, at 500 °C, the main product was metallic Fe; in contrast at 800 °C, the main product became $LiFePO_4$ with minor Fe impurity, according to the XRD patterns shown in Figure 4.14.

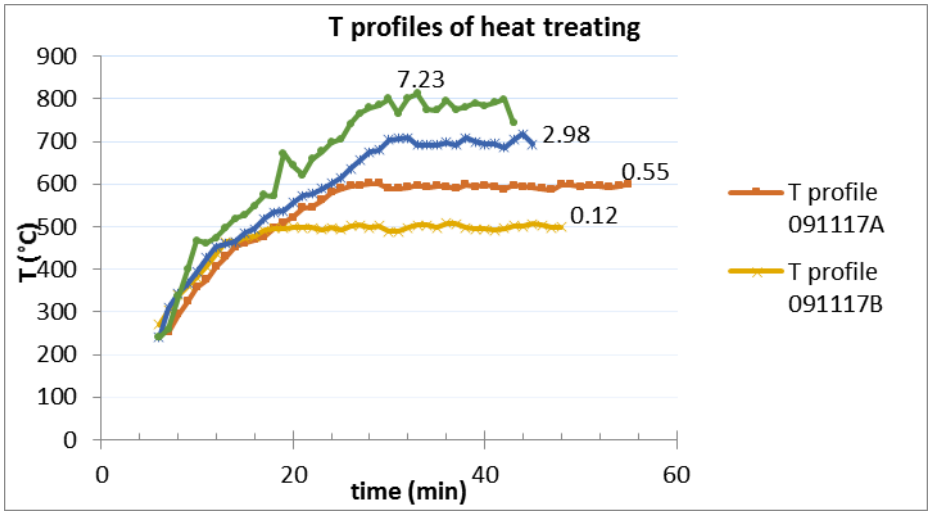

Figure 4.13. T profiles of heat treating for several samples and the approximate ratios of $LiFePO_4$ to Fe

The third choice of the atmosphere was 5% forming gas. The best heat treatment condition consisted in a very rapid T rise from room T to 800 °C in 13 min and staying at 800 °C for 15 min. The XRD pattern of sample 100212A is shown in Figure 4.15. Slow T rises were found to favor the Fe^{2+} reduction, since the formation of the $LiFePO_4$ only occurs at a higher T. Note, according to all the XRD patterns, in samples where Fe was found, Li_3PO_4 was detected as well.

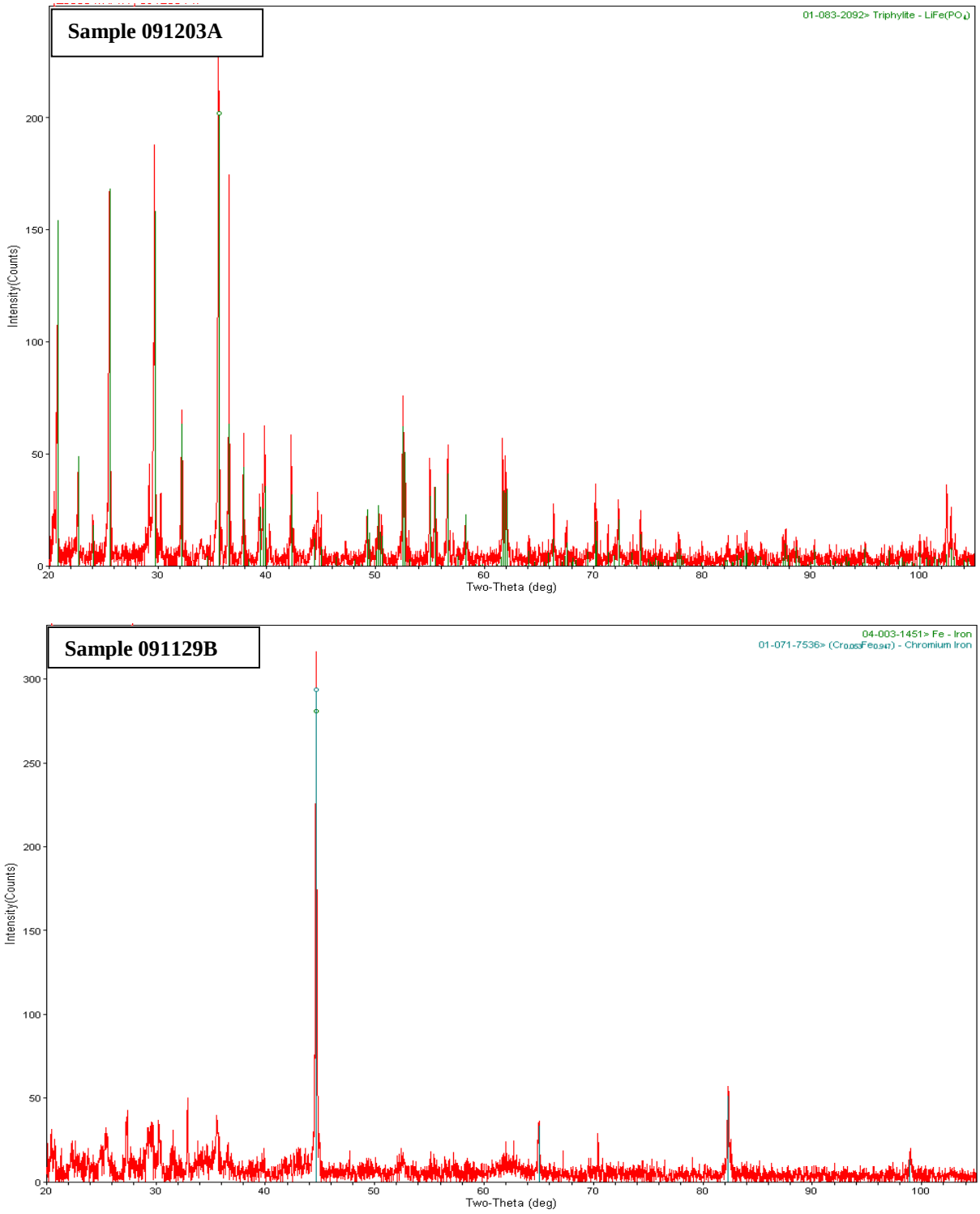

Figure 4.14. XRD patterns of 091203A and 091129B

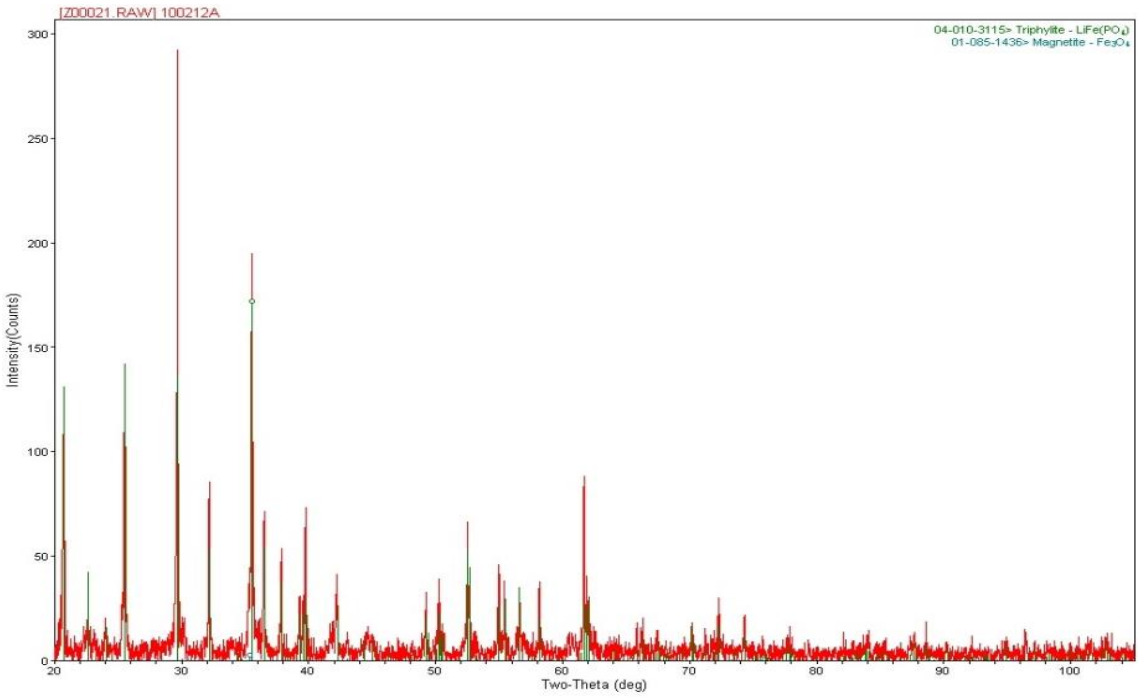

Figure 4.15. XRD pattern of 100212A; 5% forming gas and rapid T raise heat treatment conditions were used.

SEM was used to reveal the morphology of the samples. Figure 4.16 shows that the surface of sample 100212A displays a very random morphology. Despite that the XRD pattern proved the synthesized material to be almost phase-pure $LiFePO_4$ except very minor content of Fe phase, the difference in contrast reveals the phase inhomogeneity at the surface. The phase inhomogeneity was further confirmed by EDX study. EDX shows that the relative ratio among C, Fe, P, O varies with the probe locations. It strongly indicates that side reactions and undesired phases take place mostly on the surface of the sample. Moreover, the contamination of Si was detected. They probably came from SiC balls during the ballmilling process.

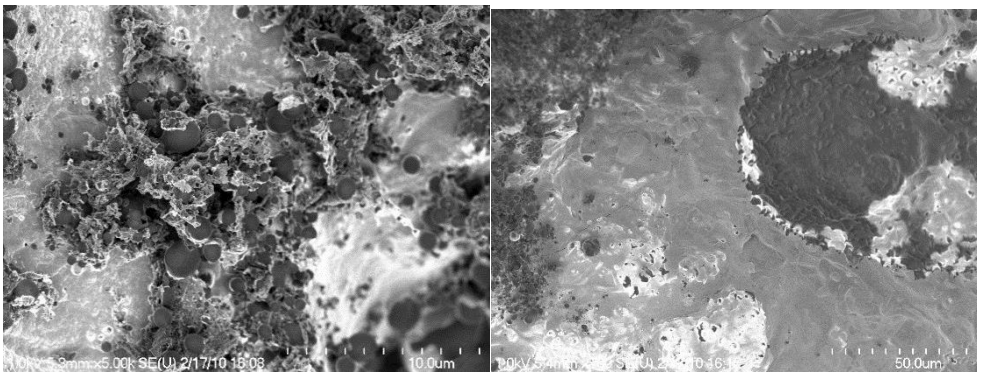

Figure 4.16. SEM micrographs of the surface morphology of the sample 100212A

4.2.3.3 Conclusion

By varying the heat treatment atmospheres, undesired phase was minimized, but not suppressed completely, as the atmospheric control of the microwave furnace was not precise. In order to avoid the Fe^{2+} reduction, a less reducing heat treatment environment (than 5 % forming gas) such as Ar should be used. Incorporation of mild reducing agents such as organic compounds may make the precursor more forgiving for the imprecise atmosphere control of the microwave furnance. On the other side, the $LiFePO_4$ formation by solid-state sintering requires very rapid heating and a relatively high T, while the side reactions such as reduction/oxidation of Fe^{2+} start at relatively low temperatures. Ideally, the desired phase should start to form at a lower T, as soon as the precursors decompose. Sol-gel method features with excellent intimate mixing of the reactants on the molecular scale, which decreases significantly the diffusion paths of the various species compared to typical solid-state reactions of mixed oxide salts. As a result, most of the multi-component oxides form directly upon pyrolysis of the polymer as phase pure. The section 4.2.4 reports the microwave-assisted modified Pechini's method for the $LiFePO_4$ synthesis.

4.2.4 Microwave-Assisted Modified Pechini's Method

4.2.4.1 Experimental

The precursor of stoichiometric $LiFePO_4$ phase was synthesized by modified Pechini's method. First, the polyanion, PO_4^{3-}, is stabilized by incorporating the phosphate group into ethylene glycol via the formation of phosphate ester chemical bonds, as shown in Figure 4.17.

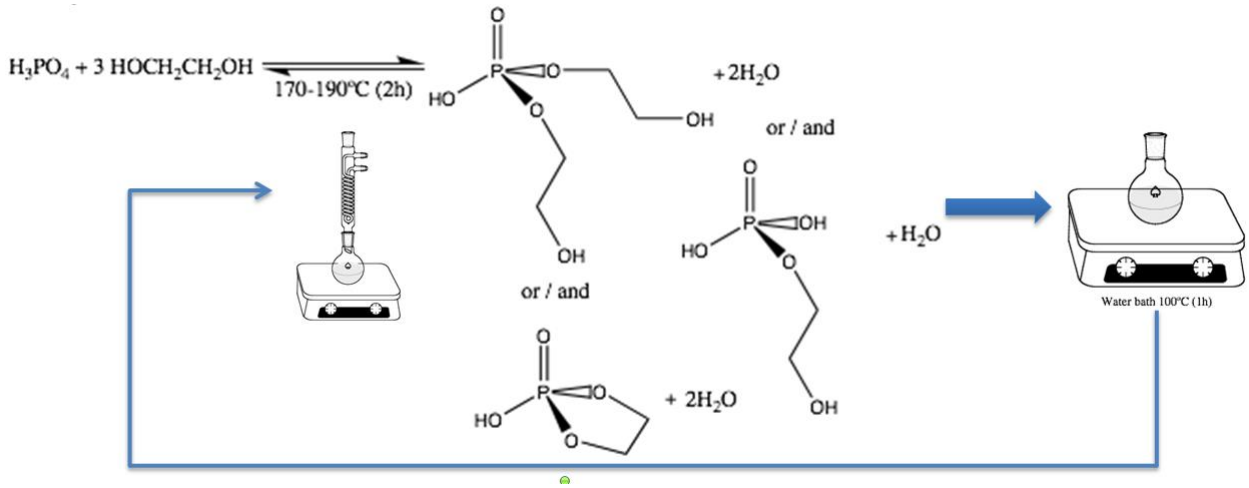

Figure 4.17. Synthesis of phosphate ester

Li^+ and Fe^{2+} will be stabilized by the excess of citric acid. Figure 4.18 shows the general synthesis steps of the precursor formation.

The synthesized polymeric precursor was then subject to the microwave heat treatment in an inert atmosphere to prevent the oxidation of Fe^{2+}. Different heat treatment trials were carried out in Ar. To be thermal budget saving, the heat treatment temperatures were targeted to < 700 °C; heat treating durations were shorter than 20 min. Note, Fe_2P tends to form at high T. Crystalline phase information of the sintered samples is evaluated from the XRD patterns.

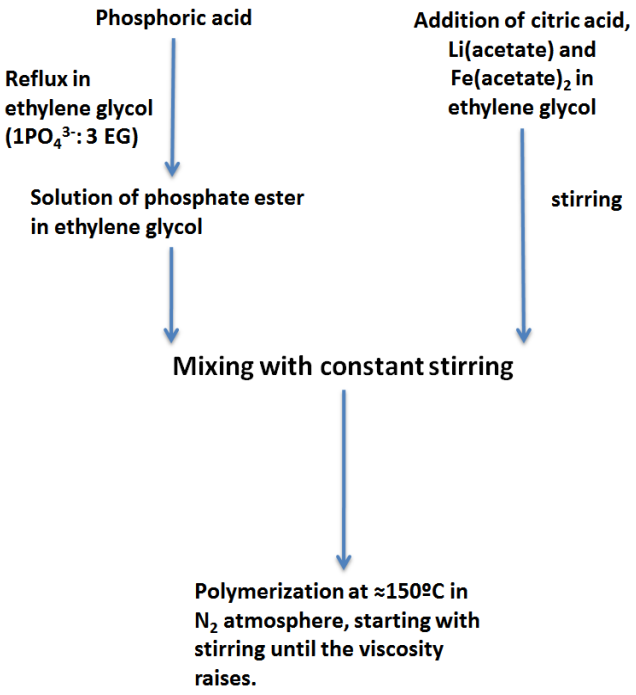

Figure 4.18, Synthesis scheme of the $LiFePO_4$ precursor

4.2.4.2 Results and Discussions

Microwave radiation is absorbed by microwave susceptors and transformed to thermal energy. The microwave absorber becomes the heat source; the surrounding atmospheric T can be much lower than the absorber itself. The T non-uniformity inside the microwave furnace makes the thermodynamic stability prediction inaccurate. In conventional furnace heating, the oxygen partial pressure can be very well controlled thermodynamically. The unique nature of the microwave local heating can induce significant oxygen partial pressure variations inside the microwave furnace. This fact forces the precursor composition to be very forgiving towards the oxygen partial pressure variation, especially when the oxidation state of a certain element is not stable at high temperatures, i.e., at 800 °C, Fe^{2+} gets oxidized to form Fe_2O_3 readily at a partial pressure of oxygen as low as 3.4×10^{-11} atm. Also, the very short reaction duration and the

relatively low heat treatment T require that all the reactants are intimately and thoroughly mixed at the molecular level, and readily transform to the desired crystalline phase in the reduced duration.

The original idea comparing to the original Pechini's method is the stabilization of PO_4^{3-} by the formation of phosphate ester. To synthesize phosphate ester, ethylene glycol and phosphoric acid were recirculated for 2 hours, followed by the removal of the by product, H_2O. This procedure was repeated several times. The resulting product was transparent, uncolored with an aromatic smell. In conventional Pechini's method, a mixture of organic aqueous solution is often used as the solvent because of the metal salts' excellent solubility in water. However, the water removal process is time-consuming and hard to complete. To avoid the potential risk of Fe^{2+} being oxidized by the presence of water during a very rapid heat treatment, an excess of ethylene glycol was used as the solvent. After mixing the phosphate esters with ethylene glycol solution that contained $Li(COOCH_3)$, $Fe(COOCH_3)_2$ and citric acid at 50 °C, the mixture was heated to 150 °C to form polymeric gel precursor.

Polymeric gel precursors were heat treated under Ar at various temperatures and for different durations. The detailed heat treatment profiles are summarized in Figure 4.19, and the resulting crystalline structures are shown in Figure 4.20.

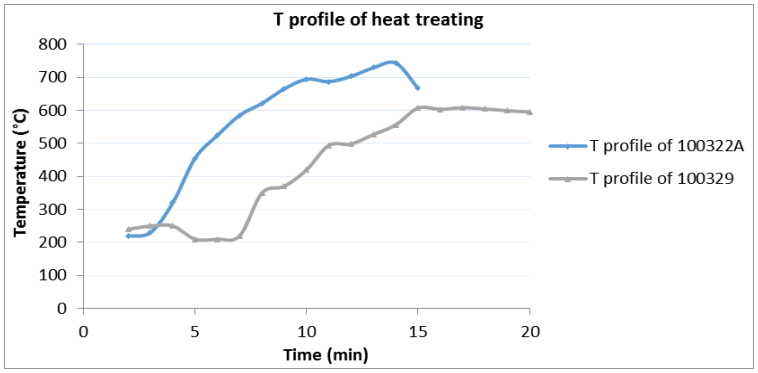

Figure 4.19. T profiles of heat treatments

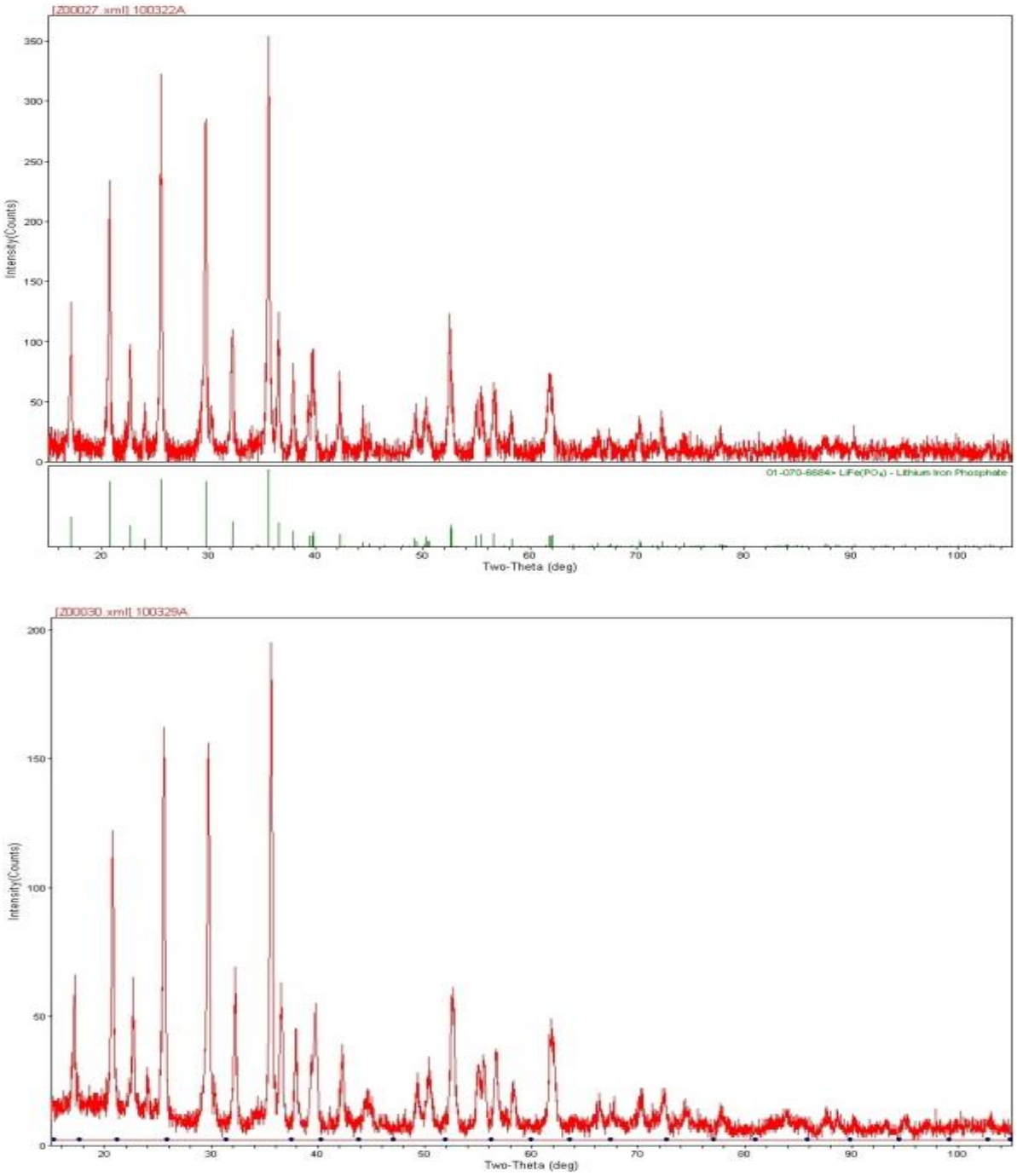

Figure 4.20. XRD patterns of 100322A and 100329A

Figure 4.21 shows the charge-discharge profiles of three samples with different crystallinities. The best cyclability was achieved in Sample A, which is the most crystalline materials among the three. Note, we did not use any extra carbon coating source, and the

morphology was not optimized. The best sample shows a capacity of about 65% of the theoretical capacity, slightly higher than solid state reaction without carbon coating and microwave assisted $LiFePO_4$ nanoparticle.(Carriazo et al. 2012) In order to increase the capacity to the theoretical value, controlling the final morphology of the powder (under 100 nm) will probably meet the requirement.

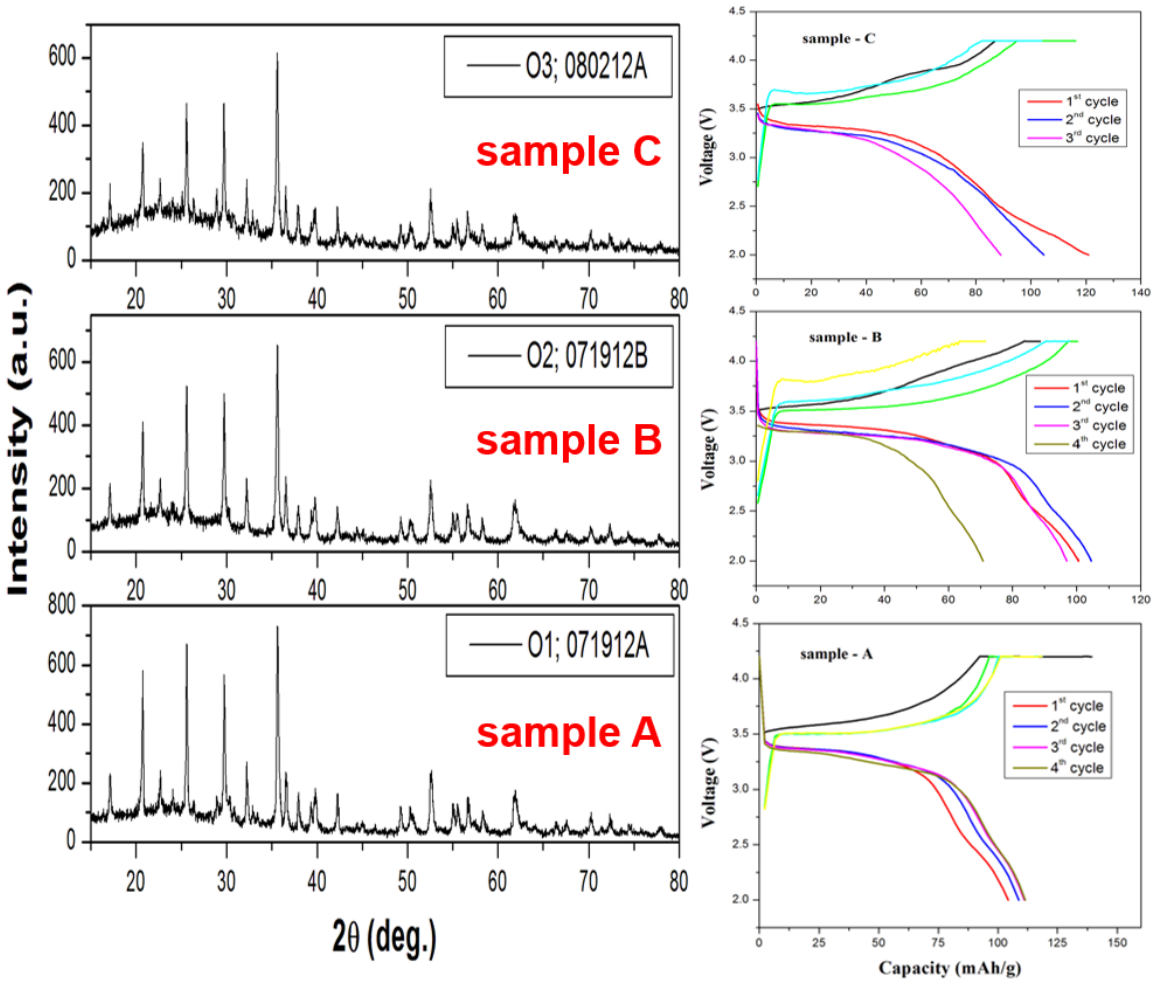

Figure 4.21. Charge-discharge profile at 0.1 C

4.2.4.3 Conclusions

In this study, we have reported the synthesis of phase-pure $LiFePO_4$ cathode material by microwave heat treating of the polymer-based precursor for only 15 minutes. The synthesis method of the polymeric precursor was modified based on the original Pechini's method, in which the polyanion, PO_4^{3-}, was stabilized as phosphate ester. The use of only organic solvent greatly decreased the effort of the by-product, H_2O, removal. It not only prevents the oxidation of Fe^{2+} by the remaining moisture but also makes the precursor more resistant to the remaining oxygen in the microwave reactor. The measured charge-discharge capacity is about 65% of the theoretical value.

The objective of the future works is to increase the capacity by controlling the morphology, particle size as well as doping with the aid of materials characterization and electrochemical characterization, such as impedance spectroscopy that can distinguish the impedance of individual process within a rather complex system.

CHAPTER

5. CONCLUDING REMARKS

The successful application of wet chemistry "bottom-up" synthesis technique has been demonstrated to the synthesis of LDH NPs following a systematic optimization of the synthesis parameters by statistic design of experiments. The LDH NP formation mechanisms have been revealed, which have a strong impact on both fundamental scientific knowledge and practical significance of the synthesis of the LDH NPs in a well-controlled fashion. The robust synthesis strategy facilitated the exploration of the potential application of the LDH NPs for biomedicine application, especially for highly efficient therapeutic drug delivery to the pancreatic cancer cells as well as the development of the ultrafast relaxation contrast agent for MRI.

In the future, the development of multifunctional core/shell layered double hydroxide nanoparticle-based nanovectors for the targeted ablation and imaging of advanced cancer disease (Figure 5.1) is considered of high interest. This novel non-polymeric platform will be designed to possess the following features: (1) silver nanorod or quantum dot core/LDH ceramic shell for imaging/therapy, (2) intercalated apoptosis-inducing/imaging agents within the ceramic LDH shell, and (3) functionalized surfaces for targeting cancer cells. In addition to NIR-imaging, the silver/gold core can also be used for hyperthermic ablation adding further multidimensionality to the platform which consists of targeting, ablation, and imaging modalities.

In the second part of the dissertation, wet-chemistry solution growth synthesis, as the alternative of vacuum technique such as CVD, MBE, or PVD, has been successfully used to synthesize of ZnO nanorods and films. The posterior sulfurization of the ZnO thin film led to the formation of ZnO/ZnS heterojunction, which was proven to form a Schottky-based solar cell with Cr-Au and produce relatively large open circuit voltage of 1.35 V. In the future,

optimization of the solar cell stack, i.e., the thickness of the ZnO, ZnS, needs to be optimized in order to increase the short circuit current and the power efficiency.

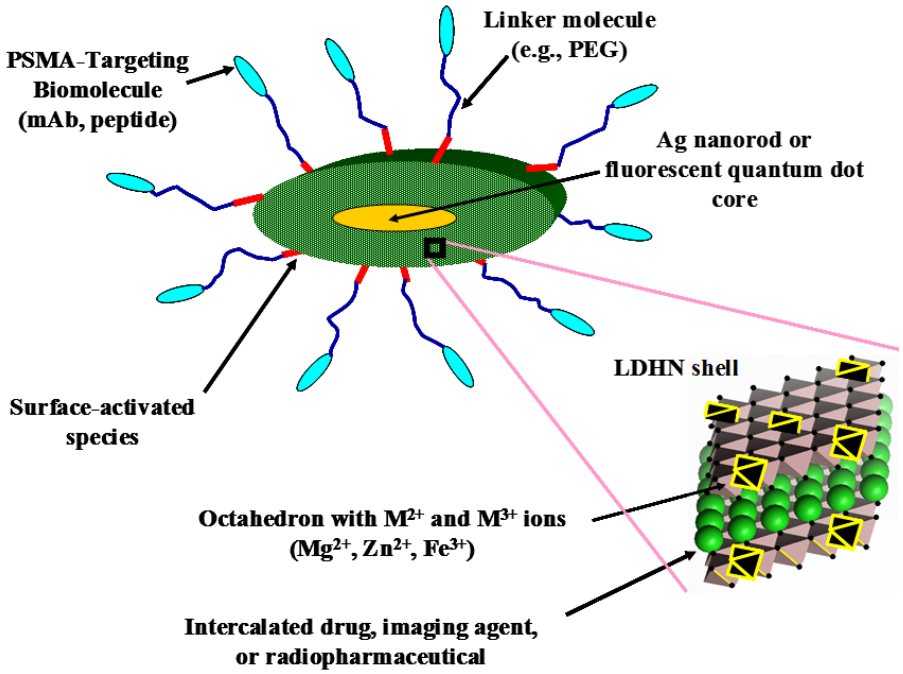

Figure 5.1. A novel drug delivery platform based on core/shell LDH NP with imaging core, intercalated therapeutic drugs in the LDH shell, and surfaces functionalized for targeting delivery

In the second part of the dissertation, wet-chemistry solution growth synthesis, as the alternative of vacuum technique such as CVD, MBE, or PVD, has been successfully used to synthesize of ZnO nanorods and films. The posterior sulfurization of the ZnO thin film led to the formation of ZnO/ZnS heterojunction, which was proven to form a Schottky-based solar cell with Cr-Au and produce relatively large open circuit voltage of 1.35 V. In the future, optimization of the solar cell stack, i.e., the thickness of the ZnO, ZnS, needs to be optimized in order to increase the short circuit current and the power efficiency.

The last part of the dissertation dedicated on the sol-gel synthesis technique. Microwave-assisted sol gel method was employed to synthesize phase-pure $LiFePO_4$ powder as a cathode

material for Li-ion battery. The charge-discharge capacity measured to be ~ 65% of the theoretical capacity. In the future, more work needs to be done in terms of controlling the nanostructure of the powder, which is considered to have direct impact on both the discharge/charge capacity as well as cyclability of the electrode material.

REFERENCES

M. Ahren, L. Selegard, A. Klasson, F. Soderlind, N. Abrikossova, C. Skoglund, T. Bengtsson, M. Engstrom, P. O. Kall, and K. Uvdal. 2010. Synthesis and characterization of pegylated Gd_2O_3 nanoparticles for mri contrast enhancement. *Langmuir* 26, no. 8: 5753-62.

S. Aime, M. Botta, M. Fasano, and E. Terreno. 1999. Prototropic and water-exchange processes in aqueous solutions of Gd(III) chelates. *Accounts of Chemical Research* 32, no. 11: 941-49.

S. Aime, M. Botta, and E. Terreno. 2005. Gd(iii)-based contrast agents for mri. *Advances in Inorganic Chemistry - Including Bioinorganic Studies, Vol 57* 57: 173-237.

R. K. Allada, A. Navrotsky, H. T. Berbeco, and W. H. Casey. 2002. Thermochemistry and aqueous solubilities of hydrotalcite-like solids. *Science* 296, no. 5568: 721-23.

R. K. Allada, E. Peltier, A. Navrotsky, W. H. Casey, C. A. Johnson, H. T. Berbeco, and D. L. Sparks. 2006. Calorimetric determination of the enthalpies of formation of hydrotalcite-like solids and their use in the geochemical modeling of metals in natural waters. *Clays and Clay Minerals* 54, no. 4: 409-17.

R. K. Allada, J. D. Pless, T. M. Nenoff, and A. Navrotsky. 2005. Thermochemistry of hydrotalcite-like phases intercalated with CO_3^{2-}, NO_3^-, Cl^-, I^-, and ReO_4. *Chemistry of Materials* 17, no. 9: 2455-59.

R. Allmann. 1970. Double layer structures with layer ions $(Me(II)_{(1-x)}Me(III)_{(x)}(OH)_2)^{x+}$ of brucite type. *Chimia* 24, no. 3: 99-&.

S. Anandhakumar, M. Sundar, and S. Selladurai. 2007. Synthesis and performance study of cobalt-substituted lithium iron phosphate. *Ionics* 13, no. 1: 19-23.

A. S. Andersson and J. O. Thomas. 2001. The source of first-cycle capacity loss in $LiFePO_4$. *Journal of Power Sources* 97-8: 498-502.

J. F. Banfield, S. A. Welch, H. Z. Zhang, T. T. Ebert, and R. L. Penn. 2000. Aggregation-based crystal growth and microstructure development in natural iron oxyhydroxide biomineralization products. *Science* 289, no. 5480: 751-54.

Allen J. Bard and Larry R. Faulkner. 2001. *Electrochemical methods-fundamentals and applications*: John Wiley & Sons.

K. C. Barick, M. Aslam, Y. P. Lin, D. Bahadur, P. V. Prasad, and V. P. Dravid. 2009. Novel and efficient MR active aqueous colloidal Fe_3O_4 nanoassemblies. *Journal of Materials Chemistry* 19, no. 38: 7023-29.

J. Barker, M. Y. Saidi, and J. L. Swoyer. 2003. Lithium iron(II) phospho-olivines prepared by a novel carbothermal reduction method. *Electrochemical and Solid State Letters* 6, no. 3: A53-A55.

F. Bellezza, A. Cipiciani, U. Costantino, M. Nocchetti, and T. Posati. 2009. Hydrotalcite-like nanocrystals from water-in-oil microemulsions. *European Journal of Inorganic Chemistry*, no. 18: 2603-11.

S. Beninati, L. Damen, and M. Mastragostino. 2008. MW-assisted synthesis of $LiFePO_4$ for high power applications. *Journal of Power Sources* 180, no. 2: 875-79.

I. Bilecka, I. Djerdj, and M. Niederberger. 2008. One-minute synthesis of crystalline binary and ternary metal oxide nanoparticles. *Chemical Communications*, no. 7: 886-88.

I. Bilecka, P. Elser, and M. Niederberger. 2009. Kinetic and thermodynamic aspects in the microwave-assisted synthesis of ZnO nanoparticles in benzyl alcohol. *Acs Nano* 3, no. 2: 467-77.

I. Bilecka, A. Hintennach, I. Djerdj, P. Novak, and M. Niederberger. 2009. Efficient microwave-assisted synthesis of $LiFePO_4$ mesocrystals with high cycling stability. *Journal of Materials Chemistry* 19, no. 29: 5125-28.

I. Bilecka, A. Hintennach, M. D. Rossell, D. Xie, P. Novak, and M. Niederberger. 2011. Microwave-assisted solution synthesis of doped $LiFePO_4$ with high specific charge and outstanding cycling performance. *Journal of Materials Chemistry* 21, no. 16: 5881-90.

J. W. Boclair and P. S. Braterman. 1999. Layered double hydroxide stability. 1. Relative stabilities of layered double hydroxides and their simple counterparts. *Chemistry of Materials* 11, no. 2: 298-302.

J. W. Boclair, P. S. Braterman, J. P. Jiang, S. W. Lou, and F. Yarberry. 1999. Layered double hydroxide stability. 2. Formation of Cr(III)-containing layered double hydroxides directly from solution. *Chemistry of Materials* 11, no. 2: 303-07.

R. D. Bolskar, A. F. Benedetto, L. O. Husebo, R. E. Price, E. F. Jackson, S. Wallace, L. J. Wilson, and J. M. Alford. 2003. First soluble m@C-60 derivatives provide enhanced access to metallofullerenes and permit in vivo evaluation of $Gd@C\text{-}60[C(COOH)_2]_{10}$ as a MRI contrast agent. *Journal of the American Chemical Society* 125, no. 18: 5471-78.

Paul S. Braterman, Zhi Ping Xu, and Faith Yarberry. 2004. In *Handbook of layered materials*, ed. Scott M. Auerbach, Kathleen A. Carrado and Prabir K. Dutta. New York: Marcel Dekker.

D. E. Bullard and D. C. Lynch. 1992. Processing of refractory ores in a microwave induced "Cold" Plasma. *MRS Proceedings* 269.

D. G. Cantrell, L. J. Gillie, A. F. Lee, and K. Wilson. 2005. Structure-reactivity correlations in MgAl hydrotalcite catalysts for biodiesel synthesis. *Applied Catalysis a-General* 287, no. 2: 183-90.

P. Caravan. 2006. Strategies for increasing the sensitivity of gadolinium based MRI contrast agents. *Chemical Society Reviews* 35, no. 6: 512-23.

P. Caravan, J. J. Ellison, T. J. McMurry, and R. B. Lauffer. 1999. Gadolinium(III) chelates as MRI contrast agents: Structure, dynamics, and applications. *Chemical Reviews* 99, no. 9: 2293-352.

D. Carriazo, M. D. Rossell, G. B. Zeng, I. Bilecka, R. Erni, and M. Niederberger. 2012. Formation mechanism of $LiFePO_4$ sticks grown by a microwave-assisted liquid-phase process. *Small* 8, no. 14: 2231-38.

F. Cavani, F. Trifiro, and A. Vaccari. 1991. Hydrotalcite-type anionic clays: Preparation, properties and applications. *Catalysis Today* 11, no. 2: 173-301.

Y. L. Chai, D. T. Ray, G. J. Chen, and Y. H. Chang. 2002. Synthesis of $La_{0.8}Sr_{0.2}Co_{0.5}Ni_{0.5}O_{3-\delta}$ thin films for high sensitivity co sensing material using the pechini process. *Journal of Alloys and Compounds* 333, no. 1-2: 147-53.

Z. Chang, D. G. Evans, X. Duan, C. Vial, J. Ghanbaja, V. Prevot, M. de Roy, and C. Forano. 2005. Synthesis of Zn-Al-Co_3 layered double hydroxides by a coprecipitation method under steady-state conditions. *Journal of Solid State Chemistry* 178, no. 9: 2766-77.

M. D. Chen, F. Teng, G. Q. Li, H. X. Shi, J. Wang, M. J. Xu, X. Q. Ji, T. Y. Lu, Y. J. Lv, and S. I. Mho. 2012. Self-assembly of highly uniform $LiFePO_4$ hierarchical nanostructures by surfactant molecules in a new mixture medium. *Ionics* 18, no. 6: 541-47.

M. Chen, J. E. McGrath, and T. C. Ward. 1989. Microwave-radiation calorimetry of thermoplastics. *Abstracts of Papers of the American Chemical Society* 197: 93-PMSE.

J. H. Choy, S. Y. Kwak, Y. J. Jeong, and J. S. Park. 2000. Inorganic layered double hydroxides as nonviral vectors. *Angewandte Chemie-International Edition* 39, no. 22: 4042-45.

J. H. Choy, S. Y. Kwak, J. S. Park, Y. J. Jeong, and J. Portier. 1999. Intercalative nanohybrids of nucleoside monophosphates and dna in layered metal hydroxide. *Journal of the American Chemical Society* 121, no. 6: 1399-400.

J. H. Choy, J. S. Park, S. Y. Kwak, Y. J. Jeong, and Y. S. Han. 2000. Layered double hydroxide as gene reservoir. *Molecular Crystals and Liquid Crystals* 341: 1229-33.

S. Y. Chung, Y. M. Kim, J. G. Kim, and Y. J. Kim. 2009. Multiphase transformation and ostwald's rule of stages during crystallization of a metal phosphate. *Nature Physics* 5, no. 1: 68-73.

U. Costantino, F. Marmottini, M. Nocchetti, and R. Vivani. 1998. New synthetic routes to hydrotalcite-like compounds - characterisation and properties of the obtained materials. *European Journal of Inorganic Chemistry*, no. 10: 1439-46.

F. Croce, A. D'Epifanioa, J. Hassoun, A. Deptula, T. Olczac, and B. Scrosati. 2002. A novel concept for the synthesis of an improved $LiFePO_4$ lithium battery cathode. *Electrochemical and Solid State Letters* 5, no. 3: A47-A50.

E. Cukierman and D. R. Khan. 2010. The benefits and challenges associated with the use of drug delivery systems in cancer therapy. *Biochem Pharmacol* 80, no. 5: 762-70.

R. Damadian. 1971. Tumor detection by nuclear magnetic resonance. *Science* 171, no. 3976: 1151-&.

J. J. De Yoreo and P. G. Vekilov. 2003. Principles of crystal nucleation and growth. *Biomineralization* 54: 57-93.

C. Del Hoyo. 2007. Layered double hydroxides and human health: An overview. *Applied Clay Science* 36, no. 1-3: 103-21.

H. G. Deng, S. L. Jin, L. Zhan, W. M. Qiao, and L. C. Ling. 2012. Nest-like $LiFePO_4$/C architectures for high performance lithium ion batteries. *Electrochimica Acta* 78: 633-37.

H. G. Deng, S. L. Jin, L. Zhan, Y. L. Wang, W. M. Qiao, and L. C. Ling. 2012. Synthesis of cage-like $LiFePO_4$/C microspheres for high performance lithium ion batteries. *Journal of Power Sources* 220: 342-47.

S. K. Dey and R. Sistiabudi. 2007. Ceramic nanovector based on layered double hydroxide: Attributes, physiologically relevant compositions and surface activation. *Materials Research Innovations* 11, no. 3: 108-17.

R. Dominko, M. Bele, M. Gaberscek, M. Remskar, D. Hanzel, J. M. Goupil, S. Pejovnik, and J. Jamnik. 2006. Porous olivine composites synthesized by sol-gel technique. *Journal of Power Sources* 153, no. 2: 274-80.

A. M. Duprat, P. Alphonse, C. Sarda, A. Rousset, and B. Gillot. 1994. Nonstoichiometry-activity relationship in perovskite-like manganites. *Materials Chemistry and Physics* 37, no. 1: 76-81.

W. Eventoff, R. Martin, and D. R. Peacor. 1972. Crystal-structure of heterosite. *American Mineralogist* 57, no. 1-2: 45.

X. S. Fang, J. Li, K. L. Huang, S. Q. Liu, C. H. Huang, S. X. Zhuang, and J. B. Zhang. 2012. Synthesis and electrochemical properties of K-doped $LiFePO_4$/C composite as cathode material for lithium-ion batteries. *Journal of Solid State Electrochemistry* 16, no. 2: 767-73.

X. S. Fang, T. Y. Zhai, U. K. Gautam, L. Li, L. M. Wu, B. Yoshio, and D. Golberg. 2011. ZnS nanostructures: From synthesis to applications. *Progress in Materials Science* 56, no. 2: 175-287.

O. C. Farokhzad and R. Langer. 2006. Nanomedicine: Developing smarter therapeutic and diagnostic modalities. *Advanced Drug Delivery Reviews* 58, no. 14: 1456-59.

M. Ferrari. 2005. Cancer nanotechnology: Opportunities and challenges. *Nature Reviews Cancer* 5, no. 3: 161-71.

M. Fevre, C. Varvenne, A. Finel, and Y. Le Bouar. 2013. Influence of atomic size mismatch on binary alloy phase diagrams. *Philosophical Magazine* 93, no. 13: 1563-81.

K. W. Gallis and C. C. Landry. 2001. Rapid calcination of nanostructured silicate composites by microwave irradiation. *Advanced Materials* 13, no. 1: 23-+.

G. Geismar, J. Lewandowski, and E. Deboer. 1991. Anion-exchange and reactions in mg-al oxide hydrates with hydrotalcite structure .2. Intercalated anion-exchange in organic-solvents and chemical-reactions. *Chemiker-Zeitung* 115, no. 12: 335-39.

F. J. Gotor, P. Odier, M. Gervais, J. Choisnet, and P. Monod. 1993. Synthesis of $YBa_2Cu_3O_{7-x}$ by sol-gel route - formation of ybacuo oxycarbonate intermediate. *Physica C* 218, no. 3-4: 429-36.

D. Y. Greenblatt, A. M. Vaccaro, R. Jaskula-Sztul, L. Ning, M. Haymart, M. Kunnimalaiyaan, and H. Chen. 2007. Valproic acid activates notch-1 signaling and regulates the neuroendocrine phenotype in carcinoid cancer cells. *Oncologist* 12, no. 8: 942-51.

R. Greenwood and K. Kendall. 1999. Selection of suitable dispersants for aqueous suspensions of zirconia and titania powders using acoustophoresis. *Journal of the European Ceramic Society* 19, no. 4: 479-88.

M. A. Gulgun, M. H. Nguyen, and W. M. Kriven. 1999. Polymerized organic-inorganic synthesis of mixed oxides. *Journal of the American Ceramic Society* 82, no. 3: 556-60.

M. A. Gulgun, O. O. Popoola, and W. M. Kriven. 1995. X-ray photoelectron-spectroscopy studies of bond structure between polyvinyl-alcohol and a titanate cross-coupling agent. *Journal of Materials Research* 10, no. 6: 1565-71.

X. F. Guo, H. Zhan, and Y. H. Zhou. 2009. Rapid synthesis of $LiFePO_4$/C composite by microwave method. *Solid State Ionics* 180, no. 4-5: 386-91.

Z. P. Guo, S. Zhong, G. X. Wang, G. Walter, H. K. Liu, and S. X. Dou. 2002. Synthesis of layered-structure $LiMn_{1-x}Cr_xO_2$ by the pechini method and characterization as a cathode for rechargeable Li/$LiMnO_2$ cells. *Journal of the Electrochemical Society* 149, no. 6: A792-A95.

Manoj Gupta and Eugene Wong Wai Leong. 2007. *Microwaves and metals*. Singapore: John Wiley and Sons.

N. A. Hamid, S. Wennig, S. Hardt, A. Heinzel, C. Schulz, and H. Wiggers. 2012. High-capacity cathodes for lithium-ion batteries from nanostructured $LiFePO_4$ synthesized by highly-flexible and scalable flame spray pyrolysis. *Journal of Power Sources* 216: 76-83.

D. Hanaor, M. Michelazzi, C. Leonelli, and C. C. Sorrell. 2012. The effects of carboxylic acids on the aqueous dispersion and electrophoretic deposition of ZrO_2. *Journal of the European Ceramic Society* 32, no. 1: 235-44.

L. L. Hench. 1998. Bioceramics. *Journal of the American Ceramic Society* 81, no. 7: 1705-28.

L. L. Hench and J. M. Polak. 2002. Third-generation biomedical materials. *Science* 295, no. 5557: 1014.

Larry L. Hench and June Wilson. 1993. *An introduction to bioceramics*. Advanced series in ceramics. Singapore; River Edge, N.J.: World Scientific.

M. Higuchi, K. Katayama, Y. Azuma, M. Yukawa, and M. Suhara. 2003. Synthesis of $LiFePO_4$ cathode material by microwave processing. *Journal of Power Sources* 119: 258-61.

Hiromitsu. 2005. Sol-gel processing. In *Handbook of sol-gel science and technology processing characterization and applications*, 1: Kluwer Academic Publishers.

K. F. Hsu, S. Y. Tsay, and B. J. Hwang. 2004. Synthesis and characterization of nano-sized lifepo4 cathode materials prepared by a citric acid-based sol-gel route. *Journal of Materials Chemistry* 14, no. 17: 2690-95.

H. C. Huang, S. Barua, G. Sharma, S. K. Dey, and K. Rege. 2011. Inorganic nanoparticles for cancer imaging and therapy. *Journal of Controlled Release* 155, no. 3: 344-57.

H. Huang, S. C. Yin, and L. F. Nazar. 2001. Approaching theoretical capacity of $LiFePO_4$ at room temperature at high rates. *Electrochemical and Solid State Letters* 4, no. 10: A170-A72.

Huang-Chiao Huang, Sutapa Barua, Gaurav Sharma, Sandwip K. Dey, and Kaushal Rege. 2011. Inorganic nanoparticles for cancer imaging and therapy. *Journal of Controlled Release*.

M. S. Islam, D. J. Driscoll, C. A. J. Fisher, and P. R. Slater. 2005. Atomic-scale investigation of defects, dopants, and lithium transport in the $LiFePO_4$ olivine-type battery material. *Chemistry of Materials* 17, no. 20: 5085-92.

kai-lun Jiang. 1995. Synthesis of $LiFePO_4$/C composites using agriculture crop waste as carbon precursor. M.S., National Central University.

Z. Q. Jiang and Z. J. Jiang. 2012. Effects of carbon content on the electrochemical performance of $LiFePO_4$/C core/shell nanocomposites fabricated using $FePO_4$/polyaniline as an iron source. *Journal of Alloys and Compounds* 537: 308-17.

JMP 10 design of experiments guide. http://support.sas.com/documentation/onlinedoc/jmp/10.0.1/DOE_Guide.pdf.

T. E. Johnson, W. Martens, R. L. Frost, Z. Ding, and J. T. Kloprogge. 2002. Structured water in hydrotalcites of formula $Mg_xZn_{6-x}Al_2(OH)_{16}(CO_3)\cdot 4H_2O$: A raman microscopic study. *Journal of Raman Spectroscopy* 33, no. 8: 604-09.

S. Y. Ju, H. R. Peng, G. C. Li, and K. Z. Chen. 2012. Synthesis and electrochemical properties of $LiFePO_4$ single-crystalline nanoplates dominated with bc-planes. *Materials Letters* 74: 22-25.

W. Kagunya, P. K. Dutta, and Z. Lei. 1997. Dynamics of water in hydrotalcite. *Physica B* 234: 910-13.

B. Kang and G. Ceder. 2009. Battery materials for ultrafast charging and discharging. *Nature* 458, no. 7235: 190-93.

O. Karaagac and H. Kockar. 2012. Effect of synthesis parameters on the properties of superparamagnetic iron oxide nanoparticles. *Journal of Superconductivity and Novel Magnetism* 25, no. 8: 2777-81.

I. A. Khalil, K. Kogure, H. Akita, and H. Harashima. 2006. Uptake pathways and subsequent intracellular trafficking in nonviral gene delivery. *Pharmacol Rev* 58, no. 1: 32-45.

A. I. Khan, L. X. Lei, A. J. Norquist, and D. O'Hare. 2001. Intercalation and controlled release of pharmaceutically active compounds from a layered double hydroxide. *Chemical Communications*, no. 22: 2342-43.

A. I. Khan and D. O'Hare. 2002. Intercalation chemistry of layered double hydroxides: Recent developments and applications. *Journal of Materials Chemistry* 12, no. 11: 3191-98.

S. Y. Kim, J. M. Oh, J. S. Lee, T. J. Kim, and J. H. Choy. 2008. Gadolinium (III) diethylenetriamine pentaacetic acid/layered double hydroxide nanohybrid as novel T_1-magnetic resonant nanoparticles. *Journal of Nanoscience and Nanotechnology* 8, no. 10: 5181-84.

N. Z. Kiss, K. Ludanyi, L. Drahos, and G. Keglevich. 2009. Novel synthesis of phosphinates by the microwave-assisted esterification of phosphinic acids. *Synthetic Communications* 39, no. 13: 2392-404.

W. F. Kladnig and J. E. Horn. 1990. Submicron oxide powder preparation by microwave processing. *Ceramics International* 16, no. 2: 99-106.

S. Komarneni, E. Breval, D. M. Roy, and R. Roy. 1988. Reactions of some calcium silicates with metal-cations. *Cement and Concrete Research* 18, no. 2: 204-20.

L. B. Kong, P. Zhang, M. C. Liu, H. Liu, Y. C. Luo, and L. Kang. 2012. Fabrication of promising $LiFePO_4$/C composite with a core-shell structure by a moderate in situ carbothermal reduction method. *Electrochimica Acta* 70: 19-24.

H. Kozuka and J. D. MacKenzie. 1991. Microwave synthesis of metal carbides. In *Microwave: Theory and application in materials procesing*, ed. D. E. Clark, F. D. Gac and W. H. Sutton:387-94. Westerville, Ohio: American Ceramic Society.

W. M. Kriven, S. Y. Kwak, M. A. Wallig, and J. H. Choy. 2004. Bio-resorbable nanoceramics for gene and drug delivery. *Mrs Bulletin* 29, no. 1: 33-37.

Hench Larry L. 1973. Ceramics, glasses, and composites in medicine. *Medical Instrumentation* 7, no. 2: 136-44.

A. N. Lagarkov, S. M. Matitson, and A. K. Sarychev. 1992. Microwave properties of polymer materials containing conducting inclusions. *Abstracts of Papers of the American Chemical Society* 203: 214-PMSE.

F. Langa, P. de la Cruz, E. Espildora, A. Gonzalez-Cortes, A. de la Hoz, and V. Lopez-Arza. 2000. Synthesis and properties of isoxazolo 60 fullerene - donor dyads. *Journal of Organic Chemistry* 65, no. 25: 8675-84.

M. Larhed, C. Moberg, and A. Hallberg. 2002. Microwave-accelerated homogeneous catalysis in organic chemistry. *Accounts of Chemical Research* 35, no. 9: 717-27.

B. I. Lee, K. S. Lee, J. H. Lee, I. S. Lee, and S. H. Byeon. 2009. Synthesis of colloidal aqueous suspensions of a layered gadolinium hydroxide: A potential MRI contrast agent. *Dalton Transactions*, no. 14: 2490-95.

J. H. Lee, Y. M. Huh, Y. Jun, J. Seo, J. Jang, H. T. Song, S. Kim, E. J. Cho, H. G. Yoon, J. S. Suh, and J. Cheon. 2007. Artificially engineered magnetic nanoparticles for ultra-sensitive molecular imaging. *Nature Medicine* 13, no. 1: 95-99.

J. H. Lee, Y. W. Jun, S. I. Yeon, J. S. Shin, and J. Cheon. 2006. Dual-mode nanoparticle probes for high-performance magnetic resonance and fluorescence imaging of neuroblastoma. *Angewandte Chemie-International Edition* 45, no. 48: 8160-62.

S. J. Lee, E. A. Benson, and W. M. Kriven. 1999. Preparation of portland cement components by poly(vinyl alcohol) solution polymerization. *Journal of the American Ceramic Society* 82, no. 8: 2049-55.

S. J. Lee and W. M. Kriven. 1998. Crystallization and densification of nano-size amorphous cordierite powder prepared by a PVA solution polymerization route. *Journal of the American Ceramic Society* 81, no. 10: 2605-12.

Q. Levan and A. Gourdenne. 1987. Microwave curing of epoxy-resins with diaminodiphenylmethane .1. General features. *European Polymer Journal* 23, no. 10: 777-80.

A. Li, L. L. Qin, W. R. Wang, R. R. Zhu, Y. C. Yu, H. Liu, and S. L. Wang. 2011. The use of layered double hydroxides as DNA vaccine delivery vector for enhancement of anti-melanoma immune response. *Biomaterials* 32, no. 2: 469-77.

B. X. Li, J. He, D. G. Evans, and X. Duan. 2004. Enteric-coated layered double hydroxides as a controlled release drug delivery system. *International Journal of Pharmaceutics* 287, no. 1-2: 89-95.

B. X. Li, J. He, D. G. Evans, and X. Duan. 2004. Inorganic layered double hydroxides as a drug delivery system - intercalation and in vitro release of fenbufen. *Applied Clay Science* 27, no. 3-4: 199-207.

D. A. Li, Y. T. Zhang, M. Yu, J. Guo, D. Chaudhary, and C. C. Wang. 2013. Cancer therapy and fluorescence imaging using the active release of doxorubicin from MSPs/Ni-LDH folate targeting nanoparticles. *Biomaterials* 34, no. 32: 7913-22.

D. Li, Y. D. Huang, N. Sharma, Z. X. Chen, D. Z. Jia, and Z. P. Guo. 2012. Enhanced electrochemical properties of $LiFePO_4$ by mo-substitution and graphitic carbon-coating via a facile and fast microwave-assisted solid-state reaction. *Physical Chemistry Chemical Physics* 14, no. 10: 3634-39.

M. J. Li, L. Q. Sun, K. Sun, S. H. Yu, R. S. Wang, and H. M. Xie. 2012. Synthesis of nano-$LiFePO_4$ particles with excellent electrochemical performance by electrospinning-assisted method. *Journal of Solid State Electrochemistry* 16, no. 11: 3581-86.

F. Liang, Y. C. Yao, Y. N. Dai, B. Yang, W. H. Ma, and T. Watanabe. 2012. Preparation of porous structure $LiFePO_4$/C composite by template method for lithium-ion batteries. *Solid State Ionics* 214: 31-36.

J. Lim, S. W. Kang, J. Moon, S. Kim, H. Park, J. P. Baboo, and J. Kim. 2012. Low-temperature synthesis of lifepo4 nanocrystals by solvothermal route. *Nanoscale Research Letters* 7: 1-7.

J. Lim, D. Kim, V. Mathew, D. Ahn, J. Kang, S. W. Kang, and J. Kim. 2011. Plate-type $LiFePO_4$ nanocrystals by low temperature polyol-assisted solvothermal reaction and its electrochemical properties. *Journal of Alloys and Compounds* 509, no. 31: 8130-35.

J. Lim, V. Mathew, K. Kim, J. Moon, and J. Kim. 2011. One-pot synthesis of multi-morphous $LiFePO_4$ nanoparticles in polyol medium. *Journal of the Electrochemical Society* 158, no. 6: A736-A40.

J. H. Lin and J. S. Chen. 2012. Synthesis and electrochemical characterization of $LiFePO_4$/C composites prepared by the microemulsion method. *Electrochimica Acta* 62: 461-67.

Y. S. Lin, S. H. Wu, Y. Hung, Y. H. Chou, C. Chang, M. L. Lin, C. P. Tsai, and C. Y. Mou. 2006. Multifunctional composite nanoparticles: Magnetic, luminescent, and mesoporous. *Chemistry of Materials* 18, no. 22: 5170-72.

Yuan-kai. Lin, Zhi-Wei Wang, and Zhen-Xin Chen. Effect of organic additives on the performance of $LiFePO_4$ cathode materials. M.S.

A. Loupy, A. Petit, J. Hamelin, F. Texier-Boullet, P. Jacquault, and D. Mathe. 1998. New solvent free organic synthesis using focused microwaves. *Synthesis-Stuttgart*, no. 9: 1213-34.

J. Ma, B. H. Li, H. D. Du, C. J. Xu, and F. Y. Kang. 2012. Inorganic-based sol-gel synthesis of nano-structured $LiFePO_4$/C composite materials for lithium ion batteries. *Journal of Solid State Electrochemistry* 16, no. 4: 1353-62.

T. V. Mani, H. K. Varma, K. G. K. Warrier, and A. D. Damodaran. 1992. Preparation of Bi(Pb)-Sr-Ca-Cu-O superconductor by decomposition of acrylate polymer precursor gel. *British Ceramic Transactions and Journal* 91, no. 4: 120-23.

C. B. Mao, L. Zhou, X. Z. Wu, and X. Y. Sun. 1996. The combination of the polymeric solution-sol-gel process and combustion synthesis to manufacture bipbsrcacuo powder. *Superconductor Science & Technology* 9, no. 11: 994-1000.

C. Marcilly, P. Courty, and B. Delmon. 1970. Preparation of highly dispersed mixed oxides and oxide solid solutions by pyrolysis of amorphous organic precursors. *Journal of the American Ceramic Society* 53, no. 1: 56-&.

E. Matijevic. 1994. Uniform inorganic colloid dispersions - achievements and challenges. *Langmuir* 10, no. 1: 8-16.

H. Mazaki, M. Kakihana, and H. Yasuoka. 1991. Complex susceptibility of $Bi_2Sr_2Ca_{1-x}Y_xCu_2O_y$ from citrate sol-gel precursors. *Japanese Journal of Applied Physics Part 1-Regular Papers Short Notes & Review Papers* 30, no. 1: 38-42.

M. Michaelis, H. W. Doerr, and J. Cinatl, Jr. 2007. Valproic acid as anti-cancer drug. *Curr Pharm Des* 13, no. 33: 3378-93.

K. Micskei, L. Helm, E. Brucher, and A. E. Merbach. 1993. O-17 NMR-study of water exchange on $Gd(DTPA)(H_2O)^{2-}$ and $Gd(DOTA)(H_2O)^{-}$ related to NMR imaging. *Inorganic Chemistry* 32, no. 18: 3844-50.

A. G. Milnes and D. L. Feucht. 1972. *Heterojunctions and metal-semiconductor junctions*. New York: Academic Press, INC.

D. M. P. Mingos and D. R. Baghurst. 1992. The application of microwaves to the processing of inorganic materials. *British Ceramic Transactions and Journal* 91, no. 4: 124-27.

S. Miyata. 1983. Anion-exchange properties of hydrotalcite-like compounds. *Clays and Clay Minerals* 31, no. 4: 305-11.

S. M. Moghimi, A. C. Hunter, and J. C. Murray. 2001. Long-circulating and target-specific nanoparticles: Theory to practice. *Pharmacological Reviews* 53, no. 2: 283-318.

M. Morcrette, Y. Chabre, G. Vaughan, G. Amatucci, J. B. Leriche, S. Patoux, C. Masquelier, and J. M. Tarascon. 2002. In situ X-ray diffraction techniques as a powerful tool to study battery electrode materials. *Electrochimica Acta* 47, no. 19.

D. Morgan, A. Van der Ven, and G. Ceder. 2004. Li conductivity in Li_xMPO_4 (M = Mn, Fe, Co, Ni) olivine materials. *Electrochemical and Solid State Letters* 7, no. 2: A30-A32.

L. Moriggi, C. Cannizzo, E. Dumas, C. R. Mayer, A. Ulianov, and L. Helm. 2009. Gold nanoparticles functionalized with gadolinium chelates as high-relaxivity MRI contrast agents. *Journal of the American Chemical Society* 131, no. 31: 10828.

S. Morpurgo, M. Lojacono, and P. Porta. 1995. Copper-zinc-cobalt-chromium hydroxycarbonates and oxides. *Journal of Solid State Chemistry* 119, no. 2: 246-53.

S. Morpurgo, M. LoJacono, and P. Porta. 1996. Copper-zinc-cobalt-aluminium-chromium hydroxycarbonates and mixed oxides. *Journal of Solid State Chemistry* 122, no. 2: 324-32.

T. Muraliganth, A. V. Murugan, and A. Manthiram. 2008. Nanoscale networking of $LiFePO_4$ nanorods synthesized by a microwave-solvothermal route with carbon nanotubes for lithium ion batteries. *Journal of Materials Chemistry* 18, no. 46: 5661-68.

A. V. Murugan, T. Muraliganth, P. J. Ferreira, and A. Manthiram. 2009. Dimensionally modulated, single-crystalline $LiMPO_4$ (M=Mn, Fe, Co, and Ni) with nano-thumblike shapes for high-power energy storage. *Inorganic Chemistry* 48, no. 3: 946-52.

A. V. Murugan, T. Muraliganth, and A. Manthiram. 2008. Comparison of microwave assisted solvothermal and hydrothermal syntheses of $LiFePO_4$/C nanocomposite cathodes for lithium ion batteries. *Journal of Physical Chemistry C* 112, no. 37: 14665-71.

---. 2008. Rapid microwave-solvothermal synthesis of phospho-olivine nanorods and their coating with a mixed conducting polymer for lithium ion batteries. *Electrochemistry Communications* 10, no. 6: 903-06.

---. 2009. One-pot microwave-hydrothermal synthesis and characterization of carbon-coated $LiMPO_4$ (M=Mn, Fe, and Co) cathodes. *Journal of the Electrochemical Society* 156, no. 2: A79-A83.

A. W. Musumeci, T. L. Schiller, Z. P. Xu, R. F. Minchin, D. J. Martin, and S. V. Smith. 2010. Synthesis and characterization of dual radiolabeled layered double hydroxide nanoparticles for use in in vitro and in vivo nanotoxicology studies. *Journal of Physical Chemistry C* 114, no. 2: 734-40.

A. Navrotsky. 2003. Energetics of nanoparticle oxides: Interplay between surface energy and polymorphism. *Geochemical Transactions* 4: 34-37.

---. 2004. Energetic clues to pathways to biomineralization: Precursors, clusters, and nanoparticles. *Proc. Natl Acad. Sci. USA* 101: 12096-101.

---. 2011. Nanoscale effects on thermodynamics and phase equilibria in oxide systems. *ChemPhysChem* 12: 2207-15.

A. Navrotsky, C. Ma, K. Lilova, and N. Birkner. 2010. Nanophase transition metal oxides show large thermodynamically driven shifts in oxidation-reduction equilibria. *Science* 330: 199-201.

Gholam-Abbas Nazri and Gianfranco Pistola. 2009. *Lithium batteries-science and technology*: Springer.

S. P. Newman and W. Jones. 1998. Synthesis, characterization and applications of layered double hydroxides containing organic guests. *New Journal of Chemistry* 22, no. 2: 105-15.

M. H. Nguyen, S. J. Lee, and W. M. Kriven. 1999. Synthesis of oxide powders by way of a polymeric steric entrapment precursor route. *Journal of Materials Research* 14, no. 8: 3417-26.

Nicomp 380 DLS user manual. 2006. Particle Sizing Systems, Inc.

S. Nishimura, G. Kobayashi, K. Ohoyama, R. Kanno, M. Yashima, and A. Yamada. 2008. Experimental visualization of lithium diffusion in Li_xFePO_4. *Nature Materials* 7, no. 9: 707-11.

B. Niu, E. L. Qi, and J. Q. Wang. 2011. A simple and facile preparation of $LiFePO_4$ by a one-step microwave hydrothermal method. *Journal of Inorganic and Organometallic Polymers and Materials* 21, no. 4: 906-12.

M. Ogawa and H. Kaiho. 2002. Homogeneous precipitation of uniform hydrotalcite particles. *Langmuir* 18, no. 11: 4240-42.

T. Ogihara, Y. Azuma, and K. Katayama. 1999. Synthesis and electrochemical property of $LiMnO_2$ precursor by complexed polymerized method. *Journal of the Ceramic Society of Japan* 107, no. 5: 465-68.

J. M. Oh, S. J. Choi, S. T. Kim, and J. H. Choy. 2006. Cellular uptake mechanism of an inorganic nanovehicle and its drug conjugates: Enhanced efficacy due to clathrin-mediated endocytosis. *Bioconjugate Chemistry* 17, no. 6: 1411-17.

Yutaka Ohya. 2005. Aqueous precursors. In *Handbook of sol-gel science and technology-processing, characterization and applications,* ed. Sumio Sakka, I: Kluwer Academic Publishers.

W. Ostwald. 1897. Studien uber die bildung und umwandlung fester korper. *Z. Phys. Chem.* 22: 289-330.

T. Ould-Ely, M. Luger, L. Kaplan-Reinig, K. Niesz, M. Doherty, and D. E. Morse. 2011. Large-scale engineered synthesis of $BaTio_3$ nanoparticles using low-temperature bioinspired principles. *Nature Protocols* 6, no. 1: 97-104.

A. K. Padhi, K. S. Nanjundaswamy, and J. B. Goodenough. 1997. Phospho-olivines as positive-electrode materials for rechargeable lithium batteries. *Journal of the Electrochemical Society* 144, no. 4: 1188-94.

M. S. Pan, X. H. Lin, and Z. T. Zhou. 2012. Electrochemical performance of $LiFePO_4$/C doped with F synthesized by carbothermal reduction method using NH_4F as dopant. *Journal of Solid State Electrochemistry* 16, no. 4: 1615-21.

H. S. Panda and D. Bahadur. 2012. Study of the preparation, properties and kinetics of anion release in drug intercalated magnetic nanohybrids. *Materials Research Bulletin* 47, no. 3: 571-79.

L. J. Pang, M. S. Zhao, X. Zhao, and Y. J. Chai. 2012. Preparation and electrochemical performance of Gd-doped $LiFePO_4$/C composites. *Journal of Power Sources* 201: 253-58.

K. S. Park, J. T. Son, H. T. Chung, S. J. Kim, C. H. Lee, and H. G. Kim. 2003. Synthesis of $LiFePO_4$ by co-precipitation and microwave heating. *Electrochemistry Communications* 5, no. 10: 839-42.

K. S. Park, P. H. Xiao, S. Y. Kim, A. Dylla, Y. M. Choi, G. Henkelman, K. J. Stevenson, and J. B. Goodenough. 2012. Enhanced charge-transfer kinetics by anion surface modification of $LiFePO_4$. *Chemistry of Materials* 24, no. 16: 3212-18.

I. Pausch, H. H. Lohse, K. Schurmann, and R. Allmann. 1986. Syntheses of disordered and A1-rich hydrotalcite-like compounds. *Clays and Clay Minerals* 34, no. 5: 507-10.

B. Pei, H. X. Yao, W. X. Zhang, and Z. H. Yang. 2012. Hydrothermal synthesis of morphology-controlled $LiFePO_4$ cathode material for lithium-ion batteries. *Journal of Power Sources* 220: 317-23.

L. Perioli, T. Posati, M. Nocchetti, F. Bellezza, U. Costantino, and A. Cipiciani. 2011. Intercalation and release of antiinflammatory drug diclofenac into nanosized ZnAl hydrotalcite-like compound. *Applied Clay Science* 53, no. 3: 374-78.

V. V. Petrykin, M. Kakihana, Y. Tanaka, H. Yasuoka, M. Abe, and S. Eriksson. 2002. Ferromagnetic and superconducting properties of pure $RuCe_{0.5}Eu_{1.5}Sr_2Cu_2O_{10}$ samples prepared by polymerizable complex method. *Physica C-Superconductivity and Its Applications* 378: 47-51.

P. Porta and S. Morpurgo. 1995. Cu/Zn/Co/Al/Cr-containing hydrotalcite-type anionic clays. *Applied Clay Science* 10, no. 1-2: 31-44.

D. A. Porter and K. E. Easterling. 1996. Phase transformation in metals and alloys. In *Phase transformation in metals and alloys*: Chapman & Hall, UK.

D. H. Powell, O. M. NiDhubhghaill, D. Pubanz, L. Helm, Y. S. Lebedev, W. Schlaepfer, and A. E. Merbach. 1996. Structural and dynamic parameters obtained from oO-17 NMR, EPR and NMRD studies of monomeric and dimeric Gd^{3+} complexes of interest in magnetic resonance imaging: An integrated and theoretically self consistent approach. *Journal of the American Chemical Society* 118, no. 39: 9333-46.

P. P. Prosini, M. Carewska, S. Scaccia, P. Wisniewski, S. Passerini, and M. Pasquali. 2002. A new synthetic route for preparing $LiFePO_4$ with enhanced electrochemical performance. *Journal of the Electrochemical Society* 149, no. 7: A886-A90.

P. P. Prosini, D. Zane, and M. Pasquali. 2001. Improved electrochemical performance of a $LiFePO_4$-based composite cathode. *Electrochimica Acta* 46, no. 23: 3517-23.

L. L. Qin, M. Xue, W. R. Wang, R. R. Zhu, S. L. Wang, J. Sun, R. Zhang, and X. Y. Sun. 2010. The in vitro and in vivo anti-tumor effect of layered double hydroxides nanoparticles as delivery for podophyllotoxin. *International Journal of Pharmaceutics* 388, no. 1-2: 223-30.

M. M. Rahman, J. Z. Wang, R. Zeng, D. Wexler, and H. K. Liu. 2012. $LiFePO_4$-Fe_2P-C composite cathode: An environmentally friendly promising electrode material for lithium-ion battery. *Journal of Power Sources* 206: 259-66.

G. V. R. Rao, D. S. S. Narayana, U. V. Varadaraju, G. V. N. Rao, and S. Venkadesan. 1995. Synthesis of $YBa_2Cu_3O_7$ through different gel routes. *Journal of Alloys and Compounds* 217, no. 2: 200-08.

L. Ratke and P. W. Voorhees. 2002. In *Growth and coarsening-ostwald ripenning in material processing*, ed. Springer.

N. Ravet, J. B. Goodenough, S. Besner, M. Simoneau, P. Hovington, and M. Armand. *The Electrochemical Society and The Electrochemical Society of Japan Meeting Abstracts* 99, no. 2.

Y. Ren and P. G. Bruce. 2012. Mesoporous $LiFePO_4$ as a cathode material for rechargeable lithium ion batteries. *Electrochemistry Communications* 17: 60-62.

R. Roy, D. Agrawal, J. P. Cheng, and S. Gedevanishvili. 1999. Full sintering of powdered-metal bodies in a microwave field (vol 399, pg 668, 1999). *Nature* 401, no. 6750: 304-04.

D. V. Safronov, S. A. Novikova, T. L. Kulova, A. M. Skundin, and A. B. Yaroslavtsev. 2012. Lithium diffusion in materials based on lifepo4 doped with cobalt and magnesium. *Inorganic Materials* 48, no. 5: 513-19.

K. Saravanan, P. Balaya, M. V. Reddy, B. V. R. Chowdari, and J. J. Vittal. 2010. Morphology controlled synthesis of $LiFePO_4$/C nanoplates for Li-ion batteries. *Energy & Environmental Science* 3, no. 4: 457-64.

K. Saravanan, M. V. Reddy, P. Balaya, H. Gong, B. V. R. Chowdari, and J. J. Vittal. 2009. Storage performance of $LiFePO_4$ nanoplates. *Journal of Materials Chemistry* 19, no. 5: 605-10.

T. Sato, T. Wakabayashi, and M. Shimada. 1986. Adsorption of various anions by magnesium aluminum-oxide ($Mg_{0.7}Al_{0.3}O_{1.15}$). *Industrial & Engineering Chemistry Product Research and Development* 25, no. 1: 89-92.

Y. Sato, K. Yoshioka, V. V. Petrykin, M. Kakihana, Y. Tanaka, A. Yamaguchi, T. Katsumata, and H. Yasuoka. 2002. Effects of Ca doping and oxygen ordering in Cu-O chains on the superconducting properties of $(Ca_xLa_{1-x})(Ba_{2-x-y}La_{x+y})Cu_3O_{7+d}$ prepared by amorphous metal complex method. *Physica C-Superconductivity and Its Applications* 378: 160-66.

Schindle.Pw. 1967. Heterogeneous equilibria involving oxides hydroxides carbonates and hydroxide carbonates. *Advances in Chemistry Series*, no. 67: 196-&.

R. P. Sear. 2012. The non-classical nucleation of crystals: Microscopic mechanisms and applications to molecular crystals, ice and calcium carbonate. *International Materials Reviews* 57, no. 6: 328-56.

B. Sels, D. De Vos, M. Buntinx, F. Pierard, A. Kirsch-De Mesmaeker, and P. Jacobs. 1999. Layered double hydroxides exchanged with tungstate as biomimetic catalysts for mild oxidative bromination. *Nature* 400, no. 6747: 855-57.

B. F. Sels, D. E. De Vos, and P. A. Jacobs. 2001. Hydrotalcite-like anionic clays in catalytic organic reactions. *Catalysis Reviews-Science and Engineering* 43, no. 4: 443-88.

C. J. Serna, J. L. Rendon, and J. E. Iglesias. 1982. Crystal-chemical study of layered $Al_2Li(OH)_6^+X^-\cdot nH_2O$. *Clays and Clay Minerals* 30, no. 3: 180-84.

R. F. Service. 2010. Nanotechnology nanoparticle trojan horses gallop from the lab into the clinic. *Science* 330, no. 6002: 314-15.

E. E. Sileo, R. Rotelo, and S. E. Jacobo. 2002. Nickel zinc ferrites prepared by the citrate precursor method. *Physica B-Condensed Matter* 320, no. 1-4: 257-60.

M. Silion, D. Hritcu, I. M. Jaba, B. Tamba, D. Ionescu, O. C. Mungiu, and I. M. Popa. 2010. In vitro and in vivo behavior of ketoprofen intercalated into layered double hydroxides. *Journal of Materials Science-Materials in Medicine* 21, no. 11: 3009-18.

M. S. Song, Y. M. Kang, J. H. Kim, H. S. Kim, D. Y. Kim, H. S. Kwon, and J. Y. Lee. 2007. Simple and fast synthesis of $LiFePO_4$-C composite for lithium rechargeable batteries by ball-milling and microwave heating. *Journal of Power Sources* 166, no. 1: 260-65.

M. S. Song, D. Y. Kim, Y. M. Kang, Y. I. Kim, J. Y. Lee, and H. S. Kwon. 2008. Amphoteric effects of Fe_2P on electrochemical performance of lithium iron phosphate-carbon composite synthesized by ball-milling and microwave heating. *Journal of Power Sources* 180, no. 1: 546-52.

J. Sun, S. B. Zhou, P. Hou, Y. Yang, J. Weng, X. H. Li, and M. Y. Li. 2007. Synthesis and characterization of biocompatible Fe_3O_4 nanoparticles. *Journal of Biomedical Materials Research Part A* 80A, no. 2: 333-41.

X. R. Sun, J. J. Li, C. S. Shi, Z. Y. Wang, E. Z. Liu, C. N. He, X. W. Du, and N. Q. Zhao. 2012. Enhanced electrochemical performance of $LiFePO_4$ cathode with in-situ chemical vapor deposition synthesized carbon nanotubes as conductor. *Journal of Power Sources* 220: 264-68.

W. H. Sutton. 1989. Microwave processing of ceramic materials. *American Ceramic Society Bulletin* 68, no. 2: 376-86.

S. M. Sze. 1981. *Physics of semiconductor devices*. New York: Wiley.

M. Takahashi, S. Tobishima, K. Takei, and Y. Sakurai. 2001. Characterization of $LiFePO_4$ as the cathode material for rechargeable lithium batteries. *Journal of Power Sources* 97-8: 508-11.

K. M. L. Taylor, J. S. Kim, W. J. Rieter, H. An, W. L. Lin, and W. B. Lin. 2008. Mesoporous silica nanospheres as highly efficient MRI contrast agents. *Journal of the American Chemical Society* 130, no. 7: 2154.

R. M. Taylor. 1984. The rapid formation of crystalline double hydroxy salts and other compounds by controlled hydrolysis. *Clay Minerals* 19, no. 4: 591-603.

J. P. Thiel, C. K. Chiang, and K. R. Poeppelmeier. 1993. Structure of $LiAl_2(OH)_7{\cdot}2H_2O$. *Chemistry of Materials* 5, no. 3: 297-304.

K. Uematsu, A. Ochiai, K. Toda, and M. Sato. 2007. Solid chemical reaction by microwave heating for the synthesis of $LiFePO_4$ cathode material. *Journal of the Ceramic Society of Japan* 115, no. 1343: 450-54.

A. Vaccari. 1999. Clays and catalysis: A promising future. *Applied Clay Science* 14, no. 4: 161-98.

Aldert van der Ziel. 1968. *Solid state physical electronics*. New Jersey: Prentice Hall.

A. Vanderpol, B. L. Mojet, E. Vandeven, and E. Deboer. 1994. Ordering of intercalated water and carbonate anions in hydrotalcite - an NMR-study. *Journal of Physical Chemistry* 98, no. 15: 4050-54.

L. Vayssieres. 2003. Growth of arrayed nanorods and nanowires of ZnO from aqueous solutions. *Advanced Materials* 15, no. 5: 464-66.

S. Velu, V. Ramaswamy, A. Ramani, B. M. Chanda, and S. Sivasanker. 1997. New hydrotalcite-like anionic clays containing Zr^{4+} in the layers. *Chemical Communications*, no. 21: 2107-08.

S. Velu, D. P. Sabde, N. Shah, and S. Sivasanker. 1998. New hydrotalcite-like anionic clays containing Zr^{4+} in the layers: Synthesis and physicochemical properties. *Chemistry of Materials* 10, no. 11: 3451-58.

S. Velu, K. Suzuki, M. Okazaki, T. Osaki, S. Tomura, and F. Ohashi. 1999. Synthesis of new sn-incorporated layered double hydroxides and their thermal evolution to mixed oxides. *Chemistry of Materials* 11, no. 8: 2163-72.

V. Venkataramani, C. Rossner, L. Iffland, S. Schweyer, I. Y. Tamboli, J. Walter, O. Wirths, and T. A. Bayer. 2010. Histone deacetylase inhibitor valproic acid inhibits cancer cell proliferation via down-regulation of the alzheimer amyloid precursor protein. *J Biol Chem* 285, no. 14: 10678-89.

D. Vollath and K. E. Sickafus. 1993. Synthesis of ceramic oxide powders by microwave plasma pyrolysis. *Journal of Materials Science* 28, no. 21: 5943-48.

J. Wan, W. Cai, X. Meng, and E. Liu. 2007. Monodisperse water-soluble magnetite nanoparticles prepared by polyol process for high-performance magnetic resonance imaging. *Chemical Communications*, no. 47: 5004-06.

D. Y. Wang, X. D. Wu, Z. X. Wang, and L. Q. Chen. 2005. Cracking causing cyclic instability of $LiFePO_4$ cathode material. *Journal of Power Sources* 140, no. 1: 125-28.

G. X. Wang, S. L. Bewlay, K. Konstantinov, H. K. Liu, S. X. Dou, and J. H. Ahn. 2004. Physical and electrochemical properties of doped lithium iron phosphate electrodes. *Electrochimica Acta* 50, no. 2-3: 443-47.

G. X. Wang, S. Needham, J. Yao, J. Z. Wang, R. S. Liu, and H. K. Liu. 2006. A study on $LiFePO_4$ and its doped derivatives as cathode materials for lithium-ion batteries. *Journal of Power Sources* 159, no. 1: 282-86.

L. Wang, Y. D. Huang, R. R. Jiang, and D. Z. Jia. 2007. Nano- $LiFePO_4$/MWCNT cathode materials prepared by room-temperature solid-state reaction and microwave heating. *Journal of the Electrochemical Society* 154, no. 11: A1015-A19.

---. 2007. Preparation and characterization of nano-sized $LiFePO_4$ by low heating solid-state coordination method and microwave heating. *Electrochimica Acta* 52, no. 24: 6778-83.

L. J. Wang, H. Y. Xing, S. J. Zhang, Q. G. Ren, L. M. Pan, K. Zhang, W. B. Bu, X. P. Zheng, L. P. Zhou, W. J. Peng, Y. Q. Hua, and J. L. Shi. 2013. A gd-doped mg-al-ldh/au nanocomposite for CT/MR bimodal imagings and simultaneous drug delivery. *Biomaterials* 34, no. 13: 3390-401.

Y. Wang, Z. S. Feng, J. J. Chen, and C. Zhang. 2012. Synthesis and electrochemical performance of $LiFePO_4$/graphene composites by solid-state reaction. *Materials Letters* 71: 54-56.

Z. H. Wang, L. X. Yuan, J. Ma, L. Qie, L. L. Zhang, and Y. H. Huang. 2012. Electrochemical performance in Na-incorporated nonstoichiometric $LiFePO_4$/C composites with controllable impurity phases. *Electrochimica Acta* 62: 416-23.

P. R. Wei, S. H. Cheng, W. N. Liao, K. C. Kao, C. F. Weng, and C. H. Lee. 2012. Synthesis of chitosan-coated near-infrared layered double hydroxide nanoparticles for *in vivo* optical imaging. *Journal of Materials Chemistry* 22, no. 12: 5503-13.

Anthony R. West. 1989. *Solid state chemistry and its applications*: John Wiley & Sons.

D. L. West and D. A. Payne. 2003. Reactive-templated grain growth of $Bi_{1/2}(Na,K)_{1/2}TiO_3$: Effects of formulation on texture development. *Journal of the American Ceramic Society* 86, no. 7: 1132-37.

A. G. Whittaker and D. M. P. Mingos. 1995. Microwave-assisted solid-state reactions involving metal powders. *Journal of the Chemical Society-Dalton Transactions*, no. 12: 2073-79.

E. L. Wickstrom, T. A. Bacon, A. Gonzalez, D. L. Freeman, G. H. Lyman, and E. Wickstrom. 1988. Human promyelocytic leukemia HL-60 cell-proliferation and c-myc protein expression are inhibited by an antisense pentadecadeoxynucleotide targeted against c-myc messengerrna. *Proceedings of the National Academy of Sciences of the United States of America* 85, no. 4: 1028-32.

M. Willert-Porada, T. Krummel, B. Rohde, and D. Moorman. 1992. Ceramic powders by metalorganic and microwave processing. In *Microwave processing of materials iii*, ed. R. L. Beatty, W. H. Sutton and M. F. Iskander, 269:199-204. Pittsburgh, Pennsylvania: Materials Research Society.

S. H. Wu and M. T. Yu. 2007. Preparation and characterization of o-$LiMnO_2$ cathode materials. *Journal of Power Sources* 165, no. 2: 660-65.

J. Xie, S. Lee, and X. Chen. 2010. Nanoparticle-based theranostic agents. *Adv Drug Deliv Rev* 62, no. 11: 1064-79.

C. Xu, J. Xie, D. Ho, C. Wang, N. Kohler, E. G. Walsh, J. R. Morgan, Y. E. Chin, and S. Sun. 2008. Au-Fe_3O_4 dumbbell nanoparticles as dual-functional probes. *Angewandte Chemie-International Edition* 47, no. 1: 173-76.

H. Xu, J. Chang, J. Sun, and L. Gao. 2012. Graphene-encapsulated $LiFePO_4$ nanoparticles with high electrochemical performance for lithium ion batteries. *Materials Letters* 83: 27-30.

Z. P. Xu, N. D. Kurniawan, P. F. Bartlett, and G. Q. Lu. 2007. Enhancement of relaxivity rates of Gd-DTPA complexes by intercalation into layered double hydroxide nanoparticles. *Chemistry-a European Journal* 13, no. 10: 2824-30.

Z. P. Xu, G. S. Stevenson, C. Q. Lu, G. Q. M. Lu, P. F. Bartlett, and P. P. Gray. 2006. Stable suspension of layered double hydroxide nanoparticles in aqueous solution. *Journal of the American Chemical Society* 128, no. 1: 36-37.

Zhi Ping Xu and G. Q. Lu. 2006. Layered double hydroxide nanomaterials as potential cellular drug delivery agents. *Pure and Applied Chemistry* 78, no. 9.

A. Yamada and S. C. Chung. 2001. Crystal chemistry of the olivine-type $Li(Mn_yFe_{1-y})PO_4$ and $(Mn_yFe_{1-y})PO_4$ as possible 4 V cathode materials for lithium batteries. *Journal of the Electrochemical Society* 148, no. 8: A960-A67.

J. L. Yang, J. J. Wang, D. N. Wang, X. F. Li, D. S. Geng, G. X. Liang, M. Gauthier, R. Y. Li, and X. L. Sun. 2012. 3D porous $LiFePO_4$/graphene hybrid cathodes with enhanced performance for Li-ion batteries. *Journal of Power Sources* 208: 340-44.

S. F. Yang, P. Y. Zavalij, and M. S. Whittingham. 2001. Hydrothermal synthesis of lithium iron phosphate cathodes. *Electrochemistry Communications* 3, no. 9: 505-08.

X. L. Yang, F. Mou, L. L. Zhang, G. Peng, Z. X. Dai, and Z. Y. Wen. 2012. Enhanced rate performance of two-phase carbon coated $LiFePO_4$/(C+G) using natural graphite as carbon source. *Journal of Power Sources* 204: 182-86.

C. H. Yim, E. A. Baranova, Y. Abu-Lebdeh, and I. Davidson. 2012. Highly ordered $LiFePO_4$ cathode material for Li-ion batteries templated by surfactant-modified polystyrene colloidal crystals. *Journal of Power Sources* 205: 414-19.

S. Y. You, J. T. Shy, C. M. Wang, and H. C. I. Kao. 1998. Preparation of submicrometre $La_3CaBa_3Cu_7O_y$ superconducting powder with a polymeric precursor method using different polyprotic acids. *Superconductor Science & Technology* 11, no. 8: 800-02.

S. X. Yu, S. Dan, G. E. Luo, W. Liu, Y. Luo, X. Y. Yu, and Y. P. Fang. 2012. Synthesis, characterization, and electrochemical performance of $LiFePO_4$/C cathode materials for lithium ion batteries using various carbon sources: Best results by using polystyrene nano-spheres. *Journal of Solid State Electrochemistry* 16, no. 4: 1675-81.

W. Y. Yu, L. L. Wu, J. B. Zhao, Y. P. Zhang, G. Z. Li, and H. D. Gai. 2012. Fabrication of porous platelike $LiFePO_4$/C cathode materials via hydrothermal process. *Powder Technology* 230: 219-24.

B. Zhang, X. J. Wang, Z. J. Liu, H. Li, and X. J. Huang. 2010. Enhanced electrochemical performances of carbon coated mesoporous $LiFe_{0.2}Mn_{0.8}PO_4$. *Journal of the Electrochemical Society* 157, no. 3: A285-A88.

Qiao Zhang, Shu-Juan Liu, and Shu-Hong Yu. 2009. Recent advances in oriented attachment growth and synthesis of functional materials: Concept, evidence, mechanism, and future. *Journal of Materials Chemistry* 19, no. 2: 191-207.

Y. Zhang, H. Feng, X. B. Wu, L. Z. Wang, A. Q. Zhang, T. C. Xia, H. C. Dong, and M. H. Liu. 2009. One-step microwave synthesis and characterization of carbon-modified nanocrystalline $LiFePO_4$. *Electrochimica Acta* 54, no. 11: 3206-10.

Z. A. Zhang, T. Zeng, C. M. Qu, H. Lu, M. Jia, Y. Q. Lai, and J. Li. 2012. Cycle performance improvement of $LiFePO_4$ cathode with polyacrylic acid as binder. *Electrochimica Acta* 80: 440-44.

R. R. Zhao, I. M. Hung, Y. T. Li, H. Y. Chen, and C. P. Lin. 2012. Synthesis and properties of Co-doped $LiFePO_4$ as cathode material via a hydrothermal route for lithium-ion batteries. *Journal of Alloys and Compounds* 513: 282-88.

R. R. Zhao, B. Y. Lan, H. Y. Chen, and G. Z. Ma. 2012. Hydrothermal synthesis and properties of manganese-doped $LiFePO_4$. *Ionics* 18, no. 9: 873-79.

Y. Zhao, F. Li, R. Zhang, D. G. Evans, and X. Duan. 2002. Preparation of layered double-hydroxide nanomaterials with a uniform crystallite size using a new method involving separate nucleation and aging steps. *Chemistry of Materials* 14, no. 10: 4286-91.

H. L. Zou, G. H. Zhang, and P. K. Shen. 2010. Intermittent microwave heating synthesized high performance spherical $LiFePO_4$/C for Li-ion batteries. *Materials Research Bulletin* 45, no. 2: 149-52.